

---

# **Modulation der DNA-Mechanik durch Methylierung und Transkriptionsfaktoren**

Philip M. D. Severin

---

Dissertation



München 2012



---

**Modulation der DNA-Mechanik  
durch Methylierung und Transkriptionsfaktoren**

---

Dissertation

vorgelegt von

Philip Magnus Dirk Severin  
aus Aachen

angefertigt an der

Fakultät für Physik  
Ludwig-Maximilians-Universität München

München, April 2012

Erstgutachter: Prof. Dr. Hermann E. Gaub

Zweitgutachter: Prof. Dr. Philip Tinnefeld

Tag der mündlichen Prüfung: 19. Juni 2012

# Inhalt

<b>1. Zusammenfassung</b> .....	3
<b>2. Einleitung</b> .....	4
<b>3. Genregulation und Transkription</b> .....	7
<b>3.1 Genregulation durch Transkriptionsfaktoren</b> .....	7
- Transkriptionsfaktoren	
- Protein-DNA Wechselwirkungen	
<b>3.2 Genregulation durch DNA-Methylierung</b> .....	10
- Die fünfte DNA-Base: Methylcytosin	
- Die sechste DNA-Base: Hydroxymethylcytosin	
<b>4. Der Molekulare Kraftsensor: Quantifizierung Biomolekularer Wechselwirkungen</b> .....	13
<b>4.1 DNA-Mechanik</b> .....	13
- DNA als programmierbarer Baustein	
- Mechanische Eigenschaften von DNA	
<b>4.2 Der Molekulare Kraftsensor</b> .....	15
- Funktionsweise auf Einzelmolekül-Ebene	
- Parallelisierung via Soft-Print Lithographie und Mikrostrukturierung	
<b>5. Ergebnisse</b> .....	22
<b>5.1 DNA als molekularer Kraftsensor für Protein-DNA Wechselwirkungen</b> .....	22
- Bestimmung von Dissoziationskonstanten über Wechselwirkungskräfte	
- Unterschiedliche Entbindungsgeometrien des molekularen Kraftsensors	
- Möglichkeiten der Miniaturisierung des Molekularen Kraft-Assays	
<b>5.2 Die Erweiterung zum „molekularen AD-Wandler“</b> .....	27
- Prinzip des „molekularen AD-Wandlers“	
- 0-Abgleichverfahren zur Quantifizierung von molekularen Wechselwirkungskräften	
- Miniaturisierung und Parallelisierung des Molekularen Kraft-Assays zum „Binding-Force-Chip“	
<b>5.3 Einfluss von epigenetischen Modifikationen auf die DNA-Mechanik</b> .....	33
- Methylcytosin verändert richtungs- und sequenzabhängig die Wechselwirkungskräfte von DNA	
- Methylcytosin verändert die Potentialweite des DNA Doppelstranges	
- Vergleich von Hydroxymethylcytosin und Methylcytosin	
<b>6. Ausblick</b> .....	40

<b>7. Anhang</b> .....	43
<b>7.1 Publikationen</b> .....	43
P1 „A High Throughput Molecular Force Assay for Protein–DNA Interactions“	
P2 „Quantitative Detection of Small Molecule/DNA Complexes Employing a Force- Based and Label-Free DNA-Microarray“	
P3 „DNA as a Force Sensor in an Aptamer-Based Biochip for Adenosine“	
P4 „Force-Driven Separation of Short Double-Stranded DNA“	
P5 „DNA-Protein Binding Force Chip“	
P6 „Cytosine Methylation alters DNA Mechanical Properties“	
P7 „Peptide:Antibody Complex as Handle for Single-Molecule Cut & Paste“	
<b>7.2 Manuskripte für Publikationen</b> .....	155
M1 „Cytosine Hydroxymethylation Affects DNA Strand Separation“	
M2 „Probing the Force-induced Globule-Coil Transition of Individual Polymer Chains via Single Molecule Force Spectroscopy“	
<b>8. Referenzen</b> .....	184
<b>9. Lebenslauf</b> .....	188
<b>10. Danksagung</b> .....	189

# 1. Zusammenfassung

Genregulation gibt der Zelle die Kontrolle über Struktur und Funktion, und ist die Basis für zelluläre Differenzierung, Morphogenese und die Vielseitigkeit und Anpassungsfähigkeit von jedem Organismus. Um zu begreifen, wie eine Zelle ihre Funktion organisiert und wie sich ganz individuelle Organismen ausbilden, obwohl die gleichen genetischen Informationen vorhanden sind, muss man die Regulation der Genexpression im Detail verstehen. Diese Regulation wirkt an verschiedenen Stellen der Genexpression und besteht aus einer Vielzahl von komplexen Prozessen, die untereinander verbunden sind. Somit ist das Verständnis der zugrundeliegenden molekularen Mechanismen und ihres Zusammenspiels für Biologie und Biophysik von großer Bedeutung.

Ziel dieser Arbeit ist die Untersuchung von Wechselwirkungen und Wechselwirkungskräften zwischen Biomolekülen, die an der Genregulation und der Epigenetik, auf der Ebene der Transkription beteiligt sind. Insbesondere konnten Protein-DNA-Wechselwirkungen und der Einfluss epigenetischer DNA-Modifikationen quantifiziert werden. Für die Messungen wurde ein molekularer Kraftsensor und als dessen Erweiterung ein molekularer Analog-Digital-Wandler entwickelt. Diese molekularen Sensoren ermöglichen die direkte Messung der Wechselwirkungskräfte zwischen DNA und Liganden. Mit dem molekularen Kraftsensor können außerdem hochparallel Messungen durchgeführt werden, wobei durch den symmetrischen, molekularen Aufbau zudem eine sehr hohe Sensitivität erreicht wird. Die Verwendung dieser Methode ermöglichte es, den Einfluss der epigenetisch modifizierten Basen Methylcytosin und Hydroxymethylcytosin („5. und 6. Base der DNA“) auf die mechanische Stabilität der DNA-Doppelhelix zu untersuchen.

Es wird gezeigt, dass mit dem aus DNA-Oligomeren aufgebauten molekularen Kraftsensor Protein-DNA-Wechselwirkungen detektiert und deren Dissoziationskonstanten bestimmt werden können. Unter anderem wird die Wechselwirkung der Endonuklease EcoRI mit ihrer DNA-Erkennungssequenz quantifiziert. Hierfür wurden molekulare Kraftsensoren in Zipper- und Scher-Geometrie entworfen. Bei dem neu entwickelten Aufbau des Kraftsensors mit integriertem Förster-Resonanzenergietransfer-Farbstoffpaar genügt schon eine Fläche von  $25 \mu\text{m}^2$ , um die Stärke von Ligand-DNA-Wechselwirkungen bestimmen zu können. Diese Fläche liegt deutlich unterhalb der Messfleckgröße aktueller DNA-Mikroarrays. Damit erfüllt der molekulare Kraftsensor bezüglich der Messfleckdichte die Voraussetzung für moderne Hochdurchsatz-Methoden.

In einem zweiten Schritt wird der molekulare Kraftsensor zu einem „molekularen Analog-Digital-Wandler“ erweitert. In Analogie zum elektronischen Flash-Analog-Digital-Wandler, bei dem mehrere Komparatoren mit unterschiedlichen Referenzschaltungen parallel geschaltet sind, werden beim molekularen Analog-Digital-Wandler parallel räumlich getrennte, molekulare Kraftsensoren mit unterschiedlich stabilen Referenz-Wechselwirkungen zur Bestimmung einer unbekanntenen molekularen Wechselwirkung verwendet. Durch eine Kompensationsmessung wird dann die Kraft von Ligand-DNA-Wechselwirkungen bestimmt. Es werden die Wechselwirkungen eines Pyrrol-Imidazol Hairpin-Polyamides, der Endonuklease EcoRI und des Transkriptionsfaktors p53 zur jeweiligen DNA-Erkennungssequenz vermessen. Eine hochparallele Version mit Messfleckgrößen mit einem Durchmesser von minimal  $15 \mu\text{m}$  konnte realisiert werden. Abgeleitet vom Bell-Evans-Modell wurde ein analytisches Modell zur Beschreibung des molekularen Analog-Digital-Wandlers entwickelt.

Neben den Protein-DNA-Wechselwirkungen werden die epigenetisch modifizierten DNA-Basen Methylcytosin (mC) und Hydroxymethylcytosin (hmC) untersucht. Es wird der Nachweis erbracht, dass sich die mechanische Stabilität der DNA-Doppelhelix bei Separation in zwei Einzelstränge in beiden Fällen signifikant um mehrere Piconewton ändert. Die Stärke des Effekts ist abhängig von der DNA-Sequenz und der Richtung der angelegten Kraft. Durch Einzelmolekül-Kraftspektroskopie wird eine Reduzierung der Potentialweite durch mC aufgezeigt. Außerdem konnte mit Hilfe von Molekulardynamik-Simulationen der Effekt für mC und teilweise auch für hmC auf molekularer Ebene aufgeklärt werden. Es wird ein Modell entwickelt, das erklärt, wie dieser Effekt einen Einfluss auf die Genregulation ausüben kann.

## 2. Einleitung

Die Beschreibung von Komplexität und komplexen Netzwerken stellt eine Herausforderung an die Physik dar. In den unterschiedlichsten Bereichen wie in der Biophysik, Biologie, Informatik und Bioinformatik, aber auch in den „Social Media“ und im Finanzwesen spielt das Verstehen und die Beschreibung von komplexen Systemen und Netzwerken eine zentrale Rolle. Durch die Erfahrungen in diesen Bereichen ist offensichtlich geworden, dass es häufig nicht mehr ausreicht, mittels Reduktionismus nur die grundlegenden Bestandteile eines derartigen Systems zu betrachten [1]. Vielmehr werden Theorien benötigt und entwickelt, die diese komplexen Netzwerke möglichst vollständig beschreiben können, und uns so helfen, diese zu verstehen und unter Umständen auch in gewissen Grenzen kontrollieren zu können. In der Medizin hat sich zum Beispiel gezeigt, dass es kein einzelnes „Krebs-Gen“ gibt, sondern ein typischer Krebspatient einige dutzend Mutationen aus einem Pool von zirka 300 relevanten Genen hat – ein schwer zu beschreibendes kombinatorisches Problem. Das Verständnis vom Bewusstsein kann nicht auf das Verständnis eines Neurons reduziert werden. Das Bewusstsein entsteht durch das Zusammenspiel von Milliarden von Synapsen. Und um die Funktionsweise einer Zelle im Ganzen zu verstehen, müssen die komplexen und ineinander verwobenen Netzwerke, in denen Biomoleküle wie DNA, Proteine und Metabolite miteinander wechselwirken, entschlüsselt werden.

Der enorme Fortschritt der letzten Jahre im Verständnis komplexer Netzwerke, wie er zum Beispiel in der molekularen Biologie stattgefunden hat, lässt sich mit einem Wort begründen: Daten [1]. Dank neuer High-Throughput-Technologien (Hochdurchsatz-Messmethoden) und kostengünstiger Sensoren konnte eine Fülle von Daten generiert werden, die das „Innenleben“ vieler dieser komplexen Systeme dokumentiert [2-5]. Zwar gibt es im Bereich der molekularen Biologie und Biotechnologie immer weitere Entwicklungen im Bereich der High-Throughput-Technologien, jedoch sind die gewonnenen Daten häufig artefakt-behaftet, verrauscht und nicht vollständig, so dass immer noch ein außerordentlicher Bedarf an neuen, präziseren Technologien vorhanden ist [6, 7]. Ein positives Beispiel für die Technologieentwicklung stellt die genomweite DNA-Sequenzierung dar. Das „Human Genome Project“ startete im Jahr 1990 und benötigte noch über 10 Jahre um 90 % des menschlichen Genomes zu sequenzieren. Heute gibt es diverse Methoden – alle aus dem Bereich der Nano-Biotechnologie – die, basierend auf unterschiedlichsten Prinzipien wie Nanopore-Sequenzierung [8, 9], Einzelmolekül-Echtzeitsequenzierung in „Zero-Mode Waveguides“ [10] oder „Ion Semiconductor Sequencing“ [11, 12], annähernd das gesamte Genom des Menschen innerhalb eines Tages mit einer äußerst geringen Fehlerrate bestimmen können.

Um zu verstehen, wie in einer Zelle die Information von bestimmten Genen in Funktion umgesetzt wird und wie sich aufgrund dessen individuelle Organismen ausbilden, muss zunächst einmal die Regulation der Genexpression verstanden werden. Kontinuierlich klammern sich in einer Zelle viele tausend Proteine an das Genom oder lösen sich ab und kreieren die dynamische Biochemie, die das Leben der Zelle antreibt. Transkriptionsfaktoren schalten die entsprechenden Gene an oder aus. Einige Proteine, im Besonderen Histone, formen die Chromosomen, indem sie an die DNA binden und die DNA in die charakteristische Spiralförmigkeit biegen und so die Expression von Genen herunterregulieren. Oder sie wickeln die DNA wieder ab und machen Gene so zugänglich für die Expression. Andere Proteine wiederum schneiden DNA an spezifischen Sequenzen oder helfen, die DNA-Doppelhelix in Einzelstränge aufzutrennen. Es ist



die Kontrolle der Genexpression, also die Genregulation, welche Gehirn von Leber und Lymphozyten von Endothelzellen differenziert [13].

Die Genregulation besteht aus einer Vielzahl von Prozessen, die miteinander verbunden sind. So gibt es zum Beispiel im menschlichen Genom um die 2600 Proteine mit DNA-Binde-Domänen, von denen die meisten Transkriptionsfaktoren sind, durch die die Transkription der DNA kontrolliert wird [14]. Am Beispiel des menschlichen Genoms, das aus zirka  $3 \times 10^9$  Basenpaaren besteht, und eines typischen DNA-bindenden Proteins, das spezifisch an mehrere, ähnliche, 6 basenpaar-lange Sequenzen mit unterschiedlicher Affinität bindet, wird klar, dass es alleine für ein Protein eine Vielzahl von Sequenzabschnitten auf dem Genom gibt, an die es mit unterschiedlicher Affinität bindet. Um das komplexe Netzwerk aus Wechselwirkungen zwischen vielen DNA-Bindestellen und DNA-bindenden Proteinen zu erforschen, zu untersuchen mit welcher Affinität dies geschieht und wie sich diese Eigenschaften unter anderen Bedingungen verändern, muss eine enorme Vielzahl an Messungen vorgenommen werden. Dafür werden neuartige High-Throughput-Techniken für die Quantifizierung von Protein-DNA Wechselwirkungen benötigt, die vollständigere und genauere Ergebnisse liefern [6, 7], indem sie z.B. einen größeren Bereich von Affinitäten abdecken.

Um derartige Genregulationsnetzwerke beschreiben zu können, müssen die einzelnen Wechselwirkungspartner bekannt und die zu Grunde liegende Funktionsweise der molekularen Wechselwirkung genau verstanden sein. Eine sehr direkte Herangehensweise ist die Bestimmung der Wechselwirkungskräfte, die zwei interagierende Biomoleküle zusammenhält, wie dies mit Einzelmolekül-Kraftspektroskopie möglich ist [15-18]. Kraftmessungen an einzelnen Molekülen erlauben einen tiefen Einblick in die Mechanik von Biomolekülen und deren dynamischen Wechselwirkungen untereinander, wie es mit anderen Methoden nicht möglich ist [19-22]. Das zentrale Problem der Einzelmolekül-Kraftmessungen stellte bis jetzt die unzureichende Parallelisierbarkeit dar, die nötig ist, um für High-Throughput-Messungen geeignet zu sein.

Neben den Transkriptionsfaktoren kann die Regulation der Transkription auch durch epigenetische Prozesse erfolgen. Die Epigenetik hat sich in den letzten Jahren rasant entwickelt [13]. Sie beschreibt Mechanismen, mit denen vererbliche Veränderungen der Genexpressionsmuster hervorgerufen werden können, ohne dabei die DNA Sequenz zu verändern. Die Epigenetik selbst besteht aus hochkomplexen und vielschichtigen Prozessen, die bis jetzt erst ansatzweise erforscht sind. Zwei bekannte Vertreter stellen die Modifikation von Histonen und die Methylierung der DNA dar. Während die biologischen Auswirkungen dieser Prozesse schon teilweise aufgedeckt sind, sind viele Zusammenhänge der molekulare Funktionsweise und die zugrunde liegenden Mechanismen noch nicht verstanden [23]. Neben der Methylierung der DNA, die bei Säugetieren am Cytosin stattfindet und aus Cytosin Methylcytosin macht, wurden in den letzten Jahren noch weitere DNA Modifikationen gefunden, welche höchstwahrscheinlich eine epigenetische Funktion besitzen [23-25]. Im Vergleich zu Transkriptionsfaktoren, bei denen die molekulare Funktionsweise schon zu großen Teilen aufgeklärt ist, ist man bei der Epigenetik immer noch sehr mit dem Verständnis der molekularen Mechanismen beschäftigt, bevor in Zukunft dieses komplexe, feingesponnene Netzwerk der Epigenetik im Ganzen beschrieben werden kann.

Zentrales Thema dieser Dissertation ist die Erforschung von Wechselwirkungen und Wechselwirkungskräften zwischen Biomolekülen, die für die Genregulation einschließlich der Epigenetik auf transkriptionaler Ebene verantwortlich sind. Erstens wurden neue Techniken entwickelt, der molekulare Kraftsensor und als Weiterentwicklung der molekulare AD-Wandler, um DNA-Ligand-Wechselwirkungen, insbesondere DNA-Protein-Wechselwirkungen hochparallelisiert mit äußerster Genauigkeit bestimmen zu können. Die Leistungsfähigkeit dieser

Techniken wurden mit unterschiedlichsten Liganden, wie einem Pyrrol-Imidazol Hairpin-Polyamide, der Endonuklease EcoRI oder dem Transkriptionsfaktor p53 erprobt. Zweitens wird mittels dieser und anderer Techniken der Einfluss von den epigenetisch modifizierten Basen Methylcytosin und Hydroxymethylcytosin, der 5. und 6. Base der DNA, auf die mechanische Stabilität der DNA-Doppelhelix erforscht und ein Modell entwickelt, das beschreibt, wie diese epigenetischen Modifikationen auf einer bis jetzt unbekannten Weise die Transkription von Genen regulieren können. Für eine detaillierte Beschreibung, ausführliche Analyse und technische Einzelheiten dieser kumulativen Dissertation wird an den entsprechenden Stellen auf die zugehörigen Publikationen im Anhang verwiesen.

### **3. Genregulation und Transkription**

In der Biologie wird die Steuerung der Genexpression – der Aktivität von Genen – als Genregulation bezeichnet. Die Genregulation bestimmt, in welcher Konzentration das von dem Gen kodierte Protein in der Zelle vorhanden sein soll. Hierbei kann die Regulation auf verschiedenen Ebenen der Genexpression stattfinden. Unter der Genexpression versteht man den Prozess des Umsetzens der im Gen enthaltenen Information in das dazugehörige Genprodukt. Die Genexpression besteht aus mehreren Schritten, einschließlich Transkription, RNA Spleißen, Translation und post-translationalen Modifikationen von Proteinen. Bei jedem dieser Schritte kann durch regulatorische Faktoren die Genexpression beeinflusst werden. Genregulation gibt der Zelle die Kontrolle über Struktur und Funktion, und ist die Basis für zelluläre Differentiation, Morphogenese und die Vielseitigkeit und Anpassungsfähigkeit von jedem Organismus.

Der erste Schritt der Genexpression ist die Transkription. Bei der Transkription wird eine komplementäre RNA-Kopie von der DNA-Sequenz erzeugt. Der Prozess teilt sich in mehrere zentrale Schritte auf: Bei der Initiation bindet ein der RNA-Polymerase-Proteinkomplex an den Promotor-Abschnitt der DNA. Bei der Elongation wird die DNA-Doppelhelix von der RNA-Polymerase entspiralisiert, so dass jeweils 10 bis 20 Basen der DNA in Form eines Einzelstrangs vorliegen. In Folge legen sich am codogenen Strang der DNA frei komplementäre Ribonukleotide an, die durch die RNA-Polymerase zu einem RNA-Strang – hauptsächlich mRNA, tRNA und rRNA – synthetisiert werden. Am Terminator wird die Transkription beendet, das RNA-Transkript wird entlassen und die RNA-Polymerase fällt von der DNA ab. Dieser Prozess unterscheidet sich für Prokaryoten und Eukaryoten unter anderem in der Komplexität in der involvierten molekularen Maschinerie.

Die Regulation der Transkription kann in drei zentrale Arten des Einflusses eingeteilt werden: genetisch, durch direktes interagieren eines Kontrollfaktors mit einem Gen, durch Modulation, bei der ein Kontrollfaktor Einfluss auf die Transkriptions-Maschinerie nimmt und drittens durch epigenetische Regulation.

#### **3.1 Genregulation durch Transkriptionsfaktoren**

Die direkte Wechselwirkung von einem Protein mit DNA stellt die einfachste und direkteste Methode dar, bei der der Transkriptionslevel eines bestimmten Gens verändert werden kann. Gene besitzen häufig mehrere Bindungsstellen für Proteine nahe der zu transkribierenden Gensequenz, mit der speziellen Funktion die Transkription zu regulieren. Dabei gibt es mehrere unterschiedliche Arten Transkriptionsfaktoren, die sich in „Enhancer“, „Insulators“, „Repressoren“ und „Silencer“ einteilen lassen. Der Mechanismus wie Transkriptionsfaktoren (TF) wirken ist sehr unterschiedlich. Es können zum Beispiel Bindungsstellen durch TF für die RNA-Polymerase blockiert werden. Andererseits können TF aber auch das Binden des RNA-Polymerase-Proteinkomplexes fördern und sogar weitere Proteine rekrutieren.

## Transkriptionsfaktoren

Es gibt zirka 2600 Proteine im menschlichen Genom, die DNA-Binde-Domänen enthalten und von denen die meisten höchstwahrscheinlich als Transkriptionsfaktoren fungieren. So gesehen sind zirka 10 % der Gene unseres genetischen Kodes Transkriptionsfaktoren, die somit die größte Protein-Familie darstellen [14].

Transkriptionsfaktoren werden nach ihrer Funktion in allgemeine (basale) und spezifische TF eingeteilt. Basale TF sind meistens Bestandteil des Präinitiations-RNA-Polymerasekomplexes und binden an allgemeine DNA-Motive beziehungsweise Promotorelemente, wie zum Beispiel der TATA-Box. Im Gegensatz dazu vermitteln spezifische TF der Polymerase welches Gen aktiviert werden soll. Die DNA-Bereiche, an die Sie binden, haben eine bestimmte Erkennungssequenz – *cis*-Elemente – die vom TF spezifisch erkannt und gebunden werden. Die Spezifität der Erkennung der Bindungssequenz und Aktivierung eines Genes wird dabei durch die Bildung von dimeren und quartären Strukturen von TF und durch kooperatives Binden von mehreren TF erhöht [26].

Transkriptionsfaktoren bestehen typischerweise aus einer DNA-Binde-Domäne, einer Transaktivierungs-Domäne und teilweise einer „Signal-Sensing“-Domäne. Die DNA-Binde-Domäne lässt sich nach der dreidimensionalen Struktur in unterschiedliche Familien einteilen: Helix-turn-helix-TF, Homöodomänen-TF Helix-loop-helix-TF, Zink-Finger-TF und Leucin-Zipper-Transkriptionsfaktoren.

## Protein-DNA Wechselwirkungen

Protein-DNA Wechselwirkungen werden von DNA-bindenden Proteinen verursacht, die eine spezifische oder allgemeine Affinität gegen einzel- oder doppelsträngige DNA haben. Dabei wird die kleine Furche („Minor Groove“), die große Furche („Major Groove“) der DNA Doppelhelix oder das Zuckerphosphat-Rückgrat der DNA von den Proteinen zum Binden an die DNA verwendet. Die Furchen stellen hydrierte Canyons dar, in die Sekundärstruktur-Elemente von Proteinen binden können. Zum Beispiel hat die große Furche einer DNA in B-Form eine genügende Breite (~11,7 Å) und Tiefe (~8,8 Å) um Platz für alpha-Helices oder beta-Faltblätter bieten zu können. Im Vergleich dazu ist die kleine Furche der DNA in B-Form enger (~5,7 Å in Breite und ~7,5 Å in Tiefe) und weniger zugänglich als die große Furche. Je nach Protein wird die dreidimensionale Struktur der DNA mehr oder weniger durch das Binden deformiert [26].

Protein-DNA Wechselwirkungen entstehen durch Wasserstoffbrückenbindungen, ionische Bindungen („Salt Bridges“), den hydrophoben Effekt und Van-der-Waals-Wechselwirkungen. Wasserstoffbrückenbindungen sind von zentraler Bedeutung für die Erkennung der DNA-Sequenz. Einen großen Beitrag zu freien Enthalpie bei der Komplexbildung liefert typischerweise der hydrophobe Effekt. Van-der-Waals-Wechselwirkungen und direkte oder durch Wassermoleküle vermittelte Wasserstoffbrückenbindungen tragen ebenfalls bei der Bildung des spezifisch gebundenen Protein-DNA-Komplexes bei.

Sequenzspezifische Erkennung geschieht einerseits durch direkte Wechselwirkungen von Wasserstoffbrückenbindungen zwischen DNA-Basen und Protein, andererseits aber auch indirekt durch die konformationsbedingte Effekte, wie die Form der DNA, die durch benachbarte Basen (zur Erkennungssequenz) auch beeinflusst wird. Die Formation des Protein-DNA-Komplexes stellt somit ein empfindliches Gleichgewicht aus Wechselwirkungen dar, die die Komplexbildung unterstützen, und energetisch ungünstigen Beiträgen. Ein gutes Modellsystem bildet die Bindung des Restriktionsenzym *EcoRI* an DNA, welches auch in Publikation P1 und P5 verwendet wurde. In Abbildung 1 sind die Röntgen-Kristallstruktur von

EcoRI und die energetischen Beiträge zur Wechselwirkung zwischen DNA-Sequenz und EcoRI dargestellt.

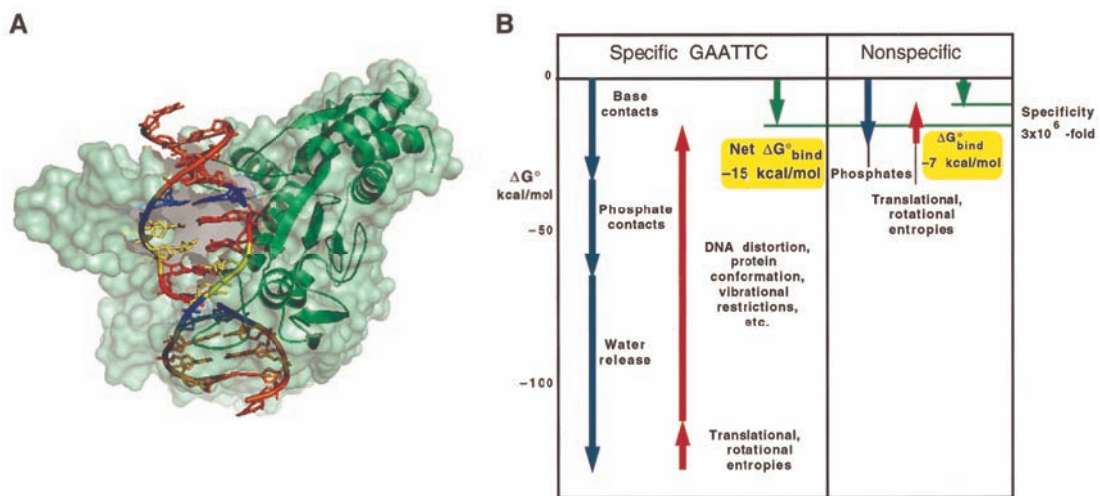


Abbildung 1: (a) 3D-Kristallstruktur von EcoRI mit spezifischer Zielsequenz GAATTC (PDB Code „1ERI“). Die Oberfläche des Homodimers ist in Grün und das Rückgrat eines einzelnen Monomers ist mit Sekundärstrukturelementen dargestellt [27]. (b) Zusammensetzung der Bindungsenergie von spezifischem zu unspezifischem Binden von EcoRI an DNA. Die Bestandteile stellen eine grobe Schätzung an Hand von Messungen dar und sind laut mit einem Fehler von bis zu 50 % behaftet. Des Weiteren können diese Beiträge zur Komplex-Bildung nicht als unabhängig voneinander betrachtet werden [28].

Grundlegende Parameter mit der sich Protein-DNA-Wechselwirkungen beschreiben lassen, sind die DNA-Erkennungssequenz und Spezifität, die Affinität, die sich durch die Dissoziationskonstante  $K_D$  beschreiben lässt, sowie die Assoziations- und Dissoziationsraten. Diese Parameter lassen sich in einem eingeschränkten  $K_D$ -Bereich teilweise mit klassischen Methoden bestimmen. Darüber hinaus hat sich die Einzelmolekül-Kraftspektroskopie zur Untersuchung von biomolekularen Wechselwirkungen, wie Protein-DNA Wechselwirkungen, als sehr nützliche Technik erwiesen.

Mit Einzelmolekül-Kraftspektroskopie können Informationen über die Protein-DNA-Wechselwirkung bestimmt werden, wie die Abrisskraft einer Bindung oder die Energielandschaft, welche anders nicht gemessen werden können. Über die Abhängigkeit der Abrisskraft von der Ladungsrate lassen sich über das Bell-Evans-Modell weitere Parameter wie die Potentialweite und die natürliche Dissoziationsrate bestimmen, die die Aktivierungsbarriere (Energiebarriere) der molekularen Bindung beschreibt. Dabei stellt die Potentialweite eine charakteristische Entfernung zur ersten Aktivierungsbarriere dar. Obwohl das Bell-Evans-Modell starke Vereinfachungen (nur eine ausgeprägte Aktivierungsbarriere, kraftunabhängige Potentialweite) beinhaltet, hat es sich experimentell als sehr hilfreich erwiesen um molekulare Wechselwirkungen zu charakterisieren. Des Weiteren konnte gezeigt werden, dass das Bell-Evans-Modell auch für komplexere molekulare Wechselwirkungen eine gute Näherung darstellt um auch die Bindung zwischen Protein und DNA zu charakterisieren.

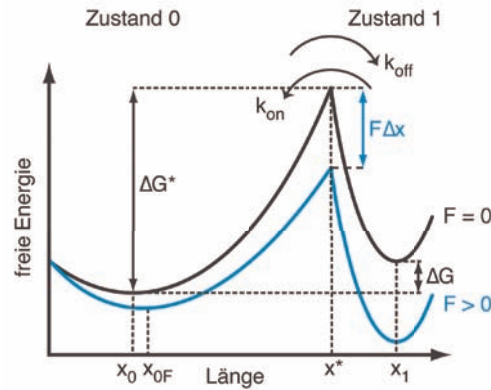


Abbildung 2: Bild: Schematische Darstellung von zwei durch eine Aktivierungsbarriere (bei  $x^*$ ) getrennten Zuständen. Durch eine externe Kraft wird die Potentiallandschaft gekippt. Auf diese Weise wird die Höhe der Energiebarriere erniedrigt und die Übergangswahrscheinlichkeit von Zustand 0 nach 1 erhöht.

Für eine ausführliche Beschreibung der Theorie zur Dissoziation molekularer Bindungen unter Kraft wird an dieser Stelle abgesehen und auf die Fachliteratur verwiesen [29-32]. Abbildung 2 zeigt schematisch, wie unter einer externen Kraft  $F$  die Energielandschaft eines Zwei-Zustand-Systems beeinflusst wird. Für kleine Änderungen des Grundzustandes ( $x_{0F} - x_0 \ll x_1 - x_0$ ) verkleinert sich die Aktivierungsbarriere zu:  $\Delta G^* = \Delta G^*(0) - F \Delta x$  (mit  $\Delta x^* = x^* - x_0$ ). Ebenso ändert sich die freie Energie zwischen Zustand 0 und Zustand 1, so dass unter Kraft für die Rate  $k_{+1}$  und die Gleichgewichtskonstante  $K_{eq}$  Folgendes gilt:

$$k_{off}(F) = a \exp\left(-\frac{\Delta G^*(0) - F \Delta x^*}{k_B T}\right) = k_{off}^0 \exp\left(\frac{F \Delta x^*}{k_B T}\right) \quad \wedge \quad K_{eq}(F) = \exp\left(-\frac{\Delta G - F \Delta x}{k_B T}\right) = K_{eq}^0 \exp\left(\frac{F \Delta x}{k_B T}\right)$$

### 3.2 Genregulation durch DNA-Methylierung

Epigenetik beschäftigt sich mit den vererblichen Änderungen in der Genexpression beziehungsweise des Phänotyps, welche durch Mechanismen verursacht werden, die nicht die DNA-Sequenz selbst beeinflussen. Epigenetische Mechanismen verändern nicht die Abfolge der Nukleotide der DNA, sondern beeinflussen welche Gene wann und wie häufig exprimiert werden. Zwei bekannte Beispiele von epigenetischer Regulation sind die DNA-Methylierung [33] und die Histon-Modifikation.

Zelluläre Differentiation von eukaryotischen Zellen stellt ein typisches Beispiel der Epigenetik dar. Während der Morphogenese verwandeln sich totipotente Stammzellen in unterschiedliche pluripotente Stammzellen eines Embryos. Die pluripotenten Stammzellen wiederum werden zu voll ausdifferenzierten Zelllinien. Mit anderen Worten, aus einer befruchteten Eizelle (Zygot) entwickeln sich viele spezialisierte Zelltypen, wie Muskelzellen, Neuronen oder Epithelzellen. Alle Zellen tragen den gleichen genetischen Kode, jedoch sind jeweils bestimmte Gene durch epigenetische Mechanismen aktiviert oder deaktiviert. Diese Modifikationen der Genexpression können über viele Zell-Generationen vererbt werden („Memory-Effect“).

## Die fünfte DNA-Base: Methylcytosin

Bei der DNA-Methylierung wird eine Methylgruppe entweder an die Position 5 des Cytosin-Pyrimidin-Ringes oder an die Position 6 des Stickstoffs des Adenin-Purin-Ringes angefügt. Während die Adenin-Methylierung bei Bakterien vorkommt und wichtige Funktionen übernimmt, konnte Cytosin-Methylierung bei allen bis jetzt untersuchten Wirbeltieren nachgewiesen werden. In Säugetieren wird Methylcytosin bis auf ein paar Ausnahmen in CpG-Dinukleotiden gefunden. 5-Methylcytosin (mC) wird als 5. Base der DNA bezeichnet und entsteht aus Cytosin durch enzymatisches Hinzufügen einer Methylgruppe an das fünfte Kohlenstoff-Atom des Kohlenstoffringes.

Methylcytosin ist grundlegend für eine normale biologische Entwicklung und spielt eine zentrale Rolle bei Prozessen, wie der genomischen Prägung, X-Chromosom Inaktivierung und der Aktivierung und Inaktivierung einzelner Gene. Methylcytosin bildet die Grundlage für die Chromatinstruktur und von zentraler Bedeutung in der Entwicklung von vielen unterschiedlichen Arten von Krebs [33].

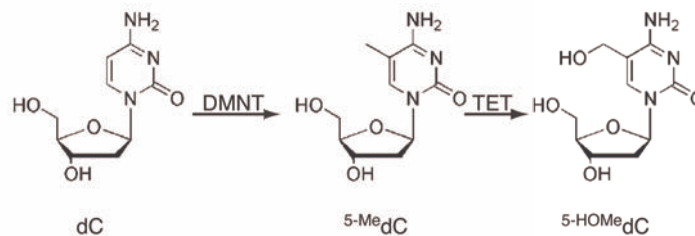


Abbildung 3: Struktur des Nucleosides von Cytosin und der postreplikativ geformten Basen 5-Methylcytosin und 5-Hydroxymethylcytosin. In Zellen übernehmen die Enzyme der DNMT- und TET-Familie die Modifikation von Cytosin und Methylcytosin (Abbildung ist von [23] adaptiert).

Während die biologische Funktionen der DNA-Methylierung immer weiter aufgedeckt werden, sind die zu Grunde liegenden molekularen Mechanismen nur teilweise verstanden und aufgeklärt. Bis jetzt sind zwei Arten bekannt, wie DNA-Methylierung den Prozess der Transkription beeinflusst. Erstens kann das Binden von Transkriptionsfaktoren an deren Promotorsequenzen verhindert werden. Zweitens Methylcytosine werden durch so genannte Methyl-CpG-Bindedomänen (MBD) von Proteinen erkannt [34, 35]. Diese Proteine rekrutieren wiederum andere Proteine, die an diese binden oder das Binden der RNA-Polymerase-Maschinerie unterbinden können [36].

Der Einfluss von Methylcytosin auf die dreidimensionale Struktur ist laut Studien vernachlässigbar klein [37-39]. In DNA-Schmelzkurvenexperimenten konnte gezeigt werden, dass Methylcytosin auch nur einen geringen Einfluss auf die thermische Stabilität der DNA hat [40, 41]. In NMR-Experimenten konnte gezeigt werden das methylierte CpG-Dinukleotide die Dynamik des Zucker-Phosphat-Rückgrats der DNA herabsetzten. In all diesen Experimenten wurden die Eigenschaften der DNA im thermischen Gleichgewicht untersucht. Allerdings sind viele biologische Prozesse, wie die DNA-Replikation oder Transkription, Nicht-Gleichgewichtsprozesse bei denen gerichtete Kräfte von Molekülen auf andere ausgeübt werden. In diesem Zusammenhang stellt sich die Frage, ob Methylcytosin einen Einfluss auf die mechanische Stabilität der DNA ausübt.

In Publikation P6 (siehe auch Kapitel 5.3) wird diese Frage mittels Einzelmolekül-Kraftspektroskopie, dem molekularen Kraftsensor und Molekular-Dynamik-Simulationen

(genauer, SMD Simulationen) untersucht. Hierbei wurde der Einfluss von Methylcytosin auf die Stabilität der DNA-Doppelhelix, die unter äußerem Krafteinfluss in zwei DNA-Einzelstränge aufgetrennt wird, untersucht.

### **Die sechste DNA-Base: Hydroxymethylcytosin**

Im Jahr 2009 wurde im Gehirn von Menschen und Mäusen und in embryonischen Stammzellen eine weitere modifizierte DNA-Base gefunden. Es handelt sich um 5-Hydroxymethylcytosin. Hydroxymethylcytosin scheint ähnlich wie Methylcytosin in jeder Art von Säugetierzelle vorzukommen, allerdings variiert im Gegensatz zur Methylierung der Grad der Hydroxymethylierung stark in unterschiedlichen Zelltypen. In neuronalen Zellen und im zentralen Nervensystem wurden höchste Konzentrationen an Hydroxymethylcytosin gefunden [24, 42, 43]. Außerdem nimmt die Konzentration an Hydroxymethylcytosin (hmC) mit dem Alter zu [24, 44]. Die Bedeutung von hmC wird von der Forschung als so wichtig eingestuft, dass hmC auch als 6. Base der DNA bezeichnet wird. Bis jetzt ist bekannt, dass Methylcytosin durch Enzyme der TET-Familie per Hydroxylierung in hmC umgewandelt wird.

Zu Beginn nahm man an, dass hmC ein Zwischenprodukt der Demethylierung von Methylcytosin darstellt. Allerdings konnte bald darauf gezeigt werden, dass hmC nicht nur ein Zwischenprodukt dieses Prozesses sein kann. Es ist bekannt, dass hmC eine wichtige Rolle in der Genregulation bei der Entwicklung von Organismen und der Karzinogenese spielt. Außerdem konnte gezeigt werden, dass hmC auch mit der Aktivierung von transkribierten Genen im Zusammenhang steht, aber wie hmC diese Funktionen auf molekularer Ebene ausübt ist unbekannt. Für Methylcytosin wurden spezifisch bindende Proteine gefunden, welche dann wiederum weitere Funktionen ausgeführt haben. Für hmC wurden bis jetzt keine derartigen Proteine entdeckt [23]. Somit bleibt trotz des großen Forschungsaufwands der letzten Jahre, der molekulare Mechanismus ungeklärt, wie hmC funktioniert.

Basierend auf den Ergebnissen über Methylcytosin (Publikation P6) wird in Manuskript M1 (siehe auch Kapitel 5.3) die Frage beantwortet, ob Hydroxymethylcytosin ebenfalls einen Einfluss auf die Stabilität der DNA-Doppelhelix hat, und wie sich der Einfluss von hmC von dem von mC unterscheidet. Hierfür wurden molekulare Kraftsensor-Experimente und SMD-Simulationen durchgeführt.



## 4. Der Molekulare Kraftsensor: Quantifizierung Biomolekularer Wechselwirkungen

### 4.1 DNA-Mechanik

#### DNA als programmierbarer Baustein

Desoxyribonucleinsäure (DNA) ist Träger der genetischen Erbinformation und somit eines der wichtigsten Moleküle, auf dem das Leben basiert. DNA zeichnet sich durch besondere Eigenschaften wie Robustheit, Spezifität und Einfachheit aus. Wegen der sequenzspezifischen molekularen Erkennung wurde DNA in der Nano-Biotechnologie als Bauelement entdeckt und wird auch in dieser Arbeit als zentraler Baustein für den Aufbau des molekularen Kraftsensors verwendet.

In Lebewesen liegt DNA hauptsächlich nicht als Einzelstrang vor, sondern setzt sich aus zwei DNA-Einzelsträngen zusammen. Hierbei besteht ein DNA-Einzelstrang aus den vier verschiedenen Basen Adenin (A), Thymin (T), Guanin (G) und Cytosin (C), die über ein Zucker-Phosphat-Rückgrat miteinander kovalent verbunden sind. Watson und Crick konnten durch Röntgenstrukturanalyse zeigen, dass sich jeweils zwei DNA-Stränge zu einer Doppelhelix zusammenlagern, wobei sich jeweils zwischen den gegenüberliegenden Basen A-T und G-C Wasserstoffbrücken ausbilden und so zur sequenzspezifischen Stabilisierung führen. Die beiden Stränge sind dabei antiparallel zueinander ausgerichtet, sodass jeweils das 5'-Ende dem 3'-Ende gegenüberliegt und umgekehrt (siehe Abbildung 4).

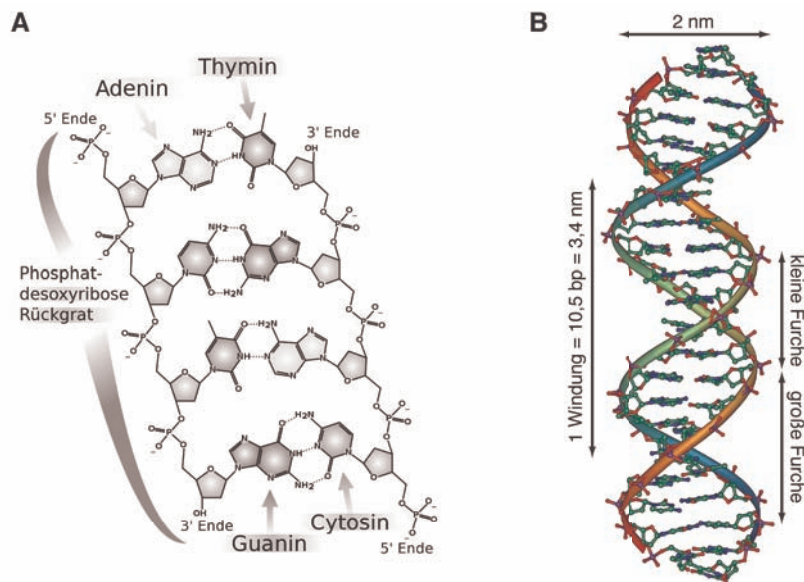


Abbildung 4: Die Struktur der DNA. Zwei komplementäre DNA-Stränge lagern sich über spezifische Basenpaarungen zu einer Doppelhelix zusammen. (a) Hierbei bilden jeweils Adenin mit Thymin und Guanin mit Cytosin ein Basenpaar (Watson-Crick-Basenpaarung). (b) Die häufigste in der Natur vorkommende 3-dimensionale Struktur der DNA-Doppelhelix ist die B-Form mit 10,5 bp pro Windung. (Abbildung nach <http://de.wikipedia.org/wiki/Desoxyribonucleinsäure>)

Diese Fähigkeit komplementärer DNA-Stränge miteinander zu hybridisieren, wird zum Beispiel für die spezifische Anbindung von Bausteinen zur Selbstassemblierung komplexer zwei- und dreidimensionaler Strukturen aus DNA, sogenannter DNA-Origamis [45-47] und zur Herstellung von „Molecular Devices“, maschinenartiger Nano-Geräte, ausgenutzt [48, 49]. Auch kann mit Hilfe der richtungsabhängigen Bindekräfte der DNA-Doppelstränge ein Kraft-Hierarchie-System entstehen, mit dem es möglich ist einzelne Moleküle nanometergenau gezielt zu positionieren. Diese Methode entstand 2008 unter dem Namen „single molecule cut-and-paste“ [50, 51]. Eine Weiterentwicklung, welche die Kombination von Proteinen mit DNA darstellt, findet sich in Publikation P7. Wichtig für die schnelle Entwicklung auf diesem Gebiet sind industriell verwendete biotechnologische Methoden, mit denen DNA-Stränge mit beliebiger Sequenz künstlich synthetisiert und mit internen Modifikationen wie Farbstoffmarkierungen oder spezifische Bindungsstellen versehen werden können.

Im Bereich der Diagnostik und als Sensor werden kurze DNA-Moleküle (DNA-Oligomere) für die unterschiedlichsten biologischen Anwendungen eingesetzt. Hierbei dient die DNA oft als Bindepartner, an den unter anderem Ionen, kleine Moleküle und Proteine andocken können. Neben der einfachen helikalen Struktur der DNA kann DNA für bestimmte Sequenzen auch andere dreidimensionale Formen einnehmen, die wiederum mit hoher Spezifität - vergleichbar mit Antikörpern - gezielt andere Biomoleküle binden können, wie es bei DNA-Aptameren der Fall ist (Publikation P3). Durch das Binden kann die Größe und Masse durch Komplexbildung oder auch Form und Struktur der DNA verändert werden. Detektiert werden diese Biomoleküle dann typischerweise optisch (turbidimetrisch, colorimetrisch oder fluoreszent), elektrochemisch, mit Quarzkristall-Mikrowaagen, Oberflächen-Plasmon-Resonanz oder mit blattfederbasierenden Methoden.

### **Mechanische Eigenschaften von DNA**

Bevor im Folgenden die mechanischen Eigenschaften von DNA beschrieben werden wie sich DNA unter äußeren Krafteinfluss verhält, ist es wichtig zu verstehen wie die Stabilität der DNA Doppelhelix zustande kommt und wodurch diese beeinflusst wird.

Zusammengefasst: Watson-Crick-Basenpaarung und „Base-Stacking“ (räumliche Anordnung der Basen) sind für die Stabilität der DNA verantwortlich. Elektrostatische Wechselwirkungen zwischen den Phosphatgruppen der beiden DNA-Stränge und entropische Effekte (Mischungs-Entropie, Konformations-Entropie) wirken hingegen destabilisierend.

Watson-Crick-Basenpaarung: das GC-Basenpaar bildet drei und das AT-Basenpaar zwei Wasserstoffbrückenbindungen aus. Dadurch können GC-Basenpaare mit einer Bindungsenergie von zirka 700 meV die Doppelhelix stärker als die AT-Basenpaare mit 360 meV Bindungsenergie stabilisieren. Allerdings müssen die Basenpaare in Lösung mit Wassermolekülen um die Wasserstoffbrücken konkurrieren. Für die Bildung eines Basenpaares müssen Wasserstoffbrücken zwischen Basen und Wassermolekülen aufgebrochen werden (zwischen Wassermolekülen Größenordnung 200 meV Bindungsenergie). Es hat sich gezeigt, dass der Beitrag der Basenpaarung zur Stabilität der DNA im Vergleich zum „Base-Stacking“ eher klein ist.

„Base-Stacking“: entscheidend für die Stabilität ist das Zusammenspiel von Watson-Crick-Basenpaarung und räumlicher Anordnung der Basen, dem Base-Stacking. Legt man Ebenen senkrecht zu dem Zucker-Phosphat-Rückgrat durch die Doppelhelix, so liegen die Watson-Crick-Basenpaare in der B-Form annähernd in diesen Ebenen. Die sequenzabhängige,

spezifische Wechselwirkung zwischen den Ebenen wird durch Dipol-Dipol-Wechselwirkungen zwischen den Basen bestimmt.

Elektrostatische Wechselwirkung: die Phosphatgruppen des Zucker-Phosphat-Rückgrats sind einfach negativ geladen. Es gibt eine elektrostatische Abstoßung zwischen den beiden Einzelsträngen. Diese Abstoßung hat eine destabilisierende Wirkung. Die Phosphatgruppen ordnen sich in der Doppelhelix so an, dass ihr Abstand maximal wird. Abhängig von der Konzentration und Ladung der Kationen im Lösungsmittel werden die negativen Ladungen des Zucker-Phosphat-Rückgrats unterschiedlich stark abgeschirmt.

Entropische Effekte: dazu gehört die Konformations-Entropie der DNA und die Entropie des Lösungsmittels. Die Persistenzlänge der Doppelhelix ist mit 60 nm in 1 M NaCl deutlich größer als die eines Einzelstranges mit einer Persistenzlänge von zirka 2 nm. Ein ungebundener Einzelstrang hat mehr Freiheitsgrade als in gebundener Form mit dem komplementären Strang. Darüber hinaus ist die Hydratation des Doppelstrangs höher als die zweier einzelner Stränge, was die Ordnung der Wassermoleküle erhöht und der Stabilität des DNA-Doppelstranges entgegenwirkt. Aus diesen Beiträgen ergeben sich nun die mechanischen Eigenschaften der DNA-Doppelhelix, welche mittels Einzelmolekülkraftspektroskopie genau untersucht werden konnten.

In dieser Arbeit sind prinzipiell zwei Möglichkeiten von Interesse, wie eine externe Kraft an DNA-Moleküle angelegt werden kann (vergleiche z.B. Abbildung 7). Erstens eine Zippergeometrie – vergleichbar mit einem Reißverschluss – bei der die Kraft an dem einen Einzelstrang am 5'-Ende und bei dem anderen Einzelstrang am 3'-Ende angelegt wird. Dadurch wird die Doppelhelix Basenpaar für Basenpaar in einem Quasi-Gleichgewichtsprozess auseinander gezogen. Die Bindungsenergie von AT- bzw. GC-Basenpaaren kann auf diese Weise direkt bestimmt werden. In [52-54] wurde gezeigt, dass die Kraft zur Trennung einer in Zippergeometrie belasteten DNA-Doppelhelix unabhängig von der Kraftladungsrate und von der Länge der Doppelhelix ist, was sich mit einem Quasi-Gleichgewichtsprozess beschreiben lässt. Jedoch ist sie vom AT- bzw. GC-Anteil der belasteten Sequenz abhängig. Wegen dem Unterschied an Wasserstoffbrückenbindungen von AT- und GC-Basenpaaren öffnen sich AT-reiche Sequenzen schon bei einer Kraft von ca. 10 pN, während GC-reiche Sequenzen erst bei einer mittleren Kraft von ca. 25 pN dissoziieren. Für Sequenzen mit gemischtem AT- und GC-Gehalt ergibt sich eine mittlere Kraft.

Des Weiteren gibt es die Möglichkeit die beiden DNA-Stränge in einer Schergeometrie (Shear-Geometrie) auseinanderzuziehen. Hierbei wird die Kraft jeweils an den 5'-Enden der Einzelstränge oder jeweils an den 3'-Enden angelegt. Dadurch wird die Doppelhelix parallel zum Rückgrat gestreckt beziehungsweise geschert und die Kraft wirkt auf alle Basenpaare der Doppelhelix gleichzeitig. In Schergeometrie sind die Abrisskräfte abhängig von der angelegten Kraftladungsrate, der Länge und den Angriffspunkten (3'-Enden oder 5'-Enden) an der DNA.

## 4.2 Der Molekulare Kraftsensor

In den letzten Jahren wurden verschiedene kraftspektroskopische Methoden entwickelt. Typischerweise wird der zu untersuchende Molekülkomplex zwischen einer Oberfläche und einer Feder eingespannt und die angelegte Kraft gegen den Abstand gemessen. Hierbei wird die Feder in den verschiedenen Techniken auf unterschiedliche Art und Weise realisiert. Die bekanntesten Vertreter sind das „Atomic Force Microscope“ (AFM) [21, 55, 56], die optische Falle [57, 58] und die Magnetische Falle [59, 60]. Beim AFM wird eine Blattfeder in Mikrometergröße als Kraftsensor verwendet. Bei der optischen Falle werden mikrometergroße

Kügelchen durch Impulsübertrag im Zentrum eines fokussierten Lasers gefangen und Auslenkungen aus dem Fokus resultieren in Kraft. Und in der Magnetischen Falle wirkt im Gradienten eines Magnetfeldes eine Kraft auf paramagnetische Partikel.

Bei all diesen Techniken wird das Auflösungsvermögen durch die von der Feder dissipierte Energie limitiert. In Referenz [61] wurde gezeigt, dass die minimal auflösbare Kraft  $F_{min}$  bei einer Bandbreite  $B$  und einem Dämpfungskoeffizienten  $\gamma$  gegeben ist durch  $F_{min} = \sqrt{4k_B T \gamma B}$ . Deshalb ist bei gleichbleibender Temperatur eine Erhöhung der Auflösung nur durch eine Verkleinerung der Dämpfung  $\gamma$  erreichbar.

Ein auf der Hand liegender Ansatz ist die Verkleinerung der Blattfeder [61, 62]. Allerdings ist die Verkleinerung der Blattfeder eine technologische Herausforderung, so dass es von Interesse sein kann alternative Techniken zu erforschen. Bei optischen oder magnetischen Fallen ist zwar die Verkleinerung des Sensors einfacher, jedoch hat in diesem Fall die Verkleinerung des Sensors eine Verkleinerung der messbaren Kräfte und des Kraftbereichs zur Folge, denn auf die kleineren Kugeln der optischen oder magnetischen Pinzetten können nur kleinere Kräfte ausgeübt werden. Da bei Rezeptor-Ligand-Systemen die Bindungsstärke von wenigen pN bis zu einigen Hundert pN betragen kann, sollte allerdings ein genügend großer Kraftbereich zugänglich sein.

Ein vom Grundsatz her unterschiedlicher Ansatz zur Verkleinerung der Größe des Sensors auf einige Nanometer ist die Verwendung eines einzigen Moleküls als Sensor, dem molekularen Kraftsensor, bei dem seine Bindung als Kraft-Standard direkt mit der Bindungskraft des Probe-Moleküls verglichen wird. Hierfür müssen die beiden Moleküle in Serie verbunden sein und es wird eine externe Kraft auf den gesamten Komplex ausgeübt [63-66].

Im Gegensatz zu AFM oder optischen Pinzetten, bei denen die absolute Kraft über die Federkonstante, wie z.B. der Blattfeder beim AFM, bestimmt wird, ist das Prinzip des molekularen Kraftsensors vergleichbar mit dem einer Balkenwaage, bei der das Probe-Gewicht in die eine Schale gelegt wird und mit einem Referenz-Gewicht in der zweiten über den Ausschlag des Zeigers der Waage verglichen wird. Die Zeigerfunktion wird dabei von einem Fluorophor übernommen.

### **Funktionsweise auf Einzelmolekül-Ebene**

Die Methode lässt sich am besten verstehen, indem man die Funktionsweise eines einzelnen molekularen Kraftsensors betrachtet (Abbildung 5). Das zu Grunde liegende Prinzip ist hierbei wie folgt: Der Kraftsensor besteht aus drei kurzen, typischerweise 30 bis 100 Basenpaaren langen DNA-Strängen (**1**, **2** und **3**), die miteinander hybridisiert sind (**1 • 2 • 3**). Diese DNA-Stränge fügen sich durch zueinander komplementäre DNA-Sequenzteile zu zwei DNA-Duplexen **1 • 2** und **2 • 3** zusammen. Diese zwei DNA-Duplexe **1 • 2** und **2 • 3** sind durch Strang **2** in Serie miteinander verbunden. Über die Stränge **1** und **3** ist der Kraftsensor zwischen zwei Flächen eingespannt.

Wenn nun die zwei Oberflächen separiert werden, baut sich eine Kraft im Kraftsensor auf bis eine der Bindungen der beiden Duplexe nachgibt. Durch einen Fluoreszenz-Marker am mittleren Strang (Strang **2**) kann nachgewiesen werden, welche der beiden molekularen Bindungen gerissen ist und welche intakt ist. Da der Bindungsbruch einer molekularen Wechselwirkung ein thermisch aktivierter Prozess ist, muss diese Messung typischerweise einige hundertmal wiederholt werden um einen Mittelwert für das Verhältnis von Bindungsbrüchen von Duplex **1 • 2** zu Duplex **2 • 3** bestimmen zu können. Dies kann entweder zeitlich nacheinander mit einem einzelnen molekularen Kraftsensor bestimmt werden oder gleichzeitig, aber dafür mit vielen

räumlich voneinander getrennten molekularen Kraftsensoren parallel durchgeführt werden, wie es im nächsten Abschnitt beschrieben ist.

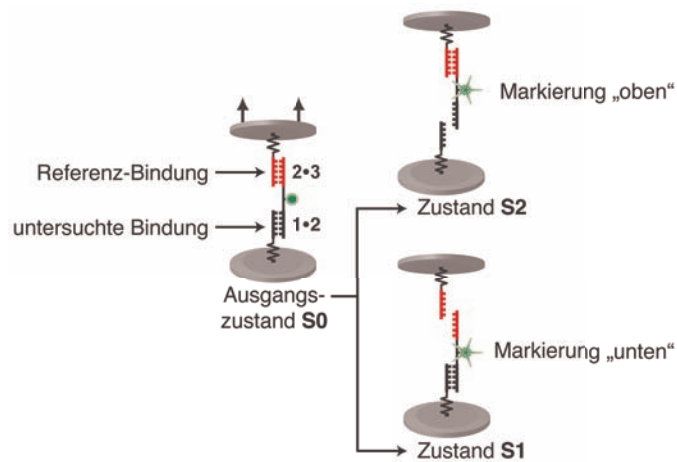


Abbildung 5: Prinzip des molekularen Kraftsensors. Der Kraftsensor besteht aus drei DNA-Strängen (1, 2 und 3), die miteinander hybridisiert sind (1 • 2 • 3) und zwischen zwei Flächen eingespannt sind. Diese DNA-Stränge fügen sich durch zueinander komplementäre DNA-Sequenzteile zu zwei DNA Duplexen 1 • 2 und 2 • 3 zusammen. Während der Separation der zwei Flächen, wird eine der beiden Bindungen 1 • 2 oder 2 • 3 reißen. Über ein Fluoreszenzfarbstoff an Strang 2 wird ausgelesen, welche der zwei Bindungen intakt ist.

Um dieses Prinzip im Experiment umsetzen zu können, bedarf es noch einiger essentieller Feinheiten, die im Folgenden beschrieben sind (siehe Publikation P1 und Abbildung 6). Hierfür wird zu Beginn der molekulare Aufbau des Kraftsensors von unten nach oben beschrieben: DNA Strang 1 ist kovalent über eine  $\text{NH}_2$ -Modifikation an die Glasoberfläche (untere Fläche) via eines (Hexaethylglycol)<sub>5</sub>-Polymerlinkers angebunden. Strang 2 besitzt sowohl eine komplementäre DNA-Sequenz zu DNA-Strang 1 als auch zu Strang 3. Zwischen diesen beiden komplementären Sequenzabschnitten trägt Strang 2 ein Cy5 Fluoreszenz-Marker. Strang 3 hat an dem einen Ende ein Cy3 Fluoreszenz-Marker und ist am anderen Ende mit Biotin modifiziert. Hierbei sind die Fluoreszenz-Marker Cy3 und Cy5 so orientiert, dass diese nahe beieinander liegen (typischerweise 7 Nukleotide einzelsträngige DNA) und ein FRET-Paar (Förster-Resonanzenergietransfer-Paar) bilden. Das Biotin an Strang 3 bildet den Anker um den molekularen Kraftsensor an die obere Fläche, den Polydimethylsiloxane (PDMS)-Stempel, binden zu können.

Der PDMS-Stempel ist mit kurzen 30 nm langen (Konturlänge) Polyethylenglycol-Linker (PEG-Linker) kovalent beschichtet. Am freien Ende ist der PEG-Linker mit einem Biotin modifiziert an welches Streptavidin spezifisch angebunden ist. Streptavidin besitzt 4 Bindungsstellen für Biotin, von denen die ersten zwei Biotin-Bindungen eine besonders hohe Affinität aufweisen. Dadurch kann Streptavidin am PDMS-Stempel, bei Kontaktierung der Glasoberfläche an Strang 3 des molekularen Kraftsensors anbinden. Auf diese Weise kann der Kraftsensor zwischen der Glasoberfläche und dem PDMS-Stempel eingespannt werden.

Der Ablauf eines Experimentes gestaltet sich wie folgt: zu Beginn sind PDMS-Stempel und die Glasoberfläche mit dem Kraftsensor separiert voneinander und das Fluoreszenzsignal wird in zwei Schritten nacheinander auf der Glasoberfläche gemessen. Zuerst wird Cy5 angeregt und das Fluoreszenzsignal von Cy5 ( $F_A^A$ ) gemessen. Darauf wird Cy3 angeregt und das über den Förster-Resonanzenergietransfer übertragene Fluoreszenzsignal von Cy5 ( $F_D^A$ ) gemessen. Im

darauf folgenden Schritt werden die Glasoberfläche und der PDMS-Stempel in Kontakt gebracht, und das Biotin vom DNA-Strang **3** vom Kraftsensor kann an das Streptavidin vom PDMS-Stempel spezifisch ankoppeln. Wenn nun die beiden Oberflächen voneinander separiert werden, baut sich eine Kraft im Kraftsensor und den Polymer-Linkern, die diesen zwischen den Oberflächen verankern, auf, bis eine der Bindungen reißt. Nachdem beide Flächen voneinander getrennt sind, wird die Fluoreszenz  $F_A^A$  und  $F_D^A$  ein zweites mal an der Glasoberfläche ausgelesen.

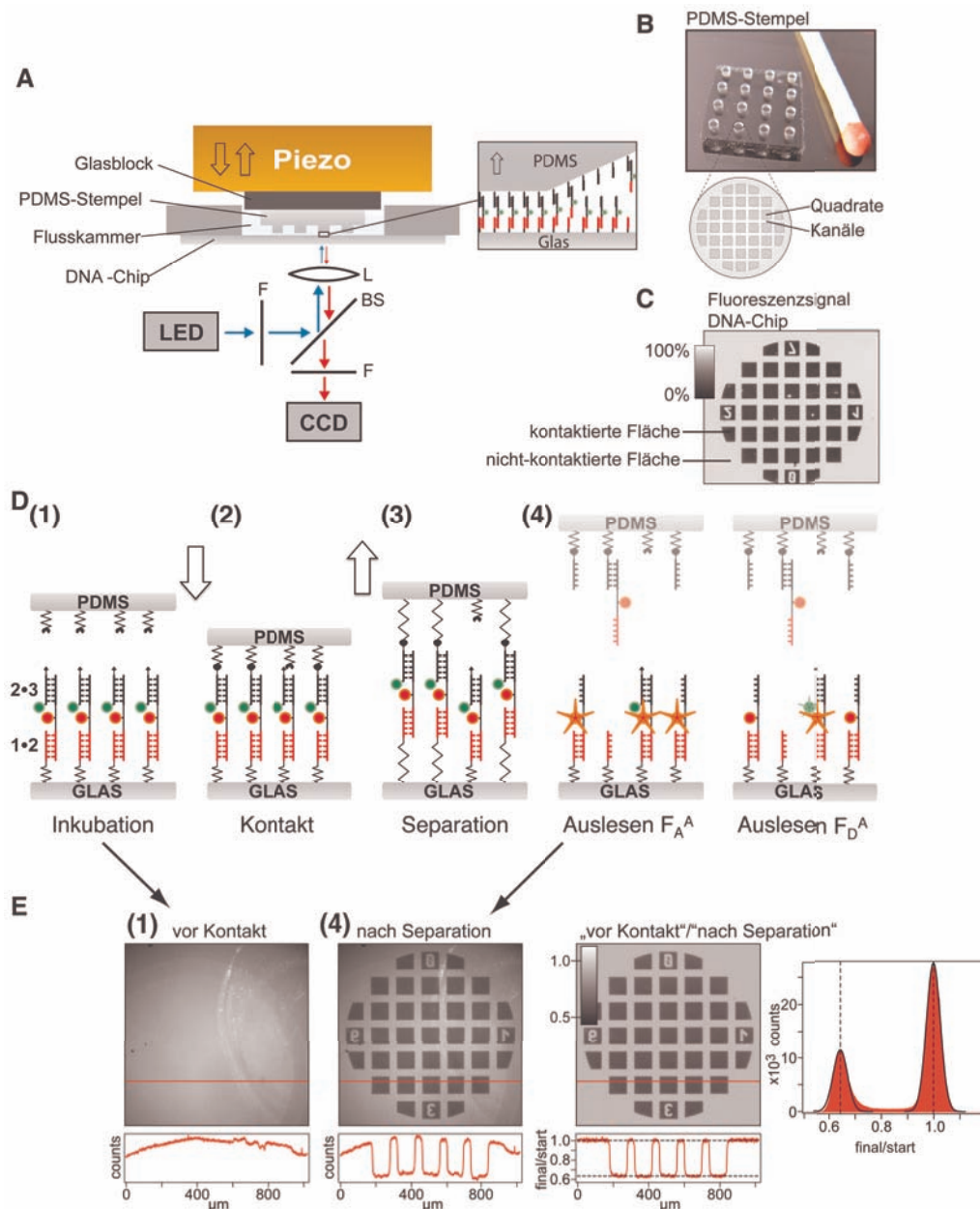


Abbildung 6: Experimentelle Realisierung des molekularen Kraft-Assays (vgl. Publ. P1). (a) Eine Fluid-zelle mit DNA-Chip befindet sich in einer Kontakteinheit mit PDMS-Stempel und Detektionssystem. Um den DNA-Chip zu kontaktieren, bewegt ein Piezo-Element den PDMS-Stempel in z-Richtung. Ein Fluoreszenzmikroskop wird verwendet um die Probe auszulesen. (b) Der PDMS-Stempel besteht aus Pads, die eine Mikrostruktur besitzen. Die Mikrostruktur besteht aus Quadraten und Kanälen. Der elastische PDMS-Stempel hat die Aufgabe sich der Oberfläche der unteren Glasoberfläche anzupassen um so das Koppeln der molekularen Kraftsensoren (~80 nm Konturlänge) zu ermöglichen. (c) Fluoreszenzbild eines Pad-Abdrucks auf dem DNA-Chip. (d) Schematische Darstellung der Versuchsdurchführung des Assays auf molekularer Ebene. Die Verbindung zwischen den Oberflächen wird über ein Streptavidin am PDMS-Stempel und Biotin an Strang 3 des molekularen Kraftsensoren hergestellt. Ein FRET-Paar (Cy3 und Cy5) erlaubt die Bestimmung der Kopplungseffizienz des molekularen Kraftsensoren an den PDMS-Stempel. (e) Vor dem Kontakt und nach der Separation werden jeweils zwei Fluoreszenzbilder aufgenommen ( $F_A^A$  und  $F_D^A$ ). Durch Auswerten dieser Bilder erhält man das Normalisierte Fluoreszenz-Bild. Das NF-Bild spiegelt das Abrissverhältnis von Duplex 1 • 2 zu 2 • 3 wider.

Nach dem Trennen der Flächen, gibt es drei unterscheidbare Zustände, in denen sich der Kraftsensor befinden kann, und die sich durch das Fluoreszenzsignal nachweisen lassen. Zustand **S1** (Stränge **1 • 2**): Wenn die molekulare Bindung von Duplex **1 • 2** intakt und von Duplex **2 • 3** gerissen ist, ist Strang **2** mit Fluorophor Cy5 auf der Glasoberfläche geblieben und Strang **3** mit Fluorophor Cy3 ist am PDMS-Stempel, so dass man ein Signal für  $F_A^A$  und kein Signal für  $F_D^A$  auf der Glasoberfläche erhält. Zustand **S2** (Strang **1**): Wenn die Bindung von Duplex **1 • 2** gerissen und von Duplex **2 • 3** intakt ist, ist Strang **2** und **3** mit Fluorophor Cy5 und Cy3 am PDMS-Stempel, so dass man auf der Glasoberfläche kein Signal für  $F_A^A$  und  $F_D^A$  erhält. Zustand **S0** (Stränge **1 • 2 • 3**): Falls ein Kraftsensor im Messprozess nicht an den PDMS-Stempel gekoppelt war und somit im Separationsprozess nicht belastet wurde, bekommt man sowohl für  $F_A^A$  als auch für  $F_D^A$  ein Signal. Auch für den Fall, dass eine der beiden Biotin-Streptavidin-Bindungen nachgegeben hat, bekommt man ein Signal sowohl für  $F_A^A$  als auch für  $F_D^A$ . Diese beiden Fälle sind in der Messung nicht unterscheidbar und werden in dem Begriff „Kopplungseffizienz“ zusammengefasst.

Im nächsten Abschnitt wird die Implementierung des Prinzips des molekularen Kraftsensors via Soft-Print Lithographie beschrieben und wie mit Hilfe der unterscheidbaren Zustände **S0**, **S1** und **S2** die molekularen Wechselwirkungen der Kraftsensoren ausgewertet und quantifiziert werden können.

### **Parallelisierung via Soft-Print Lithographie und Mikrostrukturierung**

Nachdem die Funktionsweise des molekularen Kraftsensors beschrieben wurde, wird nun die Implementierung des Kraftsensors in das Experiment beschrieben und wie aus den experimentellen Daten die molekularen Wechselwirkungen quantifiziert werden können.

Da das Aufbrechen der molekularen Bindung unter Kraft ein thermisch aktivierter, statistischer Prozess ist, wird eine große Zahl, typischerweise einige hundert Kraftsensormessungen für ein aussagekräftiges Ergebnis benötigt. Dies kann entweder zeitlich nacheinander mit einem Kraftsensor durchgeführt werden oder gleichzeitig parallel mit vielen Kraftsensoren, die räumlich getrennt voneinander gemessen werden. An dieser Stelle ist es wichtig zu erwähnen, dass es sich um eine hochparallele Methode handelt, bei der die intermolekularen Kräfte auf Einzelmolekülebene untersucht werden, da Duplex **1 • 2** und **2 • 3** in jedem Kraftsensor einzeln gegeneinander gemessen werden. Dafür müssen weder die Kräfte zwischen den Oberflächen noch der Trennprozess der zwei Flächen analysiert werden.

Der Aufbau setzt sich aus den zentralen Einheiten DNA-chip und PDMS-Stempel zusammen, auf denen durch Oberflächenchemie und Selbstassemblierung (self-assembly) die molekularen Kraftsensoren (auf dem DNA-Chip) und deren Streptavidin-Anker (PDMS-Stempel) aufgebaut werden [67]. Die Messflecken auf den DNA-chip weisen eine Dichte in der Größenordnung von  $10^4$  Kraftsensoren pro  $\mu\text{m}^2$  auf. Der PDMS-Stempel wird über eine Wafer-Schablone durch standardisierte Verfahren hergestellt und kann einfach in Form und Oberflächen-Mikrostrukturierung variiert werden [67]. Dabei kann sich das flexible PDMS den Unebenheiten der Glasoberfläche anpassen und so die Nähe zur Glasoberfläche herstellen, die wegen der Größe der molekularen Kraftsensoren (typische Konturlänge  $\sim 80$  nm), benötigt wird. Auf diese Weise können die einige 10 nm großen Kraftsensoren ohne Probleme über eine Fläche von 1 cm x 1 cm kontaktiert werden. Standardmäßig wurde eine Mikrostrukturierung verwendet, bei der 100  $\mu\text{m}$  x 100  $\mu\text{m}$  große Quadrate durch 41  $\mu\text{m}$  breite und 5  $\mu\text{m}$  tiefe Kanäle getrennt sind. Die Kanäle dienen als Drainagesystem, so dass die Quadrate den Messpuffer verdrängen können und den Kontakt zur Glasoberfläche herstellen können.



Neben der Möglichkeit den molekularen Kraftsensor mit hohen Dichten auf einer Oberfläche assemblieren zu können, ist der molekulare Kraftsensor auch für Multiplexverfahren geeignet und ist mit gängigen Mikroarray-basierenden Methoden, wie sie in der Bioanalytik und biomedizinischen Diagnostik verwendet werden, kompatibel. Hierfür werden unterschiedliche molekulare Kraftsensoren räumlich separiert als Messflecken auf einem Substrat angebunden. Die Kraftsensor-Messflecken auf dem DNA-Chip können wiederum durch Techniken der Mikrostrukturierung, wie z.B. Mikroplottern, auf einen Durchmesser von zirka 15 µm reduziert werden, was derzeit dem unteren Limit in Messfleckengröße der kommerziell erwerblichen DNA Mikroarrays mit entsprechender DNA Sequenzlänge darstellt.

Für Kontaktierung und Separation des PDMS-Stempels und DNA-Chip wird eine speziell dafür angefertigte Kontakteinheit verwendet, die auf einem invertierten Epi-Fluoreszenzmikroskop aufgebaut ist. Die Realisierung des experimentellen Aufbaus wird im Detail in Publikation P1 beschrieben, soll aber wegen seiner sehr technischen Ausprägung hier nicht weiter ausgeführt werden.

Wie im vorherigen Abschnitt beschrieben, wird der molekulare Kraftsensor über Fluoreszenz ausgelesen. Im Experiment wird die Fluoreszenz flächig mit einer CCD-Kamera aufgenommen. Die Pixel der Fluoreszenzbilder entsprechen je nach Vergrößerung einer Fläche von 300 nm x 300 nm bis 1,2 µm x 1,2 µm auf dem DNA-Chip. Die Anzahl der Fluorophore (Kraftsensoren) ist proportional zu der gemessenen Intensität pro Pixel. Somit kann über die Intensität auf die Anzahl der Fluorophore geschlossen werden. Und folglich aus der relativen Änderung der Intensität auf die relative Änderung der Anzahl der Fluorophore. Aus den Fluoreszenzbildern  $F_A^A$  und  $F_D^A$  vor dem Kontakt und nach dem Trennen, lassen sich nach Hintergrund- und Bleichkorrektur die relativen Änderungen räumlich aufgelöst Pixel für Pixel (vor Kontakt und nach Trennen) von  $F_A^A$  und  $F_D^A$  bestimmen.

Um das Verhältnis der gebrochenen Duplexe **1 • 2** zu den gebrochenen Duplexen **2 • 3** korrekt bestimmen zu können, bedient man sich der Zustände **S0**, **S1** und **S2**, die sich durch die Fluoreszenzbilder  $F_A^A$  und  $F_D^A$  darstellen lassen. Über das FRET-Paar lassen sich die Kraftsensoren, die nicht an den PDMS-Stempel gekoppelt waren und deshalb nach dem Trennen der Oberflächen noch im Zustand **S0** sind, von den Kraftsensoren in Zustand **S1** unterscheiden. Auf diese Weise lässt sich die Normalisierte Fluoreszenz (NF) bestimmen:

$$NF = \frac{S1}{S1 + S2} = \frac{(F_A^A)_{ratio} - (F_D^A)_{ratio}}{1 - (F_D^A)_{ratio}}$$

Die Normalisierte Fluoreszenz ist definiert als das Verhältnis von molekularen Kraftsensoren, bei denen Duplex **2 • 3** nachgegeben hat, zu der Gesamtzahl von Kraftsensoren an die eine Kraft angelegen ist. Somit ist die Normalisierte Fluoreszenz eine Maßeinheit mit der die relative mechanische Stabilität zwischen den molekularen Bindungen **1 • 2** und **2 • 3** bestimmt wird.

Im Vergleich zu den klassischen Methoden, die biomolekulare Wechselwirkungskräfte typischerweise absolut bestimmen, wird hier eine relative Kraftmessung durchgeführt. Durch den symmetrischen Aufbau können die molekularen Wechselwirkungen direkt verglichen werden und kleinste Unterschiede oder Veränderungen detektiert werden. Systematische Fehler, die durch die Kalibrierung eines klassischen Kraftsensors wie zum Beispiel einer AFM-Blattfeder entstehen, werden vermieden.

## 5. Ergebnisse

In den Kapiteln 3 und 4 wurde ein Überblick über die biologische Fragestellung, den biophysikalischen Grundlagen und der dafür weiterentwickelten Methode gegeben, mit der diese Fragen beantwortet werden sollen. In diesem Kapitel werden die Ergebnisse dieser Arbeit zusammengefasst.

### 5.1 DNA als molekularer Kraftsensor für Protein-DNA-Wechselwirkungen

In den Kapiteln 2 und 3 wurde gezeigt, dass ein großer Bedarf herrscht Techniken zu entwickeln um Protein-DNA-Wechselwirkungen genauer untersuchen zu können. Wobei sich „genauer“ auf die Bestimmung weiterer biophysikalischer Parameter, wie zum Beispiel der Potentialweite der Bindung und den Bindungskräften, als auch Affinitäten und Bindungsraten bezieht. Allerdings ist man nach heutigem Wissen an dem Punkt angekommen, dass alleine die Eigenschaften einer einzelnen Bindung für ein Protein-DNA-Paar zu bestimmen bei weitem nicht mehr ausreicht um die biologischen Zusammenhänge und Funktionen eines Proteins in Zell-Kontext zu verstehen. Vielmehr ist es nötig diese Eigenschaften für viele Protein-DNA-Paare mit hoher Präzision zu bestimmen, um die komplexen biologischen Zusammenhänge und deren Netzwerke von molekularen Interaktionen verstehen zu können. Techniken, die molekulare Bindungskräfte untersuchen, haben sich als sehr nützlich erwiesen, allerdings hat keine dieser Techniken das Potential zu einer sogenannten High-Throughput-Methode erweitert zu werden, die teilweise Millionen von Wechselwirkungen in einem Ansatz charakterisieren kann.

In der hier beschriebenen Erweiterung des molekularen Kraftsensors (Publikation P1), soll erstens dessen Anwendbarkeit auf Protein-DNA-Wechselwirkungen gezeigt werden. Zweitens soll untersucht werden, ob durch den hier neu entwickelten Aufbau aus Epi-Fluoreszenzmikroskop und Kontakteinheit, kombiniert mit der Implementierung eines FRET-Paares in den Kraftsensor für die Bestimmung der Kopplungseffizienz, eine für High-Throughput-Methoden notwendige Miniaturisierung erreicht werden kann.

Neben dem Nachweis von Protein-DNA-Wechselwirkungen lässt sich der molekulare Kraftsensor auch allgemeiner zur Detektion anderer Liganden verwenden. So werden zum Beispiel in Publikation P2 DNA-bindende Polyamide nachgewiesen [68, 69]. Auch lässt sich durch eine gezielte Wahl der DNA-Sequenz ein DNA-Aptamer in den molekularen Kraftsensor einfügen, so dass Moleküle, wie zum Beispiel ATP, detektiert werden können (Publikation P3).

#### Bestimmung von Dissoziationskonstanten über Wechselwirkungskräfte

Die Detektion von DNA-Bindern mit dem molekularen Kraftsensor beruht auf einer Verschiebung in Entbindungskräften verursacht durch die Komplex-Bildung aus Binder und DNA. Wie in Kapitel 4 beschrieben besteht der Kraftsensor aus zwei DNA-Duplexen, deren Stabilität gemessen wird, in Analogie zu einer Balkenwaage, bei der die Gewichtskräfte verglichen werden. Um DNA-Liganden nachzuweisen wird ein gut ausgeglichener, möglichst symmetrisch aufgebauter Kraftsensor aus zwei – in Entbindungskräften gesprochen – gleichwertigen DNA-Duplexen verwendet. Der eine DNA-Duplex, der „Ziel-Duplex“, enthält eine spezifische Bindungssequenz für den Liganden, während der andere Duplex, der „Referenz-Duplex“ keine Bindungsstelle ausweist. Durch das Binden des Liganden an den Ziel-

Duplex entsteht ein Komplex dessen mechanische Stabilität sich im Vergleich zu dem Ziel-Duplex ohne Ligand verändert hat. Das Binden des Liganden an nur einen der zwei Duplexe „verstimmt“ den symmetrischen Aufbau des molekularen Kraftsensors, was durch eine Verschiebung in der Normalisierten Fluoreszenz nachgewiesen werden kann. Da der molekulare Kraftsensor Änderungen von einigen Piconewton (pN) detektieren kann, können kleinste Änderungen durch die DNA-Ligand-Komplexbildung gemessen werden.

Als Modellsystem wurde die Endonuklease EcoRI als Ligand verwendet. EcoRI ist ein Restriktionsenzym, welches in der Anwesenheit von  $Mg^{2+}$ -Ionen DNA an der palindromischen Erkennungssequenz 5'-GAATTC-3' schneidet. In *Escherichia coli* dient EcoRI als ein Schutzsystem, welches fremde DNA an der Erkennungssequenz schneidet. *Escherichia coli* schützt seine eigene DNA durch Methylierung dieser Sequenzstellen. In Abwesenheit von  $Mg^{2+}$ -Ionen bindet EcoRI als Homo-Dimer (a 32 kDa) ohne zu schneiden. EcoRI zeichnet sich durch eine hohe Affinität (Dissoziationskonstante  $K_D \approx$  nM) und Spezifität gegen seine Erkennungssequenz aus und ist somit ideal als „*proof of principle*“ geeignet.

Um die Affinität des Liganden mittels molekularen Kraftsensors bestimmen zu können, wird der Versuch wie in Kapitel 4 beschrieben jeweils für verschiedene Konzentrationen an EcoRI durchgeführt und so die NF in Abhängigkeit von der EcoRI-Dimer-Konzentration gemessen.

### **Unterschiedliche Entbindungsgeometrien des molekularen Kraftsensors**

Wie in Abbildung 7 (c) und (d) dargestellt, kann der molekulare Kraftsensor in zwei verschiedenen Entbindungsgeometrien (Zipper- und Schergeometrie) aufgebaut werden. Es wurde gezeigt, dass die mittlere Abrisskraft für ein 30 Basenpaar DNA-Duplex in Schergeometrie bei moderaten Ladungsraten ( $\sim 10^3$  pN/s) um die 60 pN liegt [70, 71]. In Zippergeometrie liegt die mittlere Abrisskraft abhängig vom GC-Gehalt und Sequenz um die 15 pN. Daraus folgt: ein molekularer Kraftsensor sollte in Zippergeometrie sensitiver sein als in Schergeometrie. In Abbildung 7 (e) und (f) ist die NF gegen die EcoRI-Dimer Konzentration aufgetragen. Die Kraftwaage ist so aufgebaut, dass der untere Duplex die Erkennungssequenz enthält, während der obere als Referenz-Duplex dient. Durch das Binden von EcoRI an den unteren Duplex wird dieser stabilisiert und die NF ist zu höheren Werten verschoben. Die Messpunkte wurden mit der Hill Gleichung gefittet. Hieraus ergeben sich die Werte für die Dissoziationskonstanten in Schergeometrie  $K_D = (0,97 \pm 0,14)$  nM und  $K_D = (0,22 \pm 0,06)$  nM in Zippergeometrie.

In einem optischen Pinzetten-Experiment konnte gezeigt werden, dass sich die Bindungseigenschaften von EcoRI an der DNA nicht wesentlich ändern, wenn die benachbarten Basenpaare der DNA in Zippergeometrie getrennt werden [17, 72]. In Schergeometrie wird allerdings an alle Basenpaare gleichzeitig eine Kraft angelegt und die 3-dimensionale Form der DNA ändert sich mit steigender Kraft bevor sich die DNA Stränge trennen. Diese Deformation der DNA kann die Affinität des gebundenen Proteins beeinflussen, so dass sich EcoRI mit einer gewissen Wahrscheinlichkeit von dem Duplex löst bevor der DNA-Duplex selber in zwei Einzelstränge übergeht. Dies würde in Schergeometrie zu einer gemessenen scheinbaren Dissoziationskonstanten führen, die über dem Wert der realen  $K_D$  beziehungsweise der  $K_D$  in Zippergeometrie liegt, wie es hier der Fall ist.

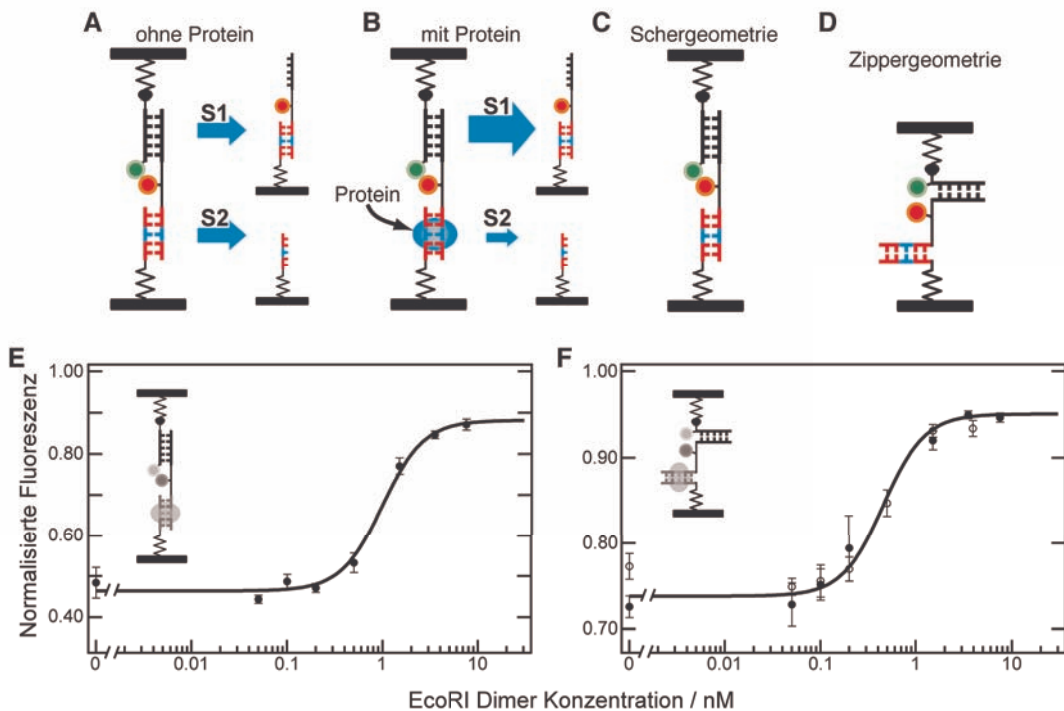


Abbildung 7: In (a) und (b) ist das Prinzip der Detektion von spezifischen Ligand-DNA-Wechselwirkungen dargestellt. Ein Duplex besitzt eine Erkennungssequenz an die der Ligand bindet (hier: der untere Duplex), während der andere DNA-Duplex keine Bindestelle besitzt. Durch das Binden des Liganden wird die Stabilität des unteren DNA-Duplexes verändert, was das Abrissverhältnis von oberen zu dem unteren DNA-Duplex und damit die NF verschiebt. Der molekulare Kraftsensor kann in zwei Versionen aufgebaut werden. Einerseits in einer Schergeometrie (c) mit Entbindungskräften von einigen 10 pN, andererseits in einer Zippergeometrie (d) bei der die DNA-Basenpaare nacheinander bei zirka 15 pN geöffnet werden. (e, f) Detektion von Protein–DNA-Wechselwirkungen unter physiologischen Bedingungen. Restriktionsenzym EcoRI bindet als Homodimer an die Erkennungssequenz 5'-GAATTC-3' im unteren DNA-Duplex. (Eine ausführliche Beschreibung findet sich in Publikation P1)

Des Weiteren muss die Zeitskala der thermischen Dissoziation vom Protein-DNA-Komplex mit der Zeitskala der Separation der DNA Stränge verglichen werden. Wenn das System die Möglichkeit hat zu equilibrieren, während die externe Kraft im Separationsprozess auf die Kraftwaage wirkt, würde dies auch zu einer scheinbar höheren  $K_D$  führen. Die mittlere Lebensdauer, beziehungsweise die inverse Dissoziationsrate, wurde für den EcoRI-DNA-Komplex experimentell bestimmt und liegt in der Größenordnung von einigen 10 s [73]. Via Einzelmolekülkraftspektroskopie konnte gezeigt werden, dass bei einem 30 bp langen DNA-Duplex in Schergeometrie, einer Zuggeschwindigkeit von  $5 \mu\text{m s}^{-1}$  und gleicher Polymer-Linkerlänge die Kraft bis zum Abriss in der Größenordnung von 10 ms aufgebaut wird. Somit geschieht die Auftrennung des DNA-Doppelstrangs auf einer viel schnelleren Zeitskala als die thermische Assoziations- oder Dissoziationsrate bei relevanten EcoRI-Konzentrationen. Daraus lässt sich folgern, dass durch den großen Unterschied in den Zeitskalen ein Schnappschuss des Zustandes, wie viele Kraftsensoren mit einem Protein besetzt sind, aufgenommen wird und damit die Dissoziationskonstante mit dieser Methode bestimmt werden kann.

### **Möglichkeiten der Miniaturisierung des Molekularen Kraft-Assays**

Da der Bindungsbruch ein thermisch aktivierter Prozess ist, werden in der Einzelmolekülkraftspektroskopie einige hundert bis tausend Events gemessen, um daraus ein Histogramm mit einer aussagekräftigen mittleren Abrisskraft erstellen zu können. Wie zuvor erwähnt, liegt die Anbindungsichte von molekularen Kraftsensoren in der Größenordnung von  $10^4$  pro  $\mu\text{m}^2$ , so dass rein von dieser Überlegung her mit einem  $\mu\text{m}^2$  sich eine aussagekräftiger Wert für die NF ergeben könnte. Allerdings gibt es Quellen, die Einfluss auf den Messprozess haben und so die effektiv benötigte Zahl an Kraftsensoren erhöht, beziehungsweise die benötigte Fläche für eine genaue Bestimmung der NF vergrößert. Hierzu zählt unter anderem das Poisson-Rauschen, verursacht durch die endliche Anzahl der gemessenen Photonen, das Bleichen der Farbstoffe, die absolute Kopplungseffizienz zwischen Kraftsensoren und PDMS-Stempel, Inhomogenitäten in der Oberflächenfunktionalisierung und auch Verunreinigungen der Proben durch fehlerhaft synthetisierte DNA-Oligomere [67]. In Publikation P1 und Abbildung 8 wird im Experiment gezeigt, dass eine Fläche von  $5 \mu\text{m} \times 5 \mu\text{m}$  noch ausreicht um die NF mit genügender Genauigkeit bestimmen zu können. Diese minimal benötigte Fläche liegt unterhalb der Feature-Größe aktueller DNA-Mikroarrays, so dass der molekulare Kraftsensor die hinreichende Voraussetzung bezüglich der Feature-Dichte für moderne High-Throughput-Methoden erfüllt. Außerdem besteht damit die Möglichkeit das molekulare Kraft-Assay als Sensor in Mikrofluidik-Systeme zu integrieren.

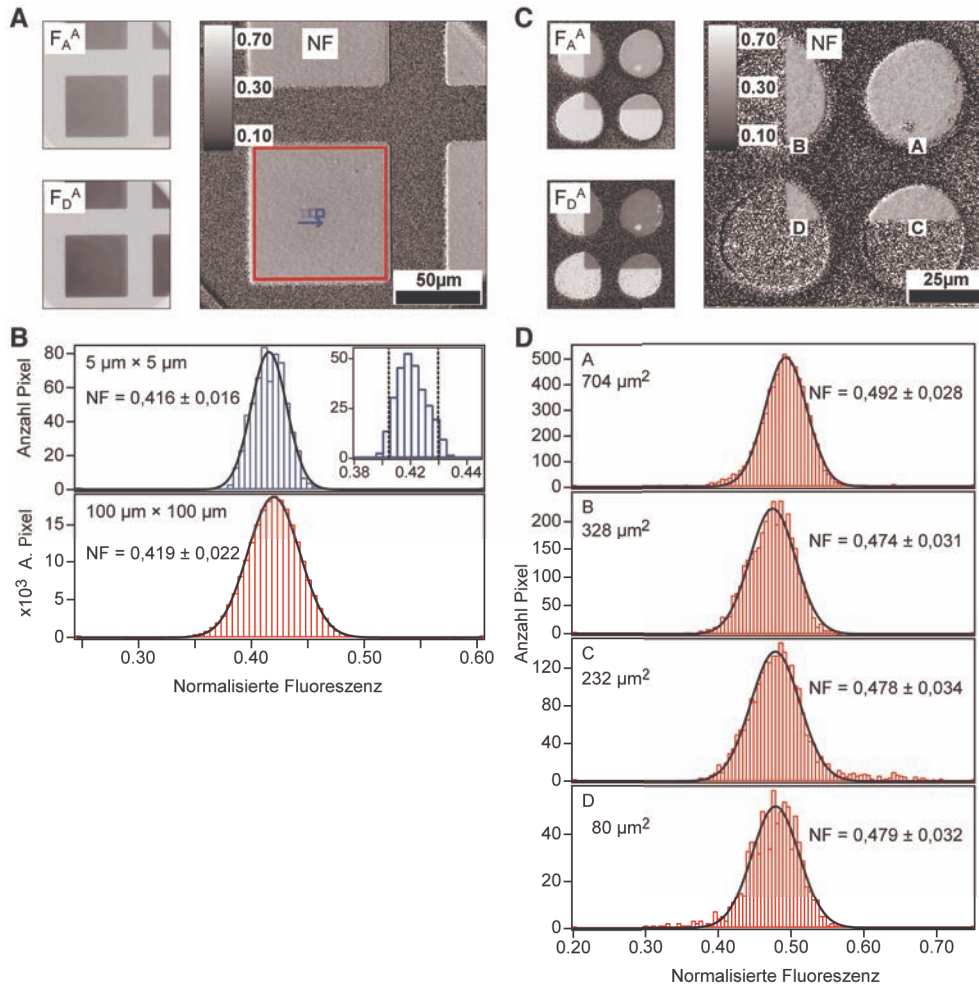


Abbildung 8: Möglichkeit der Miniaturisierung des molekularen Kraft-Assays. In (a) ist ein Ausschnitt eines hochauflösenden NF-Bildes dargestellt. Das rote und das blaue Quadrat zeigen die ROI für die NF-Histogramme in (b). Das kleine eingefügte Histogramm in (b) zeigt die Verteilung der mittleren NF-Werte für alle 400  $5 \times 5 \mu\text{m}$  großen Quadrate innerhalb des roten  $100 \times 100 \mu\text{m}$  Quadrates. Die vertikalen gestrichelten Linien sind die Perzentile von 5% und 95%. (c) NF-Bild eines Mikroarrays bestehend aus identischen molekularen Kraftsensoren. Das PDMS-Quadrat hat das Mikroarray so kontaktiert, dass verschieden große Kontaktflächen entstanden sind. In (d) sind Histogramme dieser vier Bereiche des NF-Bildes dargestellt. Alle Bereiche stimmen in der mittleren NF sehr präzise miteinander überein.

## 5.2 Die Erweiterung zum „molekularen A/D-Wandler“

### Prinzip des „molekularen A/D-Wandlers“

Im vorigen Kapitel wurde die Funktionsweise des molekularen Kraftsensors erklärt. Verallgemeinert beschrieben sind dabei zwei molekulare, nicht-kovalente Bindungen in Serie miteinander verbunden. Dies kann theoretisch ein beliebiges Rezeptor-Ligand-System sein, aber in diesem Fall wurden zwei kurze DNA-Doppelstränge verwendet, die sich unter einer extern angelegten Kraft in jeweils zwei Einzelstränge auftrennen lassen. Wenn nun eine externe Kraft an den molekularen Kraftsensor angelegt wird, wird eine der beiden Bindungen nachgeben und die andere intakt bleiben. Ausgelesen wird dies über einen Fluoreszenzfarbstoff am mittleren DNA Strang, der anzeigt ob sich der mittlere DNA-Strang an der oberen Fläche (PDMS-Stempel) oder der unteren Fläche (Glas-Slide) befindet.

Dieser Prozess lässt sich anhand einiger Analogien mit Elementen aus der Elektrotechnik vergleichen. Daraus lassen sich inhärente Vorteile der Technik des molekularen Kraftsensors aufzeigen, als auch die Weiterentwicklung zum „molekularen A/D-Wandler“ motivieren (Publikation P5).

In Analogie zum Komparator aus der Elektrotechnik wird beim molekularen Kraftsensor die mechanische Stabilität zweier molekularer Bindungen verglichen. Als Ergebnis erhält man für jeden einzelnen Kraftsensor eine binäre Antwort, „unterer DNA-Duplex abgerissen, oberer DNA-Duplex intakt“ bzw. „unterer DNA-Duplex intakt, oberer DNA-Duplex abgerissen“. Als analoge Eingangssignale haben dabei die mechanischen Stabilitäten der zwei DNA-Duplexe gedient. Im Folgenden soll der untere DNA-Duplex der Referenz-Duplex sein und der obere Duplex der Ziel-Duplex.

In der Erweiterung zum „molekularen A/D-Wandler“ werden nun anstatt eines molekularen Kraftsensors mehrere unterschiedliche Kraftsensoren für eine Messung verwendet. Dies lässt sich in Anlehnung an den Flash-A/D-Wandler (Abbildung 9) wie folgt erklären. Bei einem Flash-A/D-Wandler sind mehrere Komparatoren parallel aufgebaut, alle an die gleiche zu messende Eingangsspannung angeschlossen, und über Widerstände ist stufenweise eine jeweils eine andere Referenzspannung je Komparator angelegt. Dies hat den Vorteil dass schnell und direkt mit einer Messung die Eingangsspannung mit der Auflösung der Spannungsstufen der Referenzspannung bestimmt werden kann. In Anlehnung daran kann nun die molekulare Version des Flash-A/D-Wandlers aufgebaut werden, die anstatt von Spannungen die molekularen Wechselwirkungskräfte misst. Hierfür werden mehrere unterschiedliche Kraftsensoren mit verschieden langen Referenz-Duplexen als eine „molekulare A/D-Wandler“-Einheit verwendet. Auf diese Weise soll mit einer einzigen Messung die Stabilität einer zu untersuchenden Ziel-Duplexes bestimmt werden.

Da der Bindungsbruch eines DNA Duplexes in seine zwei Einzelstränge ein thermisch aktivierter Prozess ist, ergibt sich für die Abrisskraft eine statistische Verteilung von Abrisskräften [29, 32, 74]. Einerseits bedeutet dies, dass über eine Vielzahl einzelner Kraftsensor-Events gemittelt werden muss. Wie in Kapitel 4 beschrieben, werden dafür viele Kraftsensoren eines Types hochparallel gemessen und aus dem Fluoreszenzsignal lässt sich dann eine Normalisierte Fluoreszenz bestimmen, welches eine Mittelung über die vielen binären Antworten darstellt. Andererseits ergibt sich hier durch die Breite der Abrisskraftverteilungen eine Überlappung der Verteilungen von Referenz- und Ziel-Duplex. Das führt dazu, dass für den molekularen A/W-Wandler kein sprunghafter Anstieg der NF ab einer bestimmten Referenz-Duplex-Länge gemessen wird, sondern ein gradueller Anstieg der NF mit der Referenz-Duplex-Länge.

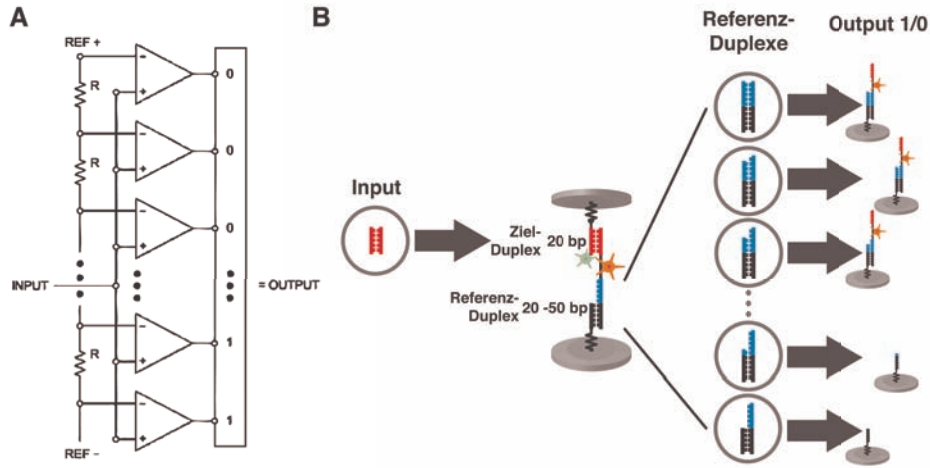


Abbildung 9: (a) Schema eines elektronischen Flash-A/D-Wandlers. (b) Prinzip des molekularen A/D-Wandlers. In Analogie zum elektronischen Flash-A/D-Wandler bei dem mehrere Komparatoren parallel mit einer stufenweise ansteigenden Referenzspannung geschaltet sind, sind beim molekularen A/D-Wandler mehrere molekulare Kraftsensoren mit unterschiedlich langen Referenz-Duplexen parallel auf einer Oberfläche aufgebaut. Anstatt von Spannungen werden die molekularen Wechselwirkungskräfte gemessen.

Über das Bell-Evans-Modell [29, 32] lässt sich hierfür ein Modell ableiten mit dem der molekulare Kraftsensor und die damit zusammenhängende NF beschrieben werden kann. Eine detaillierte Beschreibung findet sich in Publikation P5. Kurz zusammengefasst: der Bindungsbruch wird im Bell-Evans-Modell mit einem Zwei-Zustands-Modell beschrieben. Es konnte mehrfach experimentell gezeigt werden, dass sich auch komplexere molekulare Wechselwirkungen [20], wie zum Beispiel auch bei kurzen doppelsträngigen DNA-Oligomeren [70, 71], in erster Näherung gut mit diesem Modell beschreiben lassen. Aus dem Bell-Evans-Modell folgt, dass sich die durch eine externe Kraft verursachte Dissoziation eines molekularen Komplexes mit einer Bindungsbruch-Wahrscheinlichkeitsdichtefunktion  $p(f, \dot{f})$  für eine gegebene Kraftladungsrate ( $\dot{f}) = df/dt$  wie folgt beschreiben lässt:

$$p(f, \dot{f}) = \frac{k_{off}}{\dot{f}} \cdot \exp\left(\frac{f \cdot \Delta x}{k_B T}\right) \cdot \exp\left(-\frac{k_{off}}{\dot{f}} \cdot \int_0^f du \cdot \exp\left(\frac{u \cdot \Delta x}{k_B T}\right)\right)$$

$k_B$  ist die Boltzmann-Konstante und  $T$  die Temperatur. Die Potentialweite  $\Delta x$  und die natürliche Dissoziationsrate  $k_{off}$  beschreiben die Eigenschaften der Bindung und lassen sich experimentell bestimmen. Im Fall von kurzen DNA-Oligomeren konnte experimentell eine Näherung gefunden werden, die  $\Delta x$  und  $k_{off}$  in Abhängigkeit von der Basenpaar-Anzahl  $n$  beschreibt [71]:

$$k_{off}(n) = 10^{\alpha - \beta n} \cdot s^{-1} \quad \text{and} \quad \Delta x(n) = (t + n \cdot m) \cdot \text{\AA}$$

mit  $\alpha = (3 \pm 1)$ ,  $\beta = (0.5 \pm 0.1)$ ,  $t = (7 \pm 3)$  und  $m = (0.7 \pm 0.3)$ . Mit Hilfe dieser zwei Zusammenhänge lässt sich die Normalisierte Fluoreszenz in wie folgt beschreiben:



$$NF(\dot{f}, n_R, n_Z) = \frac{1}{2} \left[ 1 + \int_{f_A}^{\infty} df (p_R(f, \dot{f}, n_R) - p_Z(f, \dot{f}, n_Z)) \right]$$

mit  $f_A$  ist der Schnittpunkt der Bindungsbruch-Wahrscheinlichkeitsdichtefunktionen vom Referenz-Duplex  $p_R$  und vom Ziel-Duplex  $p_Z$  und  $n_{R/Z}$  die Anzahl von Basenpaaren für Referenz- und Ziel-Duplex. Für beliebige  $\Delta x$  und  $k_{\text{off}}$  lässt sich eine verallgemeinerte Beschreibung für  $NF$  finden:

$$NF(\dot{f}, \Delta x_R, k_{\text{off}R}, \Delta x_Z, k_{\text{off}Z}) = \frac{1}{2} \left[ 1 + \int_{f_A}^{\infty} df (p_R - p_Z) + \int_{f_B}^{\infty} df (p_R - p_Z) \right]$$

mit  $p_R = p_R(f, \dot{f}, \Delta x_R, k_{\text{off}R})$  und  $p_Z = p_Z(f, \dot{f}, \Delta x_Z, k_{\text{off}Z})$

und  $f_B$  und  $f_A$  ist der erste und zweite Schnittpunkt der Bindungsbruch-Wahrscheinlichkeitsdichtefunktionen und  $\Delta x_{R/Z}$  und  $k_{\text{off}R/Z}$  sind die zu Referenz- und Ziel-Duplex gehörigen Potentialweiten und Dissoziationsraten.

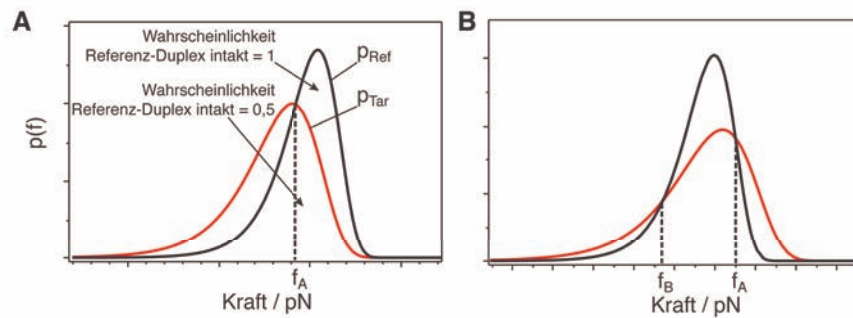


Abbildung 10: Beispiel für Wahrscheinlichkeitsdichtefunktionen nach Bell und Evans (vgl. Publikation P5). (a) Überlappende Wahrscheinlichkeitsdichtefunktionen mit einem Schnittpunkt. (b) Allgemeiner Fall mit zwei Schnittpunkten für beliebige  $\Delta x$  und  $k_{\text{off}}$  für Referenz- und Ziel-Duplex.

Wegen der in der Literatur vorhandenen, experimentell bestimmten Werte  $\Delta x$  und  $k_{\text{off}}$  für DNA-Oligomere (siehe Referenz [71]) und den vielfach erfolgreichen Beschreibung von biomolekularen Wechselwirkungen mittels Bell-Evans-Modell [20], war es empfehlenswert dieses Modell für die Beschreibung des molekularen A/D-Wandlers zu verwenden. Jedoch stellt das Zwei-Zustands-Modell von Bell und Evans eine starke Vereinfachung des Bindungsbruchs von DNA-Oligomeren da. Ein im Vergleich dazu verbessertes Modell, um den Bindungsbruch von kurzen DNA-Strängen in Schergeometrie zu beschreiben, findet sich in Publikation P4. Über ein 3-Zustands-Gleichgewichtsmodell werden die Raten für den Bindungsbruch des DNA-Doppelstranges und die Abrisskraft-Verteilung als eine Funktion der Trenngeschwindigkeit des End-zu-End-Abstandes berechnet.

## 0-Abgleichverfahren zur Quantifizierung von molekularen Wechselwirkungskräften

Im vorherigen Abschnitt wurde Aufbau und Funktionsweise des molekularen A/D-Wandlers beschrieben. In diesem Abschnitt wird die Anwendung des molekularen A/D-Wandlers zur Charakterisierung von molekularen Wechselwirkungskräften beschrieben.

Von zentraler Bedeutung ist in diesem Zusammenhang die Idee eine Kompensationsmessung durchzuführen ähnlich wie bei einer Wheatstone'schen Messbrücke, bei der durch ein 0-Abgleichverfahren mit höchster Präzision der Wert eines Widerstandes bestimmt werden kann. Bei dem molekularen A/D-Wandler lässt sich dieses Prinzip wie folgt umsetzen. In Abwesenheit von Liganden erwartet man bei einem ausgeglichenen molekularen Kraftsensor – z.B. bestehend aus 20 bp Referenz- und Ziel-Duplex – eine NF von 0,5. Wenn nun die Messung mit einem Liganden durchgeführt wird, der spezifisch nur an den Ziel-Duplex (oberer DNA-Duplex) bindet, wird die NF zu Werten kleiner 0,5 verschoben (vergleiche Kapitel 5.1). Die Idee ist nun, dieselbe Messung mit Liganden und mit der eben beschriebenen molekularen A/D-Wandler-Einheit, die verschieden lange Referenz-Duplexe besitzt, durchzumessen und so die Referenz-Duplex-Länge zu bestimmen, die nötig ist um die mechanische Stabilität des Komplexes aus Ligand und Ziel-Duplex zu kompensieren und eine NF von 0,5 zu bekommen. Die Differenz in Basenpaaren (siehe Abbildung 11) spiegelt dann die Änderung in mechanischer Stabilität wieder, welche durch das Binden des Liganden verursacht wurde.

Daraus folgt, dass die mechanische Stabilität beim molekularen A/D-Wandler in der Einheit „Basenpaare“ (oder genauer, in der Einheit „Stabilität von Basenpaaren“) quantifiziert wird. Es ist möglich die Einheit „Basenpaare“, die die mechanische Stabilität beschreibt, über Einzelmolekül-Kraftspektroskopie-Messungen in Piconewton zu übersetzen: bei einer Ladungsrate von  $10^5$  pN/s hat ein 10 bp DNA-Duplex eine mittlere Abrisskraft von 45 pN und ein 30 bp DNA-Duplex eine mittlere Abrisskraft von 54 pN. Da die Kraft zum Trennen eines DNA-Duplexes auch von GC-Gehalt abhängt, wäre für eine möglichst genaue Übersetzung von der „Stabilität von Basenpaaren“ in Piconewton die Messung der mittleren Abrisskraft der verwendeten Referenz-Duplexen mittels Einzelmolekül-Kraftspektroskopie möglich.

Um die Eigenschaften des molekularen A/D-Wandlers bezüglich der Quantifizierung von molekularen Wechselwirkungskräften zu testen, wurden drei unterschiedliche Liganden gemessen. Hierfür wurden drei verschiedene A/D-Wandler-Versionen mit Ziel-Duplexen spezifisch gegen drei Liganden konstruiert und gemessen. Es wurden für alle drei Liganden immer die gleichen 8 Referenz-Duplexe verwendet, um die molekularen Wechselwirkungskräfte der drei Liganden optimal vergleichen zu können. Es wurden unterschiedliche Arten von Liganden verwendet: (i) ein Polyamid (entwickelt um einen Transkriptionsfaktor von seiner spezifischen DNA-Bindungsstelle zu verdrängen), welches mit einer sehr niedrigen Dissoziationskonstanten ( $K_D \approx \mu\text{M}$ ) in die „Minor Groove“ der DNA bindet und mit ca. 10 kDa sehr klein ist [75, 76]. (ii) ein Restriktions-Enzym, welches als Dimer (je 32 kDa) mit einer hohen Spezifität und einer  $K_D$  im nM-Bereich in die „Major Groove“ seiner Erkennungssequenz bindet. (iii) die DNA-Bindedomäne des Transkriptionsfaktors p53 [77, 78], welches zu der Superklasse der „Beta-Scaffold Transkriptionsfaktoren mit Minor Groove-Kontakten“ gehört, die mit einer etwas höheren  $K_D$  in der Größenordnung von  $\approx 100$  nM an die ausgewählte Erkennungssequenz ebenfalls als Dimer bindet.

In Abbildung 11 (a) wird die Wechselwirkung des Pyrrol-Imidazol Hairpin-Polyamides (P1) mit seiner Erkennungssequenz 5'-TGGTCA-3' gezeigt. Abbildung 11 (b) zeigt das Binden der Typ II Restriktions-Endonuklease (EcoRI), die in Abwesenheit von  $\text{Mg}^{2+}$ -Ionen an die Erkennungssequenz 5'-GAATTC-3' bindet, ohne enzymatisch aktiv zu sein. Als drittes Beispiel wurde die Wechselwirkung des Transkriptionsfaktors p53 mit der Promotorsequenz CON2x5

vermessen. Wie aus Abbildung 11 abzulesen ist, wird für den P1-Ziel-Duplex ein Referenz-Duplex von 29,5 bp Länge benötigt um die NF auf 0,5 zu bekommen. Das heißt, die Wechselwirkung von P1 stabilisiert den Ziel-Duplex um 9,5 bp. Die Wechselwirkung von EcoRI ist noch stärker und entspricht einer Stabilisierung von 27,7 bp. Um die Wechselwirkung von p53 quantifizieren zu können, müsste der Referenz-Duplex um mehr als 30 bp erweitert werden.

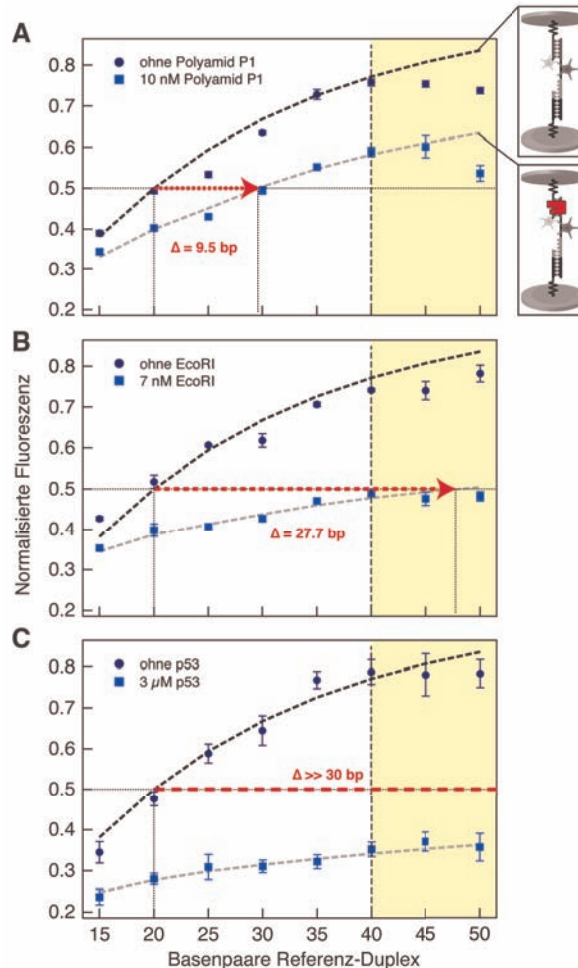


Abbildung 11: Charakterisierung der Wechselwirkungskräfte von drei Liganden mit dem molekularen A/D-Wandler: (a) Polyamid P1 (b) Endonuklease EcoRI und (c) DNA-Binde-Domäne des Transkriptionsfaktors p53. Der Stärke der Stabilisierung durch den Liganden ist mit einem roten Pfeil in „Stabilität von Basenpaaren“ angegeben. Oberhalb einer Referenz-Duplexlänge von 40 bp (gelb hinterlegt) reichen die Abrisskräfte signifikant in den BS-Übergang von DNA bei 65 pN hinein, was ein Plateau in NF zur Folge hat (vgl. auch Publikation P7). Die gestrichelten Kurven stellen die analytische Lösung nach dem Bell-Evans Zwei-Zustandsmodell dar (siehe Publikation P5).

### Miniaturisierung und Parallelisierung des Molekularen A/D-Wandlers zum „Binding-Force-Chip“ via Mikrostrukturierung

Um Protein-DNA-Wechselwirkungen biologisch und biophysikalisch besser verstehen zu können (siehe Kapitel 2), ist es sehr wichtig, diese Wechselwirkung eines bestimmten Proteins oder Protein-Familie mit einer Vielzahl unterschiedlicher DNA-Sequenzen zu vermessen.

Hierfür werden High-Throughput-Methoden benötigt. In Kapitel 5.1 wurde unter anderem die Möglichkeit der Miniaturisierung der Messfleckengröße, beziehungsweise der Erhöhung der Feature-Dichte gezeigt. Hier wird nun die experimentelle Umsetzung einer High-Throughput-Version des molekularen Kraftsensors demonstriert.

Um die Dichte an unterschiedlichen Kraftsensoren zu erhöhen, muss die Messfleckengröße verkleinert werden. Dies wurde mit Hilfe eines Mikroplotters zu Mikrostrukturierung der Oberfläche erreicht, der in der Größenordnung von 1  $\mu\text{l}$  Lösungen absetzt. Dafür musste die verwendete Oberflächenchemie, wie in Publikation P5 in Detail beschrieben, angepasst werden. Es konnten minimale Messfleckengrößen bis zu einem Durchmesser von 15  $\mu\text{m}$  bis 20  $\mu\text{m}$  erreicht werden.

In Abbildung 12 ist die experimentelle Realisierung des molekularen A/D-Wandlers in unterschiedlichen Größenskalen dargestellt. Dabei bilden 8 molekulare Kraftsensoren mit dem gleichen Ziel-Duplex und 8 verschiedenen langen Referenz-Duplexen (15 bp bis 50 bp) eine A/D-Wandler-Einheit. Ein Vergleich der NF-Werte für die verschiedenen großen molekularen A/D-Wandler ist in Abbildung 12 (d) gezeigt. Die gestrichelte Kurve zeigt die theoretisch bestimmten Werte nach dem analytischen Modell für den molekularen Kraftsensor, das von Bell und Evans hergeleitet wurde (siehe ersten Abschnitt Kapitel 5.2 und Publikation P5).

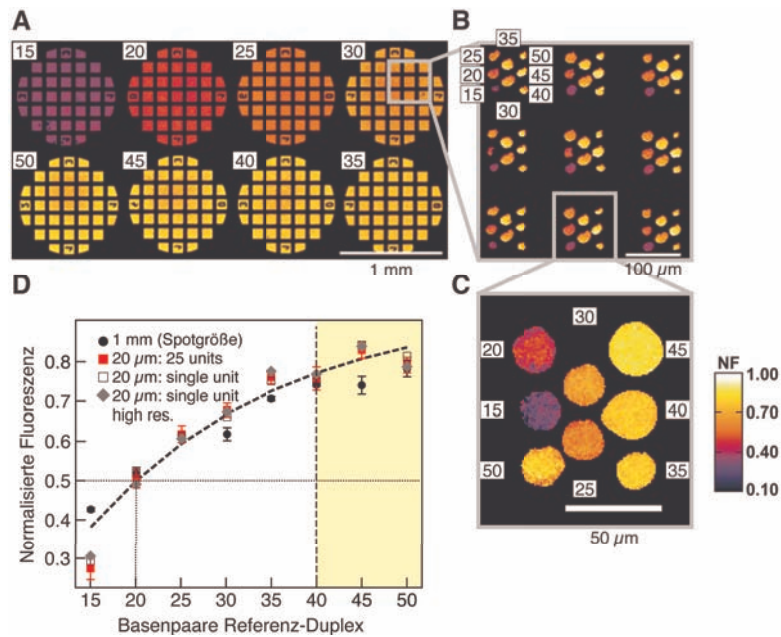


Abbildung 12: Miniaturisierung und Parallelisierung des Molekularen A/D-Wandlers zum „Binding-Force-Chip“. (a) NF-Bilder eines typischen Experiments bei einer Messfleckengröße von 1 mm pro molekularen Kraftsensor-Typ. (b) Verkleinerung des molekularen A/D-Wandlers zum „Binding-Force-Chip“. (c) Hochauflösendes NF-Bild einer molekularen A/D-Wandler-Einheit. Die Zahlen in den weißen Boxen geben die Länge des Referenz-Duplexes an. (d) Mittlere NF-Werte sind gegen die Referenz-Duplexlänge aufgetragen.

### 5.3 Einfluss von epigenetischen Modifikationen auf die DNA-Mechanik

DNA-Methylierung spielt eine grundlegende Rolle in der Epigenetik. So kann durch DNA-Methylierung ein gezieltes Gen oder auch ein vollständiges Chromosom abgeschaltet werden. Während die biologische Funktion immer besser verstanden wird, sind die zu Grunde liegenden Mechanismen der methylierungs-induzierten Genregulation noch kaum verstanden.

In diesem Kapitel und in Publikation P6 wird der Einfluss der DNA-Methylierung auf die mechanischen Eigenschaften von DNA untersucht, ob und wie das Auftrennen des DNA-Doppelstranges in zwei Einzelstränge durch die Methylierung von der Base Cytosin beeinflusst wird. Hierzu werden kurze doppelsträngige DNA-Oligomere mit unterschiedlichen Methylierungsmustern sowohl per Einzelmolekül-Kraftspektroskopie als auch mit dem molekularen Kraftsensor untersucht. Darüber hinaus haben Dr. X. Zou und Professor K. Schulten von der Universität in Illinois (Urbana, Illinois, USA) die gleichen DNA-Sequenzen mittels Molekuldynamik-Simulationen untersucht, um neben den experimentellen Daten den Effekt der Methylierung mit atomarer Auflösung untersuchen zu können.

2009 wurde neben dem schon erwähnten Methylcytosin (mC), welches wegen seiner Wichtigkeit in der Biologie als 5. Base bezeichnet wurde, noch eine 6. Base gefunden, das Hydroxymethylcytosin (hmC) [79, 80]. Zu Beginn wurde angenommen, hmC könnte unter Umständen nur ein Zwischenprodukt im Abbauprozess des mC sein. Allerdings konnte gezeigt werden, dass dies nicht der Fall ist [23]. Erste mögliche biologische Funktionen konnten in den letzten zwei Jahren identifiziert werden, jedoch ist auf molekularer Ebene über den zu Grunde liegenden Mechanismus von hmC noch weniger bekannt als über mC. In Publikation M1 wird hmC analog zu den DNA-Methylierungs-Messungen und Simulationen untersucht.

Sowohl für die Methylierung als auch für die Hydroxymethylierung von Cytosin konnte experimentell ein signifikanter Einfluss auf die mechanische Stabilität des DNA-Doppelstranges bei Separation in zwei DNA-Einzelstränge nachgewiesen werden. Es wird ein Modell vorgeschlagen, wie dieser Effekt einen Einfluss auf die Genregulation ausüben könnte. Mit Hilfe der MD-Simulationen konnte der Effekt für mC und teilweise für hmC auf molekularer Ebene aufgeklärt werden.

#### **Methylcytosin verändert richtungs- und sequenzabhängig die Bindekräfte von DNA**

Untersucht wurde der Einfluss von Methylcytosin anhand eines 20 Basenpaaren langen DNA-Duplexes mit keinem (nDNA), einem (mC-1c-DNA), oder drei mC (mC-3-DNA) pro DNA-Strang (Abbildung 13 (a)). Im molekularen Kraftsensor wurden diese drei verschiedenen DNA-Duplexe immer gegen einen gleichen Referenz-Duplex in Schergeometrie gemessen.

In Abbildung 13 (b) und (c) ist ein repräsentatives Messergebnis dargestellt, in Abbildung 13 (d) die Zusammenfassung von sechs Experimenten, bestehend im Mittel aus jeweils 4 x 13 analysierten Messflecken. Im Vergleich zu nDNA ist die NF für mC-3-DNA zu höheren Werten und für mC-1c-DNA zu kleineren Werten verschoben. Dies bedeutet, dass mC-3-DNA eine höhere mechanische Stabilität ( $\Delta NF = 0,104$ ) und mC-1c-DNA eine niedrigere mechanische Stabilität ( $\Delta NF = 0,063$ ) als nDNA besitzt. Der Ausdruck „mechanische Stabilität der DNA“ bezieht sich hier und im Folgenden auf das Auftrennen des DNA-Doppelstranges in zwei DNA-Einzelstränge.

Somit wird für mC in mC-3-DNA ein stabilisierender Effekt beobachtet, während in mC-1c-DNA ein destabilisierender Effekt auftritt. Um diese Diskrepanz des Einflusses der Methylierung weiter zu untersuchen, wurde mC-1d-DNA und mC-1u-DNA gemessen. Ähnlich wie bei mC-1c-DNA ist nur ein mC pro Strang vorhanden, allerdings ist bei mC-1d-DNA und

mC-1u-DNA nicht wie bei mC-1c-DNA das mittlere der drei CpG methyliert, sondern jeweils ein CpG nahe am Anfang oder am Ende der Sequenz. Im Gegensatz zu mC-1c-DNA hat das einzelne mC-Paar in mC-1d-DNA und mC-1u-DNA einen stabilisierenden Effekt. Somit kann ein einzelnes mC-Paar sowohl einen stabilisierenden als auch einen destabilisierenden Effekt haben. mC-1c-DNA, mC-1d-DNA und mC-1u-DNA unterscheiden sich jeweils in den zu CpG benachbarten Basenpaaren, was die Vermutung nahelegt, dass der Einfluss von mC – stabilisierend oder destabilisierend – abhängig vom Sequenzkontext ist und von den benachbarten Basenpaaren beeinflusst wird. Ein Grund dafür könnte in der dreidimensionalen Struktur der DNA zu finden sein, die von der DNA-Sequenz abhängt [81, 82]. Um die Sequenzabhängigkeit genauer verstehen zu können, werden in Zukunft Messungen zur systematischen Erprobung der zu CpG benachbarten Basenpaaren benötigt.

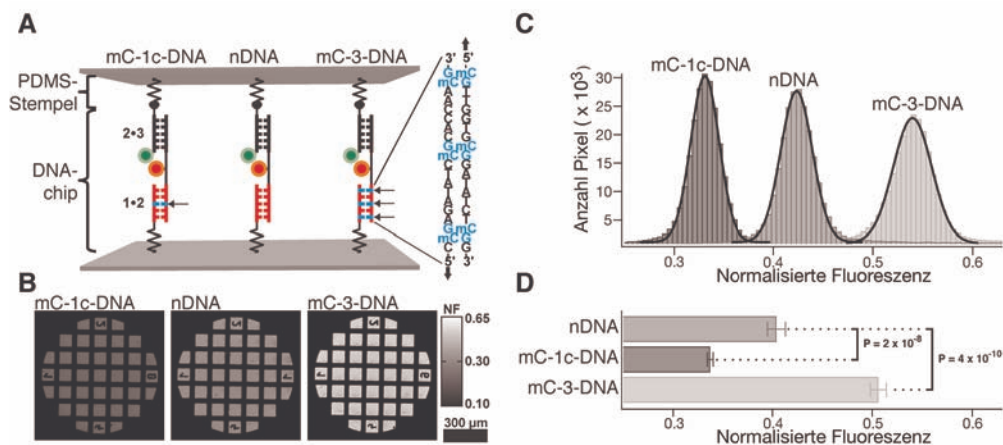


Abbildung 13: (a) Schematische Darstellung des Aufbaus des Experiments. (b) NF-Bilder eines typischen Experiments. (c) Histogramme zu den NF-Bildern aus (b). Zusammenfassung von 6 Experimenten (im Mittel 4 x 13 analysierte Pads pro Experiment).

Neben der Schergeometrie ist es auch möglich die Kraft orthogonal in einer Zippergeometrie anzulegen. Zum Beispiel ist die Richtung der Kraft, die eine Helikase auf den DNA-Doppelstrang ausübt, vergleichbar mit der Richtung der Kraft in einer Zippergeometrie und somit von biologischer Relevanz. In Publikation P6 wurde mit dem molekularen Kraftsensor neben der Schergeometrie auch die Zippergeometrie gemessen. In diesem Fall wurde ein stabilisierender Effekt gemessen, der mit der Anzahl der mC unabhängig vom Sequenzkontext zunimmt. Dies lässt sich erklären, da in Zippergeometrie der DNA-Duplex Basenpaar für Basenpaar aufgetrennt wird und die Kraft immer nur am nächsten zu öffnenden Basenpaar anliegt. Im Vergleich dazu liegt die Kraft in Schergeometrie an allen Basenpaaren gleichzeitig an. Im Unterschied zur Schergeometrie ist in der Zippergeometrie der stabilisierende Effekt nicht so stark ausgeprägt aber dennoch signifikant.

### Methylcytosin verändert die Potentialweite und die „bubble formation“ im DNA Doppelstrang

In Abbildung 14 ist der Aufbau für die Einzelmolekül-Kraftspektroskopie-Messung dargestellt. Eine ausführliche Beschreibung und Diskussion des Versuches und der Ergebnisse findet sich in Publikation P6. Es werden die gleichen DNA-Sequenzen verwendet, wie im vorherigen Abschnitt beschrieben.

Der Versuch lässt sich zusammengefasst wie folgt beschreiben. Es wird ein DNA-Strang über einen PEG-Linker an eine Glasoberfläche angebunden und der komplementäre DNA-Strang in gleicher Weise an der Blattfeder eines Rasterkraftmikroskopes (AFM) immobilisiert. Wird die Blattfeder auf die Oberfläche bewegt, können die zwei zueinander komplementären DNA-Stränge hybridisieren. Wenn die Blattfeder von der Oberfläche entfernt wird, baut sich eine Kraft mit wachsendem Abstand von Blattfeder und Oberfläche auf bis der hybridisierte Doppelstrang nachgibt und in zwei Einzelstränge zerfällt. Dieser Vorgang wird zyklisch wiederholt um die Verteilung der Abrisskräfte und daraus eine wahrscheinlichste Abrisskraft bestimmen zu können (Abbildung 14).

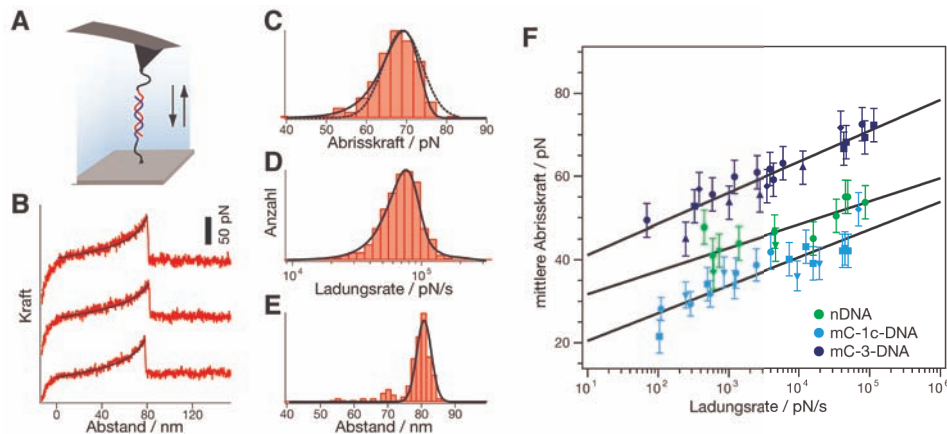


Abbildung 14: (a) Einzelmolekül-Kraftspektroskopie Aufbau (b) Typische Kraft-Abstands-Kurven eines mC-3-DNA Duplexes. Die Kraft-Abstands-Kurven des PEG-DNA Komplexes folgen den „freely jointed chain“-Fit (schwarze Kurve). (c) Typisches Histogramm der Abrisskraft des mC-3-DNA Duplexes. Das Histogramm besteht aus zirka 300 Abriss-Events. Das Histogramm ist mit Wahrscheinlichkeitsdichtefunktion (Bell-Evans-Modell, schwarze Kurve) und einer Normalverteilung (schwarze gestrichelte Kurve) gefittet worden. Die mittlere Abrisskraft beträgt 68 pN. (d) Histogramm der Ladungsraten entsprechend zu (c). Das Histogramm ist mit der Wahrscheinlichkeitsdichtefunktion nach dem Bell-Evans-Modell gefittet worden (schwarze Kurve). (e) Histogramm der Abstandsverteilung der Abrisse entsprechend zu (c) und (d). (f) Der Graph zeigt die wahrscheinlichste Abrisskraft gegen die dazugehörige wahrscheinlichste Ladungsrate für nDNA, mC-1c-DNA und mC-3-DNA. Aus Histogrammen von (c) und (d) werden die Datenpunkte gewonnen. Mit dieser ladungsratenabhängigen Analyse lassen sich nach dem Bell-Evans-Modell durch Fit Werte für  $\Delta x$  und  $k_{off}$  bestimmen.

Werden diese Einzelmolekül-Kraftspektroskopie-Messungen für unterschiedliche Zugeschwindigkeiten bzw. Ladungsraten durchgeführt („Dynamische Kraftspektroskopie“), lässt sich aus der Abhängigkeit der wahrscheinlichsten Abrisskraft von der Ladungsrate über das Bell-Evans-Modell die Potentialweite und die natürliche Dissoziationsrate der molekularen Wechselwirkung bestimmen (vergleiche Kapitel 5.2 und Publikation P6). In Abbildung 14 ist die wahrscheinlichste Abrisskraft in Abhängigkeit von der Ladungsrate für nDNA, mC-1c-DNA und mC-3-DNA dargestellt. Wie in Abbildung 14 (f) dargestellt, hat mC-3-DNA eine höhere wahrscheinlichste Abrisskraft im Vergleich zu nDNA (14 pN Differenz bzw. 31 % bei 3 nN/s), während mC-1c-DNA eine niedrigere wahrscheinlichste Abrisskraft als nDNA hat (19% bei 3 nN/s). Somit zeigen die AFM-Messungen die gleiche Krafthierarchie wie die Messungen des molekularen Kraftsensors. Die Potentialweite und die natürliche Dissoziationsrate zu Abbildung 14 (f) sind in folgender Übersicht dargestellt:

	Potentialweite $\Delta x$ [nm]	Natürliche Dissoziationsrate $k_{\text{off}}$ [ $\text{s}^{-1}$ ]
nDNA	$1.66 \pm 0.35$	$8.4 \times 10^{-6} \pm 3.52 \times 10^{-5}$
mC-1c-DNA	$1.44 \pm 0.18$	$1.7 \times 10^{-4} \pm 2.6 \times 10^{-4}$
mC-3-DNA	$1.24 \pm 0.12$	$9.4 \times 10^{-6} \pm 1.72 \times 10^{-5}$

Sowohl mC-3-DNA als auch mC-1c-DNA zeigen eine deutlich geringe Potentialweite als nDNA. Aus der natürlichen Dissoziationsrate lässt sich wegen des großen Fehlers (typisch für  $k_{\text{off}}$  Bestimmung mittels AFM) nur ein leichter Trend von mC-1c-DNA zu einer höheren  $k_{\text{off}}$  erkennen. Eine verringerte Potentialweite von mC-3-DNA und mC-1c-DNA zu nDNA lässt auf eine „steifere“ Wechselwirkung mit weniger Fluktuationen als in nDNA schließen, die unter Kraft in einer „kompakteren“ Form bis zum Bindungsbruch bleibt.

Im Rahmen dieses Forschungsprojektes wurden von Dr. X. Zou und Professor K. Schulten von der Universität in Illinois „Steered Molecular Dynamics“ (SMD)-Simulationen durchgeführt. Da die Simulationen vom Kollaborationspartner durchgeführt wurden, wird hier nur das Endergebnis präsentiert. Eine ausführliche Beschreibung des Versuches, der Ergebnisse und der Diskussion findet sich in Publikation P6. Dank der räumlichen und zeitlichen Auflösung von SMD-Simulationen können *in silico* biomolekulare Mechanismen in Einzelmolekül-experimenten untersucht werden.

In Abbildung 15 (a) ist die „Stacking Energie“ der DNA-Basen in Abhängigkeit von der Dehnung der DNA-Duplexe unter konstanter Zuggeschwindigkeit dargestellt. Und in Abbildung 15 (b) ist die „Stacking Energie“ gegen die Ausdehnung des DNA-Duplexes unter einer konstanten Kraft von 200 pN über 90 ns gezeigt. Unter Kraft zeigen die methylierten DNA-Duplexe (mC-1c-DNA und mC-3-DNA) eine geordnete Struktur und kompaktere Form als die unmehtylierte DNA, was durch eine verstärkte Wechselwirkung der Stacking Energie herrührt. Dies spiegelt sich auch in den Trajektorien der Simulation in Form von weniger sich bildenden DNA-„bubbles“ (Blasen) wider. Dieses molekulare Bild ist im Einklang mit der reduzierten Potentialweite für methylierte DNA, die in den Einzelmolekülexperimenten gemessen wurde.

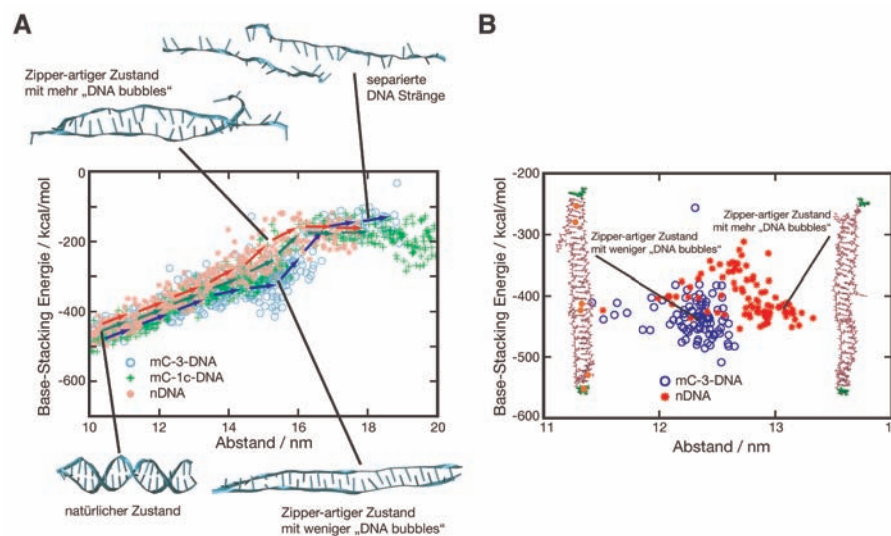


Abbildung 15: SMD-Simulationen: Entbindungspfad der DNA unter extern angelegter Kraft in Schergeometrie. (a) „Base Stacking“-Energie gegen Abstand von jeweils 5 Trajektorien bei einer Zuggeschwindigkeit von 10 Å/ns. Die Pfeile deuten die unterschiedlichen Entbindungspfade von nDNA, mC-1c-DNA und mC-3-DNA an. (b) „Base Stacking“-



Energie gegen Abstand bei konstanter Kraft von 200 pN über jeweils 90 ns. mC-3-DNA behält eine kürzere, geordnete Form mit weniger „DNA bubbles“ als nDNA.

## Vergleich von Hydroxymethylcytosin und Methylcytosin

Analog zu Methylcytosin wurden molekulare Kraftsensor-Messungen und SMD-Simulationen für Hydroxymethylcytosin durchgeführt. Um mC mit hmC direkt vergleichen zu können, wurde für die Hydroxymethylierung der gleiche 20 bp lange DNA-Duplex wie für die Methylierung verwendet und es wurden die gleichen CpG hydroxymethyliert, die zuvor methyliert waren (Abbildung 16). Die molekularen Kraftsensor-Experimente wurden in Scher- und Zippergeometrie durchgeführt.

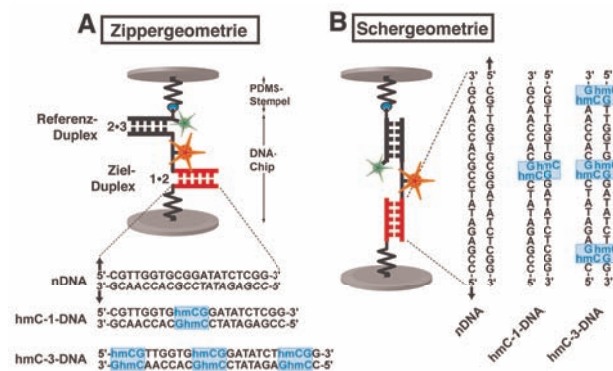


Abbildung 16: Schematische Darstellung des Aufbaus des Experiments. Der Ziel-Duplex 1 • 2 besteht in drei Varianten, ohne Hydroxymethylcytosin (nDNA), einem hmC pro DNA-Strang (hmC-1-DNA) oder 3 hmC pro DNA-Strang (hmC-3-DNA). Der Referenz-Duplex 2 • 3 ist bei allen drei molekularen Kraftsensoren der Gleiche. Abhängig von der Orientierung der DNA-Stränge sind die molekularen Kraftsensoren entweder in einer Zippergeometrie oder einer Schergeometrie (b) aufgebaut.

In Abbildung 17 (a) und (c) ist das Ergebnis eines typischen Experiments gezeigt, und in Abbildung 17 (b) und (d) ist die Auswertung von 42 Kontaktflächen („Pads“) von 4 Experimenten dargestellt. Ähnlich wie bei der methylierten DNA wird bei der hydroxymethylierten DNA in Schergeometrie sowohl ein stabilisierender Effekt (hmC-3-DNA,  $\Delta NF = 0,155$ ) als auch ein destabilisierender Effekt (hmC-1-DNA,  $\Delta NF = 0,105$ ) im Vergleich zu nDNA beobachtet. Daher lässt sich vermuten, dass hmC eine ähnliche DNA-Sequenzabhängigkeit wie mC besitzt. In Zippergeometrie nimmt die mechanische Stabilität des DNA-Duplexes mit dem Grad der Hydroxymethylierung zu, ohne eine Sequenzabhängigkeit zu zeigen (hmC-1-DNA,  $\Delta NF = 0,017$  und hmC-3-DNA,  $\Delta NF = 0,034$ ).

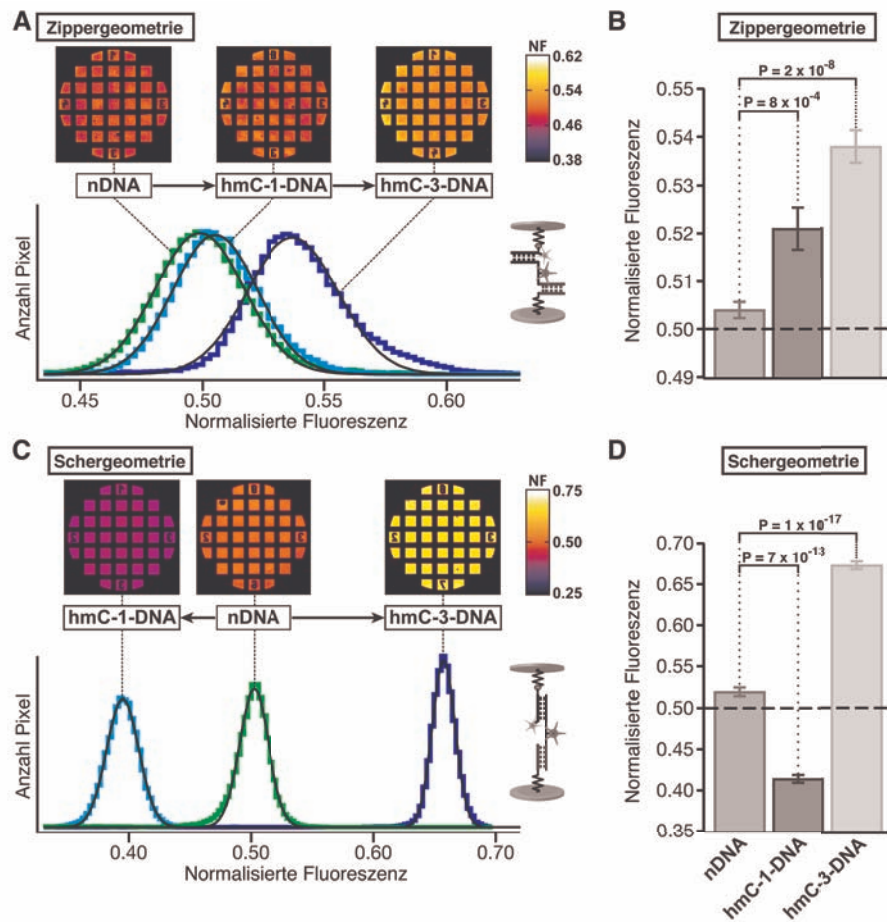


Abbildung 17: (a) und (c): NF-Bilder und Histogramme eines typischen Experiments. (b) Auswertung von 4 Experimenten mit insgesamt 42 Pads in Zippergeometrie. Die mittlere Abrisskraft, gemessen in NF, nimmt mit der Anzahl an hmC pro Strang zu. (d) Auswertung von 4 Experimenten mit insgesamt 39 Pads in Schergeometrie. Im Gegensatz zum Experiment in Zippergeometrie, zeigt hmC-1-DNA eine niedrigere mittlere Abrisskraft und hmC-3-DNA eine höhere mittlere Abrisskraft als nDNA. Dieser Effekt wurde ebenfalls für Methylcytosin beobachtet. Allerdings ist der Effekt von Hydroxymethylcytosin auf die mechanische Stabilität der DNA noch stärker ausgeprägt als für Methylcytosin.

Der Effekt ist in Zippergeometrie schwächer ausgeprägt als in Schergeometrie (zirka um einen Faktor 5). Somit zeigen sich qualitativ die gleichen Tendenzen – stabilisierend bzw. destabilisierend – wie für die methylierte DNA. Betrachtet man jedoch den relativen Unterschied in NF von methylierter und hydroxymethylierter DNA ( $[\Delta NF(\text{hmC-x-DNA}) - \Delta NF(\text{mC-x-DNA})] / \Delta NF(\text{mC-x-DNA})$ ) in Schergeometrie, so erhält man für hmC-1-DNA einen zirka 70 % höheren Wert in NF als für mC-1c-DNA und für hmC-3-DNA einen zirka 50 % höheren NF-Wert als mC-3-DNA. In Zippergeometrie ist es nicht sinnvoll den relativen Unterschied zu berechnen, da  $\Delta NF$  in der Größenordnung des mittleren Fehlers (s.e.m.) ist.

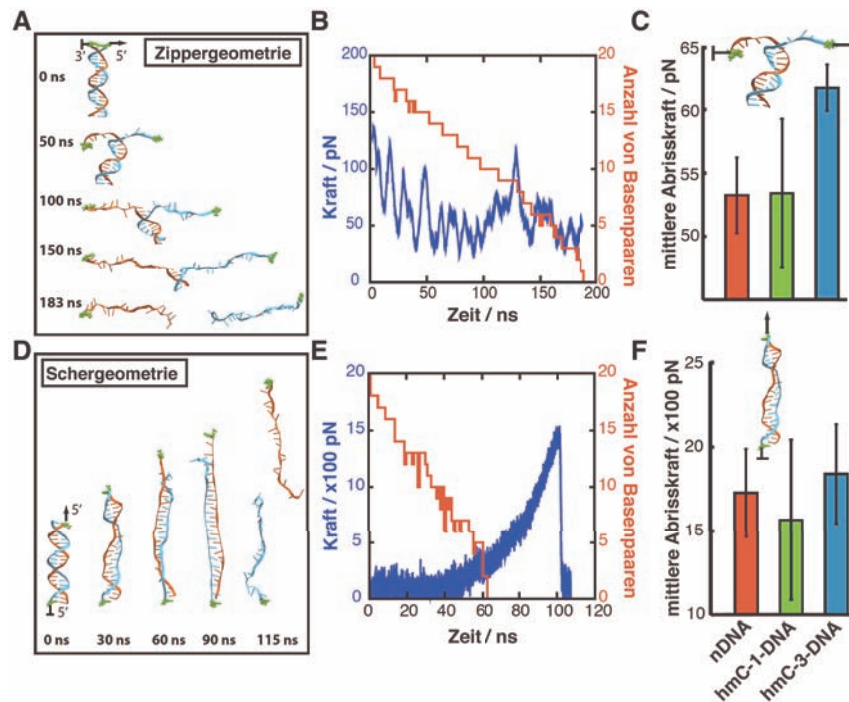


Abbildung 18: SMD-Simulationen von hydroxymethylierter DNA. (a) und (d) zeigen Momentaufnahmen der SMD-Simulationen (b) Typische Kraft-Zeit-Kurve (blau) von DNA in Zippergeometrie. In Rot ist die dazugehörige zeitliche Entwicklung der Anzahl der Basenpaare dargestellt. (c) Histogramm der mittleren Abrisskraft in Zippergeometrie. (e) Typische Kraft-Zeit-Kurve (blau) von DNA in Schergeometrie. In Rot ist die dazugehörige zeitliche Entwicklung der Anzahl der Basenpaare dargestellt. (f) Histogramm der mittleren Abrisskraft in Schergeometrie. Es lässt sich der gleiche Trend für die Abrisskräfte wie im Experiment erkennen. Allerdings ist wegen der hohen Zuggeschwindigkeit und der geringen Anzahl an Simulationen der Fehler zu groß um eine eindeutige Aussage treffen zu können.

Somit lässt sich zusammenfassen, dass die Hydroxymethylierung einen Einfluss auf die mechanische Stabilität der DNA hat, ähnlich wie die Methylierung. Der Effekt von hmC scheint den von mC sogar zu übersteigen, was zumindest in Schergeometrie gezeigt werden konnte. Wie zuvor beschrieben, könnte dies ein oder der molekulare Mechanismus sein, durch den die biologische Funktion von hmC beziehungsweise mC ausgeübt wird. Besonders ist hervorzuheben, dass für hmC bis jetzt keine Proteine gefunden wurden, die gezielt an hmC binden, wie es der Fall für mC und methyl-CpG-bindende Proteine ist [23]. Somit ist der in dieser Arbeit beschriebene Einfluss von hmC auf die mechanische Stabilität des DNA-Doppelstranges die erste Beobachtung, die die Funktionsweise von hmC auf molekularer Ebene erklären könnte.

Um diese Hypothese zu testen, müsste in einer zukünftigen Arbeit der Einfluss von mC und hmC auf den Transkriptions-Mechanismus auf molekularer Ebene untersucht werden. In früheren Publikationen konnte gezeigt werden, dass zum Beispiel die Prozessivität von Polymerasen und Helikasen durch Kräfte im pN-Bereich um einige Größenordnungen beeinflusst werden konnte [83-85].

## 6. Ausblick

Die neuen Erkenntnisse dieser Arbeit auf dem Gebiet epigenetischer Modifikationen und molekularer Wechselwirkungskräfte von Protein-DNA-Komplexen haben direkte Anknüpfungspunkte für das Verständnis der Genregulation und darüber hinaus eine neue Basis für die Systembiologie geschaffen. In diesem abschließenden Teil der Arbeit werden konkrete, bereits geplante Forschungsvorhaben und generelle Ansätze zur Weiterführung dieses Gebietes vorgestellt.

Ziel ist es die Funktionsweise der Genregulation auf molekularer Ebene zu verstehen. Einerseits wurde in dieser Arbeit eine Methode entwickelt um Wechselwirkungskräfte von Protein-DNA Komplexen hochparallel charakterisieren zu können, um das komplexe Netzwerk aus Transkriptionsfaktoren und DNA-Bindestellen vermessen zu können. Andererseits wurde ein neuartiger Effekt der epigenetischen DNA-Modifikationen entdeckt, der potentiell genregulatorisch wirkt.

Um die Funktionsweise der Genregulation auf molekularer Ebene verstehen zu können, wurde der Ansatz gewählt, molekulare Wechselwirkungen zu charakterisieren indem die Wechselwirkungskräfte direkt vermessen werden. Einzelmolekül-Kraftspektroskopie bietet die Möglichkeit detaillierte Eigenschaften über eine molekulare Wechselwirkung, wie Höhe und Position von Energiebarrieren zu bestimmen, die mit anderen Techniken nicht möglich sind. Jedoch stellt die nur in geringem Maße mögliche Parallelisierbarkeit der Messmethode einen zentralen Nachteil der Einzelmolekül-Kraftspektroskopie dar. In dieser Arbeit konnte dieser Nachteil behoben werden und es wurde gezeigt, dass der molekulare Kraftsensor und die Erweiterung, der molekulare A/D Wandler, das Potential einer High-Throughput-Technik besitzt.

In einem nächsten Schritt werden molekularer Kraftsensor und molekularer A/D-Wandler mit einer High-Throughput-Mikrofluidik kombiniert. Von besonderem Interesse ist hierbei der MITOMI-Chip („Mechanically Induced Trapping Of Molecular Interactions“), ein High-Throughput-Mikrofluidik-Chip, welcher an der Stanford Universität entwickelt wurde [3, 4, 86]. Der MITOMI-Chip bietet durch die Verwendung von zwei übereinander liegenden Ebenen von Mikrokanälen die Möglichkeit den für den molekularen Kraftsensor benötigten Kontaktprozess über Druckluft im Chip integriert zu kontrollieren. Neben kleinen Probenvolumina bietet dieser Chip außerdem die Möglichkeit hunderte bis tausende von Proteinen auf dem Chip per *in vitro*-Expression zu produzieren, sodass der Grad der Anzahl an möglichen Kombinationen aus DNA-Sequenzen und Proteinen vervielfacht wird. In der Zukunft wird es ein Ziel sein, einen Mikrofluidik-Chip zu entwickeln der die Vorteile der kraftbasierenden Messungen des molekularen Kraftsensors besitzt. Es werden damit zentrale Schwachstellen derzeitiger High-Throughput-Techniken für Protein-DNA-Wechselwirkungen umgangen, wie zum Beispiel die Detektion von schwachen Bindern, unspezifische Wechselwirkungen von den zu untersuchenden Proteinen mit Oberflächen und dem Markieren des zu untersuchenden Proteins über Antikörper, Farbstoffe oder anderer „Tags“.

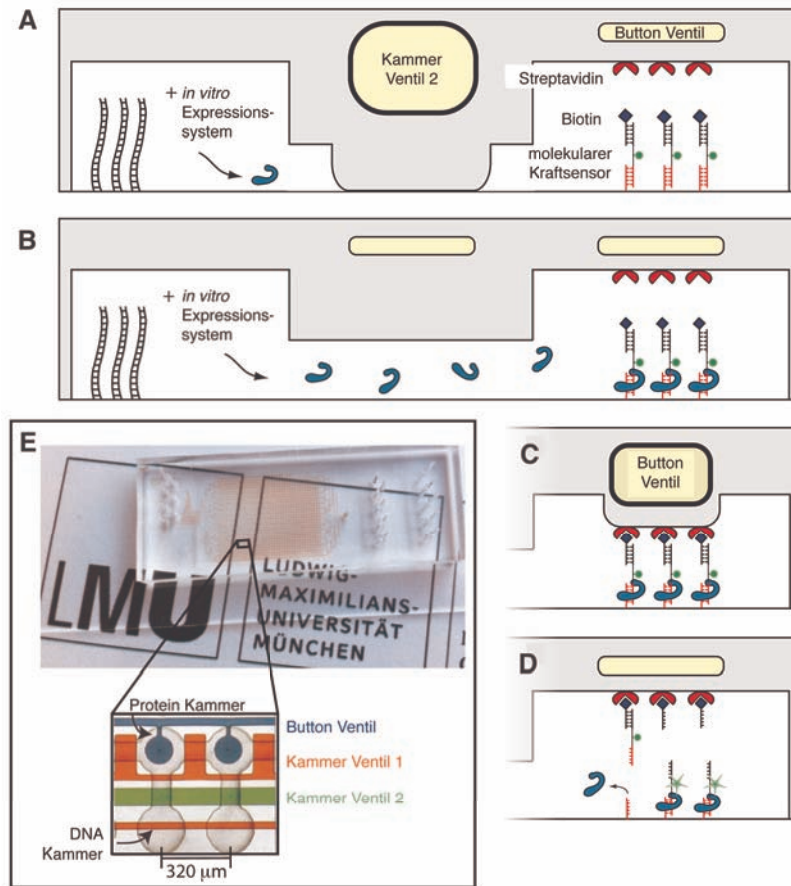


Abbildung 19: Das Schema in (a) bis (d) zeigt eine mögliche Implementierung des molekularen Kraftsensors bzw. molekularen A/D-Wandlers in eine Doppelkammer eines MITOMI-Mikrofluidik-Chips. Eine zweite Ebene von pneumatischen Mikrofluidik-Kanälen erlaubt die Ansteuerung des Chips, inklusive der Kontaktierung der Kraftsensoren. Der MITOMI-Chip erlaubt *in vitro* on Chip-Expression von Proteinen. (e) Photographie eines MITOMI-Chips mit 640 Doppelkammern.

Ausgehend vom molekularen Kraftsensor und MITOMI-Chip lässt sich basierend auf dem gleichen Prinzip in das äußerst interessante Gebiet von Protein-Protein-Wechselwirkungen vorstoßen. Das zu Grunde liegende Prinzip des molekularen Kraftsensors besteht aus zwei Rezeptor-Ligand-Systemen, die in Serie verbunden sind. Anstatt den molekularen Kraftsensor vollständig aus DNA aufzubauen, kann dieser auch aus einem Protein-Protein-Komplex und einem hybridisierten DNA-Doppelstrang oder auch zwei Protein-Protein-Komplexen bestehen. Während die Kombination aus DNA- und Protein-Komplex die Möglichkeit bietet programmiert über die Sequenz der DNA per Selbstassemblierung gezielt an dem DNA-Gegenstrang auf einem Chip anzubinden, und so viele unterschiedliche Kraftsensoren gezielt aufgebaut werden könnten, könnte die Herstellung des DNA-Protein-Chimäres (mittlerer Teil des molekularen Kraftsensors) eine Herausforderung darstellen. Die andere Alternative wäre ein molekularer Kraftsensor, welcher vollständig aus Proteinen bzw. Peptidketten hergestellt wird. Zur Markierung könnte ein GFP oder RFP mit einem der zu untersuchenden Proteine koexprimiert werden. Als Referenz-Bindung würde sich zum Beispiel ein anti-GFP-Nanobody anbieten. Ähnlich zu Protein-DNA-Wechselwirkungen werden auch für Protein-Protein-Wechselwirkungen Techniken benötigt, die die komplexen Netzwerke aus vielen Wechselwirkungs-

partnern und unterschiedlichen Affinitäten möglichst genau und vollständig vermessen können. Hierbei besitzen derzeitige High-Throughput-Techniken für Protein-Protein-Wechselwirkungen ähnliche Schwachstellen wie die für Protein-DNA-Wechselwirkungen, sodass auch auf diesem Gebiet der Ansatz, molekulare Wechselwirkungskräfte zu messen, entscheidende Vorteile birgt.

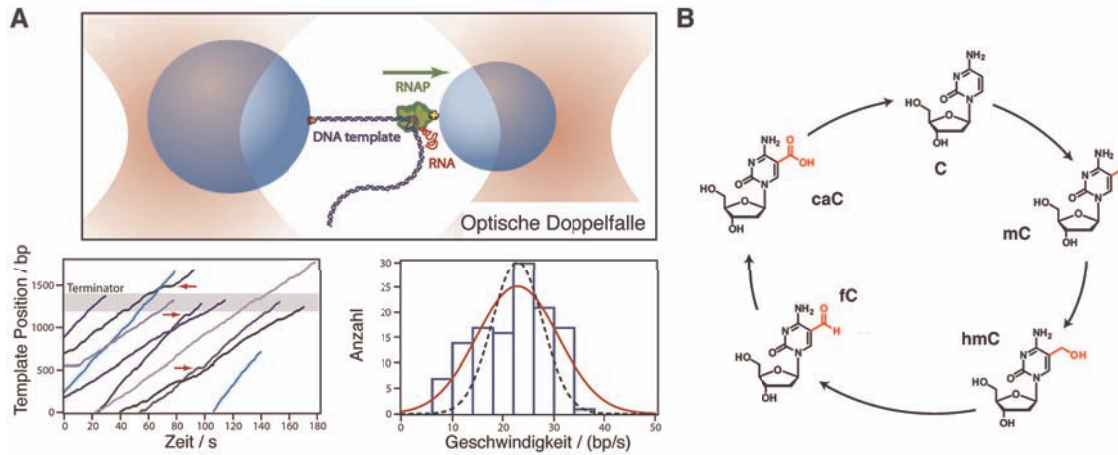


Abbildung 20: (a) Experimenteller Aufbau einer optischen Pinzette. Zwei Polystyrol-Kugeln werden in einer optischen Doppelfalle gehalten. Eine RNA-Polymerase (grün) ist an der einen Kugel befestigt und ein DNA-Doppelstrang am der anderen. Die Transkription erfolgt in Richtung des grünen Pfeils, so dass die angelegte Spannung der optischen Pinzette in diesem Fall die Translokation unterstützt. Auf diese Weise lässt sich die Transkription an einzelnen Molekülen untersuchen und zum Beispiel die Prozessivität in bp/s der RNAP messen (Abbildungen sind von [87, 88] adaptiert). (b) Vermeintlicher Zyklus der Methylierung und oxidativen Demethylierung von Cytosin. Hierbei stellen 5-Formylcytosin und 5-Carboxylcytosin zwei weitere, bis vor kurzem unbekannte DNA-Modifikationen dar (Abbildung ist von [25] adaptiert).

Neben Methylcytosin und Hydroxymethylcytosin wurden letztes Jahr 5-Formylcytosin und 5-Carboxylcytosin als zwei weitere DNA-Modifikationen entdeckt [23, 25]. Erste Versuche haben ergeben, dass diese Basen ebenfalls epigenetische Funktion besitzen könnten. In dieser Arbeit konnte gezeigt werden, dass sowohl Methylcytosin als auch Hydroxymethylcytosin die mechanische Stabilität der DNA-Doppelhelix beim Auftrennen in zwei DNA-Einzelstränge beeinflussen. Somit stellt sich die Frage, inwieweit dies auch für 5-Formylcytosin und 5-Carboxylcytosin zutrifft. Abgesehen von der Untersuchung der mechanischen Stabilität der DNA selbst, ist es von Interesse die in der vorgelegten Arbeit aufgestellte Hypothese experimentell (zum Beispiel durch optische Pinzetten-Experimente wie in Abbildung 20 [83, 89-91]) zu testen, ob die Veränderung der mechanischen Stabilität, hervorgerufen durch epigenetische Modifikationen der DNA, die Prozessivität der Transkriptionsmaschinerie beeinflusst, und ob auf diese Weise Expressionslevel von Genen in Zellen und Organismen moduliert werden.

## 7.1 Publikationen

P1:

Severin, P.M.D., D. Ho, and H.E. Gaub, *A high throughput molecular force assay for protein-DNA interactions*. **Lab Chip**, 2011. **11**(5): p. 856-62.

P2:

Ho, D., C. Dose, C.H. Albrecht, P.M.D. Severin, K. Falter, P.B. Dervan, and H.E. Gaub, *Quantitative detection of small molecule/DNA complexes employing a force-based and label-free DNA-microarray*. **Biophys J**, 2009. **96**(11): p. 4661-4671.

P3:

Ho, D., K. Falter, P.M.D. Severin, and H.E. Gaub, *DNA as a force sensor in an aptamer-based biochip for adenosine*. **Anal Chem**, 2009. **81**(8): p. 3159-64.

P4:

Ho, D., J.L. Zimmermann, F.A. Dehmelt, U. Steinbach, M. Erdmann, P.M.D. Severin, K. Falter, and H.E. Gaub, *Force-driven separation of short double-stranded DNA*. **Biophys J**, 2009. **97**(12): p. 3158-3167.

P5:

Severin, P.M.D., and H.E. Gaub, *DNA-protein binding force chip*. **Small**, 2012, accepted

P6:

Severin, P.M.D., X. Zou, H.E. Gaub, and K. Schulten, *Cytosine methylation alters DNA mechanical properties*. **Nucleic Acids Research**, 2011. **39**(20): p. 8740-8751.

P7:

Strackharn, M., S.W. Stahl, P.M.D. Severin, T. Nicolaus, and H.E. Gaub, *Peptide-antibody complex as handle for single-molecule cut & paste*. **Chemphyschem**, 2012. **13**(4): p. 914-917.

Cite this: *Lab Chip*, 2011, **11**, 856

www.rsc.org/loc

PAPER

## A high throughput molecular force assay for protein–DNA interactions†

Philip M. D. Severin, Dominik Ho and Hermann E. Gaub\*

Received 16th August 2010, Accepted 1st December 2010

DOI: 10.1039/c0lc00302f

An accurate and genome-wide characterization of protein–DNA interactions such as transcription factor binding is of utmost importance for modern biology. Powerful screening methods emerged. But the vast majority of these techniques depend on special labels or markers against the ligand of interest and moreover most of them are not suitable for detecting low-affinity binders. In this article a molecular force assay is described based on measuring comparative unbinding forces of biomolecules for the detection of protein–DNA interactions. The measurement of binding or unbinding forces has several unique advantages in biological applications since the interaction between certain molecules and not the mere presence of one of them is detected. No label or marker against the protein is needed and only specifically bound ligands are detected. In addition the force-based assay permits the detection of ligands over a broad range of affinities in a crowded and opaque ambient environment. We demonstrate that the molecular force assay allows highly sensitive and fast detection of protein–DNA interactions. As a proof of principle, binding of the protein EcoRI to its DNA recognition sequence is measured and the corresponding dissociation constant in the sub-nanomolar range is determined. Furthermore, we introduce a new, simplified setup employing FRET pairs on the molecular level and standard epi-fluorescence for readout. Due to these advancements we can now demonstrate that a feature size of a few microns is sufficient for the measurement process. This will open a new paradigm in high-throughput screening with all the advantages of force-based ligand detection.

### Introduction

DNA-binding proteins coordinate a variety of fundamental functions in cells such as transcriptional regulation, replication and DNA repair. For instance the interactions between transcription factors and their DNA binding sites are an essential part of the gene regulatory networks that control development, core cellular processes and responses to environmental perturbations. These networks and systems may exhibit interactions between as many as thousands of unique elements. A profound understanding of protein–DNA interactions as well as their quantitative evaluation is therefore of utmost importance for modern molecular and systems biology. As a consequence, many different high-throughput methods for the characterization of protein–DNA interactions emerged over the last decade. The most prominent representatives are chromatin immunoprecipitation on a DNA-chip (ChIP-chip)<sup>1–3</sup> and protein binding microarrays (PBMs).<sup>4,5</sup> Both techniques are well established and thanks to microarray technology capable of high-throughput. But despite of all advantages to identify *in vivo* locations, ChIP-chip has some inherent challenges that can make the

identification of DNA-binding sites delicate.<sup>6,7</sup> Especially, both condition-specific binding and antibody limitations may prevent sufficient enrichment of bound fragments in the immunoprecipitated sample.<sup>7,8</sup> PBMs in turn are limited by their stringent washing requirements, which may cause loss of weakly bound proteins. This impairs the determination of transient and low-affinity binding sites. But for instance during fly embryonic development these very sites are suggested to contribute as much as high-affinity sites.<sup>9</sup> To solve this issue the Quake group introduced an *in vitro* assay that mechanically trapped the interacting molecules (MITOMI).<sup>10</sup>

What ChIP-chip, PBMs and MITOMI have in common, is the need of an antibody against the DNA binding protein of choice or against an epitope-tag of this protein. Either the protein is fished out like in ChIP-chip or MITOMI, or it is marked with a fluorescent antibody for detection like in PBMs. So in addition to the binding DNA sequence these established methods rely on a second binding partner specific against the DNA-binding protein. Hence it follows: first, the success and vulnerability of these assays depend on the affinity and specificity of the antibodies. Second, the DNA-binding protein must have a common tag, or, if not, an antibody with high specificity against the protein must be available.

A different approach for the detection of protein–DNA interactions evolved in recent years with the advancement of single molecule force spectroscopy.<sup>11–14</sup> In single molecule force

Lehrstuhl für Angewandte Physik and Center for Nanoscience (CeNS), Ludwig-Maximilians-Universität, Amalienstrasse 54, 80799 Munich, Germany. E-mail: gaub@physik.uni-muenchen.de; Fax: +49 89-2180-2050  
† Electronic supplementary information (ESI) available: Preparation of DNA-chip and PDMS-stamp. See DOI: 10.1039/c0lc00302f



spectroscopy a variety of experimental tools based on measuring and applying forces between molecules in the piconewton regime have been developed and have contributed to a better understanding of the mechanics of biomolecules and molecular bonds.<sup>15–18</sup> However, there are two major bottlenecks, which have hindered the widespread use of single-molecule mechanics: sizable instrumental effort and limited force resolution. To solve these issues a new technique, the molecular force assay (MFA), has been introduced by our group.<sup>19,20</sup> The MFA measures unbinding forces with a high sensitivity like single mismatches in DNA<sup>21</sup> and with low-budget and simple instrumentation compared to AFM, optical or magnetic tweezers. Since with the state-of-the-art instrumentation the force resolution is limited only by thermal fluctuations of the force sensor, shrinking the sensor size improves the signal-to-noise ratio.<sup>22,23</sup> Instead of a trapped bead or a microscopic cantilever, MFA employs a precisely defined bond like a DNA duplex as force sensor. To increase the precision even further, the assay is built in a comparative measurement format, where rupture forces of two molecular complexes are directly compared with each other. The difference in stability of the two bonds is then translated into a fluorescent signal. In contrast to other single molecule force techniques, the MFA has a high degree of parallelization of force sensors built up in a chip-like format, which allows to test in the order of  $10^4$  per  $\mu\text{m}^2$  molecular force probes (MFPs).<sup>24</sup> But although a large number of molecules are probed simultaneously, the actual force measurement is still performed at the single molecule level, because each sample bond is probed individually by a single reference bond.<sup>19</sup>

In our previous work we could demonstrate the advantages of the MFA for label-free ligand detection of small binding molecules like hairpin polyamides<sup>24,25</sup> or adenosine *via* an aptamer-based sensor<sup>26</sup> in a molecular crowded environment with dissociation constants reaching from pM to mM concentrations. The assays permitted up to 16 distinct force sensors to be placed in 16 different spots (diameter 1–2 mm) per experiment on a DNA-chip. After several washing and incubation steps the sample was read out *via* a laser scanner.

In this article we describe the further simplification and advancement of the MFA to a microfluidic compatible assay. We show for the first time the label-free detection of protein–DNA interactions *via* MFA. As a proof of principle, we used the binding of EcoRI, a restriction enzyme, to its DNA recognition site. Moreover we demonstrate the possibility for sensor size shrinking down to  $5\ \mu\text{m} \times 5\ \mu\text{m}$ . Now with the possibility of such a high density of different force probes, the label-free format and the wide range of detectable dissociation constants without restrictions the MFA shows the potential for DNA binding site screening with several advantages over the existing methods.

## Molecular force assay

Below, the working principle and implementation of the MFA are described. Although the instrumentation is comparable to a microcontact printing setup, the key to the MFA lies within the molecular setup, the molecular force probes. The MFPs are assembled as follows: one strand, oligomer **1**, is connected to a glass support, the bottom surface, *via* a (hexaethyleneglycol)<sub>5</sub> spacer. The complementary strand, oligomer **2**, which also

carries a Cy5 fluorescence label, possesses an overhang containing the sequence for the reference duplex **2·3**. The complementary DNA strand, oligomer **3**, carries a Cy3 dye on the one site and is biotin-modified at the end of a polythymine linker and completes the **1·2·3** complex on the glass slide. As a result two duplexes, **1·2** (target duplex) and **2·3** (reference duplex), are assembled and connected in series with a fluorescent label (Cy5) in between. Cy3 and Cy5 of strands **3** and **2** are in close proximity (7nt ssDNA) forming a FRET pair. The PDMS surface of the stamp is functionalized with streptavidin attached to  $3400\ \text{g mol}^{-1}$  PEG linkers.

Fig. 1a illustrates the very basic principle on a molecular level as the assay successively processes. At the beginning of the experiment the MFPs are attached to the glass slide but are still separated from the soft PDMS stamp. First the Cy5 is excited and the fluorescence signal of the MFP layer is measured ( $F_A^\Delta$ ). Secondly the Cy3 is excited and the fluorescence signal of Cy5 is measured ( $F_D^\Delta$ ). After readout the PDMS surface is brought in contact with the glass slide, allowing for biotin·streptavidin complexation; thus, the MFPs are grafted in parallel between both surfaces. After 10 min, the surfaces are separated at a constant velocity. Thereby the polymeric anchors are stretched and a force builds up gradually until the chain of molecular complexes ruptures either at the **1·2** or **2·3** duplex. So the unbinding force of each target DNA duplex is compared individually against a separate reference duplex. The biotin·streptavidin complex persists, since under our experimental conditions a 30 bp DNA duplex unbinds at around 40 to 50 pN, whereas biotin·streptavidin unbinds under these conditions beyond 100 pN.<sup>16,27–29</sup> The typical number of bp per DNA duplex used in our studies is limited by the thermal dissociation rate to around 15 bp at room temperature in  $1 \times \text{PBS}$ . The stamp is moved away from the surface and the fluorescence signals  $F_A^\Delta$  and  $F_D^\Delta$  on the glass slide are read out a second time. Depending if the bond between **2·3** or **1·2** ruptures, strand **2** with its Cy5 fluorophore ends up on the glass slide or PDMS stamp. The result, *i.e.*, the fractions of broken target and broken reference bonds, is stored in a binary fluorophore distribution; fluorophore on the top or bottom surface. So the number of remaining Cy5 fluorophores reflects the relative difference in mechanical stability of the target duplexes compared to the reference duplexes. The number of Cy5 fluorophores is proportional to the measured intensity.<sup>24</sup> Finally, to correct for MFPs, which did not couple to the PDMS surface (Fig. 1a, third MFP from the right), DNA oligomer **3** is modified with a Cy3 label at the end close to Cy5 to form a FRET pair. After separation this FRET pair on the bottom surface is only intact, when the MFP was not probed and strand **3** is still attached to the MFP. To readout the signal of the FRET pair Cy3 is excited and the emission of the acceptor Cy5 is detected. Because forced bond rupture is a thermally assisted process and the force detector is limited by thermal noise, several hundred experiments are typically performed in single molecule force spectroscopy to determine the rupture forces with sufficient accuracy.<sup>23,30</sup> Here, we probe approximately  $10^4$  duplicates of these MFPs per  $\mu\text{m}^2$  in parallel in a single experiment.

## Technical implementation

In Fig. 1b the technical implementation is illustrated. The DNA chip consists of a  $4 \times 4$  pattern of spots (diameter 1–2 mm) with

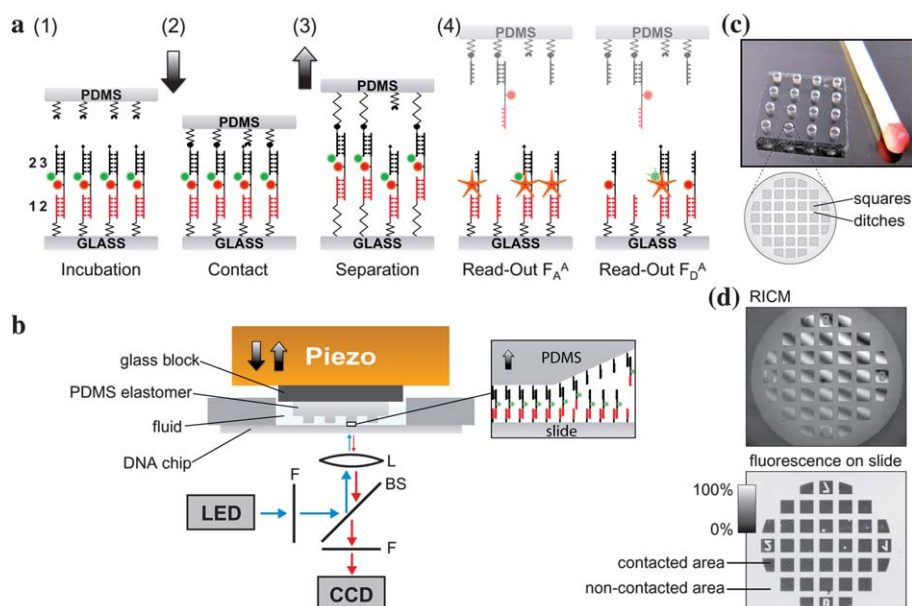


**Fig. 1** Molecular force assay based on soft-print lithography. (a) Schematic representation of the MFA on a molecular level showing the basic principle and successively the assay processes. (a1) The molecular force probes (MFPs) are anchored *via* DNA strand 1 to the glass support. Each MFP comprises of 3 DNA strands. These 3 DNA strands hybridize in two DNA duplexes, 1·2 and 2·3, coupled in series. DNA strand 2 carries a Cy5 as fluorescent marker and strand 3 a Cy3. The PDMS surface and the glass surface are still separated. (a2) The PDMS stamp is moved down to contact the glass surface. Thereby the biotin on DNA strand 3 couples to the streptavidin of the PDMS stamp and thus forms a bridge between the glass and PDMS. (a3) The surfaces are separated and a force builds up along both DNA duplexes of the MFPs until one of the two DNA duplexes ruptures. (a4) To count the number of intact, remaining 1·2 duplexes, the glass slide is readout *via* the fluorescence Cy5 dye on strand 2. During the readout the PDMS stamp is far out of the focal plane. In the last step Cy5 is excited *via* FRET to mark all MFPs that did not couple to the PDMS stamp while in contact. (b) The fluid well with the DNA chip was placed in the contact device with PDMS stamp and detection system. A piezoelectric actuator moves the PDMS stamp along the *z*-axis to contact the DNA-chip. A standard fluorescence microscope with LED illumination and CCD camera is used to read out the sample. (c) The PDMS stamp consists of 16 pads. Each pad has a diameter and height of 1 mm. The microstructure on a pad comprises  $100 \times 100 \mu\text{m}$  squares with an elevation of  $5 \mu\text{m}$ . The trenches between the squares are about  $41 \mu\text{m}$  wide. (d) The planar adjustment between stamp and DNA chip as well as the contact process is controlled *via* reflection interference contrast microscopy. After contact, the fluorescence readout gives quantitative information about the ratio of broken reference and target duplexes.

different MFPs matching the pads of the soft PDMS stamp (Fig. 1c). The glass slide is attached to a PMMA well with silicone lip seal and fixed on a stainless steel stage with permanent magnets. The PDMS elastomer is placed upside down on a glass block connected vertically to a closed-loop piezoelectric actuator (PZ 400, Piezo Systems Jena, Germany) and a DC motorized translation stage (Physik Instrumente GmbH, Germany). The whole contact device is mounted on an inverted microscope (Axio Observer Z1, Carl Zeiss MicroImaging GmbH, Germany) with an *xy* DC motorized high-accuracy translation stage (Physik Instrumente GmbH, Germany). The planar adjustment between stamp and DNA chip as well as the contact process (Fig. 1d) are controlled *via* reflection interference contrast microscopy.<sup>31</sup>

One novel advancement is the direct readout of the DNA chip placed in the contact device. First it allows the fluorescence readout of the sample directly before and after the contact process in buffer solution without any stringent washing steps as done previously. Due to the diminishment of the systematic error caused by washing steps, the reproducibility and robustness of the experiment could be improved further. Secondly we could move away from the confocal microarray scanner to epi-fluorescence microscopy, which has several advantages including a simpler setup, improved signal-to-noise ratio and an elevated

reliability against surface inhomogeneities as depicted later. High-power LEDs (Philips Lumileds Lighting Comp. CA) were used for illumination. A simple cooling system composed of heat sink and fans combined with low-noise current drivers stabilizes the intensity of the LEDs with less than per mil deviation per hour. A standard CCD camera (MRm, Carl Zeiss MicroImaging GmbH, Germany) was used for detection. The entire contact and detection process is semi-automated *via* customized control software (LabVIEW, National Instruments Germany GmbH).

## Analysis

To determine the ratio between broken target and reference bonds, a more subtle analysis is required, since it cannot be assumed that all MFPs physically connect perfectly to both surfaces *via* the biotin-streptavidin bond. Uncoupled MFPs result in a background signal. In order to calculate the normalized fluorescence (NF) intensity the background signal caused by uncoupled MFPs has to be identified and subtracted from the latter one. For simplicity, the unlikely case that the biotin-streptavidin bond ruptures is not further considered, since the MFP remains in the state  $S_0$  (1·2·3) and does not affect the final result. The NF is defined as the ratio between broken reference bonds and the total amount of MFPs that have been

under load. The detailed derivation for the NF has been given previously.<sup>24</sup> In short: initially, all molecular setups are present in the state S0 and were detected *via* the Cy5 labeled oligomer 2 (Fig. 1(a1)). After separation, the molecular setups on the glass slide exist in three different states, S0 (1·2·3), S1 (1·2), and S2 (1), as shown in Fig. 1(a4). An unbinding force was applied only to the molecular setups in states S1 and S2. Molecular setups in state S0 did not couple to the PDMS streptavidin surface and therefore retained the Cy3 labeled oligomer 3. Because S1 and S0 cannot be distinguished only by Cy5, the MFPs in state S0 are identified *via* the signal of the FRET pair Cy3/Cy5. The  $F_A^A$  and  $F_D^A$  fluorescence images allow the quantification of the relative amounts of S0, S1, and S2. 
$$NF = \frac{S1}{S1 + S2} = \frac{(F_A^A)_{ratio} - (F_D^A)_{ratio}}{1 - (F_D^A)_{ratio}}$$

Therefore the  $F_A^A$  final image (after contact) is divided by the  $F_A^A$  start image (Fig. 2). Thus not only the Gaussian illumination profile but also inhomogeneities in the MFP layer cancel out perfectly. Afterwards the resulting  $(F_A^A)_{ratio}$  image is corrected for bleaching by normalizing the non-contacted areas to 1. In the same way the  $F_D^A$  final image is divided by the  $F_D^A$  start image and normalized to obtain the  $(F_D^A)_{ratio}$  image that reflects the coupling efficiency.

## Miniaturization

Typical force-histograms in single molecule force spectroscopy comprise normally of a few hundreds to thousands of force measurements to achieve an adequate force distribution to determine a mean value of force. On the other hand as mentioned in the last paragraph the density of MFPs is around  $10^4$  per  $\mu\text{m}^2$ . So the question arises: what is the minimum spot-size of the MFPs at a given signal to noise ratio? Fig. 3a shows a normalized fluorescence image (2 s exposure time,  $63\times$  objective). One can easily recognize the area that was contacted by the microstructure of the PDMS-stamp. The histogram in Fig. 3b depicts the NF of an entire  $100\ \mu\text{m} \times 100\ \mu\text{m}$  area in red and a  $5\ \mu\text{m} \times 5\ \mu\text{m}$  area in blue (blue square in Fig. 3a). For a more detailed conclusion the  $5\ \mu\text{m} \times 5\ \mu\text{m}$  ROI was moved in  $5\ \mu\text{m}$  steps over the  $100\ \mu\text{m} \times 100\ \mu\text{m}$  area. The mean NF values of each Gaussian fit of each  $5\ \mu\text{m} \times 5\ \mu\text{m}$  ROI are shown in the inset

histogram of Fig. 3b. The vertical dashed lines at  $NF = 0.405$  and  $NF = 0.438$  are the percentiles of 5% and 95%. For a further investigation a MFP-microarray with a spot-size of approximately  $30\ \mu\text{m}$  was contacted with the PDMS-surface in a way that a different large fraction of each spot was probed as shown in Fig. 3c and d. The probed areas “A” to “D” have different sizes since they were contacted by different areas of the PDMS-square (at the middle, the etches and at the corner). Though, the mean values of NF of the histograms “A” to “D” match very precisely. As a result we conclude that even a feature size as small as a few micrometres is sufficient to achieve the meaningful NF and standard deviation.

## Detection of protein–DNA interactions

Force-based ligand detection in general relies on the shift of the unbinding forces due to receptor·ligand complex formation. In the same way the force-based ligand detection *via* MFA is based on a shift of mechanical stability due to DNA·ligand complex formation of one of the two DNA·duplexes (target duplex). Thereby the second duplex may be designed such that it does not bind ligand and therefore serves as a reference duplex. The molecular design can be seen as a well adjusted force balance which is detuned by the interaction of one of the balance arms with a ligand. Fig. 4a and b depict the basic principle in detail: without loss of generality in a perfect constructed MFP both DNA·duplexes comprise the same mechanical stability for a given force loading rate and the  $NF = 0.5$ . The target duplex—here, the lower DNA·duplex—carries a recognition site for a specific ligand and the reference duplex (upper bond) does not. Upon binding of the ligand to its recognition site, only the mechanical stability of the target duplex is altered. This leads to an imbalance and a shift in NF. Since the MFA is capable of detecting changes in the range of a few pN,<sup>21</sup> even the smallest changes in stability due to complexation result in a detectable shift in NF. As depicted in Fig. 4c and d it is possible to construct the MFPs in a shear (Fig. 4c) and a zipper-like pulling geometry (Fig. 4d). As shown with AFM the shear geometry comprises a reference force of around 60 pN for a 30 bp DNA duplex at moderate loading rates.<sup>27,29</sup> In comparison with that, in zipper

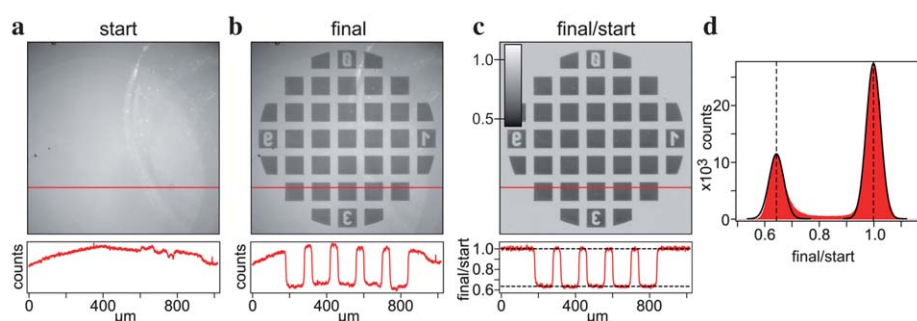


**Fig. 2** Pixel-by-pixel analysis accomplished through image division. The fluorescence images (Cy5, exposure time 2 s) show a distinct ROI on the DNA-chip before (a) and after contact (b). (c) After background subtraction from images (a) and (b), image (b) is divided through image (a). As a result illumination curvature as well as artifacts and inhomogeneities in the MFP layer are perfectly corrected. In the last step, this image is corrected for fluorophore bleaching, so that the non-contacted area is normalized to 1. The intensities measured in the contacted areas give the fraction of remaining fluorophores respectively the intact lower DNA duplexes of the MFPs on the DNA-chip. (d) Histogram of image (c). Here, 64% of the lower DNA duplexes of the MFPs are still intact on the DNA-chip.

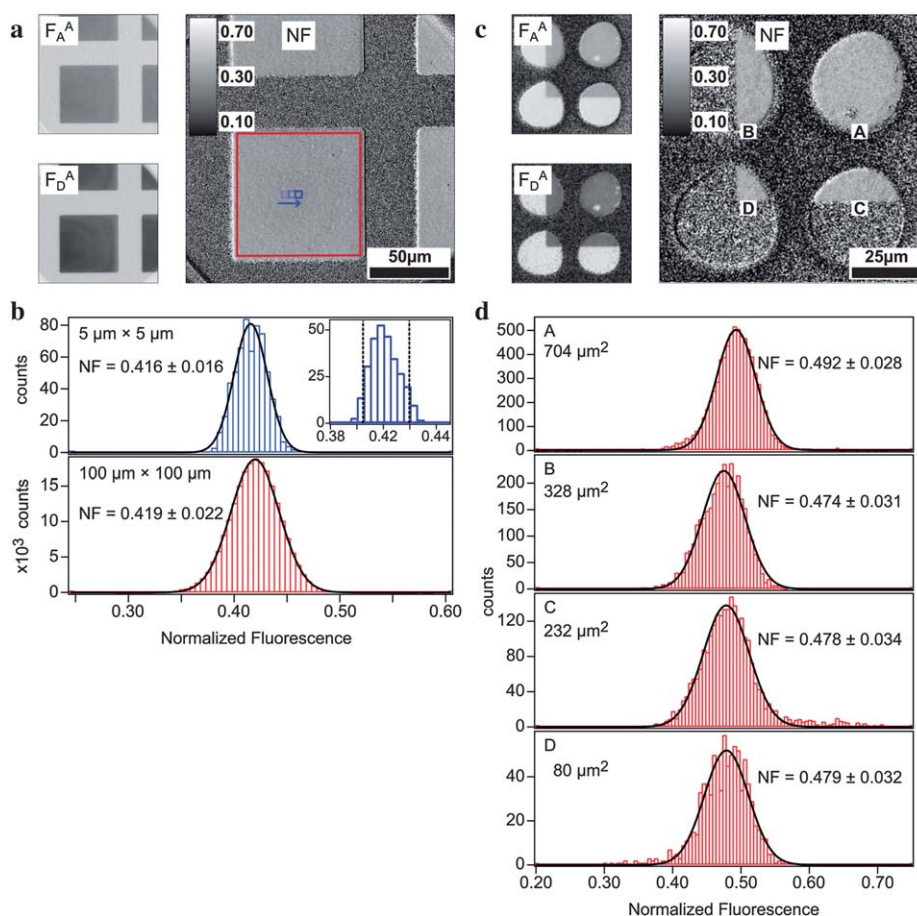


**Fig. 3** Miniaturization of the MFA. (a) Fluorescence images  $F_A^A$  and  $F_D^A$  ( $63\times$  objective, 2 s exposure time). On the right the calculated NF image; a blue square marks a ROI of  $5 \mu\text{m} \times 5 \mu\text{m}$ . (b) Histogram of (a): in red a  $100 \mu\text{m} \times 100 \mu\text{m}$  square of the microstructure ( $\text{NF} = 0.419 \pm 0.022$ ), in blue the  $5 \mu\text{m} \times 5 \mu\text{m}$  ROI ( $\text{NF} = 0.416 \pm 0.016$ ). The inset histogram shows the distribution of mean NF values as the  $5 \mu\text{m} \times 5 \mu\text{m}$  ROI was moved in  $5 \mu\text{m}$  steps over the entire  $100 \mu\text{m} \times 100 \mu\text{m}$  area. The vertical dashed lines at  $\text{NF} = 0.405$  and  $\text{NF} = 0.438$  are the percentiles of 5% and 95%. (c) Fluorescence images  $F_A^A$  and  $F_D^A$  ( $40\times$  objective, 1 s exposure time) of a MFP-microarray. On the right the calculated NF image. All spots of the microarray are composed of the same kind of MFPs to compare the influence of the geometry of the PDMS surface with the NF. The PDMS-square has contacted in such a way 4 spots of the MFP-microarray that the spots feature varied sizes of contacted areas. (d) Histogram of (c): for all 4 spots the whole contacted area is plotted in histograms. Even spot "D" ( $80 \mu\text{m}^2$ ), which was contacted with the corner of the PDMS-square, matches very precisely the mean NF of the other 3 spots. The possibility to scale the MFA to a few micrometres down opens the opportunity to incorporate the MFA as sensor in microfluidics. Furthermore it is now possible to build MFA arrays with a very high density comparable to microarray technology.

geometry, the DNA duplex ruptures depending on the base content and composition at around 15 pN in a quasi-equilibrium process.<sup>32,33</sup> Hence the zipper geometry allows the design of an even more sensitive force sensor compared to shear geometry.

As a model system we chose the binding of EcoRI, a type II restriction endonuclease, to its DNA recognition sequence. In *Escherichia coli*, EcoRI serves as a protection system against foreign DNA and cleaves in the presence of  $\text{Mg}^{2+}$  ion cofactor, its unmethylated target sequence. Restriction endonucleases exhibit high affinities with dissociation constants in the low nM range concomitant with a very high sequence specificity. Under physiological salt conditions, the ratio of specific to non-specific binding of EcoRI reaches  $10^9$ .<sup>34-37</sup> EcoRI binds in the absence of  $\text{Mg}^{2+}$  ion cofactor as a dimer to the palindromic DNA target site 5'-GAATTC-3'. Commercial grade EcoRI (32 kDa per monomer,  $2 \times 10^6$  U  $\text{mg}^{-1}$  specific activity, 100 000 U  $\text{ml}^{-1}$  stock concentration) was purchased from NEB and used directly

without further purification. If not indicated otherwise, all experiments were performed at room temperature in the same buffer solution composed of 10 mM HEPES, 50  $\mu\text{M}$  DTT, 100  $\mu\text{g}$   $\text{ml}^{-1}$  BSA, 170 mM NaCl and 1 mM EDTA at a pH of 7.6. The typical sample volume was 40  $\mu\text{l}$  per PDMS-pad for a high degree of reproducibility. The minimum sample volume needed is 5  $\mu\text{l}$  per PDMS-pad. First the EcoRI monomer concentration of the stock solution was determined twice *via* a quantitative SDS-PAGE to 100 nM with good reproducibility. Secondly we checked the affinity of EcoRI to the DNA constructs 1·2 and 2·3 *via* electrophoretic mobility shift assay (EMSA). Only the target duplex 1·2 exhibits strong binding to EcoRI with a  $K_D = 1.8 \pm 1.0$  nM, whereas the reference duplex 2·3 did not show any binding in the whole accessible range from 0 nM to 50 nM EcoRI. The MFA measurements were carried out as follows: prior to measurement the DNA-chip was incubated with EcoRI for at least 2 hours. In Fig. 5 two MFA titration curves for

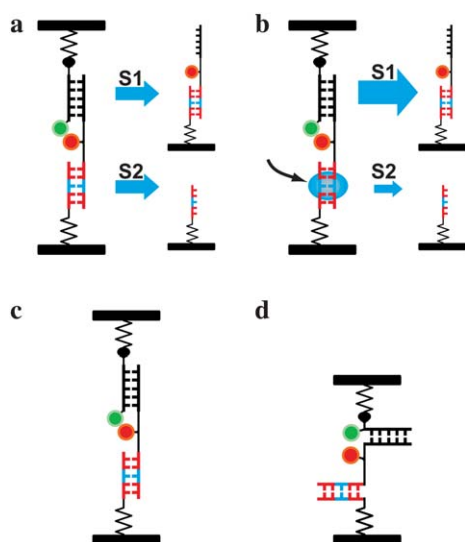


**Fig. 4** The principle of ligand detection *via* MFA. The lower DNA-duplex comprises a target sequence for ligand binding, the upper one is the reference duplex without binding site. (a) In a perfect constructed MFP the lower and upper DNA-duplex have the same mechanical stability and the rupture probabilities for the duplexes S1 and S2 are the same. (b) If a ligand is bound to the lower DNA-duplex, the mechanical stability of that duplex is altered and the probability, that the reference duplex ruptures, shifts (typically: S1 > S2). Furthermore the MFP can be assembled in different geometries allowing unbinding forces to shear the DNA duplex in the range of 50 to 60 pN (c) or to unzip the duplex at around 15 pN (d).

different pulling geometries are presented. The graph in Fig. 5a depicts the change in NF against the EcoRI concentration. The target site for EcoRI is in the lower DNA-duplex. The upper reference duplex does not contain any binding site for the enzyme. The pulling direction of the MFP is in shear geometry on the 5'-ends of the DNA. The pulling velocity was  $5 \mu\text{m s}^{-1}$ . The data were fitted by a hill equation isotherm, since EcoRI binds as a homodimer to its DNA recognition site:  $\text{NF}_{\min} = 0.46 \pm 0.01$ ,  $\text{NF}_{\max} = 0.88 \pm 0.01$  and  $K_D = 0.97 \pm 0.14 \text{ nM}$ . In zipper configuration (Fig. 5b) with different pulling velocities of  $100 \text{ nm s}^{-1}$  (cycles) and  $5 \mu\text{m s}^{-1}$  (filled cycles) the fit of the data resulted in  $\text{NF}_{\min} = 0.74 \pm 0.01$ ,  $\text{NF}_{\max} = 0.95 \pm 0.01$  and  $K_D = 0.22 \pm 0.06 \text{ nM}$ .

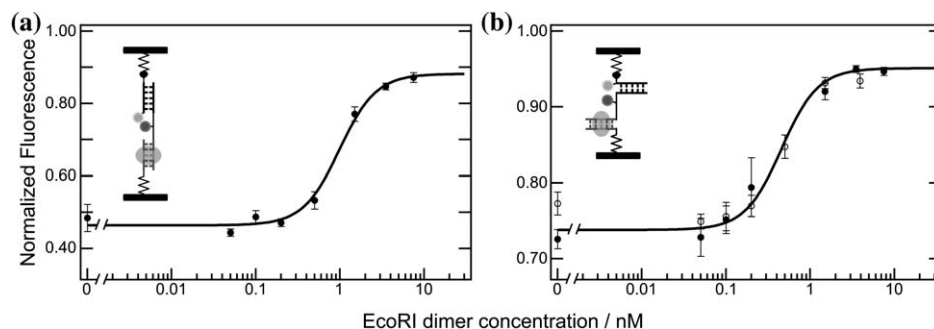


**Fig. 5** Detection of protein–DNA interactions at physiological conditions. The restriction enzyme EcoRI binds as homodimer to its DNA target sequence 5'-GAATTC-3'. The target site for EcoRI is in the lower DNA-duplex. The upper DNA duplex does not contain any binding site for the enzyme and serves as reference duplex. (a) Pulling direction of the MFP in shear geometry at the 5'-ends of the DNA. The pulling velocity is  $5 \mu\text{m s}^{-1}$ . The NF rises with increasing EcoRI concentration until saturation. The data are fitted by a hill equation isotherm:  $\text{NF}_{\min} = 0.46 \pm 0.01$ ,  $\text{NF}_{\max} = 0.88 \pm 0.01$ ,  $K_D = 0.97 \pm 0.14 \text{ nM}$ . (b) MFPs in zipper geometry with different pulling velocities of  $100 \text{ nm s}^{-1}$  (cycles) and  $5 \mu\text{m s}^{-1}$  (filled cycles).  $\text{NF}_{\min} = 0.74 \pm 0.01$ ,  $\text{NF}_{\max} = 0.95 \pm 0.01$ ,  $K_D = 0.22 \pm 0.06 \text{ nM}$ .

$0.22 \pm 0.06 \text{ nM}$ . So the NF in both cases rose with increasing EcoRI concentration until saturation. Longer incubation times (up to 24 hours) did not further increase the NF. The  $K_D$  values from the MFA are in very good agreement with literature.<sup>12</sup> The  $K_D$  value obtained from EMSA is slightly higher than both MFA measurements, which might be due to different conditions caused by the gel in the EMSA.

Optical tweezer experiments have shown that the stability of the EcoRI: DNA bond is not influenced by the unzipping of the neighboring DNA bases even at slow loading rates down to  $10 \text{ pN s}^{-1}$ .<sup>12,38</sup> In shear geometry, however, all bases in the DNA duplex are loaded simultaneously and the structure of the DNA duplex might change prior to rupture, *e.g.* by unwinding, which might detach the bound protein with a certain probability from the DNA before the duplex itself ruptures.

As already described previously,<sup>24</sup> it is essential to compare the timescale of the thermal dissociation of the complex with the timescale of the force loading rate. If the system is allowed to equilibrate during the force ramp, the external force shifts the equilibrium away from the complex, which would result in an increased apparent  $K_D$ . The lifetime or inverse dissociation rate for an EcoRI·dsDNA complex was experimentally determined to be in the order of tens of seconds.<sup>39</sup> At  $5 \mu\text{m s}^{-1}$  separation velocity and similar linker lengths, the force needed to rupture a 30 bp DNA duplex is built up on timescales in the order of  $t = 10 \text{ ms}$ .<sup>27</sup> The DNA duplex unbinding occurs therefore on a much faster timescale  $t$  than the association or dissociation of the EcoRI-dsDNA complex at relevant ligand concentrations. Furthermore as shown for the zipper configuration the NF did not depend on pulling velocity corroborating our assumption that the rupture process of DNA unzipping occurs close to equilibrium.<sup>33,40</sup> This independency of the pulling velocity in the zipper configuration enhances the reproducibility of the MFA for quantitative ligand detection, since the detachment velocity of the stamp must not be controlled exactly.

## Discussion and outlook

In the present article we have demonstrated a molecular force assay for the detection of protein–DNA interactions. The assay is based on the direct comparison of unbinding forces of

biomolecules at the single molecule level in a highly parallel format, which allows the direct readout of roughly  $10^4$  molecular force probes per  $\mu\text{m}^2$ . Besides the highly parallel format and the scalability, the major advantage of the MFA lies in the detection of interaction forces between specific molecules. Not the presence of a certain binder, but rather its interaction strength is measured, which allows the discrimination between the specific interaction of interest and non-specific binding to the surface.

In this article we introduced a new low cost and easy to use setup, which allows force measurement and optical readout on the same instrument with a very high degree of reproducibility and enhancement in simplification of the measurement process. For this purpose we implemented a FRET pair in the molecular force probes to determine the ratio of MFPS under load. For the optical readout, standard epi-fluorescence was employed with LED illumination and a simple CCD camera for detection. The combination of both features leads to a robust biomolecular sensor based on unbinding forces. Besides the technical development we presented for the first time the detection of protein–DNA interactions and the quantification of the corresponding dissociation constant *via* the MFA. In addition we demonstrated successfully ligand detection with different pulling geometries of molecular force probes and advantages of the DNA zipper geometry for ligand detection. Moreover, we could show that a feature size as small as  $5\ \mu\text{m} \times 5\ \mu\text{m}$  is sufficient to determine the NF. For this, it follows that the MFA is capable of screening for protein–DNA interactions comparable to PBMs, ChIP-chip and MITOMI. Compared to these high-throughput methods the following advantages arise: (i) no stringent washing between force measurement and readout is needed, (ii) a wide range of affinities is accessible, even weak binders,<sup>26</sup> (iii) a quantitative and robust analysis due to the simple image division for normalization, (iv) and no label or marker against the protein is needed since the MFA relies on the detection of the specific interaction of binding protein and DNA.

In summary, the MFA has the potential to evolve to a new and valuable tool for the screening of biomolecular interactions with several advantages due to its force-based detection principle. In the future the MFA will be extended to different kinds of biomolecular interactions like protein–protein interactions and will be implemented or combined with microfluidic devices.

## Acknowledgements

The authors thank P. Tinnefeld, R. David, K. Falter, U. Steinbach and J. Vogelsang for helpful discussions. P. Severin and D. Ho are grateful to the Elite Network of Bavaria (IDK-NBT) for a doctoral fellowship. Financial support was provided by the Deutsche Forschungsgemeinschaft and the Nanosystems Initiative Munich.

## References

- V. Iyer, C. Horak, C. Scafe, D. Botstein, M. Snyder and P. Brown, *Nature*, 2001, **409**, 533–538.
- B. Ren, F. Robert, J. Wyrick, O. Aparicio, E. Jennings, I. Simon, J. Zeitlinger, J. Schreiber, N. Hannett, E. Kanin, T. Volkert, C. Wilson, S. Bell and R. Young, *Science*, 2000, **290**, 2306–2309.
- A. R. Wu, J. B. Hiatt, R. Lu, J. L. Attema, N. A. Lobo, I. L. Weissman, M. F. Clarke and S. R. Quake, *Lab Chip*, 2009, **9**, 1365–1370.
- M. F. Berger, A. A. Philippakis, A. M. Qureshi, F. S. He, P. W. Estep and M. L. Bulyk, *Nat. Biotechnol.*, 2006, **24**, 1429–1435.
- S. Mukherjee, M. F. Berger, G. Jona, X. S. Wang, D. Muzzey, M. Snyder, R. A. Young and M. L. Bulyk, *Nat. Genet.*, 2004, **36**, 1331–1339.
- M. L. Bulyk, *Curr. Opin. Biotechnol.*, 2006, **17**, 422–430.
- T. Lee, N. Rinaldi, F. Robert, D. Odom, Z. Bar-Joseph, G. Gerber, N. Hannett, C. Harbison, C. Thompson, I. Simon, J. Zeitlinger, E. Jennings, H. Murray, D. Gordon, B. Ren, J. Wyrick, J. Tagne, T. Volkert, E. Fraenkel, D. Gifford and R. Young, *Science*, 2002, **298**, 799–804.
- C. Harbison, D. Gordon, T. Lee, N. Rinaldi, K. Macisaac, T. Danford, N. Hannett, J. Tagne, D. Reynolds, J. Yoo, E. Jennings, J. Zeitlinger, D. Pokholok, M. Kellis, P. Rolfe, K. Takusagawa, E. Lander, D. Gifford, E. Fraenkel and R. Young, *Nature*, 2004, **431**, 99–104.
- E. Segal, T. Raveh-Sadka, M. Schroeder, U. Unnerstall and U. Gaul, *Nature*, 2008, **451**, 535–540.
- S. J. Maerkl and S. R. Quake, *Science*, 2007, **315**, 233–237.
- F. Bartels, B. Baumgarth, D. Anselmetti, R. Ros and A. Becker, *J. Struct. Biol.*, 2003, **143**, 145–152.
- S. J. Koch, A. Shundrovsky, B. C. Jantzen and M. D. Wang, *Biophys. J.*, 2002, **83**, 1098–1105.
- F. Kuhner, L. Costa, P. Bisch, S. Thalhammer, W. Heckl and H. Gaub, *Biophys. J.*, 2004, **87**, 2683–2690.
- A. R. Bizzarri and S. Cannistraro, *Chem. Soc. Rev.*, 2010, **39**, 734–749.
- Y. Cao, M. M. Balamurali, D. Sharma and H. Li, *Proc. Natl. Acad. Sci. U. S. A.*, 2007, **104**, 15677–15681.
- R. Merkel, P. Nassoy, A. Leung, K. Ritchie and E. Evans, *Nature*, 1999, **397**, 50–53.
- V. Moy, E. Florin and H. Gaub, *Science*, 1994, **266**, 257–259.
- K. Uhrig, R. Kurre, C. Schmitz, J. E. Curtis, T. Haraszti, A. E.-M. Clemen and J. P. Spatz, *Lab Chip*, 2009, **9**, 661–668.
- C. H. Albrecht, K. Blank, M. Lalic-Mülthaler, S. Hirler, T. Mai, I. Gilbert, S. Schiffmann, T. Bayer, H. Clausen-Schaumann and H. E. Gaub, *Science*, 2003, **301**, 367–370.
- K. Blank, T. Mai, I. Gilbert, S. Schiffmann, J. Rankl, R. Zivin, C. Tackney, T. Nicolaus, K. Spinnler, F. Oesterheld, M. Benoit, H. Clausen-Schaumann and H. Gaub, *Proc. Natl. Acad. Sci. U. S. A.*, 2003, **100**, 11356–11360.
- C. H. Albrecht, H. Clausen-Schaumann and H. E. Gaub, *J. Phys.: Condens. Matter*, 2006, **18**, 581–599.
- F. Gittes and C. Schmidt, *Eur. Biophys. J.*, 1998, **27**, 75–81.
- M. Viani, T. Schaffer, A. Chand, M. Rief, H. Gaub and P. Hansma, *J. Appl. Phys.*, 1999, **86**, 2258–2262.
- D. Ho, C. Dose, C. H. Albrecht, P. Severin, K. Falter, P. B. Dervan and H. E. Gaub, *Biophys. J.*, 2009, **96**, 4661–4671.
- C. Dose, D. Ho, H. E. Gaub, P. B. Dervan and C. H. Albrecht, *Angew. Chem., Int. Ed.*, 2007, **46**, 8384–8387.
- D. Ho, K. Falter, P. Severin and H. E. Gaub, *Anal. Chem.*, 2009, **81**, 3159–3164.
- J. Morfill, F. Kuehner, K. Blank, R. A. Lugmaier, J. Sedlmair and H. E. Gaub, *Biophys. J.*, 2007, **93**, 2400–2409.
- F. Pincet and J. Husson, *Biophys. J.*, 2005, **89**, 4374–4381.
- T. Strunz, K. Oroszlan, R. Schäfer and H. J. Güntherodt, *Proc. Natl. Acad. Sci. U. S. A.*, 1999, **96**, 11277–11282.
- E. Evans and K. Ritchie, *Biophys. J.*, 1997, **72**, 1541–1555.
- G. Wiegand, K. Neumaier and E. Sackmann, *Appl. Opt.*, 1998, **37**, 6892–6905.
- C. Bustamante, Z. Bryant and S. Smith, *Nature*, 2003, **421**, 423–427.
- M. Rief, H. Clausen-Schaumann and H. Gaub, *Nat. Struct. Biol.*, 1999, **6**, 346–349.
- A. Jeltsch, J. Alves, H. Wolfes, G. Maass and A. Pingoud, *Biochemistry*, 1994, **33**, 10215–10219.
- L. Jen-Jacobson, *Biopolymers*, 1997, **44**, 153–180.
- D. R. Lesser, M. R. Kurpiewski and L. Jen-Jacobson, *Science*, 1990, **250**, 776–786.
- N. Sidorova and D. Rau, *J. Mol. Biol.*, 2001, **310**, 801–816.
- S. Koch and M. Wang, *Phys. Rev. Lett.*, 2003, **91**, 028103.
- N. Sidorova and D. Rau, *Biopolymers*, 2000, **53**, 363–368.
- C. Bustamante, S. Smith, J. Liphardt and D. Smith, *Curr. Opin. Struct. Biol.*, 2000, **10**, 279–285.

## Supporting Material

### DNA Chip (Immobilization of MFPs on Slides , bottom surface)

DNA oligomers **1**, **2**, and **3** were purchased HPLC grade from IBA GmbH (Goettingen, Germany). Sequences and modifications of all oligonucleotides are the following: shear geometry: **1<sub>s</sub>**, NH<sub>2</sub>-(HEGL)<sub>5</sub>-5'-(T)<sub>10</sub>-CTG CAG GAA TTC GAT ATC AAG CTT ATC GAT-3'; **2<sub>s</sub>**, 3'-GAC GTC CTT AAG CTA TAG TTC GAA TAG CTA C-(T)<sub>7</sub>-5'-5'-T(Cy5)-(T)<sub>7</sub>-C GAC GTC CTT AAG CTA TAG TTC GAA TAG CTA-3'; **3<sub>s</sub>**, biotin-5'-(T)<sub>10</sub>-TAG CTA TTC GAA CTA TAG CTT AAG GAC GTC(Cy3)-3'. Zipper geometry: **1<sub>z</sub>**, 5'-CTG CAG GAA TTC GAT ATC AAG CTT ATC GAT-(T)<sub>10</sub>-(HEGL)<sub>5</sub>-NH<sub>2</sub>-3'; **2<sub>z</sub>**, 5'-GAC GTC CTT AAG CTA TAG TTC GAA TAG CTA C-(T)<sub>7</sub>-T(Cy5)-(T)<sub>8</sub>-C ATC GAT AAG CTT GAT ATC GAA TTC CTG CAG-3'; **3<sub>z</sub>**, biotin-5'-(T)<sub>10</sub>-TAG CTA TTC GAA CTA TAG CTT AAG GAC GTC(Cy3)-3'. The five hexaethyleneglycol (HEGL) linkers are connected via phosphate groups. DNA oligomer **1** is amine-modified, which allows covalent linkage to aldehyde-functionalized glass slides (Schott GmbH, Jena, Germany). We spotted 1 μL drops of 5× SSC (saline sodium citrate; Sigma-Aldrich GmbH, Munich, Germany) containing 25 μM oligomer **1** on the aldehyde slide in a 4 × 4 pattern and incubated the slide in a saturated NaCl ddH<sub>2</sub>O atmosphere overnight. After washing the slide with ddH<sub>2</sub>O containing 0.2% sodium dodecyl sulfate (SDS; VWR Scientific GmbH, Darmstadt, Germany) and thoroughly rinsing the slide with ddH<sub>2</sub>O we reduced the resulting Schiff bases with 1% aqueous NaBH<sub>4</sub> (VWR Scientific GmbH, Darmstadt, Germany) for 90 min. Subsequently, the slide was washed with 1× SSC and thoroughly rinsed with ddH<sub>2</sub>O. In order to reduce nonspecific binding, the slides were blocked in 1× SSC containing 4% bovine serum albumin (BSA; Sigma-Aldrich GmbH, Munich, Germany) for 20 min. Custom-made 16-well silicone isolators (Grace-Biolabs, OR) were placed on top of the immobilized DNA oligomer **1**. The 100 nM Cy5-modified oligomer **2** and 200 nM biotin-modified oligomer **3** were hybridized to the latter for 30 min, completing the **1 · 2 · 3** complex on the glass slide. After removing the silicone isolators the slides were washed with a self-made fluidic system driven by a multi-channel peristaltic pump (Ismatec GmbH, Wertheim-Mondfeld, Germany) to remove any unspecific bound DNA oligomers. The 4 × 4 pattern was rinsed subsequently with 2× SSC, 0.2× SSC containing 0.1% Tween 20 (VWR Scientific GmbH, Darmstadt, Germany) and 1× PBS each with 50 ml in 5 min.

## PDMS stamp (Top Surface)

The stamp is made of polydimethylsiloxane (PDMS) and is fabricated as detailed previously with some modifications.<sup>1</sup> PDMS stamps are fabricated by casting 10:1 (base/crosslinker) (Sylgard, Dow Corning, MI) into a custom-made micro- and millistructured silicon wafer (HSG-IMIT, Villingen-Schwenningen, Germany).<sup>2</sup> After curing was complete, the PDMS was taken out of the mold and cut into a 4 × 4 pillar arrangement. Each pillar is 1 mm diameter, is 1 mm high, and carries a microstructure on the flat surface: 100 mm × 100 mm pads are separated by 41 mm wide and 5 mm deep trenches allowing for liquid drainage during the contact and separation process. Free polymers were extracted in toluene for at least one day.<sup>3</sup> The PDMS was activated overnight in 12.5% hydrochloric acid and subsequently derivatized with (3-glycidoxypropyl)-trimethoxysilane (ABCRC, Karlsruhe, Germany) to generate epoxide groups. NH<sub>2</sub>-PEG-Biotin (3400 g/mol; Rapp Polymere, Tuebingen, Germany) was melted at 80°C, and ~1 mL was spotted on each pillar followed by overnight incubation in argon atmosphere at 80°C. The excess polymers were thoroughly removed with ddH<sub>2</sub>O. Shortly before the experiment, the PDMS was incubated with 1 mg/mL streptavidin (Thermo Fisher Scientific, Bonn, Germany) in 1× PBS and 0.4% bovine serum albumin for 60 min, washed with 1× PBS containing 0.1% Tween 20, with 1× PBS and gently dried with N<sub>2</sub> gas.

## References

1. D. Ho, C. Dose, C. H. Albrecht, P. Severin, K. Falter, P. B. Dervan and H. E. Gaub, *Biophys J*, 2009, **96**, 4661-4671.
2. C. H. Albrecht, H. Clausen-Schaumann and H. E. Gaub, *Journal of Physics: Condensed Matter*, 2006, **18**, 581-599.
3. S. Perutz, E. Kramer, J. Baney and C. Hui, *Macromolecules*, 1997, **30**, 7964-7969.



# Quantitative Detection of Small Molecule/DNA Complexes Employing a Force-Based and Label-Free DNA-Microarray

Dominik Ho,<sup>†‡</sup> Christian Dose,<sup>§</sup> Christian H. Albrecht,<sup>†</sup> Philip Severin,<sup>†</sup> Katja Falter,<sup>†</sup> Peter B. Dervan,<sup>§</sup> and Hermann E. Gaub<sup>†\*</sup>

<sup>†</sup>Lehrstuhl für Angewandte Physik and Center for Nanoscience Ludwig-Maximilians-Universität, 80799 Munich, Germany; <sup>‡</sup>Munich Center For Integrated Protein Science (CIPSM) Ludwig-Maximilians-Universität, 81377 Munich, Germany; and <sup>§</sup>Division of Chemistry and Chemical Engineering California Institute of Technology, Pasadena, CA 91125

**ABSTRACT** Force-based ligand detection is a promising method to characterize molecular complexes label-free at physiological conditions. Because conventional implementations of this technique, e.g., based on atomic force microscopy or optical traps, are low-throughput and require extremely sensitive and sophisticated equipment, this approach has to date found only limited application. We present a low-cost, chip-based assay, which combines high-throughput force-based detection of dsDNA·ligand interactions with the ease of fluorescence detection. Within the comparative unbinding force assay, many duplicates of a target DNA duplex are probed against a defined reference DNA duplex each. The fractions of broken target and reference DNA duplexes are determined via fluorescence. With this assay, we investigated the DNA binding behavior of artificial pyrrole-imidazole polyamides. These small compounds can be programmed to target specific dsDNA sequences and distinguish between D- and L-DNA. We found that titration with polyamides specific for a binding motif, which is present in the target DNA duplex and not in the reference DNA duplex, reliably resulted in a shift toward larger fractions of broken reference bonds. From the concentration dependence nanomolar to picomolar dissociation constants of dsDNA·ligand complexes were determined, agreeing well with prior quantitative DNase footprinting experiments. This finding corroborates that the forced unbinding of dsDNA in presence of a ligand is a nonequilibrium process that produces a snapshot of the equilibrium distribution between dsDNA and dsDNA·ligand complexes.

## INTRODUCTION

Small DNA-binding molecules are in the spotlight of many fields of research. Whether it is genomics, systems biology, or molecular medicine, the knowledge if and how strong a molecule interacts with a specific DNA sequence is of utmost interest. The formation of such complexes is typically linked to changes in the double-helical structure and may even result in the displacement or blocking of other molecules. This enables important functions in e.g., transcription, recombination, and DNA repair (1,2).

Given the importance of understanding the basis of molecular recognition, assays are needed that allow for fast, sensitive, and quantitative detection of dsDNA·ligand complexes. Traditionally, DNase footprinting experiments are employed to identify the binding sites of a ligand on dsDNA and also quantify the respective affinities. Although certainly powerful, DNase footprinting is a complex procedure and requires several days of preparation (3). Very rapid and also label-free quantification of even minuscule amounts of ligand becomes possible with microcantilever arrays (4). They suffer, however, from the costs associated with the fabrication and chemical modification of large numbers of cantilevers.

It is often of importance to identify the full DNA recognition profile of a certain DNA binder to understand what kind

of role the binder plays within a living organism. Chip-based methods accommodate the need for massively parallel analysis of dsDNA·ligand interactions: chromatin immunoprecipitation-on-chip (ChIP-on-chip) is a widespread technique allowing for a genome-wide identification of protein-binding sites (5,6). ChIP-on-chip relies on nonspecific cross-linking of DNA with a DNA-binding molecule *in vivo*. Cross-linking efficiencies vary from molecule to molecule, and some interactions may even be missed (7). In particular, the detection of small molecules interacting with DNA is nontrivial. Today, a growing number of *in vitro* chip-based assays are available allowing for the analysis of dsDNA·ligand interactions under controlled experimental conditions. In an experiment by Warren et al. (8,9), all permutations of an eight basepair dsDNA sequence were displayed on a single chip. Ligand binding was detected directly by fluorescence and the cognate sites were ranked in the order of increasing affinity. However, fluorescence trades fast and sensitive readout for a labeled ligand, and the label may alter the sequence specificity profile of the ligand in an unbiased manner. A widespread label-free detection method is surface plasmon resonance imaging. Due to the small change in refractive index, the detection of small molecules with surface plasmon resonance imaging is complicated and requires larger features compared to fluorescence-based techniques (10,11). Depending on the application, the background signal caused by unwanted adsorption imposes a substantially challenge to all chip-based methods. The

Submitted November 4, 2008, and accepted for publication February 25, 2009.

\*Correspondence: gaub@lmu.de

Editor: Jane Clarke.

© 2009 by the Biophysical Society  
0006-3495/09/06/4661/11 \$2.00

doi: 10.1016/j.bpj.2009.02.059

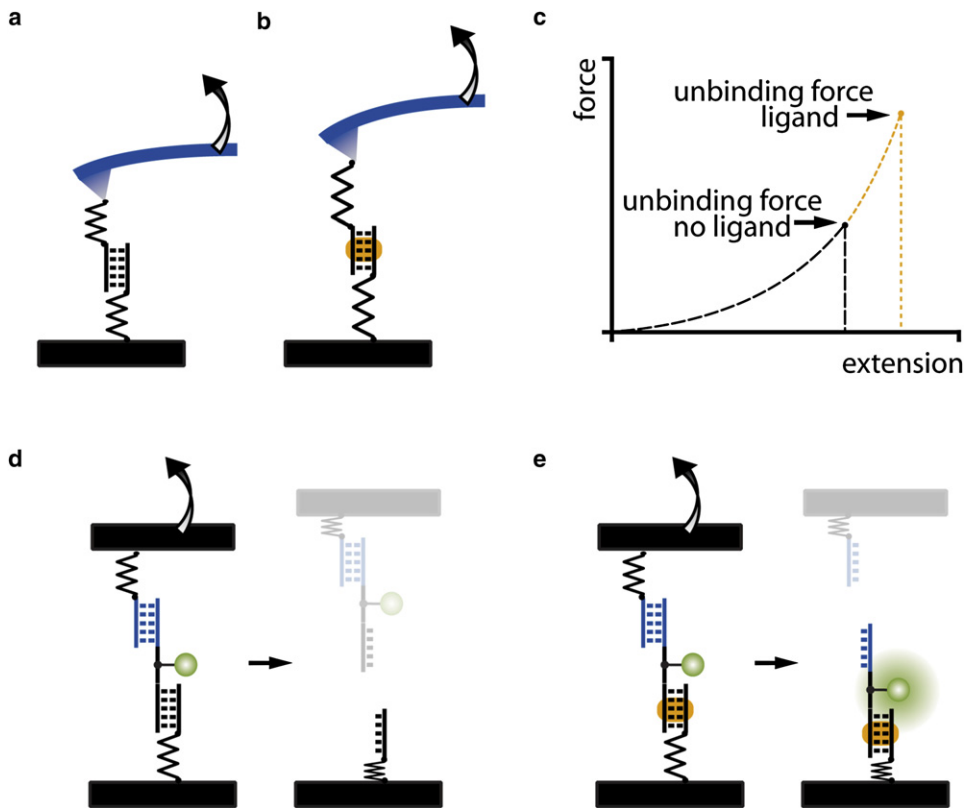


FIGURE 1 (a) Conventional, AFM-based single molecule force spectroscopy, in which the force required to unbind a molecular bond, such as a target DNA duplex, is measured with a cantilever spring. (b) A ligand bound to the target DNA duplex alters the force required for unbinding. (c) Single molecule force spectroscopy data are typically presented as force-extension traces. From two absolute force measurements, the consequences of ligand binding can be investigated. (d) The CUFA replaces the cantilever spring by a known reference bond. Upon loading the chain of target DNA duplex and reference DNA duplex, the weaker of the two bonds has a higher probability of unbinding than the stronger one. (e) In case a ligand forms a complex with the target DNA duplex and stabilizes it, significantly more fluorophores end up on the side of the target DNA duplex after separation of the two surfaces.

fabrication of inert surfaces is even considered as the main bottleneck for further development of the latter (12).

Here, we present a microarray compatible dsDNA·ligand complex detection format, which is based on the comparative unbinding force assay (CUFA). CUFA has already been applied to detect single nucleotide polymorphisms (13), to study differences of antibody/antigen interactions (14), to eliminate cross-reactions on protein microarrays (15), and to investigate the chiral selectivity of small peptides (16). For dsDNA·ligand interaction detection, CUFA relies on the alteration of the unbinding forces of a target dsDNA as a result of ligand binding (17–19). This effect was demonstrated in single molecule experiments employing atomic force microscopy (AFM) (20) (21,22), optical tweezers (23), and magnetic tweezers (24) (Fig. 1, *a–c*).

Instead of a microscopic, spring-like object, e.g., a cantilever or a trapped bead, CUFA employs a precisely defined molecular bond as force sensor. Thereby, the target DNA duplex is directly compared against a reference DNA duplex and merely fluorescence is required to readout the experiment (Fig. 1, *d* and *e*). In comparison with conventional force-based measurements, many of the experimental uncertainties are removed. With no calibration offsets or instrument drift the comparative unbinding force experiments are more accurate and independent of the experimental apparatus. Naturally, such experiments are primed to be carried out in parallel by using a chip format with many duplicates (in the order of  $10^4/\mu\text{m}^2$ ) of the same experiment contributing to the excellent

sensitivity of the measurement. The resulting assay is fluorescence based; however, it does not require a labeled ligand. Only the DNA linker between the target and reference DNA duplex is conjugated to a fluorophore at a noninteracting basepair. Rather than detecting the mere presence of the ligand, the change of unbinding forces of the target DNA duplex due to ligand binding is detected. By this means the assay is insensitive to nonspecific adsorption and deals with one of the major bottlenecks of current biochips.

As a model system, we investigated sequence programmable pyrrole-imidazole hairpin polyamides (25). These molecules recognize the minor groove of DNA with affinities and specificities comparable to naturally occurring DNA-binding proteins (26,27). The sequence specificity arises from interactions of pairs of the aromatic amino acids *N*-methylpyrrole (Py), *N*-methylimidazole (Im), and *N*-methylhydroxypyrrole (Hp) with the edges of the Watson-Crick DNA basepairs. A pairing of Im opposite to Py targets a G·C basepair, and Py/Im recognizes a C·G basepair, whereas a Py/Py pair comprises a preference for both A·T and T·A (28). The discrimination of T·A from A·T using Hp/Py pairs completes the four basepair letter code (29). Eight-ring hairpin polyamides provide a good compromise between synthetic ease and molecular recognition properties. In this binding motif, a  $\gamma$ -aminobutyric acid residue connects the carboxylic terminus of one strand to the amino terminus of the other (30). The turn residue also serves as a DNA recognition element for A·T and T·A basepairs. Further,

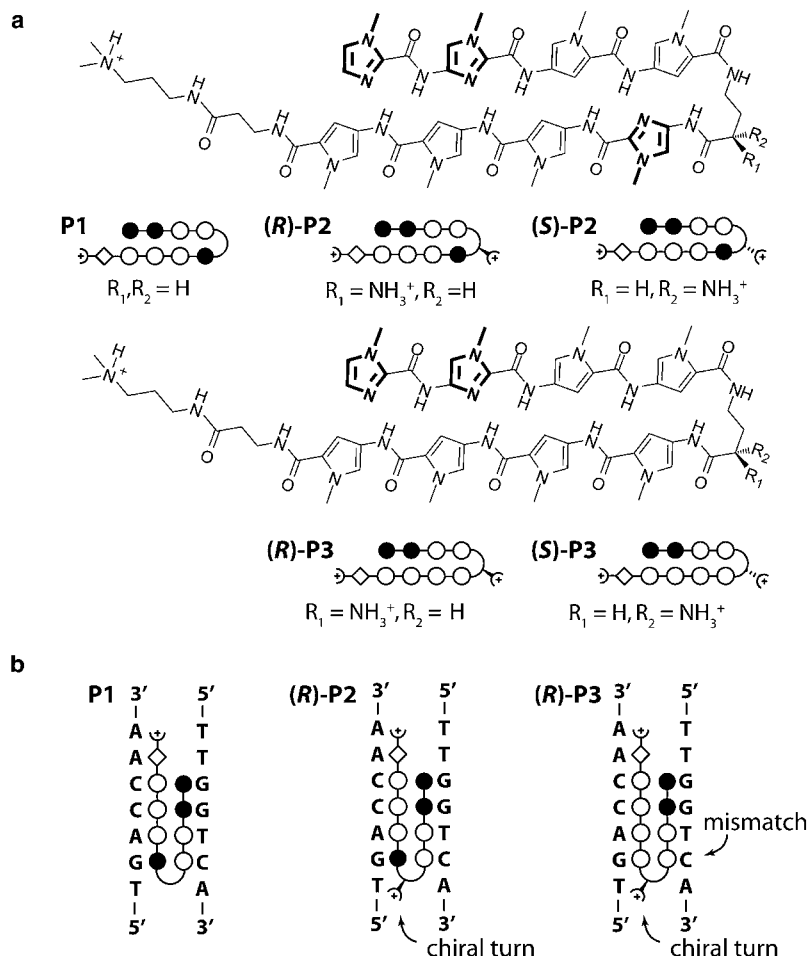


**FIGURE 2** (a) Chemical structures of matched hairpin polyamides **P1**, **(R)-2**, and **(S)-2** as well as single basepair mismatched compounds **(R)-P3** and **(S)-P3**. The ball and stick model represents imidazole and pyrrole as solid and open circles, respectively. The  $\beta$ -alanine residue is shown as a diamond, and the dimethylaminopropylamide tail is shown as a half circle with a plus. The chiral diaminobutyric acid turn residue is represented as a turn, to which a semicircle with a plus is linked. *R* and *S* chirality is indicated by a solid and dashed connection of the semicircle to the turn, respectively. (b) Ball and stick representation for the three different hairpin motifs bound to the same target DNA sequence. **P1** binds sequence specific to the target DNA sequence. **(R)-2** is modified with a chiral diaminobutyric acid turn, which increases the overall binding affinity. **(R)-3** is also modified with a chiral diaminobutyric acid turn, however contains a single basepair mismatch that reduces the overall binding affinity.

a  $\beta$ -alanine residue and a dimethylaminopropylamide tail at the C-terminus each confer a specificity for A·T and T·A basepairs (31). This general addressability of the DNA minor groove is supported by x-ray and NMR structure studies (32,33) and has been utilized in several applications, including, for example, DNA nanostructures (34,35), recruitment of DNA-binding proteins (36,37), and the inhibition of gene expression within living cells (38–40).

Here we report the application of CUFA to accurately determine the thermal dissociation constant  $K_D$  of three different dsDNA·polyamide interactions (Fig. 2 a). In particular, we investigated the influence of a chiral turn as well as a single mismatch to the overall affinity of an eight-ring hairpin polyamide to the same target DNA sequence (Fig. 2 b).

## MATERIALS AND METHODS

### DNA constructs

DNA oligomers **1**:  $NH_2$ -(hexaethyleneglycol)<sub>5</sub>-5'-TTT TTT TTT TCA GTC GCT GAC CAA CCT CGT-3', **2**: 3'-GTC AGC GAC TGG TTG GAG CAC TTT T(Cy3)-5'-5'-TTT TTC TGC TCC AAC CAG TCG CTG AC -3', **3**: Biotin-5'-TTT TTT TTT TGT CAGCGACTGGTTGGAGCA, **4**: 3'-GTC

AGC GAC TGG TTG GAG CAC TTT T(Cy3)-5'-5'-TTT TTC ACG AGG TTG GTC AGC GAC TG-3', and **5**: Biotin-5'-TTT TTT TTT TCA GTC GCT GAC CAA CCT CGT-3' were purchased HPLC grade from IBA GmbH (Goettingen, Germany). Italic letters in oligomers **4** and **5** represent L-DNA bases. In upside-down experiments the  $NH_2$ -(hexaethyleneglycol)<sub>5</sub> (HEGL) and biotin modifications were exchanged.

### Molecular setup preparation (DNA slide)

Each individual molecular chain consisting of a reference and a target DNA duplex is referred to as a "molecular setup". Oligomer **1** is amine-modified at the 5' end and allows covalent attachment to an aldehyde-functionalized glass slide (Schott GmbH, Jena, Germany). Two microliter drops of 5× phosphate buffered saline (PBS; Roche GmbH, Grenzach, Germany) containing 25  $\mu$ M oligomer **1** were spotted on an aldehyde glass slide in a 4 × 4 pattern and were incubated in a saturated NaCl ddH<sub>2</sub>O atmosphere overnight. After washing the slide with ddH<sub>2</sub>O containing 0.2% sodium dodecyl sulfate (VWR Scientific GmbH, Darmstadt, Germany) and thoroughly rinsing the slide in ddH<sub>2</sub>O, the resulting Schiff bases were reduced with 1% aqueous NaBH<sub>4</sub> (VWR Scientific GmbH, Darmstadt, Germany) for 20 min. After thoroughly rinsing the slide in ddH<sub>2</sub>O, the slides were blocked in 1× PBS containing 4% bovine serum albumin (Sigma-Aldrich GmbH, Munich, Germany) for 30 min. A custom-made 16-well silicone isolator (Grace-Biolabs, OR) was placed on the top of the immobilized DNA oligomer **1** spots. Three microliters of 1× PBS containing 1  $\mu$ M oligomer **2** and 2  $\mu$ M oligomer **3** were added to each well and incubated for 1 h, completing the **1·2·3** molecular setups. Then, the slide was washed with 1× PBS containing 0.05% sodium dodecyl sulfate and thoroughly rinsed with 1× PBS. The

silicon isolator remained on the slide throughout the experiment, and care was taken that after hybridization the slide always remained immersed in 1× PBS. The 1·4·5 and upside-down molecular setups were prepared accordingly.

## PDMS stamp

The polydimethylsiloxane (PDMS) stamp was fabricated by casting 10:1 (base/crosslinker) (Sylgard, Dow Corning, MI) into a custom-made micro- and millistructured silicon wafer (HSG-IMIT, Villingen-Schwenningen, Germany) (41). After curing was complete, the PDMS was taken out of the mold and cut into a 4 × 4 pillar arrangement. Each pillar is 1 mm diameter, is 1 mm high, and carries a microstructure on the flat surface: 100 × 100 μm<sup>2</sup> pads are separated by 41 μm wide and 5 μm deep trenches allowing for liquid drainage during the contact and separation process. Free polymers were extracted in toluene for at least 1 day (42). The PDMS was activated overnight in 12.5% hydrochloric acid and subsequently derivatized with (3-glycidioxypropyl)-trimethoxysilane (ABC, Karlsruhe, Germany) to generate epoxide groups. NH<sub>2</sub>-PEG-Biotin (3400 g/mol; Rapp Polymere, Tübingen, Germany) was melted at 80°C, and ~1 μL was spotted on each pillar followed by overnight incubation in argon atmosphere at 80°C. The excess polymers were thoroughly removed with ddH<sub>2</sub>O. Shortly before the experiment, the PDMS was incubated with 1 μg/ml streptavidin (Thermo Fisher Scientific, Bonn, Germany) in 1× PBS and 0.4% bovine serum albumin for 30 min, washed with 1× PBS containing 0.05% Tween 20 (VWR Scientific GmbH, Darmstadt, Germany), with 1× PBS and gently dried with N<sub>2</sub> gas.

## Ligand incubation

Sixteen-well silicone isolators allowed the addition of up to 16 different concentrations of the dsDNA ligands within a single experiment. Because of technical convenience, we restricted ourselves to the addition of eight different concentrations. Fifty milliliters volume of polyamides in 1× PBS was circulated through each well for at least 2 h using a self-made fluidic system driven by a 16-channel peristaltic pump (Ismatec GmbH, Wertheim-Mondfeld, Germany).

## Coupling and separation

The streptavidin functionalized PDMS stamp was approached to the DNA slide using high-precision stepper motors (OWIS GmbH, Staufen, Germany) and a piezo actuator (Piezo Systems Jena, Jena, Germany), monitored by reflection interference contrast microscopy (43). The biotinylated molecular complexes and the multivalent streptavidin coated PDMS stamp were allowed to couple via a biotin·streptavidin·biotin complex for 10 min, followed by retraction of the PDMS stamp at a velocity of 5 μm/s. Biotin·streptavidin is an extremely strong molecular interaction and is of significantly greater stability than short dsDNA at the applied separation velocity (44,45). In separate controls, we determined that no noteworthy amount of fluorescently labeled streptavidin was transferred from the PDMS to the DNA array during an experiment.

## Analysis

Fluorescence images of the DNA slide were recorded in solution using a confocal scanner with 4 μm resolution (Tecan Austria GmbH, Austria) before and after the contact. The fluorescence per unit area was assumed to be proportional to the fluorescently labeled species per unit area (see Fig. S1 in the Supporting Material). The normalized fluorescence intensity (NF) is defined as the number of broken reference bonds normalized to the total number of individual molecular setups that have been under load. For the 1·2·3 molecular setups, it was determined as follows: initially, all molecular setups are present in the state S0 and were detected via the Cy3 labeled oligomer 2 (Fig. 3 a). After separation, the molecular setups on the glass slide exist in three different states, S0 (1·2·3), S1 (1·2), and S2

(1), as shown in Fig. 3 b. An unbinding force was applied only to the molecular setups in state S1 and S2. Molecular setups in state S0 did not couple to the PDMS streptavidin surface and therefore retained the biotinylated oligomer 3. Because S1 and S0 cannot be distinguished, the latter was labeled with the spectrally distinct fluorescent marker streptavidin Alexa Fluor 647 (AF; Fig. 3 c). The labeling was performed subsequent to the Cy3 readout to avoid quenching or fluorescence resonance energy transfer effects. The Cy3 and AF fluorescence images allow the quantification of the relative amounts of S0, S1, and S2 (Fig. 3, d and e). The Cy3 and AF fluorescence images recorded after contact contain square-like features corresponding to the contacted area. From each square-like feature the Cy3<sub>Rem</sub> and AF<sub>Rem</sub> were determined individually. Cy3<sub>Initial</sub> and AF<sub>Initial</sub> were determined from the noncontacted regions adjacent to each square-like feature.

$$S0 = AF_{\text{Ratio}} \quad (1)$$

$$S1 = Cy3_{\text{Ratio}} - AF_{\text{Ratio}} \quad (2)$$

$$S2 = 1 - Cy3_{\text{Ratio}} \quad (3)$$

$$Cy3_{\text{Ratio}} = \frac{Cy3_{\text{Rem}}}{Cy3_{\text{Initial}}} \quad (4A)$$

$$AF_{\text{Ratio}} = \frac{AF_{\text{Rem}}}{AF_{\text{Initial}}} \quad (4B)$$

S0, S1, and S2 are normalized such that the relation S0 + S1 + S2 = 1 is always true. As defined above, the NF is given by the number of broken 2·3 bonds (S1) normalized to the number of bonds that have been under load (S1 + S2):

$$NF = \frac{S1}{S1 + S2} = \frac{Cy3_{\text{Ratio}} - AF_{\text{Ratio}}}{1 - AF_{\text{Ratio}}} \quad (5)$$

The NF directly reflects the relative mechanical stability, a physical quantity inherent to a pair of molecular complexes, and is not influenced by the amount of molecules under load. The NF should not be confused with the Cy3<sub>Ratio</sub>. For a fixed mechanical stability, the latter depends on the number of coupled molecular complexes, whereas the NF does not. The NFs presented in this work are the averages of the NFs determined from all square-like features of an experiment. The 1·4·5 and upside-down molecular setups were analyzed accordingly.

## Polyamide synthesis

Polyamide conjugates were synthesized on solid-phase using published Boc-based protocols and purified by reverse-phase HPLC (≥95% purity) (46). Ultraviolet-visible spectra were recorded in water on a Hewlett-Packard Model 8452 A diode array spectrophotometer. All polyamide concentrations were determined using an extinction coefficient of 69,200 M<sup>-1</sup>cm<sup>-1</sup> at λ<sub>max</sub> near 310 nm. Matrix-assisted, LASER desorption/ionization time-of-flight mass spectrometry (MALDI-TOF MS) was performed using an Applied Biosystems Voyager DR Pro spectrometer. Polyamide P1: MALDI-TOF [M+H]<sup>+</sup> calcd for C<sub>57</sub>H<sub>71</sub>N<sub>22</sub>O<sub>10</sub><sup>+</sup> = 1223.6, observed = 1223.4, (R)-P2: MALDI-TOF [M+H]<sup>+</sup> calcd for C<sub>57</sub>H<sub>72</sub>N<sub>23</sub>O<sub>10</sub><sup>+</sup> = 1238.6, observed = 1238.6, (S)-P2: MALDI-TOF [M+H]<sup>+</sup> calcd for C<sub>57</sub>H<sub>72</sub>N<sub>23</sub>O<sub>10</sub><sup>+</sup> = 1238.6, observed = 1238.5, (R)-P3: MALDI-TOF [M+H]<sup>+</sup> calcd for C<sub>58</sub>H<sub>73</sub>N<sub>22</sub>O<sub>10</sub><sup>+</sup> = 1237.6, observed = 1237.3, (S)-P3: MALDI-TOF [M+H]<sup>+</sup> calcd for C<sub>58</sub>H<sub>73</sub>N<sub>22</sub>O<sub>10</sub><sup>+</sup> = 1237.6, observed = 1237.5.

## Melting temperature analysis

Melting temperatures were monitored on a Beckman ultraviolet-visible spectrometer at 260 nm within 25–90°C by applying a heating rate of

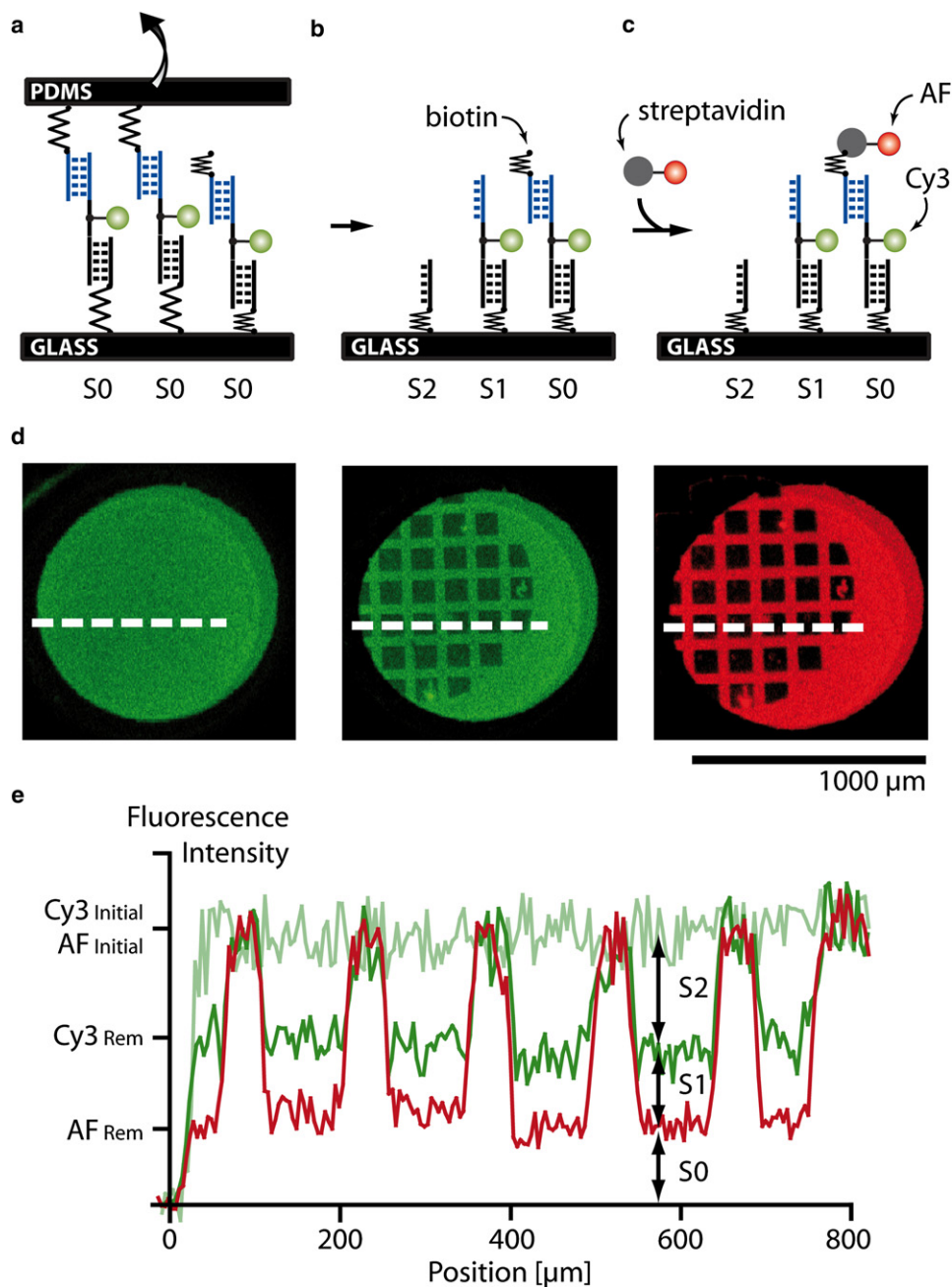


FIGURE 3 Comparative unbinding force experiment on the molecular level. (a) Before separation of the two surfaces, all molecular setups are in the state S0. (b) After separation, either target (state S2) or reference (state S1) bond is broken or no coupling (state S0) occurred. (c) Because states S0 and S1 cannot be distinguished by fluorescence, the free biotin of state S0 is labeled with streptavidin Alexa Fluor 647 (AF). (d) Fluorescence images of the glass slide before and after separation as well as after incubation with AF. The dark square-like features correspond to the area contacted with a microstructured PDMS stamp. (e) Corresponding line plots. From the fluorescence intensities the relative amounts of the states S0, S1, and S2 can be determined.

0.5°C/min. Measurements were performed in a degassed buffer containing 2 μM DNA duplex/polyamide (1:1), 10 mM NaCl, and 100 mM NaH<sub>2</sub>PO<sub>4</sub> at pH 7.0.  $T_m$ -values are defined as the maximum of the first derivative of the melting curve.

## RESULTS AND DISCUSSION

Force-based ligand detection relies on the alteration of unbinding forces due to dsDNA·ligand complex formation. In the course of conventional single molecule experiments, one strand of a DNA duplex is immobilized to solid support via a polyethyleneglycole (PEG) linker. In the same way, the complementary strand is immobilized to a microscopic force

detector such as an AFM cantilever. Upon contacting the AFM cantilever with the solid support, the two complementary DNA strands hybridize. During separation of the support and the detector surface, the PEG linkers act like entropic springs (47,48), and an increasing force builds up until the DNA duplex unbinds (Fig. 1, a and b). The force extension curve is recorded and the unbinding force determined. Because unbinding is a thermally activated process (49) and the force detector is limited by thermal noise (50), several hundred experiments are typically performed to determine the unbinding forces with sufficient accuracy. As demonstrated by Krautbauer et al. (17) as well as Koch et al. (18), complex formation of a DNA duplex with a small

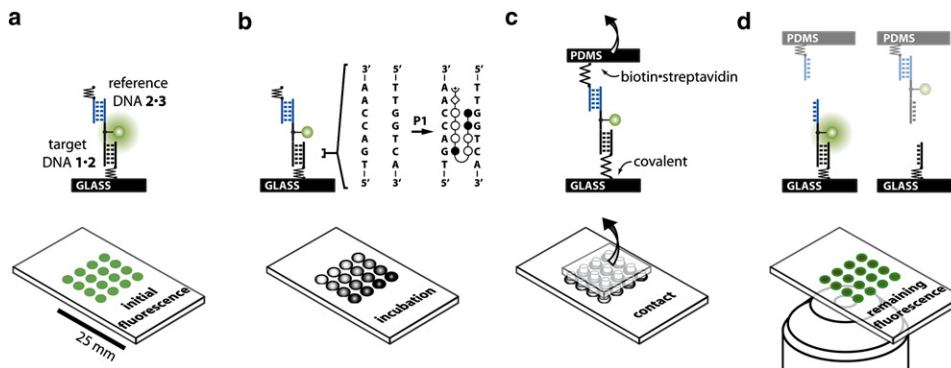


FIGURE 4 Schematics of CUFA experiments. (a) The molecular setup consists of two DNA duplexes, i.e., the 1·2 target and the 2·3 reference DNA duplex, linked in series. (b) A simple fluidic system allows incubation of 16 identical DNA spots with eight different polyamide P1 concentrations. (c) The molecular setups are linked between glass support and PDMS. Separation of the surfaces applies a load to the chain of duplexes until the weaker fails. (d) The fluorescently labeled linking DNA oligomer 2 is more likely to remain on the side of the more stable DNA·ligand complex.

molecule or a protein is accompanied by a shift of the unbinding forces (Fig. 1 c). In our comparative unbinding force experiments, a known molecular bond carrying a fluorescent label replaces the microscopic force detector (Fig. 1, d and e).

Fig. 4 a illustrates the molecular setup schematically. Target DNA duplex 1·2 is immobilized to glass support via a (hexaethyleneglycol)<sub>5</sub> linker of oligomer 1. Reference DNA duplex 2·3 is bridged to 1·2 via a 10 basepair single stranded polythymine linker carrying a Cy3 fluorescence label. Oligomer 3 carries a biotin modification at the end of another polythymine linker. Before the force experiment, a fluidic system allows for incubation of the molecular setups with different ligand concentrations (Fig. 4 b). In Fig. 4 c, a soft PDMS stamp is brought in contact with the 1·2·3 complexes on the glass slide analogously to a microcontact-printing experiment (51,52). 1·2·3 couples to the PDMS stamp via biotin·streptavidin complex formation. Upon retraction of the PDMS stamp at 5  $\mu\text{m/s}$  force is built up gradually acting along the molecular chain consisting of the linkers as well as the 1·2 and 2·3 duplexes until either 1·2 or 2·3 breaks (Fig. 4 d).

Approximately  $10^4$  duplicates of the same experiment are performed per  $\mu\text{m}^2$ . The absolute force needed to pull the two surfaces apart is neither recorded nor analyzed. Instead, the unbinding force of each target DNA duplex is compared individually against a separate reference duplex. For each molecular chain, the two possible experimental outcomes are distinguished by determining the location of the fluorescently labeled oligomer 2. In case the fluorophore remained on the glass slide, the 2·3 DNA duplex is broken, and in case the fluorophore was transferred to the PDMS stamp, the 1·2 DNA duplex is broken.

The target and the reference DNA duplex are comprised of the same basepair composition, and the outcome “1·2 is broken” should be close to equally likely to the outcome “2·3 is broken” (53). Experimentally, we determined a NF (see Materials and Methods) of 38.4% with an error of 1.6%, which we estimated from repeated measurements (Fig. 5 a). We attribute this deviation from the expected

NF of 50% to the symmetry break due to the different surfaces to which the oligomers are attached. DNA duplexes are sensitive to solution conditions such as pH and ionic strength (54), which may differ depending on the proximity of the DNA duplex to the PDMS or the glass surface. This minor imbalance does not affect the quantitative detection of dsDNA·ligand complexes.

### Nonchiral hairpin polyamide

To investigate whether the CUFA is applicable to determine the thermal dissociation constant  $K_D$  of dsDNA·ligand interactions, we incubated 1·2·3 molecular setups with different concentrations of hairpin polyamide P1. Thereby, we make use of a symmetry breaking property, such that P1 only binds to the target and not the reference DNA duplex: hairpin polyamides bind sequence specific with a preference for N→C orientation with respect to the 5'→3' direction of the adjacent DNA strand (55,56). The preferred binding motif 5'-TGACCAA-3' of polyamide P1 is present in the 1·2 target DNA duplex, whereas the 2·3 reference DNA duplex contains the reverse-binding motif 5'-AACCAGT-3', to which P1 binds with significantly decreased affinity.

On a single chip, we incubated 16 identical spots of immobilized 1·2·3 molecular setups with eight different P1 concentrations ranging from 0 to 2.7 nM and performed a CUFA experiment as described above. The NF increased with increasing polyamide concentration from 38.4% (Fig. 5 a) until it saturated at 63.1% (Fig. 5 b). This is in agreement with a stabilizing effect of P1 on the 1·2 duplex. As it is common for quantitative dsDNA·polyamide interaction studies, we fitted the titration data to the Hill equation isotherm (a more detailed discussion follows at the end of this section) (9,58). The apparent thermal dissociation constant  $K_D$  was determined to be 105 pM with a 95% confidence interval of [65 pM, 169 pM] agreeing well with previously published quantitative DNase footprinting and microarray data (58). The NF data including the fit are shown in Fig. 5 c.

To ensure that the molecular setup responds as expected, we investigated the upside-down molecular setup 3·2·1.

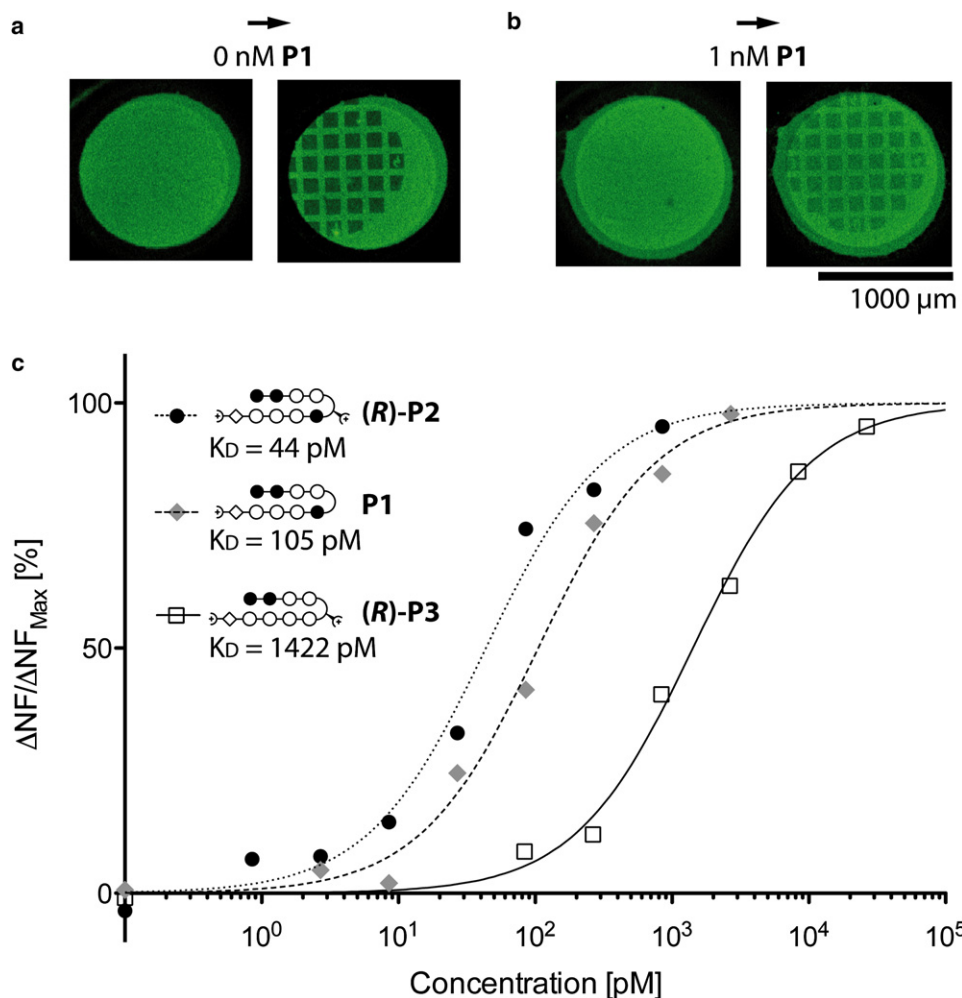


FIGURE 5 (a) Cy3 fluorescence image of 1·2·3 molecular setups on a glass slide before and after contact with a PDMS stamp in absence of P1. (b) Cy3 fluorescence image of 1·2·3 molecular setups on a glass slide before and after contact with a PDMS stamp in presence of 1 nM P1. The fluorescence intensity of the contacted area is higher compared to the 0 nM case. (c) Relative change in NF due to titration with three different polyamide compounds.

Here, the position of the target and the reference DNA duplex is exchanged, and thus the response to the addition of P1 should be inverted. Indeed, the NF decreased from 31.9% to 7.7% upon increasing the P1 concentration from 0 to 10 nM. In this case, the polyamide binds preferentially to the DNA duplex adjacent to the PDMS stamp, and therefore the amount of fluorescently labeled oligomer 2 transferred to the PDMS stamp was increased in presence of P1.

### Chiral hairpin polyamide

In previous work, we demonstrated that chiral hairpin polyamides distinguish between D- and L-DNA (16). Chiral selectivity is introduced by an amine substituent on the  $\gamma$ -turn amino acid of the hairpin polyamide that was also shown to lead to an increase in binding affinity (47). The chiral hairpin polyamide (R)-P2, which recognizes the same sequence as P1, was examined employing the 1·4·5 molecular setup. 1·4 is identical to the 1·2 target DNA duplex, and 4·5 is the mirrored DNA duplex to 1·4. (R)-P2 binds preferentially to the 1·4 5'-TGACCA-3' binding motif, whereas 4·5 presents less optimal binding sites due to its opposite chirality.

Analogous to the previous experiment, an increase in concentration of (R)-P2 from 0 to 1 nM lead to an increase of the NF from 47.1% to 80.3%, agreeing with a stabilizing effect on the D-DNA duplex 1·4. Fitting the titration data to a Hill equation isotherm revealed an apparent thermal dissociation constant  $K_D$  of 44 pM with a 95% confidence interval of [23 pM, 83 pM]. The  $K_D$  for the (R)-P2 hairpin polyamide has not been reported yet. However, a lowered  $K_D$  compared to P1 is consistent with prior experiences with the addition of an amine substituent to the  $\gamma$ -turn amino acid of regular polyamide hairpins (47). The NF data including the fit are shown in Fig. 5 c.

For control, the 5·4·1 upside-down molecular setup in combination with (R)-P2 was measured at 0 nM and 10 nM yielding 32.8% and 12.9%, respectively. The regular molecular setup 1·4·5 in combination with mirror imaged polyamide (S)-P2 was also measured at 0 nM and 10 nM resulting in NF of 44.1% and 20.9%. The two controls demonstrated that the response of the assay was as expected: in the 5·4·1 upside-down molecular setup, the target and reference DNA duplex are essentially mirrored (target and reference are of identical sequence but opposite chirality).

In this case, the ligand recognizes the DNA duplex adjacent to the PDMS stamp and the change in NF due to ligand binding was inverted. In case the ligand was mirrored and incubated with the **1·4·5** molecular setup, the ligand recognized the reference bond as its preferential binding motif and the change in NF was also inverted.

### Mismatched hairpin polyamide

Introducing the single basepair mismatched polyamide (**(R)-P3**) to the **1·4·5** molecular setup is expected to form a DNA-ligand complex of lower affinity (57). In detail, **1·4** provides a binding motif for (**R**)-**P3** with a single basepair mismatch. The affinity to **4·5** is even further decreased, because the binding motif contains a single basepair mismatch and, in addition, is of opposite chirality. Incubation of the **1·4·5** molecular setup with increasing concentrations of (**R**)-**P3** increased the NF from 47.1% at 0 nM to 71.2% at 27 nM. The apparent  $K_D$ , determined from a fit of the NF to the Hill equation isotherm, was 1442 pM with a 95% confidence interval of [932 pM, 2169 pM]. The NF data including the fit are shown in Fig. 5 c.

Controls were performed with the **5·4·1** upside-down molecular setup in absence and presence of 10 nM (**R**)-**P3**, yielding NF of 32.8% and 15.4%, respectively. For the regular **1·4·5** molecular setup, the NF fluorescence also decreased from 47.1% in absence to 25.6% in presence of 10 nM mirrored compound (**S**)-**P3**. Both controls, in which either the molecular setup or the ligand was mirrored, produced an inverted change in NF as response to the addition of the ligand.

### Melting temperatures

To ensure that the differences in unbinding forces were a result of target DNA duplex stabilization by hairpin polyamides, the melting temperatures of the dsDNA·polyamide complexes were determined. The results clearly showed a larger increase in melting temperature for the target duplexes in presence of the polyamides compared to the reference duplexes (Fig. 6).

### Thermal dissociation constant

The affinity of a hairpin polyamide for its dsDNA binding site is characterized by the thermal dissociation constant  $K_D$ . The experimental data suggest that the Hill equation isotherm governs the response of the NF, from which the  $K_D$  characteristic for the dsDNA·polyamide complex under investigation is easily determined. In the following, we derive the response of CUFA beginning with the law of mass action.

The law of mass action describes the amounts of dsDNA·ligand complexes, unbound dsDNA, and free ligands at chemical equilibrium with a dsDNA·ligand complex characteristic thermal  $K_D$  defined as



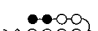
Polyamide	Target [°C] <b>1·2 / 1·4</b>	Reference [°C] <b>2·3</b>	Reference [°C] <b>4·5</b>
none	70	70	70
<b>P1</b> 	77	73	-
<b>(R)-P2</b> 	83	-	75
<b>(R)-P3</b> 	76	-	71

FIGURE 6 Melting temperatures of the target and reference DNA duplex in presence and absence of polyamides. The polyamides and DNA duplexes are mixed at a stoichiometry of 1:1 at 2  $\mu$ M.

$$K_D = \frac{k_{\text{off}}}{k_{\text{on}}} = \frac{[\text{dsDNA}][\text{ligand}]}{[\text{dsDNA} \cdot \text{ligand}]} \quad (6)$$

In our experiments, the total amount of added ligand exceeded the available dsDNA binding sites by at least two orders of magnitude. As a result, the probability  $p$  of a dsDNA binding site to be occupied by a ligand is given by the Hill equation isotherm and depends on the ligand concentration and  $K_D$  only (58):

$$p = \frac{[\text{ligand}]}{[\text{ligand}] + K_D} \quad (7)$$

For further analysis, it is crucial to compare the timescale of association to a single binding site to the timescale of the force probing. The apparent  $K_D$  determined from the CUFA experiment may vary from the initial thermal  $K_D$ , if the system is allowed to equilibrate during the application of the external force: at equilibrium and ligand concentrations around the thermal  $K_D$  the association rate, given by  $[\text{ligand}] \cdot k_{\text{on}}$ , is of the same order of magnitude as the dissociation rate  $k_{\text{off}}$ . The lifetime or inverse dissociation rate for a dsDNA·polyamide complex was experimentally determined to be  $\sim 500$  s (59). At 5  $\mu$ m/s separation velocity and similar linker lengths, the force needed to rupture a 20 basepair DNA duplex is built up on timescales in the order of  $\tau = 0.01$  s (44). The DNA duplex unbinding occurs therefore on a much faster timescale  $\tau$  than the association or dissociation of the dsDNA·ligand complex at relevant ligand concentrations:

$$\tau \ll \frac{1}{[\text{ligand}] \cdot k_{\text{on}}} \quad (8)$$

Although the natural off-rate of polyamides is very low, dissociation of the ligand from the DNA duplex during force probing may be nonnegligible. Studies suggest that the B-S transition of DNA under force can be explained by a tilt of the basepairs and a significant reorganization of the helical structure of the DNA (60–62). The B-S transition has not been observed for 20 basepair duplexes yet (44). However, even small deformations of the dsDNA helical structure may lead to the dissociation of the ligand, especially because hairpin polyamides are particularly sensitive to deformations



of the minor groove. This results in a decreased fraction of occupied binding sites at the time of dsDNA unbinding compared to the initial situation before force is applied. Given that the association rate is slow, rebinding of the ligand to the dsDNA is neglected and the fraction of occupied binding sites is reduced by a constant factor  $f$ .

$$p' = f \cdot p = f \cdot \frac{[\text{ligand}]}{[\text{ligand}] + K_D}, \quad (9)$$

where  $f$  lies within the interval  $[0,1]$ . The probability of a binding site to be occupied by a ligand is still governed by the Hill equation isotherm; however with increasing ligand concentration, the probability  $p'$  saturates at  $f < 1$  instead of 1. Importantly, the apparent  $K_D$  is identical with the thermal  $K_D$ .

The target DNA sequence was designed such that there is only one preferred polyamide-binding site. Without loss of generality, the no-ligand case is assumed to yield  $NF_0$ , whereas the bound-ligand case is assumed to yield  $NF_1$ . The fluorescence signals of these two states superimpose each other, and the expected total fluorescence signal as a function of the polyamide concentration is the sum of the NFs of the two states weighted by their relative occurrence:

$$\begin{aligned} NF &= p' \cdot NF_1 + (1 - p') \cdot NF_0 \\ &= NF_0 + f \cdot (NF_1 - NF_0) \cdot \frac{[\text{ligand}]}{[\text{ligand}] + K_D}. \end{aligned} \quad (10)$$

The dissociation of ligands from the DNA duplex results in a decrease of the maximal change in NF, whereas the apparent  $K_D$  is not affected. To conclude, in case Eq. 8 holds, the forced unbinding of dsDNA in presence of a ligand is a nonequilibrium process that produces a snapshot of the equilibrium distribution between dsDNA and dsDNA·ligand complexes from which the thermal dissociation constant  $K_D$  can be determined.

## CONCLUSION

The CUFA was successfully applied to quantify the thermal dissociation constants of three different dsDNA-polyamide complexes. For this purpose, polyamide concentrations as low as 10 pM were detected. This level of sensitivity is comparable to conventional chip methods, which work with fluorescently labeled ligands (9). Labeling, however, may alter the binding behavior compared with the unlabeled ligand and is not always applicable. Label-free high-throughput techniques, such as surface plasmon resonance, are challenged when they are confronted with small molecules like polyamides, which are easily detected employing CUFA. Our approach not only avoids labeling of the interacting molecules (a label is attached to linking DNA strand at a noninteracting basepair), but also permits the combination of different experiments as well as controls on one chip. The current DNA-feature size is hundreds of micrometers but can be

reduced to several micrometers using conventional microarray spotter. Miniaturization will allow for a high degree of parallelization and significantly reduced sample volumes.

We foresee CUFA in combination with microarray technology to be used as a tool to rapidly determine and quantify the sequence-recognition profile of small molecules like transcription factors, drugs, or other DNA-binding molecules. In separate experiments, we demonstrated that short-lived molecular interactions are captured in molecular crowded environments, as will be published elsewhere (63). Thus, the sensitivity range covers molecular complexes with micromolar to picomolar thermal dissociation constants and CUFA may prove to be the ideal tool for systems biologists, who have a growing interest in techniques that obtain affinity binder data with sufficient accuracy in a high-throughput fashion (64,65). The experimental procedure is as simple as contacting and separating two surfaces and can be implemented in any laboratory equipped with a quantitative fluorescence microscope.

## SUPPORTING MATERIAL

One figure is available at [http://www.biophysj.org/biophysj/supplemental/S0006-3495\(09\)00680-8](http://www.biophysj.org/biophysj/supplemental/S0006-3495(09)00680-8).

D. Ho and P. Severin are grateful to the Elite Network of Bavaria (IDK-NBT) for a doctoral fellowship. C. Dose is grateful to the Alexander von Humboldt foundation for a postdoctoral fellowship.

Financial support was provided by the Nanosystems Initiative Munich, the Deutsche Forschungsgemeinschaft, the Fonds der Chemischen Industrie, and the National Institutes of Health.

## REFERENCES

- Gottesfeld, J. M., L. Neely, J. W. Trauger, E. E. Baird, and P. B. Derivan. 1997. Regulation of gene expression by small molecules. *Nature*. 387:202–205.
- Majmudar, C. Y., and A. K. Mapp. 2005. Chemical approaches to transcriptional regulation. *Curr. Opin. Chem. Biol.* 9:467–474.
- Connaghan-Jones, K., A. Moody, and D. Bain. 2008. Quantitative DNase footprint titration: a tool for analyzing the energetics of protein–DNA interactions. *Nat. Protocols*. 3:900–914.
- Zhang, J., H. Lang, F. Huber, A. Bietsch, W. Grange, et al. 2006. Rapid and label-free nanomechanical detection of biomarker transcripts in human RNA. *Nat. Nanotechnol.* 1:214–220.
- Ren, B. 2000. Genome-wide location and function of DNA binding proteins. *Science*. 290:2306–2309.
- Harbison, C. T., D. B. Gordon, T. I. Lee, N. J. Rinaldi, K. D. Macisaac, et al. 2004. Transcriptional regulatory code of a eukaryotic genome. *Nature*. 431:99–104.
- Solomon, M. J., and A. Varshavsky. 1985. Formaldehyde-mediated DNA-protein crosslinking: a probe for in vivo chromatin structures. *Proc. Natl. Acad. Sci. USA*. 82:6470–6474.
- Warren, C., N. Kratochvil, K. Hauschild, S. Foister, M. Brezinski, et al. 2006. Defining the sequence-recognition profile of DNA-binding molecules. *Proc. Natl. Acad. Sci. USA*. 103:867–872.
- Puckett, J., K. Muzikar, J. Tietjen, C. Warren, A. Ansari, et al. 2007. Quantitative microarray profiling of DNA-binding molecules. *J. Am. Chem. Soc.* 129:12310–12319.

10. Boozer, C., G. Kim, S. Cong, H. Guan, and T. Londergan. 2006. Looking towards label-free biomolecular interaction analysis in a high-throughput format: a review of new surface plasmon resonance technologies. *Curr. Opin. Biotechnol.* 17:400–405.
11. Wang, J., and H. S. Zhou. 2008. Aptamer-based Au nanoparticles-enhanced surface plasmon resonance detection of small molecules. *Anal. Chem.* 80:7174–7178.
12. Gurard-Levin, Z. A., and M. A. Mrksich. 2008. Combining self-assembled monolayers and mass spectrometry for applications in biochips. *Annu. Rev. Anal. Chem.* 1:767–800.
13. Albrecht, C., K. Blank, M. Lalic-Multhaler, S. Hirler, T. Mai, et al. 2003. DNA: a programmable force sensor. *Science.* 301:367–370.
14. Blank, K., T. Mai, I. Gilbert, S. Schiffmann, J. Rankl, et al. 2003. A force-based protein biochip. *Proc. Natl. Acad. Sci. USA.* 100:11356–11360.
15. Blank, K., A. Lanckenau, T. Mai, S. Schiffmann, I. Gilbert, et al. 2004. Double-chip protein arrays: force-based multiplex sandwich immunoassays with increased specificity. *Anal. Bioanal. Chem.* 379:974–981.
16. Dose, C., D. Ho, H. E. Gaub, P. B. Dervan, and C. H. Albrecht. 2007. Recognition of “mirror-image” DNA by small molecules. *Angew. Chem.* 46:8384–8387.
17. Krautbauer, R., S. Fischerlander, S. Allen, and H. E. Gaub. 2002. Mechanical fingerprints of DNA drug complexes. *Single Mol.* 3:97–103.
18. Koch, S. J., A. Shundrovsky, B. C. Jantzen, and M. D. Wang. 2002. Probing protein-DNA interactions by unzipping a single DNA double helix. *Biophys. J.* 83:1098–1105.
19. Leuba, S. H., M. A. Karymov, M. Tomschik, and R. Ramjit. 2003. Assembly of single chromatin fibers depends on the tension in the DNA molecule: magnetic tweezers study. *Proc. Natl. Acad. Sci. USA.* 100:495–500.
20. Puchner, E. M., A. Alexandrovich, A. L. Kho, U. Hensen, L. V. Schäfer, B. Brandmeier, F. Gräter, H. Grubmüller, H. E. Gaub, and M. Gautel. 2008. Mechanoenzymatics of titin kinase. *Proc. Natl. Acad. Sci. USA.* 105:13385–13390.
21. Schlierf, M., F. Berkemeier, and M. Rief. 2007. Direct observation of active protein folding using lock-in force spectroscopy. *Biophys. J.* 93:3989–3998.
22. Wiita, A., R. Perez-Jimenez, K. Walther, F. Gräter, B. Berne, et al. 2007. Probing the chemistry of thioredoxin catalysis with force. *Nature.* 450:124–127.
23. Clemen, A. E. M., M. Vilfan, J. Jaud, J. S. Zhang, M. Barmann, et al. 2005. Force-dependent stepping kinetics of myosin-V. *Biophys. J.* 88:4402–4410.
24. Gosse, C., and V. Croquette. 2002. Magnetic tweezers: micromanipulation and force measurement at the molecular level. *Biophys. J.* 82:3314–3329.
25. Dervan, P. B., A. T. Poulin-Kerstien, E. J. Fechter, and B. S. Edelson. 2005. Regulation of gene expression by synthetic DNA-binding ligands. *Top. Curr. Chem.* 253:1–31.
26. Dervan, P. B., and B. S. Edelson. 2003. Recognition of the DNA minor groove by pyrrole-imidazole polyamides. *Curr. Opin. Struct. Biol.* 13:284–299.
27. Dervan, P. B. 2001. Molecular recognition of DNA by small molecules. *Bioorg. Med. Chem.* 9:2215–2235.
28. White, S., J. W. Szewczyk, J. M. Turner, E. E. Baird, and P. B. Dervan. 1998. Recognition of the four Watson-Crick base pairs in the DNA minor groove by synthetic ligands. *Nature.* 391:468–471.
29. Kielkopf, C. L., R. E. Bremer, S. White, J. W. Szewczyk, J. M. Turner, et al. 2000. Structural effects of DNA sequence on T.A recognition by hydroxypyrrole/pyrrole pairs in the minor groove. *J. Mol. Biol.* 295:557–567.
30. Mrksich, M., M. E. Parks, and P. B. Dervan. 1994. Hairpin peptide motif - a new class of oligopeptides for sequence-specific recognition in the minor-groove of double-helical DNA. *J. Am. Chem. Soc.* 116:7983–7988.
31. Swalley, S. E., E. E. Baird, and P. B. Dervan. 1999. Effects of  $\gamma$ -turn and  $\beta$ -tail amino acids on sequence-specific recognition of DNA by hairpin polyamides. *J. Am. Chem. Soc.* 121:1113–1120.
32. Kielkopf, C. L., S. White, J. W. Szewczyk, J. M. Turner, E. E. Baird, et al. 1998. A structural basis for recognition of A center dot T and T center dot A base pairs in the minor groove of B-DNA. *Science.* 282:111–115.
33. deClairac, R. P. L., B. H. Geierstanger, M. Mrksich, P. B. Dervan, and D. E. Wemmer. 1997. NMR characterization of hairpin polyamide complexes with the minor groove of DNA. *J. Am. Chem. Soc.* 119:7909–7916.
34. Cohen, J. D., J. P. Sadowski, and P. B. Dervan. 2007. Addressing single molecules on DNA nanostructures. *Angew. Chem.* 46:7956–7959.
35. Schmidt, T. L., C. K. Nandi, G. Rasched, P. P. Parui, B. Brutschy, et al. 2007. Polyamide struts for DNA architectures. *Angew. Chem.* 46:4382–4384.
36. Arndt, H. D., K. E. Hauschild, D. P. Sullivan, K. Lake, P. B. Dervan, et al. 2003. Toward artificial developmental regulators. *J. Am. Chem. Soc.* 125:13322–13323.
37. Stafford, R. L., H. D. Arndt, M. L. Brezinski, A. Z. Ansari, and P. B. Dervan. 2007. Minimization of a protein-DNA dimerizer. *J. Am. Chem. Soc.* 129:2660–2668.
38. Olenyuk, B. Z., G. J. Zhang, J. M. Klco, N. G. Nickols, W. G. Kaelin, Jr., et al. 2004. Inhibition of vascular endothelial growth factor with a sequence-specific hypoxia response element antagonist. *Proc. Natl. Acad. Sci. USA.* 101:16768–16773.
39. Nickols, N. G., and P. B. Dervan. 2007. Suppression of androgen receptor-mediated gene expression by a sequence-specific DNA-binding polyamide. *Proc. Natl. Acad. Sci. USA.* 104:10418–10423.
40. Nickols, N. G., C. S. Jacobs, M. E. Farkas, and P. B. Dervan. 2007. Modulating hypoxia-inducible transcription by disrupting the HIF-1-DNA interface. *ACS Chem. Biol.* 2:561–571.
41. Albrecht, C. H., H. Clausen-Schaumann, and H. E. Gaub. 2006. Differential analysis of biomolecular rupture forces. *J. Phys. Condens. Matter.* 18:S581–S599.
42. Perutz, S., E. J. Kramer, J. Baney, and C. Y. Hui. 1997. Adhesion between hydrolyzed surfaces of poly(dimethylsiloxane) networks. *Macromolecules.* 30:7964–7969.
43. Wiegand, G., K. R. Neumaier, and E. Sackmann. 1998. Microinterferometry: three-dimensional reconstruction of surface microtopography for thin-film and wetting studies by reflection interference contrast microscopy (RICM). *Appl. Opt.* 37:6892–6905.
44. Morfill, J., F. Kuhner, K. Blank, R. Lugmaier, J. Sedlmair, et al. 2007. B-S transition in short oligonucleotides. *Biophys. J.* 93:2400–2409.
45. Merkel, R., P. Nassoy, A. Leung, K. Ritchie, and E. Evans. 1999. Energy landscapes of receptor-ligand bonds explored with dynamic force spectroscopy. *Nature.* 397:50–53.
46. Herman, D. M., E. E. Baird, and P. B. Dervan. 1998. Stereochemical control of the DNA binding affinity, sequence specificity, and orientation preference of chiral hairpin polyamides in the minor groove. *J. Am. Chem. Soc.* 120:1382–1391.
47. Kienberger, F., V. P. Pastushenko, G. Kada, and H. J. Gruber. 2000. Static and dynamical properties of single poly(ethylene glycol) molecules investigated by force spectroscopy. *Single Mol.* 78:123–128.
48. Friedsam, C., A. K. Wehle, F. Kuhner, and H. E. Gaub. 2003. Dynamic single-molecule force spectroscopy: bond rupture analysis with variable spacer length. *J. Phys. Condens. Matter.* 15:S1709–S1723.
49. Evans, E., and K. Ritchie. 1997. Dynamic strength of molecular adhesion bonds. *Biophys. J.* 72:1541–1555.
50. Viani, M., T. Schäffer, A. Chand, M. Rief, H. E. Gaub, and P. Hansma. 1999. Small cantilevers for force spectroscopy of single molecules. *J. Appl. Phys.* 86:2258–2262.
51. Xia, Y., and G. M. Whitesides. 1998. Soft lithography. *Annu. Rev. Mater. Sci.* 28:153–184.
52. Bernard, A., J. P. Renault, B. Michel, and H. R. Bosshard. 2000. Microcontact printing of proteins. *Adv. Mater.* 12:1067–1070.

53. Neuert, G., C. H. Albrecht, and H. E. Gaub. 2007. Predicting the rupture probabilities of molecular bonds in series. *Biophys. J.* 93:1215–1223.
54. Rouzina, I., and V. A. Bloomfield. 2001. Force-induced melting of the DNA double helix. 2. Effect of solution conditions. *Biophys. J.* 80:894–900.
55. White, S., E. E. Baird, and P. B. Dervan. 1997. Orientation preferences of pyrrole-imidazole polyamides in the minor groove of DNA. *J. Am. Chem. Soc.* 119:8756–8765.
56. Hawkins, C. A., R. P. de Clairac, R. N. Dominey, E. E. Baird, S. White, et al. 2001. Controlling binding orientation in hairpin polyamide DNA complexes. *J. Am. Chem. Soc.* 122:5235–5243.
57. Hsu, C. F., J. W. Phillips, J. W. Trauger, M. E. Farkas, J. M. Belitsky, et al. 2007. Completion of a programmable DNA-binding small molecule library. *Tetrahedron.* 63:6146–6151.
58. Halperin, A., A. Buhot, and E. Zhulina. 2006. On the hybridization isotherms of DNA microarrays: the Langmuir model and its extensions. *J. Phys. Condens. Matter.* 18:S463–S490.
59. Baliga, R., E. Baird, D. Herman, C. Melander, P. B. Dervan, et al. 2001. Kinetic consequences of covalent linkage of DNA binding polyamides. *Biochemistry.* 40:3–8.
60. Rief, M., H. Clausen-Schaumann, and H. E. Gaub. 1999. Sequence dependent mechanics of single DNA molecules. *Nat. Struct. Biol.* 6:346–349.
61. Lebrun, A., and R. Lavery. 1996. Modeling extreme stretching of DNA. *Nucleic Acids Res.* 24:2260–2267.
62. Smith, S. B., Y. J. Cui, and C. Bustamante. 1996. Overstretching B-DNA: the elastic response of individual double-stranded and single-stranded DNA molecules. *Science.* 271:795–799.
63. Ho, D., K. Falter, P. Severin, and H. E. Gaub. 2009. DNA as a force sensor in an aptamer-based biochip for ATP. *Anal. Chem.* n press.
64. Titz, B., M. Schlesner, and P. Uetz. 2004. What do we learn from high-throughput protein interaction data? *Expert Rev. Proteomics.* 1:111–121.
65. Kitano, H. 2002. Systems biology: a brief overview. *Science.* 295:1662–1664.

Biophysical Journal, Volume 96

**Supporting Material**

**Quantitative detection of small molecule/DNA complexes employing a force-based and label-free DNA-microarray**

Dominik Ho, Christian Dose, Christian H. Albrecht, Philip Severin, Katja Falter, Peter B. Dervan, and Hermann E. Gaub

## SUPPLEMENTARY INFORMATION

### “Quantitative detection of small molecule/DNA complexes employing a force-based and label-free DNA-microarray”

*Dominik Ho<sup>1,2</sup>, Christian Dose<sup>3</sup>, Christian H. Albrecht<sup>1</sup>, Philip Severin<sup>1</sup>, Katja Falter<sup>1</sup>, Peter B. Dervan<sup>3</sup>, Hermann E. Gaub<sup>1</sup>*

<sup>[1]</sup> Lehrstuhl für Angewandte Physik and Center for Nanoscience  
Ludwig-Maximilians-Universität  
Amalienstrasse 54, 80799 Munich, Germany  
Fax: (+49) 89-2180-2050  
E-mail: gaub@lmu.de

<sup>[2]</sup> Munich Center For Integrated Protein Science (CIPSM)  
Ludwig-Maximilians-Universität  
Butenandtstrasse 5-13, 81377 Munich, Germany  
E-mail: dominik.ho@web.de

<sup>[3]</sup> Division of Chemistry and Chemical Engineering  
California Institute of Technology  
Pasadena, California 91125, USA  
Fax: (+1) 626-683-8753  
E-mail: dervan@caltech.edu

**DNA surface density.** Quantitative analysis of the fluorescence images relies on the assumption that the amount of fluorescently labeled species per unit area is proportional to the obtained fluorescence intensity per unit area. To investigate this relationship, we titrated identically prepared oligomer **1** spots on a glass slide with different amounts of oligomer **2** ranging from 0 to 0.6 pMol. After 2 hours of incubation the slide was washed thoroughly in 1x PBS and read out via fluorescence. The fluorescence intensities were summed over all pixels of each well divided by the fluorescence spot area, which was on average 1.8 mm of diameter. The fluorescence intensity was proportional to the amount of added ligand for amounts of DNA oligomer **2** less than 0.4 pMol. At higher amounts the fluorescence intensity saturated and deviated significantly from a line fit.

The observed saturation can be explained by electrostatic repulsion between the dsDNA. Short dsDNA is a rod like, cylindrical molecule, which is most densely packed in a parallel arrangement. Close packing of short dsDNA on a surface is thus equivalent to the problem of close packing of hard disks. The total hard disk radius is the sum of the dsDNA radius and the length of electrostatic repulsion. The former is known to be 0.95 nm [1] and the latter is best described by the Debye length that is approximately 0.62 nm at 147 mM Na<sup>+</sup> [2]. The total disk radius is therefore 1.57 nm. Randomly packing discs results in a packing efficiency of 82% [2]. The packing efficiency and the total disk radius yield the theoretical maximum in short dsDNA surface density  $\rho_{\text{Debye}}$  of 0.11 molecules per nm<sup>2</sup> in good agreement with literature values [3].

To compare whether the onset of fluorescence intensity saturation coincides with  $\rho_{\text{Debye}}$  the densities of **1**•**2** complexes per unit area were determined from the fluorescence spot size and the assumption that all oligomers **2** hybridized to free oligomers **1** immobilized to the surface. Further, the expected maximal fluorescence intensity was determined by extrapolating the line fit for low densities to  $\rho_{\text{Debye}}$  yielding  $I_{\text{Debye}}$ . In Figure S1 the fluorescence intensity ratio  $I/I_{\text{Debye}}$  was plotted against the corresponding calculated surface density ranging from 0 to 0.13 molecules per nm<sup>2</sup>. The observed saturation of fluorescence intensity at around 0.09 molecules per nm<sup>2</sup> is in good agreement with  $\rho_{\text{Debye}}$ . Remaining free ssDNA strands that also occupy a small fraction of the surface area may explain the slightly lower experimentally determined value.

It is entirely possible that a non-linearity between amount of oligomer **2** per unit area and fluorescence signal at high surface densities contributes to the observed saturation effect. Hence, the molecular setups in the present study were prepared at  $\rho_0$  of 0.06 molecular setups per nm<sup>2</sup>. This is a surface density for which we have shown the fluorescence per unit area to

be proportional to the fluorescently labeled species per unit area. Nonetheless, the surface density is rather high: the Flory radius, which is deduced from the radius of gyration, is a good measure of the volume a polymer encompasses [1] [4]. From the actual lengths and the persistence lengths of dsDNA [5], ssDNA [6] and PEG [7] we calculate a Flory radius of 9.38 nm for the **1·2·3** molecular setups used in our experiments. Assuming again a close packing of disks yields an upper limit of 0.003 molecular setups per nm<sup>2</sup> for the regime wherein the constructs do not interact with each other. The densities used in our experiments are an order of magnitude higher than that. This is a fact that should be kept in mind if the binding of larger and less robust ligands like proteins to dsDNA is going to be investigated. In this case, the surface densities of the molecular setups may have to be decreased further in order to avoid steric hindrance and unwanted interactions.

## REFERENCES

- [1] Halperin, A., A. Buhot and E. Zhulina. 2006. On the hybridization isotherms of DNA microarrays: the Langmuir model and its extensions. *J. Phys.: Condens. Matter*, 18:S463-S490.
- [2] Berryman, J. G. 1983. Random close packing of hard spheres and disks. *Phys. Rev. A*. 27:1053-1061.
- [3] Ray, S., S. Daube, G. Leitus, Z. Vager and R. Naaman. 2006. Chirality-Induced Spin-Selective Properties of Self-Assembled Monolayers of DNA on Gold. *Phys. Rev. Lett.* 96: 036101.
- [4] Israelachvili, J. N. 1991. *Intermolecular and Surface Forces*. Academic Press, New York.
- [5] Marko, J. F. and E. D. Siggia. 1995. Stretching DNA. *Macromolecules*. 28:8759-8770.
- [6] Rief, M., H. Clausen-Schaumann and H. E. Gaub. 1999. Sequence dependent mechanics of single DNA molecules. *Nat. Struct. Biol.* 6:346-349.
- [7] Oesterhelt, F., M. Rief and H. E. Gaub. 1999. Single molecule force spectroscopy by AFM indicates helical structure of poly (ethylene-glycol) in water. *New J. Phys.* 1:6.1-6.11.

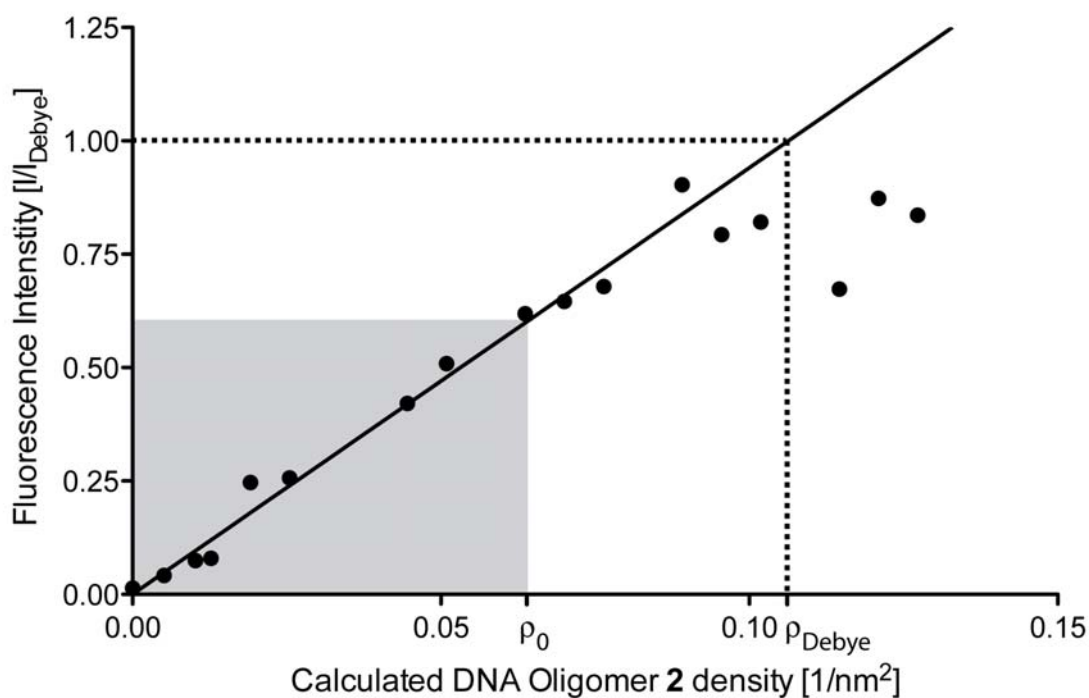


**Figure S1.** Different amounts of oligomer **2** were incubated with identically prepared oligomer **1** spots. The fluorescence intensities per unit area are plotted against the calculated surface densities. The dashed line indicates the highest possible density of oligomer **2** per unit area based on the electrostatic repulsion argument. The CUFA experiments are performed at densities of oligomer **2** per unit area, wherein the fluorescence intensity per unit area is proportional to the presence of fluorescently labeled oligomer **2** per unit area (highlighted in grey).



# DNA as a Force Sensor in an Aptamer-Based Biochip for Adenosine

Dominik Ho, Katja Falter, Philip Severin, and Hermann E. Gaub\*

Lehrstuhl für Angewandte Physik and Center for Nanoscience (CeNS), Ludwig-Maximilians-Universität, Amalienstrasse 54, 80799 Munich, Germany, and Munich Center For Integrated Protein Science (CIPSM), Ludwig-Maximilians-Universität, Butenandtstrasse 5-13, 81377 Munich, Germany

Without prior signal amplification, small molecules are difficult to detect by current label-free biochip approaches. In the present study, we developed a label-free capture biochip based on the comparative measurement of unbinding forces allowing for direct detection of small-molecule–aptamer interactions. The principle of this assay relies on increased unbinding forces of bipartite aptamers due to complex formation with their cognate ligands. The bipartite aptamers are immobilized on glass support via short DNA duplexes that serve as references to which unbinding forces can be compared. In a simple model system, adenosine is captured from solution by an adenosine-selective aptamer. Linking the molecular chains, each consisting of a short DNA reference duplex and a bipartite aptamer, between glass and a poly(dimethylsiloxane) (PDMS) surface and subsequently separating the surfaces compares the unbinding forces of the two bonds directly. Fluorescence readout allows for quantification of the fractions of broken aptamer and broken reference bonds. The presence of micromolar adenosine concentrations reliably resulted in a shift toward larger fractions of broken reference bonds. Because of the force-based design, the interactions between the bipartite aptamer and the target, rather than the presence of the target, are detected and no washing step disturbing the equilibrium state prior to probing and no reporter aptamer or antibody is required. The assay exhibits excellent selectivity against other nucleotides and detects adenosine in the presence of a complex molecular background. Multiplexing was demonstrated by performing whole titration experiments on a single chip revealing an effective half-maximal concentration of 124.8  $\mu\text{M}$  agreeing well with literature values.

A current goal within the field of bioanalytical methods is the development of label-free detection formats, which probe multiple interactions simultaneously employing massively parallel assays.<sup>1</sup> High impact of DNA biochips on the field of biology provides motivation to develop arrays for other classes of molecules,

including peptides, proteins, and small molecules.<sup>2</sup> DNA or RNA aptamers are promising candidates for fabrication of microarray surfaces, which simply and effectively capture above-mentioned analytes from solution. Numerous reports confirm that aptamers specifically respond to all kinds of molecules<sup>3</sup> such that they are increasingly recognized as rivals for antibodies in in vitro diagnostics<sup>4</sup> and molecular sensor applications,<sup>5–7</sup> surpassing them in terms of small molecular weight, ease of modification, and ability to detect toxins.<sup>8</sup> In contrast to proteins, which are difficult to immobilize on surfaces due to their tendency to adsorb unspecifically and thus lose activity,<sup>9</sup> standard protocols for oligonucleotide microarrays are used for aptamer biochips.

The development of such arrays has proven to be more difficult than expected. Small molecules in particular are rarely detected due to several reasons: First, their small size induces only small signals using current biochip-compatible, label-free detection techniques (e.g., surface plasmon resonance,<sup>10</sup> electrochemical,<sup>11</sup> or cantilever bending<sup>12</sup> based sensors). Second, background signals are generally large in biochip assays due to the tendency of molecules to adsorb to basically all man-made surfaces.<sup>13–15</sup> Third, aptamers developed against small molecules are generally of low affinity,<sup>16</sup> prohibiting washing steps that would increase the signal-to-background ratio. The combination of small signal, high background, and no option for stringent washes creates an overwhelming technical hurdle for the quantification of small molecules without prior signal amplification. Here, we present a widely applicable strategy for the direct detection of small-

- (2) Lockhart, D. J.; Winzeler, E. A. *Nature* **2000**, *405*, 827–836.
- (3) Hermann, T.; Patel, D. J. *Science* **2000**, *287*, 820–825.
- (4) Rimmele, M. *ChemBioChem* **2003**, *4*, 963–971.
- (5) Zhang, S.; Xia, J.; Li, X. *Anal. Chem.* **2008**, *80*, 8382–8388.
- (6) Wang, J.; Zhou, H. S. *Anal. Chem.* **2008**, *80*, 7174–7178.
- (7) Navani, N. K.; Li, Y. F. *Curr. Opin. Chem. Biol.* **2006**, *10*, 272–281.
- (8) Tang, J.; Xie, J.; Shao, N.; Yan, Y. *Electrophoresis* **2006**, *27*, 1303–1311.
- (9) Kusnezow, W.; Hoheisel, J. J. *Mol. Recognit.* **2003**, *16*, 165–176.
- (10) Boozer, C.; Kim, G.; Cong, S.; Guan, H.; Londergan, T. *Curr. Opin. Biotechnol.* **2006**, *17*, 400–405.
- (11) Xu, D.; Xu, D.; Yu, X.; Liu, Z.; He, W.; Ma, Z. *Anal. Chem.* **2005**, *77*, 5107–5113.
- (12) Zhang, J.; Lang, H.; Huber, F.; Bietsch, A.; Grange, W.; Certa, U.; Mckendry, R.; Güntherodt, H.; Hegner, M.; Gerber, C. *Nat. Nanotechnol.* **2006**, *1*, 214–220.
- (13) Haab, B. B.; Dunham, M. J.; Brown, P. O. *Genome Biol.* **2001**, *2*, 0004.10004.13.
- (14) Michaud, G.; Salcius, M.; Zhou, F.; Bangham, R.; Bonin, J.; Guo, H.; Snyder, M.; Predki, P.; Schweitzer, B. *Nat. Biotechnol.* **2003**, *21*, 1509–1512.
- (15) Ma, H.; Horiuchi, K. *Drug Discovery Today* **2006**, *11*, 661–668.
- (16) Hamula, C.; Guthrie, J.; Zhang, H.; Li, X.; Le, X. *TrAC, Trends Anal. Chem.* **2006**, *25*, 681–691.

\* To whom correspondence should be addressed. Phone: +49 89 2180 3172. Fax: +49 89 21 80 2050. E-mail: gaub@physik.lmu.de.

(1) Gurard-Levin, Z. A.; Mrksich, M. *Annu. Rev. Anal. Chem.* **2008**, *1*, 767–800.

molecule–aptamer complex formation. Our approach reports interactions between small molecules and aptamers, rather than the mere presence of small molecules close to a sensor surface. Thereby, nonspecific adhesion, the major bottleneck in the development of next-generation biochips, is rendered insignificant.

For detection of the bound analyte we applied the comparative unbinding force assay (CUFA), which operates label-free and is insensitive to nonspecifically adsorbed target molecules. CUFA has already been applied to detect single-nucleotide polymorphisms,<sup>17</sup> to study differences of antibody/antigen interactions,<sup>18</sup> to eliminate cross-reactions on protein microarrays,<sup>19</sup> and to investigate the chiral selectivity of small peptides.<sup>20</sup> Whereas standard single-molecule force spectroscopy experiments measure the unbinding forces of molecular complexes by a microscopic, springlike object, e.g., an atomic force microscopy (AFM) cantilever<sup>21</sup> or a bead in an optical trap,<sup>22</sup> CUFA reduces the force detector to a single DNA reference duplex. Many molecular chains, each consisting of a bipartite aptamer and a DNA reference duplex, are grafted between two surfaces. The linker between the bonds is conjugated to a fluorophore. Upon separation of the surfaces, a force gradually builds up within the molecular chain and the unbinding forces of the bipartite aptamer structure are compared directly against the unbinding forces of the short DNA reference duplex. The result, i.e., the fractions of broken aptamer and broken reference bonds, is stored in a binary fluorophore distribution (fluorophore top or bottom surface). If complex formation between aptamer and ligand results in increased unbinding forces of the aptamer structure, a shift toward larger fractions of broken reference bonds is expected. Thereby, CUFA combines the advantages of fluorescence-based techniques, namely, fast and sensitive detection employing commercially available scanners or fluorescence microscopes, with the advantages of label-free methods, namely, no undesirable label interactions and the option for simultaneous detection of multiple analytes. Importantly, high specificity when investigating molecular interactions is a major strength of CUFA. Current fluorescent<sup>23</sup> and label-free biochip methods do not allow for discrimination between specifically and nonspecifically adhered analytes, which may lead to false-positives. Washing steps are performed to reduce nonspecific adhesion. However, if molecular interactions with equilibrium dissociation constants in the micromolar range need to be characterized, specifically but weakly interacting molecules are also removed resulting in false-negatives. CUFA overcomes these difficulties by detecting the interaction between the capture

aptamer and its target and not merely the presence of the target.

In the present study, we investigated the interaction between adenosine and an adenosine-selective aptamer. This model system is instructive for the reasons that the aptamer is well-characterized,<sup>24–26,28</sup> the interaction is very weak, and the analyte is so small that it cannot be detected directly with surface plasmon resonance.<sup>6</sup>

## EXPERIMENTAL SECTION

**Immobilization of Aptamer–DNA Unbinding Force Complex on Slides (Bottom Surface).** DNA oligomers **1**, **2**, and **3** were purchased HPLC grade from IBA GmbH (Göttingen, Germany). Sequences and modifications of all oligonucleotides are the following: **1**, NH<sub>2</sub>-(hexaethyleneglycol)<sub>5</sub>-5'-TTT TTT TTT TCG GTC TGT CGC GTA CTT GCA-3'; **2**, 3'-GCC AGA CAG CGC ATG AAC GTT TTT T-5'-5'-T(Cy3) TTT TTC AAC ATA CCT GGG GGA GTA TAT AAT GAC TGA CCC C-3'; **3**, biotin-5'-TTT TTT TTT TGG GGT CAG TCA TTA TAG CGG AGG AAG GTA TGT TG-3'. For the upside-down experiment the NH<sub>2</sub>-(hexaethyleneglycol)<sub>5</sub> (HEGL) and biotin modifications are exchanged. The five HEGL linkers are connected via phosphate groups. DNA oligomer **1** is amine-modified, which allows covalent linkage to aldehyde-functionalized glass slides (Schott GmbH, Jena, Germany). We spotted 2  $\mu$ L drops of 5 $\times$  SSC (saline sodium citrate; Sigma-Aldrich GmbH, Munich, Germany) containing 25  $\mu$ M oligomer **1** on the aldehyde slide in a 4  $\times$  4 pattern and incubated the slide in a saturated NaCl ddH<sub>2</sub>O atmosphere overnight. After washing the slide with ddH<sub>2</sub>O containing 0.2% sodium dodecyl sulfate (SDS; VWR Scientific GmbH, Darmstadt, Germany) and thoroughly rinsing the slide with ddH<sub>2</sub>O we reduced the resulting Schiff bases with 1% aqueous NaBH<sub>4</sub> (VWR Scientific GmbH, Darmstadt, Germany) for 20 min. Subsequently, the slide was washed with 1 $\times$  SSC and thoroughly rinsed with ddH<sub>2</sub>O. In order to reduce nonspecific binding, the slides were blocked in 1 $\times$  SSC containing 4% bovine serum albumin (BSA; Sigma-Aldrich GmbH, Munich, Germany) for 30 min. Custom-made 16-well silicone isolators (Grace-Biolabs, OR) were placed on top of the immobilized DNA oligomer **1**. The 0.1  $\mu$ M Cy3-modified oligomer **2** and 0.2  $\mu$ M biotin-modified oligomer **3** were hybridized to the latter for 1 h, completing the **1**•**2**•**3** complex on the glass slide. The slides were washed with 1 $\times$  SSC containing 0.05% SDS and thoroughly rinsed with 1 $\times$  SSC. The silicone isolators stayed on the slide throughout the experiment, and care was taken that after hybridization the slide remained immersed in 1 $\times$  SSC.

**Ligand Incubation.** The 16-well silicon isolators allow for incubation with different concentrations of the ligand molecule on one slide. An amount of 100  $\mu$ L of the respective solutions was circulated through the wells employing a self-made microfluidic system. The latter was driven by two 16-channel peristaltic pumps (Ismatec GmbH, Wertheim-Mondfeld, Germany) pumping the different solutions through tubing and blunt needles leading into and out of the wells in a closed circuit. The tubing was

- (17) Albrecht, C.; Blank, K.; Lalic-Multhaler, M.; Hirler, S.; Mai, T.; Gilbert, I.; Schiffmann, S.; Bayer, T.; Clausen-Schaumann, H.; Gaub, H. E. *Science* **2003**, *301*, 367–370.
- (18) Blank, K.; Mai, T.; Gilbert, I.; Schiffmann, S.; Rankl, J.; Zivin, R.; Tackney, C.; Nicolaus, T.; Spinnler, K.; Oesterhelmt, F.; Benoit, M.; Clausen-Schaumann, H.; Gaub, H. E. *Proc. Natl. Acad. Sci. U.S.A.* **2003**, *100*, 11356–11360.
- (19) Blank, K.; Lankenau, A.; Mai, T.; Schiffmann, S.; Gilbert, I.; Hirler, S.; Albrecht, C.; Benoit, M.; Gaub, H. E.; Clausen-Schaumann, H. *Anal. Bioanal. Chem.* **2004**, *379*, 974–981.
- (20) Dose, C.; Ho, D.; Gaub, H. E.; Dervan, P. B.; Albrecht, C. *Angew. Chem., Int. Ed.* **2007**, *46*, 8384–8387.
- (21) Florin, E. L.; Moy, V. T.; Gaub, H. E. *Science* **1994**, *264*, 415–417.
- (22) Svoboda, K.; Schmidt, C. F.; Schnapp, B. J.; Block, S. M. *Nature* **1993**, *365*, 721–727.
- (23) Warren, C.; Kratochvil, N.; Hauschild, K.; Foister, S.; Brezinski, M.; Dervan, P.; Phillips, G., Jr.; Ansari, A. *Proc. Natl. Acad. Sci. U.S.A.* **2006**, *103*, 867–872.

- (24) Huizenga, D. E.; Szostak, J. W. *Biochemistry* **1995**, *34*, 656–665.
- (25) Lin, C. H.; Patel, D. J. *Chem. Biol.* **1997**, *4*, 817–832.
- (26) Stojanovic, M. N.; de Prada, P.; Landry, D. W. *J. Am. Chem. Soc.* **2000**, *122*, 11547–11548.
- (28) Jhaveri, S. D.; Kirby, R.; Conrad, R.; Maglott, E. J.; Bowser, M.; Kennedy, R. T.; Glick, G.; Ellington, A. D. *J. Am. Chem. Soc.* **2000**, *122*, 2469–2473.

passivated prior to use with 1× SSC containing 4% BSA for 30 min. Adenosine triphosphate (ATP), adenosine monophosphate (AMP), and guanosine triphosphate (GTP) were obtained from Roche (Roche GmbH, Grenzach, Germany).

**Immobilization of Streptavidin on Poly(dimethylsiloxane) Stamp (Top Surface).** Micro- and macrostructured poly(dimethylsiloxane) (PDMS) stamps were fabricated by casting 1:10 cross-linker/base (Sylgard, Dow Corning, MI) into a custom-made Pyrex/silicon wafer (HSG-IMIT, Villingen-Schwenningen, Germany) according to standard procedures.<sup>29</sup> The resulting PDMS stamp carries pillars of 1 mm diameter and 1 mm height in a square pattern on a 3 mm thick basis. The spacing between two adjacent pillars is 3 mm. The flat pillar surface is microstructured with 100 μm × 100 μm pads separated by 41 μm wide and 5 μm deep rectangular trenches allowing for drainage of liquid during the contact and separation process. Before free polymers were extracted from the device in toluene using a Soxhlet device, the PDMS was cut in 4 × 4 pillar pieces. PDMS was then activated in 12.5% HCl overnight and derivatized with (3-glycidoxypropyl)-trimethoxysilane (ABC-R, Karlsruhe, Germany) in order to generate epoxide groups. NH<sub>2</sub>-PEG-biotin (3400 g/mol; Rapp Polymere, Tübingen, Germany) was molten at 80 °C, and roughly 1 μL was spotted on each pillar followed by overnight incubation in argon atmosphere at 80 °C. The excess polymers were thoroughly removed with ddH<sub>2</sub>O. Shortly before the experiment the PDMS was incubated with 1 μg/mL streptavidin (Thermo Fisher Scientific, Bonn, Germany) in 1× SSC and 0.4% BSA for 30 min, washed with 1× SSC containing 0.05% Tween 20 (VWR Scientific GmbH, Darmstadt, Germany), and gently dried with N<sub>2</sub> gas.

**Contact Process and Fluorescence Readout.** On an inverted microscope (Carl-Zeiss MicroImaging GmbH, Göttingen, Germany) the slide was fixed on a stainless steel stage with permanent magnets. The PDMS device was placed upside down on a glass block connected to a xyz stepper motor system (OWIS GmbH, Staufen, Germany) and a closed-loop piezo (Piezo Systems Jena, Germany). Prior to the contact process, the slide and the PDMS stamp were aligned parallel to each other, employing reflection interference microscopy<sup>30</sup> and a commercially available gimbal adjustment system (OWIS GmbH, Germany) mounted to the piezo. With the use of the latter, contact was established. Care was taken that each individual pillar is compressed not more than 3 μm. The separation of the two surfaces was carried out at constant velocity of 1 μm/s. Fluorescence images were recorded before and after the contact process employing a Tecan microarray scanner (Tecan Austria GmbH, Grödig, Austria).

## RESULTS AND DISCUSSION

### Detection Principle of the Force-Based Aptamer Sensor.

The implementation of this format is shown schematically in Figure 1. Although the instrumentation is almost identical to a microcontact printing setup,<sup>31</sup> the key to the comparable unbinding force assay lies within the molecular setup (Figure 1a). A short DNA duplex in shear geometry serves as a force reference. One

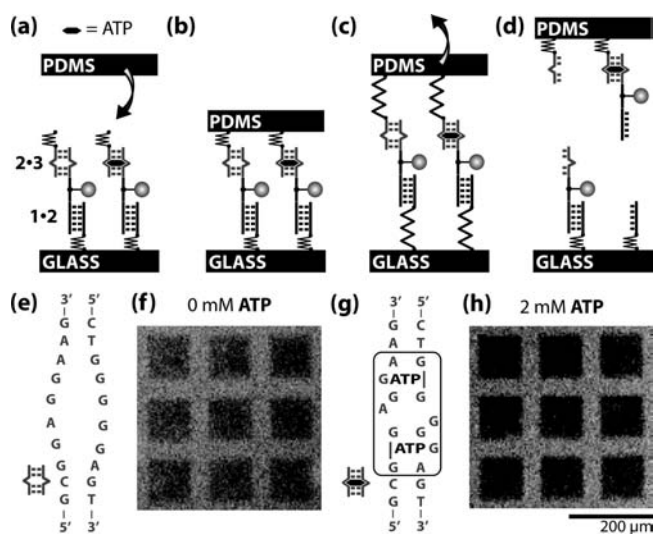


**Figure 1.** Schematic representation of the comparative unbinding force assay for the detection of small molecules. (a) DNA reference duplexes **1·2** and bipartite aptamers **2·3** are bound in series via PEG spacers to glass support. Depending on the presence of ATP, the aptamer is in its bound or free state. A streptavidin-functionalized PDMS surface is approached to the glass surface. (b) PDMS couples to the **3** oligomers of the bipartite aptamers via biotin-streptavidin complex formation. (c) The two surfaces are separated, and an increasing force builds up until either the reference duplex or the bipartite aptamer breaks. (d) Aptamer-ATP complex formation increases the unbinding forces of the bipartite aptamer. In comparison to the case that no ATP is present, a larger fraction of linking DNA strands conjugated to fluorophores is transferred from the glass to the PDMS. (e) At 0 mM ATP the bipartite aptamer is present as a loose bubble flanked by Watson-Crick base-paired stem regions. (f) Fluorescence on glass after contact without prior incubation with ATP. The squarelike features (100 × 100 μm<sup>2</sup>) correspond to the area contacted with microstructured PDMS. (g) At 2 mM ATP the bipartite aptamer bases show enhanced stacking upon binding of two molecules of ATP. (h) Fluorescence on glass after contact with prior incubation with 2 mM ATP. In comparison to the 0 mM ATP case, a larger fraction of fluorescence was transferred from the glass to the PDMS.

strand, oligomer **1**, is connected to glass support (bottom surface) via a (hexaethyleneglycol)<sub>5</sub> spacer. The complementary strand, oligomer **2**, which also carries a Cy3 fluorescence label, possesses an overhang containing the sequence of one part of the bipartite ATP aptamer. The complementary aptamer strand, oligomer **3**, is biotin-modified at the end of a polythymine linker and completes the **1·2·3** complex on the glass slide. We chose the reference force duplex and the stem regions flanking the aptamer such that their calculated free energies<sup>32</sup> are similar, assuming that similar free energies also imply similar unbinding forces under an external load. The spontaneous off-rates are sufficiently slow such that the complex is stable for days under physiological conditions.

In Figure 1b the **1·2·3** complex on the glass surface was brought into contact with a PDMS surface functionalized with streptavidin attached to 3400 g/mol PEG linkers, allowing for biotin-streptavidin complexation. After 10 min, the surfaces were separated at a constant velocity of 1 μm/s (Figure 1c). Thereby, the polymeric anchors were stretched and a force gradually built up until the chain of molecular complexes ruptured either at the

(29) Wilbur, J. L.; Kumar, A.; Kim, E.; Whitesides, G. M. *Adv. Mater.* **1994**, *6*, 600–604.

(30) Wiegand, G.; Neumaier, K. R.; Sackmann, E. *Appl. Opt.* **1998**, *37*, 6892–6905.

(31) Bernard, A.; Renault, J. P.; Michel, B.; Bosshard, H. R. *Adv. Mater.* **2000**, *12*, 1067–1070.

(32) Kibbe, W. A. *Nucleic Acids Res.* **2007**, *35*, 43–46.

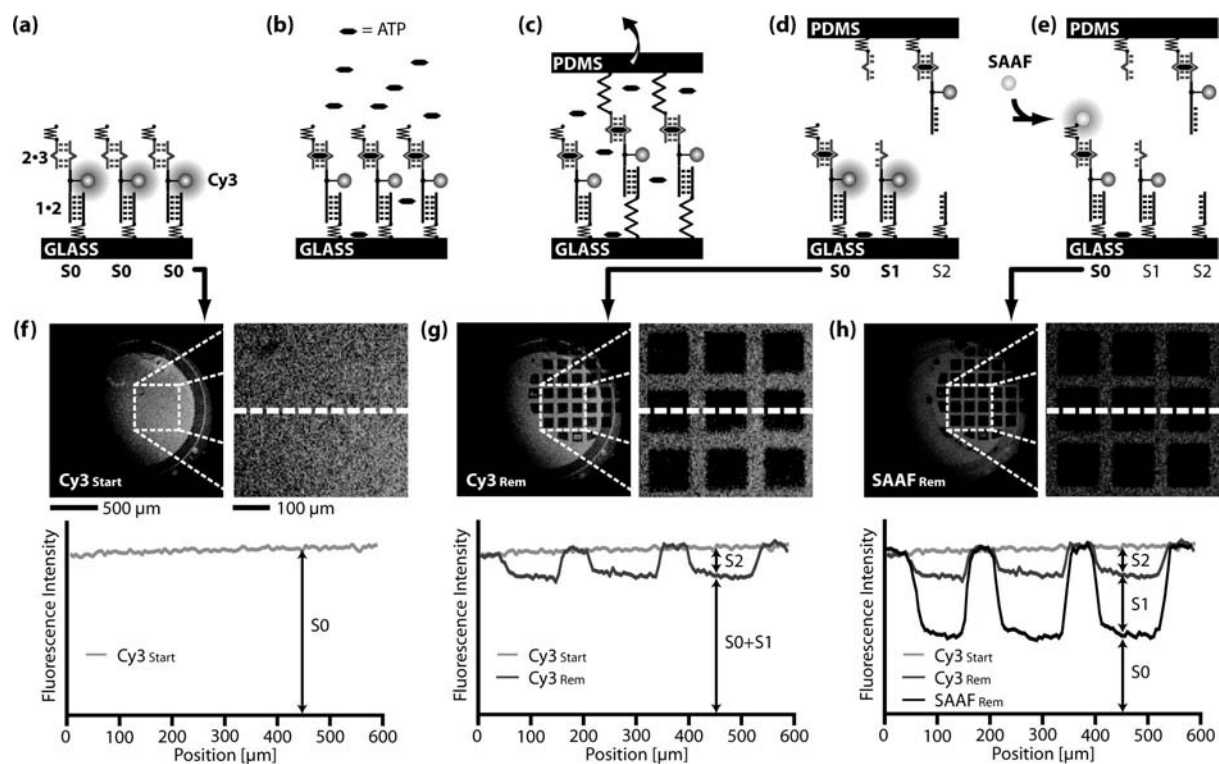


**Figure 2.** Detailed schematic of data acquisition and processing. (a) Initially all DNA-hybrids are in the state S0. The chip fluorescence is recorded at 550–600 nm ( $Cy3_{Start}$ ). (b) Incubation with ATP. (c) Coupling of the DNA-hybrids to a second surface and separation of the surfaces in the presence of ATP. (d) DNA-hybrids appear in the states S0, S1, and S2. The chip fluorescence is recorded again at 550–600 nm ( $Cy3_{Rem}$ ). (e) Labeling of noncoupled DNA-hybrids with streptavidin Alexa Fluor 647 (SAAF) and recording of fluorescence at 655–695 nm ( $SAAF_{Rem}$ ). (f)  $Cy3_{Start}$  chip fluorescence image and corresponding line profile allowing for determination of the initial amount of DNA-hybrids. (g)  $Cy3_{Rem}$  chip fluorescence image and corresponding line profile allowing for determination of the fraction S2. (h)  $SAAF_{Rem}$  chip fluorescence image and corresponding line profile allowing for determination of the fractions S0 and S1. The fluorescence line profiles are averaged over 40  $\mu\text{m}$ .

1·2 reference or at the 2·3 aptamer. We neither recorded nor analyzed the macroscopic force needed to pull the two surfaces apart. The unbinding forces are compared intrinsically and independently for each molecular chain. Aptamer–ATP complex formation is expected to increase the aptamer unbinding forces and as a result increase the fraction of the broken reference bonds (Figure 1d). Macroscopically, the fractions of broken reference bonds and broken aptamer bonds were determined via the location of the fluorescently labeled oligomers 2. Parts f and h of Figure 1 show the fluorescence intensity of the DNA-hybrids after contact with and without the presence of 2 mM ATP. The squarelike features correspond to the contacted area. It is qualitatively observed that without the presence of ATP a smaller fraction of fluorophores is transferred from the glass slide to the PDMS compared to the case when the spot is incubated with 2 mM ATP. This is in agreement with ATP stabilizing the aptamer bond and thus an increased probability that the reference bonds fail. Consequently, the fraction of retained oligomers 2 and thus fluorophores on the glass slide is reduced.

The breakage of the biotin·streptavidin bond may be neglected since it unbinds at significantly higher forces than short double-stranded DNA. However, unbinding forces strongly depend on the applied force loading rates. Since in our case the force loading rates were not recorded, they are estimated from single-molecule experiments. For the combination of an applied separation velocity of 1  $\mu\text{m/s}$ , a combined PEG linker of 10 000 g/mol and a 20 bp DNA duplex, a force-loading rate in the order of  $10^3$  pN/s is

typically obtained.<sup>33</sup> Under these conditions a 20 bp DNA duplex unbinds at around 40 pN,<sup>33</sup> whereas biotin·streptavidin unbinds at around 80 pN or even higher forces.<sup>34,35</sup>

**Quantitative Fluorescence Analysis.** Quantitative determination of the ratio between broken aptamer bonds and broken reference bonds requires a more complex analysis, since it cannot be assumed that all DNA-hybrids physically connect to both surfaces via the biotin·streptavidin bond. Uncoupled DNA-hybrids result in a background signal. In our experiments, we determined and subtracted the latter for each squarelike feature individually in order to calculate the normalized fluorescence (NF). The NF is defined as the ratio between broken 2·3 complexes and total amount of DNA-hybrids, to which a load was applied, and is determined as follows: Initially, when the 1·2·3 DNA-hybrids are immobilized on glass, a fluorescence image is taken (Figure 2, parts a and f). The DNA-hybrids are incubated with ATP (Figure 2b). The PDMS stamp is lowered toward the glass surface allowing the DNA-hybrids to couple to the PDMS via biotin·streptavidin complexation. In the presence of the ATP the PDMS is retracted (Figure 2c), and an increasing force is built up until one of the links breaks. Not all of the DNA-hybrids are coupled via the biotin·streptavidin bond. As illustrated in Figure 1d, the DNA-hybrids appear in three different states 1·2·3 (S0), 1·2 (S1),

(33) Morfill, J.; Kuhnner, F.; Blank, K.; Lugmaier, R.; Sedlmair, J.; Gaub, H. E. *Biophys. J.* **2007**, *93*, 2400–2409.

(34) Merkel, R.; Nassoy, P.; Leung, A.; Ritchie, K.; Evans, E. *Nature* **1999**, *397*, 50–53.

(35) Pincet, J. *Biophys. J.* **2005**, *89*, 4374–4381.

and **1** (S2) on the glass slide. For simplicity we refer to the amounts of S0, S1, and S2 as fractions normalized to all DNA-hybrids, i.e., the relation  $S0 + S1 + S2 = 1$  is always true. Only molecules in state S1 and S2 were exposed to an unbinding force. Molecules in the state S0 were not coupled to the PDMS surface and therefore retained the biotinylated oligomer **3**. From the Cy3 fluorescence intensity per unit area the fraction of S2 is determined (Figure 2, parts d and g, eq 3). In order to distinguish S0 and S1, the former is labeled with the spectrally distinct fluorescent marker streptavidin Alexa Fluor 647 (SAAF, Figure 2, parts e and h). The labeling is performed subsequent to the Cy3 readout in order to avoid quenching or fluorescence resonance energy transfer (FRET) effects. This allows us to determine the fractions of S0 and S1 from SAAF fluorescence (eqs 1 and 2).

$$S0 = \text{SAAF}_{\text{Ratio}} \quad (1)$$

$$S1 = \text{Cy3}_{\text{Ratio}} - \text{SAAF}_{\text{Ratio}} \quad (2)$$

$$S2 = 1 - \text{Cy3}_{\text{Ratio}} \quad (3)$$

$$\text{Cy3}_{\text{Ratio}} = \frac{\text{Cy3}_{\text{Result}}}{\text{Cy3}_{\text{Start}}} \quad (4a)$$

$$\text{SAAF}_{\text{Ratio}} = \frac{\text{SAAF}_{\text{Result}}}{\text{SAAF}_{\text{Start}}} \quad (4b)$$

For the analysis only the  $\text{Cy3}_{\text{Rem}}$  and  $\text{SAAF}_{\text{Rem}}$  fluorescence images are employed.  $\text{SAAF}_{\text{Start}}$  and  $\text{Cy3}_{\text{Start}}$  are determined from the noncontacted regions adjacent to each squarelike feature. The NF is given by the fraction of broken **2·3** bonds (S1) normalized to the fraction of bonds that have been under load (S1 + S2).

$$\text{NF} = \frac{S1}{S1 + S2} = \frac{\text{Cy3}_{\text{Ratio}} - \text{SAAF}_{\text{Ratio}}}{1 - \text{SAAF}_{\text{Ratio}}} \quad (5)$$

The NF directly reflects the relative unbinding forces, a physical quantity inherent to a pair of molecular complexes, and is not influenced by the number of molecules under load. The NF should not be confused with  $\text{Cy3}_{\text{Ratio}}$ . For a fixed mechanical stability, the latter depends on the fraction of coupled DNA-hybrids, whereas the NF does not. The NFs presented in this work are the averages of all squarelike features contacted properly within an experiment. The NF experimental error is estimated from repeated blank measurements yielding a standard deviation of 0.018.

**CUFA Detects the Concentration of Adenosine.** Varying concentrations of ATP (0–2000  $\mu\text{M}$ ) were applied to the different DNA-hybrid spots on one slide (Figure 3a). This way a whole concentration range was measured within a single experiment. Under physiological buffer conditions (15 mM sodium citrate, 150 mM NaCl, 1 mM  $\text{MgCl}_2$ , pH 7.4), the **1·2·3** sensor reliably reported the presence of its target. At zero concentration the normalized fluorescence was  $0.792 \pm 0.018$ . Upon addition of micromolar concentrations of ATP, the normalized fluorescence decreased and reached its minimum of  $0.683 \pm 0.018$  at 0.5 mM as shown in Figure 3b. This is in agreement with a stabilizing effect of ATP on the aptamer structure. Fitting the ATP titration data to the Hill equation with slope  $n = 2$  revealed a half-

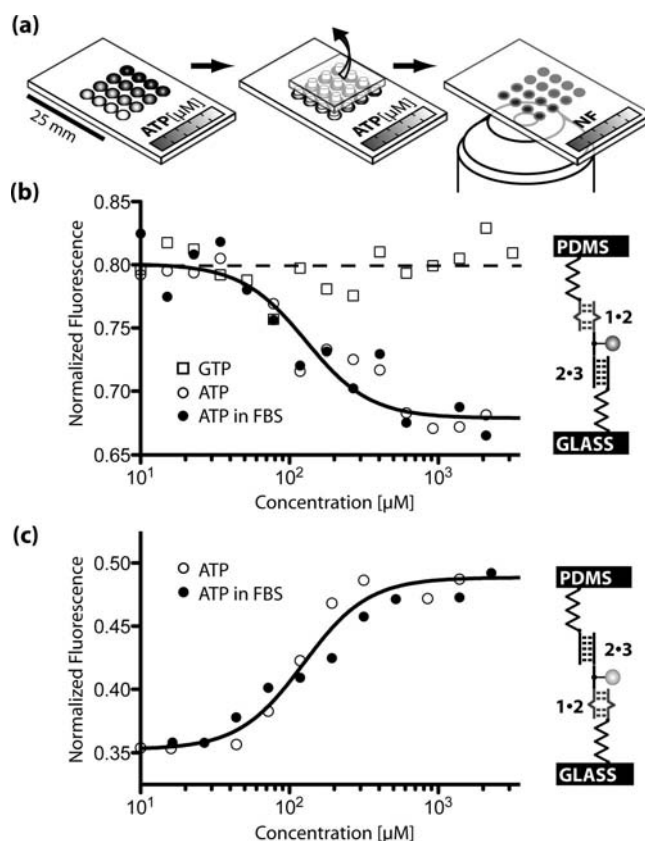


**Figure 3.** (a) Self-made microfluidic device allows incubation of 16 identical DNA-hybrid spots with different concentrations of ATP on a single chip. In the presence of ATP, the chip is contacted with a 16 pillar PDMS contact device and read out via fluorescence. (b) Normalized fluorescence for increasing concentrations of ATP and GTP in the regular configuration **1·2·3**. The solid line is the corresponding fit to the Hill equation. (c) Upside-down configuration **3·2·1**.

maximal effective concentration  $\text{EC}_{50} = 124.8 \mu\text{M}$  with a 95% confidence interval of  $[102.8 \mu\text{M}, 151.4 \mu\text{M}]$ . Huizenga and Szostak demonstrated that the equilibrium dissociation constant of the adenosine–aptamer interaction depends upon the specific salt and  $\text{Mg}^{2+}$  concentrations.<sup>24</sup> For the present buffer conditions, the experimentally obtained  $\text{EC}_{50}$  value is in agreement with previously published values of the equilibrium dissociation constant.<sup>24–28</sup>

In order to ensure that the molecular setup responds as expected, we investigated, analogously to the regular configuration **1·2·3**, the upside-down configuration **3·2·1**. Here, the position of the target and reference bond is exchanged, and thus the response to the addition of adenosine should be inverted. Indeed, the NF increased from  $0.353 \pm 0.018$  to a maximal NF of  $0.489 \pm 0.018$  upon increasing the ATP concentration from 0 to 0.5 mM (Figure 3c). The aptamer bond is now adjacent to the glass slide. Upon binding of the target molecule, the aptamer is less likely to break and a larger fraction of fluorophores remains on the glass slide.

**Sensitivity.** The sensitivity of our assay is estimated from the signal-to-noise ratio. For ATP concentrations below  $53.5 \mu\text{M}$  the latter is lower than 1, and thus ATP is not detectable. From  $53.5$

(27) Stojanovic, M. N.; de Prada, P.; Landry, D. W. *J. Am. Chem. Soc.* **2001**, *123*, 4928–4931.

to 310.3  $\mu\text{M}$ , ATP is quantified via the change in normalized fluorescence. At higher ATP concentrations the change in normalized fluorescence saturates, and thus ATP is detected; however, it cannot be quantified. This is comparable to fluorescent sensors based on aptamer assembly<sup>26</sup> or folding.<sup>27,28</sup> In recent publications, several groups demonstrated the use of structure-switching aptamer sensors in combination with signal amplification techniques using gold nanoparticles. For these assays larger ranges of sensitivity were reported.<sup>5,6</sup>

**Selectivity.** To demonstrate the selectivity of our force-based assay, separate experiments were conducted on GTP (Roche GmbH, Grenzach, Germany) and AMP (Roche GmbH, Grenzach, Germany). Since the aptamer recognizes adenosine, the addition of AMP resulted in a similar response like ATP (Supporting Information Figure S1). Conversely GTP, where the adenosine base is exchanged with a guanosine base, produced no detectable response (Figure 3c). The results demonstrated that the developed strategy has sufficient selectivity to detect the interaction between adenosine and the antiadenosine aptamers immobilized on the chip surface.

**Detection of Adenosine in Molecular Crowded Environment.** The experiments presented above were performed in pure  $1\times$  SSC buffer. However, because of the force-based design, the experimental result should only be susceptible to molecules interacting directly with the aptamer structure. In order to demonstrate this, we repeated the ATP experiments in  $1\times$  SSC buffer and 10% fetal bovine serum (FBS, Sigma-Aldrich, Germany). While the force comparison was carried out in the presence of the ligand and a molecular crowded solution, the readout of the result occurred subsequently and is therefore insensitive to additional washing steps, as long as these do not dissociate the DNA-hybrids. As shown in Figure 3, parts b and c, the same response is observed in the presence of FBS as for the FBS-free measurements.

## CONCLUSIONS

In the present study, we employed the CUFA as a label-free aptamer-based capture biochip. The design relies on an increased stability of bipartite aptamers upon binding of its target molecules. The assay reliably reported the presence of adenosine for concentrations above 53.5  $\mu\text{M}$  and allowed quantitative detection of adenosine for concentrations between 53.5 and 310.3  $\mu\text{M}$ . The

Hill equation governs the response of the assay with an  $\text{EC}_{50} = 124.8 \mu\text{M}$  agreeing well with literature values for the equilibrium dissociation constant of the antiadenosine aptamer.

The limited sensitivity range and the dependence of the equilibrium constant (and thus of the assay response) upon specific salt and  $\text{Mg}^{2+}$  concentrations renders quantitative detection of adenosine impracticable. Ionic concentrations of real samples are hardly ever known, and adenosine detection assays with superior sensitivity ranges are available. The strength of the assay lies within the fast and reliable characterization of the equilibrium dissociation constant of the interaction between a small molecule and a low-affinity aptamer. This was demonstrated in pure SSC buffer as well as in a molecular crowded solution. Producing reliable equilibrium binding data within the micromolar regime still poses a challenge for existing high-throughput techniques.<sup>36</sup> Conversely, implementing aptamers of higher affinity can yield more sensitive sensors for their cognate molecules. Due to the label-free, microarray-compatible design, it is easily imaginable to test the presence of various analytes in parallel—basically only limited by the number of available aptamer structures. Detection of proteins and peptides, simultaneous detection of multiple analytes, and miniaturization will be reported elsewhere.

## ACKNOWLEDGMENT

We thank P. Tinnefeld, F. Weinert, P. Baaske, S. Duhr, U. Steinbach, F. Dehmelt, J. Vogelsang, S. Kufer, and C. Albrecht for helpful discussions. Support was provided by the Nanosystem Initiative Munich and the Deutsche Forschungsgemeinschaft. D.H. and P.S. are grateful to the Elite Network of Bavaria (IDK-NBT) for a doctoral fellowship. K.F. is grateful for a Max-Weber fellowship.

## SUPPORTING INFORMATION AVAILABLE

Additional information as noted in text. This material is available free of charge via the Internet at <http://pubs.acs.org>.

Received for review December 31, 2008. Accepted February 24, 2009.

AC802766J

(36) Titz, B.; Schlesner, M.; Uetz, P. *Expert Rev. Proteomics* **2004**, *1*, 111–121.

# Supporting Information

## DNA as a force sensor

### in an aptamer-based biochip for adenosine

*Dominik Ho, Katja Falter, Philip Severin and Hermann E. Gaub\**

Lehrstuhl für Angewandte Physik and Center for Nanoscience (CeNS), Ludwig-Maximilians-Universität, Amalienstrasse 54, 80799 Munich, Germany

Munich Center For Integrated Protein Science (CIPSM), Ludwig-Maximilians-Universität, Butenandtstrasse 5-13, 81377 Munich, Germany

[gaub@physik.lmu.de](mailto:gaub@physik.lmu.de)

#### **CONTENTS**

Experiments with AMP (S2)

## Experiments with AMP

Additional to the experiments with ATP, we conducted experiments on the **1•2•3** molecular setup in presence and absence of 2 mM AMP. Within the experimental error, the change in normalized fluorescence was identical compared to the addition of 2 mM ATP. Explicitly, the normalized fluorescence was  $0.80 \pm 0.018$  for the 0 mM case and  $0.67 \pm 0.018$  for the 2 mM case.

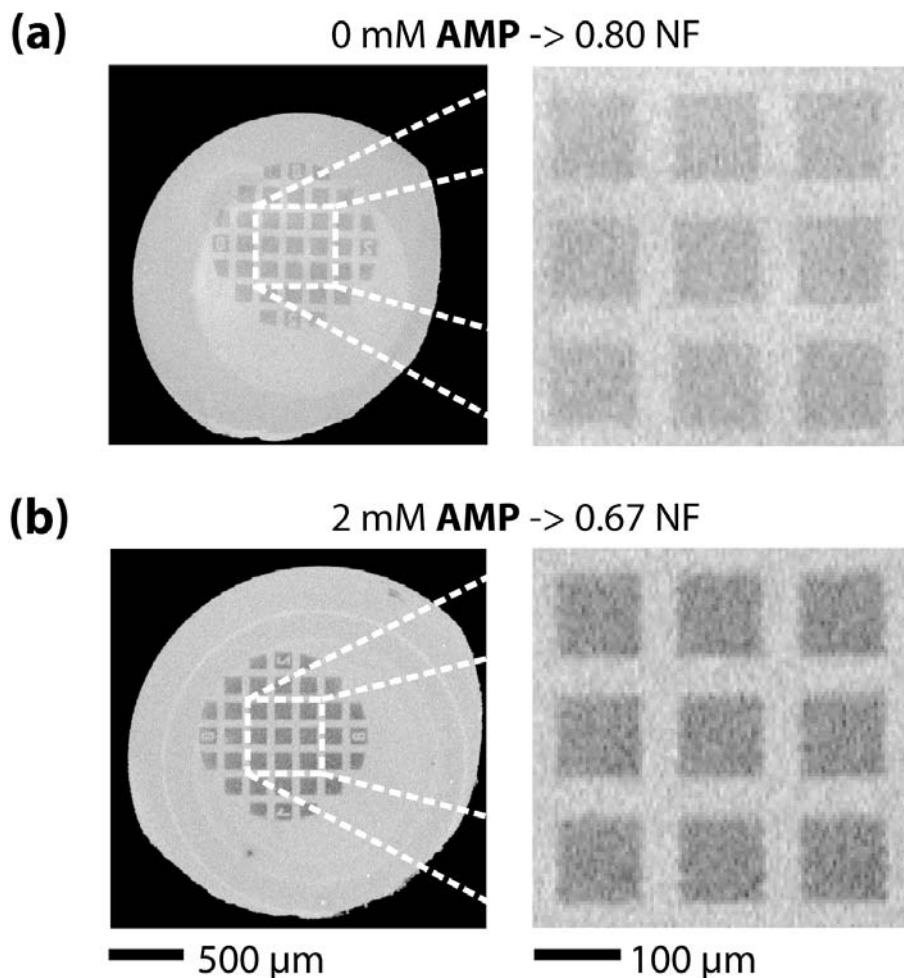


**Figure S1.** (a) Fluorescence on glass after contact without prior incubation with AMP. The square-like features ( $100 \times 100 \mu\text{m}^2$ ) correspond to the area contacted with microstructured PDMS. (b) Fluorescence on glass after contact with prior incubation with 2 mM AMP. Compared to the 0 mM AMP case, a larger fraction of fluorescence was transferred from the glass to the PDMS.



## Force-Driven Separation of Short Double-Stranded DNA

Dominik Ho,<sup>†\*</sup> Julia L. Zimmermann,<sup>†</sup> Florian A. Dehmelt,<sup>†</sup> Uta Steinbach,<sup>†</sup> Matthias Erdmann,<sup>†</sup> Philip Severin,<sup>†</sup> Katja Falter,<sup>†</sup> and Hermann E. Gaub<sup>†</sup>

<sup>†</sup>Lehrstuhl für Angewandte Physik and Center for Nanoscience, Ludwig-Maximilians-Universität, Munich, Germany; and <sup>\*</sup>Munich Center For Integrated Protein Science (CIPSM), Ludwig-Maximilians-Universität, Munich, Germany

**ABSTRACT** Short double-stranded DNA is used in a variety of nanotechnological applications, and for many of them, it is important to know for which forces and which force loading rates the DNA duplex remains stable. In this work, we develop a theoretical model that describes the force-dependent dissociation rate for DNA duplexes tens of basepairs long under tension along their axes (“shear geometry”). Explicitly, we set up a three-state equilibrium model and apply the canonical transition state theory to calculate the kinetic rates for strand unpairing and the rupture-force distribution as a function of the separation velocity of the end-to-end distance. Theory is in excellent agreement with actual single-molecule force spectroscopy results and even allows for the prediction of the rupture-force distribution for a given DNA duplex sequence and separation velocity. We further show that for describing double-stranded DNA separation kinetics, our model is a significant refinement of the conventionally used Bell-Evans model.

### INTRODUCTION

Double-stranded DNA (dsDNA) is an extensively studied polymer offering a number of striking properties. Among these properties are interstrand recognition according to the Watson-Crick basepairing rules, stability under a broad range of conditions, and ease of synthesis that allows for fast and cost-efficient production of any desired sequence with almost any kind of chemical modification. Within the past several years, various areas of application of DNA have been identified, and nanotechnology, specifically, is increasingly harnessing the potential of this versatile polymer (1). Whereas in earlier published work DNA merely served as simple molecular handles for single-molecule experiments (2,3), today DNA serves as molecular building blocks for complex self-assembled nanostructures (4–7), as well as DNA computing (8). In our laboratory, DNA was even used as a programmable force sensor for detection of single-nucleotide polymorphisms (9), multiplexed antibody sandwich assays (10,11), investigation of chiral preference of small DNA-binding molecules (12), quantitative detection of DNA-binding molecules (13), and aptamer sensors (14). Recently, our laboratory applied this DNA force sensor concept to “single-molecule cut and paste” experiments (15) for the bottom-up assembly of nanoparticles (16) and for single-molecule fluorescence applications (17). For many of the abovementioned applications, it is insightful, if not critical, to know what forces a given DNA duplex may withstand. In particular, such knowledge would make it possible not only to predict, tune, and analyze DNA force sensor experiments, but also to design more stable DNA scaffolds.

The elastic response and force-dependent dissociation rate of DNA duplexes has been extensively studied in microma-

nipulation experiments employing atomic force microscopy (AFM) (18,19), magnetic beads (20), glass microneedles (21), and optical tweezers (22,23). Here, we discuss the stretching of dsDNA along its axis (“shear geometry”) only in contrast to the gradual unzipping of DNA perpendicular to its axis (“unzip geometry”). Stretching a DNA duplex with thousands of basepairs along its axis results in an elastic response with a distinct force plateau at 60–65 pN (18,21,22). During this elongation at almost constant force, the DNA molecule stretches up to a factor of 1.7 of its contour length. This behavior is highly reproducible, independent of the stretching velocity, and commonly attributed to a highly cooperative conversion from regular B-DNA into an overstretched conformation called S-DNA (24–27). On the contrary, Rouzina and Bloomfield (28), as well as Piana (29), argue that S-DNA is not a distinct conformation of the polymer, but simply the melting of the dsDNA into two single strands. However, not only does the B-S transition appear to be too cooperative for a common melting process, but it has been shown also that dsDNA remains stable at forces significantly higher than 65 pN (30), with an elastic response distinct from one single-stranded DNA (ssDNA) polymer or two parallel ssDNA polymers (24). Further support for S-DNA being a distinct conformation is provided by the experimental observation of a second transition in the range 150–200 pN, which is thought to be the final melting transition (18,24) instead of the B-S transition. Based on the assumption that S-DNA is in fact a distinct conformation, several recent theoretical studies have modeled the elongation of DNA duplexes applying three-state (B-DNA, S-DNA, and ssDNA) equilibrium approaches (24,25). These studies concluded that S-DNA is the thermodynamically preferred and stable state for forces between 65 and 130 pN.

Individual basepairing interactions are relatively weak (free energy  $\sim 1\text{--}3 k_B T$ ), and thermal fluctuations cause opening (“breathing”) of the DNA duplex from its ends,

Submitted July 3, 2009, and accepted for publication September 21, 2009.

\*Correspondence: dominik.ho@web.de

Julia L. Zimmermann’s present address is Max-Planck-Institut für extraterrestrische Physik, Giessenbachstrasse, 85748 Garching, Germany.

Editor: David P. Millar.

© 2009 by the Biophysical Society  
0006-3495/09/12/3158/10 \$2.00

doi: 10.1016/j.bpj.2009.09.040

as well as the formation of bubbles, which are regions of ssDNA (opened basepairs) between regions of dsDNA. The shorter the DNA duplex, the more likely it is that all basepairs open up for an instant and the two strands separate even at forces well below 130 pN. For DNA duplexes tens of basepairs long, Strunz and colleagues (31) and Morfill and colleagues (32) observed strand separation at forces as low as 40–70 pN. Repeated measurements resulted in rupture-force distributions that were shifted to higher forces for higher separation velocities. From a theoretical point of view, this can be described as a thermally driven escape process from a free-energy potential and has typically been discussed within the framework of the Bell-Evans model. Herein, the trapping potential is assumed to be a one-dimensional harmonic free-energy potential, and strand separation is treated as the crossing of an energy barrier according to a time dependence similar to that described by the Arrhenius law (31–35). Application of a force tilts the energy landscape, reduces the energy barrier proportional to the applied force, and therefore increases the dissociation rate of the DNA duplex. According to the experimental data, the model predicts higher rupture forces for higher separation velocities (33). Although the experiments are explained quite well by the Bell-Evans model, that model does not allow for the prediction of rupture forces for a given DNA duplex sequence and separation velocity. Apart from the Bell-Evans theory, molecular dynamics simulations, employing force fields and initial molecular structures, provided insight into the DNA separation process. Unfortunately, these simulations cost a significant amount of computation time, such that the timescales accessible for *in silico* experiments are much shorter than what is experimentally observable (26, 27). Therefore, it is apparent that a theory is needed to fill the gap between the Bell-Evans model, which is too simplistic, and the detailed molecular dynamics simulations, with which mechanics can currently be simulated on very short timescales only.

In this work, we develop a model that describes and predicts the DNA duplex rupture forces for any given sequence and experimentally accessible pulling velocities. To be specific, we derive the dissociation rate as a function of the applied force based on a combination of recent work on DNA equilibrium theory and the canonical transition state theory. On this basis, we calculate the force-extension traces and the rupture-force distribution for a 20- and a 30-basepair-long DNA duplex and compare the obtained results to actual single-molecule experimental data (Fig 1 *a* and *b*). Further, we are able to show that for the description of double stranded DNA separation kinetics, our model is a significant refinement of the conventionally used Bell-Evans model.

## RESULTS AND DISCUSSION

The result of this work is a theoretical model that predicts the rupture force of dsDNA tens of basepairs long as it is applied

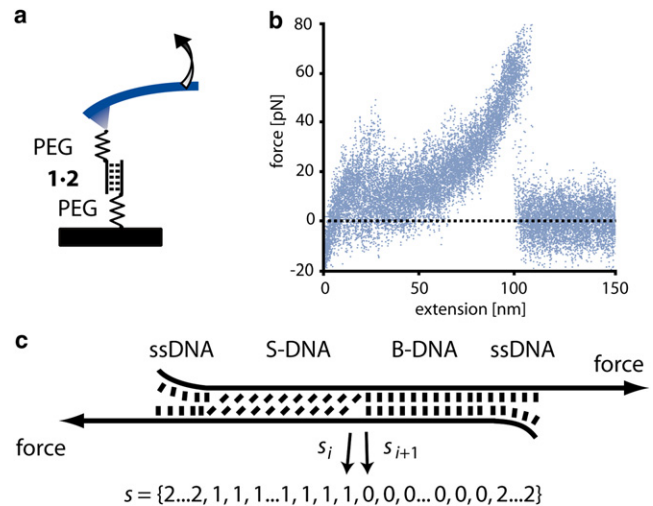


**FIGURE 1** (*a*) Schematic of a single-molecule DNA stretching experiment. The 5' ends of a short, double-stranded DNA duplex are attached to a surface and an atomic force microscope cantilever via elastic poly(ethylene glycol) (PEG) polymers. Separation of the substrate and the cantilever at constant velocity leads to an increasing end-to-end distance and thus to an increasing force. (*b*) Superposition of 20 experimentally obtained force-extension traces obtained from the same 30-basepair  $1 \times 2$  DNA duplex with a separation velocity of  $1 \mu\text{m/s}$ . The duplex dissociates at  $\sim 60$ – $65$  pN. (*c*) Schematic of the three-state model. Every basepair of the DNA duplex appears in one of three states: B-DNA, S-DNA, or single-stranded DNA. Every state  $s$  of an  $N$ -basepair-long DNA may thus be represented by a list of length  $N$  with entries 0 (B-DNA), 1 (S-DNA), and 2 (ssDNA) for every basepair.

in a DNA force sensor, in DNA nanostructure, and in DNA computing applications. For this purpose, we first set up a three-state equilibrium model similar to a model used previously to describe the force-extension traces of long dsDNA (24). Second, we apply the canonical transition state theory to this equilibrium model, which in turn permits calculation of the rate of duplex dissociation at a given force  $f$ . Theoretical results are compared to actual AFM experiments on the 20-basepair ( $1 \times 2$ ) and the 30-basepair ( $1 \times 3$ ) duplex. Details about DNA oligomers 1–3, as well as about the experimental procedures, are provided in the [Supporting Material](#).

### Equilibrium theory

Analogous to the Bragg-Zimm theory (36) and a variety of work published recently on the force-induced opening of dsDNA in unzip geometry (37–39,40) and shear geometry (28), as well as the opening of coiled coils (41,42), we calculate the equilibrium free energy of DNA duplexes: The DNA duplex is described as a one-dimensional polymer for which every basepair  $i$  is considered to be present in one of three discrete states, namely, regular B-DNA ( $s_i = 0$ ), over-stretched S-DNA ( $s_i = 1$ ), and single-stranded DNA ( $s_i = 2$ ) conformations. Thus, any configuration  $s$  of an  $N$ -basepair DNA duplex is represented by an  $N$ -tuple,

$$s = (s_1, s_2, \dots, s_N), \quad (1)$$

where the  $i$ th entry represents the state of the  $i$ th basepair, counting from the 5' to the 3' end.

Two contributions to the free energy/basepair are taken into account:  $w$ , the elastic free energy/basepair at a given force  $f$ , and  $j$ , the basepairing free energy we derive from a nearest-neighbor model and assume to be independent of the applied force. The free energy of the  $i$ th basepair can be determined by

$$g_{s_i, s_{i+1}}(f) = w_{s_i, s_{i+1}}(f) + j_{s_i, s_{i+1}}. \quad (2)$$

These two energy contributions yield the total free energy,  $G_{\text{total}}(s, f)$ , for any possible configuration  $s$  at any force  $f$ ,

$$G_{\text{total}}(s, f) = \sum_{i=1}^{N-1} g_{s_i, s_{i+1}}(f) + w_{s_N}(f), \quad (3)$$

where the term  $w_{s_N}(f)$  corresponds to the  $N$ th basepair, which does not have a next neighbor it can interact with such that  $j_{s_N, s_{N+1}} = 0$ .

#### Elastic energy

The free energies due to the elastic deformation of the three different DNA conformations are obtained by simply integrating their extensions with respect to the force:

$$w(f) = - \int_0^f x(f') df'. \quad (4)$$

Phenomenological polymer extension models reproduce the force-extension traces well (see Fig. 2 *a*). In the [Supporting Material](#), we derive the elastic free energy/basepair from such polymer extension models for B-DNA ( $w_B$ ), S-DNA ( $w_S$ ), and ssDNA ( $w_{ss}$ ) explicitly. Assuming an average basepairing energy of  $2.4 k_B T$ , as is the case for the  $1 \times 2$  and  $1 \times 3$  DNA duplexes (Fig. 2 *b*), which DNA configuration is most favorable for forces between 0 and 200 pN? B-DNA remains thermodynamically stable for forces  $< 60$  pN. S-DNA is stable between 60 and  $\sim 130$  pN and ssDNA is the energetically most favorable state at forces  $> 130$  pN. Since we employ a nearest-neighbor model to calculate the partition sum of the system, it is convenient to represent the free energy due to the elastic behavior of DNA in a  $3 \times 3$  matrix form,

$$w_{s_i, s_{i+1}}(f) = \begin{bmatrix} w_B(f) & w_B(f) & w_B(f) \\ w_S(f) & w_S(f) & w_S(f) \\ w_{ss}(f) & w_{ss}(f) & w_{ss}(f) \end{bmatrix}, \quad (5)$$

where the rows correspond to the state of basepair  $i$  and the columns to the state of basepair  $i + 1$ . Thus, in our model, the elastic free energy of basepair  $i$  is independent of the state of basepair  $i + 1$ .

#### Interaction free energy

It has been observed in experiments that the stability of a given basepair depends not only on whether the basepair

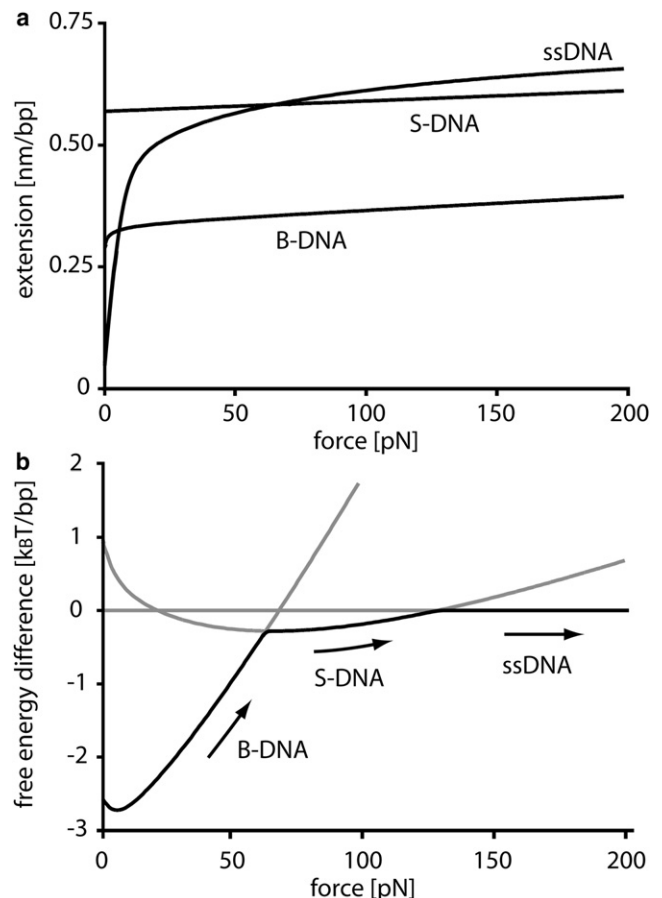


FIGURE 2 (a) Force-extension traces obtained from phenomenological models for the three different states of double-stranded DNA. (b) Corresponding free-energy difference/basepair between B-DNA and ssDNA as well as between S-DNA and ssDNA. A free-energy penalty of  $2.4 k_B T$ , the average basepair free energy of the  $1 \times 2$  and  $1 \times 3$  DNA duplexes, is introduced to the free energy of ssDNA due to the loss of basepairing interactions. Highlighted in black is the state that is thermodynamically most favorable. The most favorable state is B-DNA for forces  $< 60$  pN, S-DNA for forces between 60 pN and 130 pN, and ssDNA for forces  $> 130$  pN.

itself is A·T or G·C, but also on the identity and orientation of adjacent basepairs, presumably due to the differences in free energy for the different possible stacking interactions (43). In our model, we employ the nearest-neighbor model of SantaLucia, which takes these experimental observations into account (44). The stacking free energy between each basepair  $i$  and  $i + 1$  is given by the constant  $J_i$  in case both are either B-DNA or S-DNA. Although the stacking free energies for B-DNA and S-DNA are independent parameters, for simplicity, we assume them to be identical.

In addition, the boundaries between regions of different states are associated with energy penalties.  $C_{B-S}$  is the energy cost associated with a boundary between B-DNA and S-DNA regions. Cluzel and colleagues estimated the B-S boundary energy from the cooperativity of the B-S transition to be close to  $3.4 k_B T$  (21). Unlike the non-nearest-neighbor models for which the latter value was derived, for

our nearest-neighbor model, the total energy penalty is given by  $C_{B-S}$  along with the loss of one additional base-stacking interaction. The average energy lost in base-stacking interaction is  $2.4 k_B T$  for the  $1 \times 2$  as well as the  $1 \times 3$  duplex, which is why we set  $C_{B-S}$  to  $2.2 k_B T$  (half a base-stacking interaction free energy subtracted from each boundary).

Furthermore, the boundaries between double-stranded and between single-stranded regions of DNA are associated with the free-energy cost,  $C_{ds-ss}$ . According to SantaLucia (44) this value is close to  $1 k_B T$ . For any given state  $s$ , there are always two boundaries at each side of the dsDNA region and, therefore, the parameter  $C_{ds-ss}$  has an impact only on the likelihood of bubbles. Within polymer theory, the latter are commonly referred to as loops. Since bubbles come along with additional degrees of freedom, polymer theory predicts an entropic energy contribution proportional to the logarithm of the bubble size, which favors the creation of bubbles:

$$Z(f) = \sum_s P(s, f) = \sum_s \exp(-G_{\text{total}}(s, f)) = \sum_s \prod_{i=1}^N \exp(-g_{s_i, s_{i+1}}(f))$$

$$= \sum_{\text{all matrix elements}} \prod_{i=1}^N \begin{bmatrix} \exp(-w_B(f) + J_i) & \exp(-w_B(f) - C_{B-S}) & \exp(-w_B(f) - C_{ds-ss}) \\ \exp(-w_S(f) - C_{B-S}) & \exp(-w_S(f) + J_i) & \exp(-w_S(f) - C_{ds-ss}) \\ \exp(-w_{ss}(f) - C_{ds-ss}) & \exp(-w_{ss}(f) - C_{ds-ss}) & \exp(-w_{ss}(f)) \end{bmatrix}. \quad (8)$$

$$\Delta G_{\text{loop}}(n_{\text{loop}}) = k_B T \ln n_{\text{loop}}^{-c}, \quad (6)$$

where  $n_{\text{loop}}$  is the number of opened basepairs within the bubble and  $c$  is the loop exponent. The value of the loop exponent is  $c = 3/2$  for an ideal loop and  $c = 2.1$  for a self-avoiding loop (45). The exact value of  $c$  for dsDNA is still under debate. Recent theoretical calculations by Einert and colleagues imply that data for long dsDNA is best fit by setting  $c = 0$ , which may be explained by the fact that DNA contains a significant numbers of nicks. Such a long-range interaction cannot be implemented into our nearest-neighbor model. Therefore, we simply chose the parameter such that theory agreed best with actual experiments and estimated a value of  $-0.25 k_B T$  for  $C_{ds-ss}$ , corresponding to an average bubble size of 4 basepairs. Note that the theoretical predictions (46–48) regarding longer-range entropic contribution to partially melted DNA are in agreement with experimental data obtained by Altan and colleagues (49). Based on Förster energy transfer measurements on tracts of A·T basepairs, they argue that initiating a bubble requires a free energy much larger than  $k_B T$ , whereas extending this bubble requires only free energies in the range  $0.05$ – $1.0 k_B T$ /basepair.

In matrix form, the interaction free-energy contributions based on the SantaLucia nearest-neighbor model and the boundary free-energy penalties are

$$j_{s_i, s_{i+1}} = \begin{bmatrix} -J_i & C_{B-S} & C_{ds-ss} \\ C_{B-S} & -J_i & C_{ds-ss} \\ C_{ds-ss} & C_{ds-ss} & 0 \end{bmatrix}, \quad (7)$$

where the rows correspond to the state of basepair  $i$  and the columns to the state of basepair  $i + 1$ . Thus, if basepair  $i$  and basepair  $i + 1$  are B-DNA then an energy gain of  $J_i$  is introduced to the base-stacking interaction. The same is true for two adjacent S-DNA basepairs. Boundaries between basepairs are associated with an energy penalty  $C_{B-S}$  or  $C_{ds-ss}$ , where  $C_{B-S}$  is  $3.4 k_B T$  and  $C_{ds-ss}$  is  $-0.25 k_B T$ , as discussed above.

### Partition sum

From the total free energy,  $G_{\text{total}}$  (Eqs. 2 and 3), of each possible state  $s$ , we calculate the partition sum, which in turn allows for determination of the force-extension trace and the likelihood of the states  $s$ .

Thus, the partition sum may be considered as the sum over all matrix elements of the product of  $N$   $3 \times 3$  matrices (50). Thereby, the  $i$ th matrix of the  $N$  matrices represents the  $i$ th basepair containing nine entries. Each entry represents the Boltzmann factor of one of the nine possible combinations of states that basepair  $i$  and basepair  $i + 1$  may adopt. We make two corrections to Eq. 8, which we explain in more detail in the [Supporting Material](#). First, we introduce two additional basepairs at  $i = 0$  and  $i = N + 1$ , which are single-stranded. This takes care of the boundary conditions at the end of the DNA duplex. Second, we do not count the states for which two or fewer basepairs remain. These states, as we discuss in more detail in the next section, correspond to already separated strands.

### Stretching curves

From the partition sum of our model, we derive the force-extension trace for a given sequence and compare it to experimentally obtained data. The equilibrium force-extension trace follows directly from the derivative of the partition sum with respect to the force (51):

$$x_{\text{DNA duplex}}(f) = k_B T \frac{\partial \ln Z(f)}{\partial f}. \quad (9)$$

The AFM experiments were prepared according to the Materials and Methods section (see [Supporting Material](#)) and are

schematically shown in Fig. 1 *a*. The two complementary single strands 1 and 2 were coupled to the cantilever tip and a substrate via long poly(ethylene glycol) linkers (5 kDa). In a typical experiment, the tip is brought into contact with the glass slide, and the two complementary strands hybridize and form the  $1 \times 2$  duplex. Upon retraction at constant velocity, the PEG spacer and dsDNA elongates, building up an increasing force until the duplex dissociates. Fig. 3 shows an average of 20 force-extension curves. Experimentally, one measures the elasticity of a chain of four elements: the dsDNA duplex, the PEG linker, the ssDNA linker, and the cantilever. The force-extension trace is a superposition of the extension profile of all four of them:

$$x(f) = x_{\text{DNA duplex}}(f) + x_{\text{DNA linker}}(f) + x_{\text{PEG linker}}(f) + x_{\text{cantilever}}(f), \quad (10)$$

where  $x_{\text{DNA duplex}}$  is specified by Eq. 9 and  $x_{\text{cantilever}}$  is the deflection of the cantilever, which is proportional to the cantilever stiffness,  $k_{\text{cantilever}} = 8 \text{ pN/nm}$ . The polymer models from which  $x_{\text{DNA linker}}$  and  $x_{\text{PEG linker}}$  are derived are described in the Supporting Material. We used the number of monomers within the PEG polymer,  $N_{\text{PEG}}$ , as a fitting parameter, since PEG polymers are typically synthesized with a rather broad size distribution (32). Fitting of the whole system resulted in a monomer number of 255, which agrees well with the expected monomer number of 227 for a total PEG linker with a molecular mass of 10 kDa.

Fig. 3 shows that the theory fits the experimental data very well for forces  $>30 \text{ pN}$ . However, for lower forces, the theo-

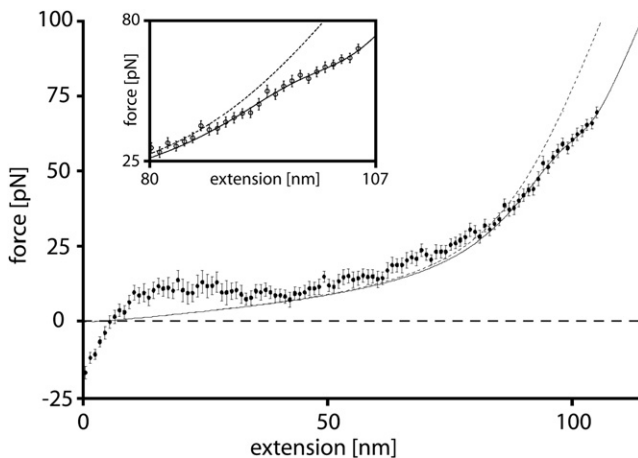


FIGURE 3 Force-extension data of short, double-stranded DNA attached to a surface and an atomic force microscope cantilever via a 5-kDa poly(ethylene glycol) linker for each strand. Data for 20 pulling experiments at a separation velocity of  $1 \mu\text{m/s}$  was binned into 1-pN intervals and averaged (circles). The solid line is the corresponding fit of the model presented here. The dashed line represents the fit in the case where the DNA duplex remains in its canonical B-form. At  $<30 \text{ pN}$ , the fit underestimates forces, an observation that we attribute to nonspecific interactions and entanglements with neighboring constructs on the surface. (Inset) For forces  $>30 \text{ pN}$ , theory and experimental data agree within the experimental error.

retical fit underestimates the experimentally obtained forces. The 10- to 15-pN plateau between 10 and 20 nm extension at the beginning of the stretching curve is typical for a DNA desorption process from a surface (52). For higher extensions, we attribute this discrepancy between theory and experiment to nonspecific interactions and entanglement of the strands with each other on the surface. This is entirely possible, since the contour length of the surface-anchored DNA strands is  $>50 \text{ nm}$  and the spacing between two of these strands is typically  $\sim 10 \text{ nm}$  (12,15,16).

## Canonical transition state theory

For an average basepairing free energy of  $2.4 k_{\text{B}}T$ , dsDNA is thermodynamically stable for forces  $<130 \text{ pN}$  (18,24,25). Still, Strunz and colleagues (31) and Morfill and colleagues (32) observed bond breakage at forces between 40 and 70 pN for 20- and 30-basepair dsDNA. They attributed this effect to thermal fluctuations like the opening or “breathing” of dsDNA from its ends, and to the formation of bubbles, which are regions of ssDNA between regions of dsDNA. Some of these fluctuations are so large that the whole duplex opens and the two strands separate.

Such a thermally activated escape process can be described by canonical transition state theory (53,54). This theory is purely classical and based on two assumptions: 1), the bond is trapped in a free-energy potential and thermodynamic equilibrium prevails; and 2), once the system has crossed a dividing surface in state space, i.e., the transition state, it will not return to the metastable state. The rate of escape follows directly from the flux through this dividing surface.

In the next paragraphs, we first define the dividing surface, i.e., the transition states, for the dsDNA equilibrium model described in the previous section. We then calculate the equilibrium flux through this dividing surface and thus obtain the rate of escape. We explicitly calculate the rupture-force distributions for the two DNA duplexes  $1 \times 2$  and  $1 \times 3$  and compare them to experimental data. At the end of this section, we discuss why the canonical transition state theory is an appropriate description of our system.

### Transition states

In the case of an  $N$ -basepair-long DNA duplex, the free-energy potential is  $N$ -dimensional and the corresponding coordinate is the state  $s$ . A dividing surface between the reactants (dsDNA) and the products (ssDNA) has to be chosen such that once the system has crossed this surface, the chances of recrossing are negligible. In our system, this dividing surface is spanned by the states  $s_{\text{1st}}$ , for which there is exactly one base-stacking interaction left. One base-stacking interaction corresponds to two adjacent B-DNA or S-DNA basepairs. Therefore, there are  $2(N - 1)$  distinct states through which the reaction may occur. For illustrative purposes we can collapse the free-energy landscape onto one coordinate:  $n$ , the number of remaining basepairs. Within this picture

(Fig. S1 in the Supporting Material), we identify the transition state as  $n_{\text{tst}} = 2$ . If another basepair opens up, the two DNA strands dissociate, i.e., the polymers will immediately reduce their end-to-end distance and reannealing of the two strands is literally impossible.

#### Equilibrium flux

The rate of escape is given by the equilibrium flux through the transition states,  $s_{\text{tst}}$ , in the direction of the product (two separate strands). The flux is essentially twice the basepair opening rate (either one of the two remaining basepairs may open), which, for simplicity, we assume to be the same for all  $s_{\text{tst}}$ . This allows us to use the collapsed free-energy landscape with only one reaction coordinate,  $n$ , the number of remaining basepairs. The equilibrium flux through the transition states,  $s_{\text{tst}}$ , becomes the probability that the system will be in the collapsed transition state,  $n_{\text{tst}}$ , multiplied by  $.n_+$ , twice the basepair opening rate. The result for the rate of escape at a given force  $f$  is

$$\begin{aligned} k(f) &= \langle \delta[n - n_{\text{tst}}]n_+ \rangle_{\text{equilibrium}} \\ &= \frac{1}{Z(f)} \sum_{s_{\text{tst}}} n_+ \exp(-\Delta G_{\text{totla}}(s_{\text{tst}}, f)). \end{aligned} \quad (11)$$

The calculations are shown explicitly in the Supporting Material. To our knowledge, the basepair opening rate of a single basepair-stacking interaction has never been determined experimentally. From the literature, we estimate the basepair opening rate at the ends of dsDNA to be between  $10^3 \text{ s}^{-1}$  and  $10^9 \text{ s}^{-1}$ : Bockelmann and colleagues performed optical tweezers measurements from which we estimate an opening rate of at least  $10^3 \text{ s}^{-1}$  (55). Fluorescence measurements investigating the end fraying of the dsDNA could not resolve any basepair opening rates on timescales  $<10^9 \text{ s}^{-1}$  (56). In their report discussing the unzipping of DNA, Cocco and colleagues assumed a value of  $10^8 \text{ s}^{-1}$  (24), and nuclear magnetic resonance amino proton exchange studies yielded rates in the order of  $10^7 \text{ s}^{-1}$  (57). For a basepair opening rate of  $.n_+ = 5 \times 10^8 \text{ s}^{-1}$  our theory agrees very well with the experimentally determined rupture forces (32). Note that the rate depends on the applied force, but since the force dependence is rather weak (40), we assume the rate to be constant. In principle, all calculations could also be performed with force- and sequence-dependent rates.

#### Rupture forces

Based on the canonical transition state theory, we derive the rupture-force distributions obtained for two given sequences, namely, the  $1 \times 2$  as well as the  $1 \times 3$  DNA duplex, and different pulling velocities,  $v$ . In experiments, we control the separation velocity between cantilever and substrate. Thus, the end-to-end distance,  $x$ , of a system composed of dsDNA, ssDNA linker, PEG linker, and AFM cantilever continuously increases in time with constant velocity  $v$ . From the end-to-end distance,  $x$ , we derive the force acting

along this chain of elastic elements. The force in turn allows us to determine the escape rate,  $k$ , as a function of time. The resulting differential equation describes the decay from a metastable state,  $N_{\text{duplex}}$ , with a time-dependent rate (33):

$$dN_{\text{duplex}} = -N_{\text{duplex}}k(t)dt, \quad (12)$$

where  $k(t) = k(f(v \times t))$ , and  $f(x)$  follows from Eq. 10.

For both the  $1 \times 2$  and the  $1 \times 3$  DNA duplexes and separation velocities between  $10 \text{ nm/s}$  and  $10 \text{ } \mu\text{m/s}$ , we numerically solved this differential equation. The obtained rupture-force distributions are shown in Fig. 4 a. A striking finding was that the rupture-force distribution of the  $1 \times 2$  DNA duplex broadens with increasing force loading rate, whereas the rupture-force distribution of the  $1 \times 3$  DNA duplex is almost independent of this parameter. We attribute this behavior to the crossing of the B-S transition at  $\sim 65 \text{ pN}$ , which is only observed for the  $1 \times 2$  DNA duplex for the experimentally applied force loading rates. For forces  $>65 \text{ pN}$ , and thus above the B-S transition, the slope of the force-extension profile increases significantly, resulting in a wider distribution of the obtained rupture forces. To verify that the broadening of the rupture-force distribution is indeed due to the crossing of the B-S transition, we calculated the  $1 \times 3$  DNA duplex rupture-force distributions for force loading rates higher than those achievable by experiment. In agreement with this interpretation, the rupture-force distribution of the  $1 \times 3$  DNA duplex broadens correspondingly for rupture forces above the B-S transition (data not shown). The experimentally obtained rupture-force distributions are further broadened by the thermal and instrumentation noise introduced to the cantilever. According to Morfill and colleagues (32), the total experimental noise was Gaussian, with a width of  $4.7 \text{ pN}$ . Therefore, to compare theory with experiment, we convolved the theoretically obtained rupture-force distribution with such a Gaussian distribution (Fig. 4 b). From these distributions, we determined the most probable rupture force via a Gaussian fit. Fig. 4 c shows this fit plotted against the corresponding most probable force loading rate for the theoretical predictions and the experimental data. The theory reproduces the data quite well within the experimental error.

Systematic errors on the experimental side are mainly due to errors of the cantilever calibration, which introduces an error of up to 5–10% (58). The presented AFM force data were obtained with two different AFM cantilever tips, one for all of the  $1 \times 2$  DNA duplex data and one for all of the  $1 \times 3$  DNA duplex data. Therefore, the set of most probable rupture forces may be shifted by up to 5–10%. Further, a small error is introduced due to pulling angles that are not perpendicular to the substrate, which is typically in the order of 2% (59).

Systematic errors on the theoretical side include the following: We chose the basepair opening rate for the B-DNA and the S-DNA conformations to be identical,

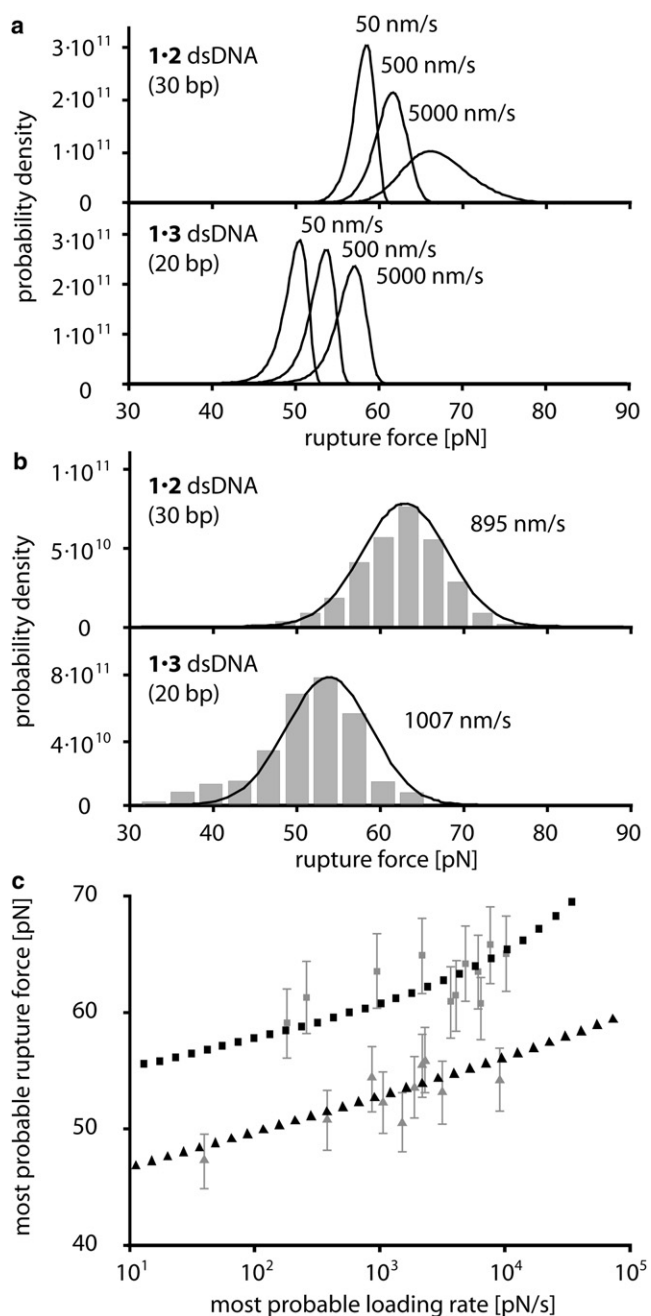


FIGURE 4 (a) Calculated rupture-force distribution for the  $1 \times 2$  and the  $1 \times 3$  duplex for 50, 500, and 5000 nm/s pulling velocity. (b) Comparison of the experimental (gray bars) and calculated (lines) rupture-force distribution for the  $1 \times 2$  and  $1 \times 3$  duplex at 895 nm/s and 1007 nm/s, respectively. The calculated rupture-force distributions were convolved with a Gaussian cantilever detection noise of 4.7 pN. (c) Comparison of the experimental and calculated most probable rupture forces for different most probable loading rates. The gray data points refer to the experimental data and the black data points to the theory data. Squares refer to the 30-basepair DNA  $1 \times 2$  duplex and triangles to the 20-basepair  $1 \times 3$  duplex.

although they are completely independent parameters. Further, the S-DNA polymer elasticity model is very crude for several other reasons. First, according to the methods of Cocco and colleagues (24), we approximated the force-exten-

sion curve of S-DNA to be linear. Second, the basepair free energy was assumed to be identical to the B-DNA interaction. Furthermore, there are most likely two types of S-DNA, depending on whether the force is applied at the 5' or the 3' ends of the dsDNA (26,60). Finally, the nearest-neighbor model does not account for long-range interactions, as they are experimentally observed in DNA bubbles, which has a strong influence on the boundary energy,  $C_{ss-ds}$ , and thus on how cooperative DNA strand separation occurs. From our calculations, we observed that a more cooperative transition between single-stranded and double-stranded DNA, i.e., a larger value for  $C_{ss-ds}$ , leads to a reduced DNA duplex length dependence on the rupture-force distribution. For values of  $C_{ss-ds}$  in the range of a few  $k_B T$ , the rupture-force distributions of the  $1 \times 2$  and the  $1 \times 3$  DNA duplexes are almost superimposed.

#### Thermodynamic equilibrium prevails

To appropriately describe the separation of dsDNA employing canonical transition state theory, thermodynamic equilibrium must prevail within the binding potential (54). Two scenarios would contradict such an assumption: Either the changes of state occur on timescales equal to or slower than the rate of escape or, to reach the transition states, an intermediate free-energy barrier needs to be crossed. In the [Supporting Material](#), we discuss these scenarios and conclude that, for the experimentally observed force range between 0 and 100 pN, canonical transition state theory is applicable.

#### Comparison to the Bell-Evans model

Typically, the rupture of molecular bonds is described employing the Bell-Evans model (34). Like our model, the latter is based on transition state theory assuming a thermally activated escape from a free-energy potential. In this section, we discuss the differences between the Bell-Evans model and our model, how they compare with each other, and why our model is a significant refinement for the description of force-induced separation of short dsDNA.

The main difference between the two models lies within the approximation of the Bell-Evans trapping potential as a harmonic free-energy landscape, which is simply tilted by an external force. As a result of this approximation, the free-energy difference between the equilibrium and the transition state decreases in proportion to the applied force:

$$\Delta G(f) = \Delta G_0 - f \times x_{\text{tst}}, \quad (13)$$

where  $\Delta G_0$  is the free-energy difference at zero force and  $x_{\text{tst}}$  is a force-independent distance between the equilibrium state and the transition state. The force-dependent rate is given by

$$k(f) = k_0 \times \exp(-\Delta G(f)), \quad (14)$$

where  $k_0$  is the natural attempt frequency of the molecular bond. In our work, we explicitly model the evolution of

the DNA duplex free-energy landscape with increasing force. To see what differences arise in comparison to the Bell-Evans approach, we calculate an effective barrier height of the transition state from the sum of the Boltzmann probabilities for the states,  $s_{\text{tst}}$ .

$$\Delta G(f) = -\ln\left(\sum_{s_{\text{tst}}} \frac{\exp(-\Delta G_{\text{total}}(s_{\text{tst}}, f))}{Z}\right). \quad (15)$$

As shown in Fig. 5 *a*, the force-dependent evolution of the effective barrier height according to Eq. 15 does exhibit significant differences from the Bell-Evans approach (Eq. 13). Below 10 pN the free-energy difference between the equilibrium state and the transition state increases with applied force. This is in agreement with Fig. 2 *b*, which shows that for increasing applied force the absolute value of the free-energy difference per basepair between B-DNA (equilibrium state for low forces) and ssDNA (transition state) increases for forces <10 pN before it decreases for forces >10 pN. The microscopic origin of this effect is that although the contour length of ssDNA is longer compared to B-DNA, the contour length of ssDNA projected onto the direction of applied force, i.e., the end-to-end distance, is shorter for low forces due to its much shorter persistence length. Thus, low forces stabilize DNA duplexes, a result that was previously shown experimentally (61,62) and discussed theoretically (28,63). Between 10 and 60 pN, the free energy decreases roughly proportionally to the applied force,  $f$ . Above 65 pN, i.e., above the B-S transition, the energy decreases linearly again, yet with a smaller slope. Taking the negative derivative of the calculated free-energy barrier height with respect to the force yields an effective distance between the equilibrium state and the transition state,  $x_{\text{tst}}$ :

$$x_{\text{tst}} = -\frac{\partial \Delta G(f)}{\partial f}.$$

$x_{\text{tst}}$  does exhibit a rather odd force dependency (Fig. 5 *b*), which we explain according to geometrical considerations: Strunz and colleagues estimated an upper limit for  $x_{\text{tst}}$  assuming that the equilibrium state is B-DNA with a contour length of 0.34 nm/basepair and that the transition state is all ssDNA (apart from two residual basepairs), with a contour length of  $\sim 0.7$  nm/basepair (31). In the case of the 30-basepair  $1 \times 2$  DNA duplex, this corresponds to a total length difference between these two states of  $\sim 10$  nm, which is significantly larger than the corresponding values of  $x_{\text{tst}}$  obtained from our calculations, as well as those from actual experiments (31,32). Two effects contribute to this deviation. First,  $x_{\text{tst}}$  is the projection of the distance between the equilibrium state and the transition state onto the direction of applied force. Therefore, a more accurate estimate of  $x_{\text{tst}}$  is the difference in end-to-end distance according to our polymer models for B-DNA and ssDNA (Fig. 5 *b*). Second, within the range 60–65 pN, the equilibrium state switches

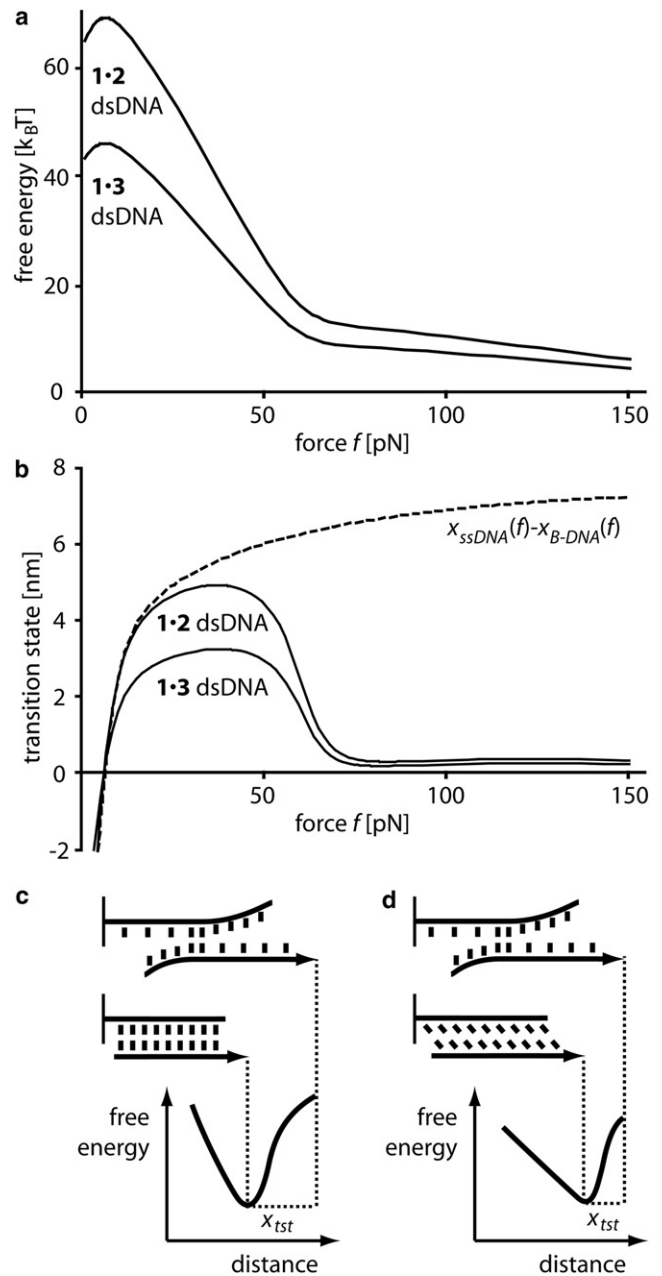


FIGURE 5 (a) Calculated effective barrier height, according to the standard Bell-Evans model. At forces between 10 and 50 pN, the free energy decreases proportionally to the applied force  $f$ . At forces >65 pN, when B-DNA is converted into S-DNA, the energy again decreases linearly, yet with a significantly smaller slope. (b) The negative derivative of the force versus free energy profile yields  $x_{\text{tst}}$ , the effective distance between the equilibrium state and the transition state. The dashed line represents the difference in end-to-end distance for B-DNA and ssDNA for the  $1 \times 2$  DNA duplex as a function of force. (c) For forces <60 pN,  $x_{\text{tst}}$  reflects the increase in end-to-end distance from B-DNA to ssDNA. (d) For forces >65 pN,  $x_{\text{tst}}$  reflects the increase in end-to-end distance from S-DNA to ssDNA.

from a predominantly B-DNA duplex to a predominantly S-DNA duplex. The difference in end-to-end distance between the equilibrium state and the transition states is much smaller for an S-DNA duplex than for a B-DNA



duplex (Fig. 5 c). Consequently,  $x_{\text{tst}}$  decreases to a fraction of a nanometer during the B-S transition.

Due to the force dependence of  $x_{\text{tst}}$ , we conclude that the standard Bell-Evans model is only a good description of the force-induced separation of DNA duplexes for forces between 10 and 50 pN and between 65 and  $\sim 100$  pN. However, for both scenarios, a different set of free-energy landscape parameters, i.e., free-energy barrier at zero force and distance between equilibrium and transition state, need to be chosen. Our refined model, on the other hand, provides a reliable description for forces between 0 and  $\sim 100$  pN. Our results are in agreement with recent literature. Hyeon and Thirumalai (64) argue that  $x_{\text{tst}}$  changes considerably if the molecular bond is soft or plastic, as is the case for dsDNA. Further, Dudko and colleagues (65) report that the position of the equilibrium state may depend on the applied force leading to a force dependence of the distance between the equilibrium state and the transition state and thus to a nonlinear dependence of the barrier height on the applied force.

## CONCLUSION

The result of this work is a theoretical model that employs a combination of a three-state equilibrium model and the canonical transition state theory to describe the force-induced strand separation of dsDNA tens of basepairs long. The three-state equilibrium model serves as a basis for a free-energy trapping landscape. Double-strand separation occurs through transition states, which we identify as the states with two adjacent basepairs remaining, i.e., one remaining stacking interaction. We calculated the rate of escape as a function of force from the total flux through these transition states, assuming a basepair opening rate of  $5 \times 10^8 \text{ s}^{-1}$ . The rate of escape in turn allowed us to explicitly calculate the rupture-force distribution for two DNA duplexes,  $1 \times 2$  and  $1 \times 3$ . The theoretically obtained results and actual single-molecule atomic force microscopy experiments are in excellent agreement. We argue that in the case of the force-induced DNA strand separation, our model is a significant refinement of the Bell-Evans model and provides a reliable description for forces between 0 and 100 pN. In the future, we foresee this theory being applied to predict, tune, and analyze the behavior of DNA force sensors.

## SUPPORTING MATERIAL

Methods and Materials and one figure are available at [http://www.biophysj.org/biophysj/supplemental/S0006-3495\(09\)01524-0](http://www.biophysj.org/biophysj/supplemental/S0006-3495(09)01524-0).

Financial support was provided by the Nanosystems Initiative Munich. D.H., P. S., and K. F. are grateful to the Elite Network of Bavaria (IDK-NBT) for a doctoral fellowship.

## REFERENCES

- Seeman, N. 2003. DNA in a material world. *Nature*. 421:427–431.
- Martin, M. 2000. DNA handles for single molecule experiments. *Single Mol.* 1:139–144.
- Essevaz-Roulet, B., U. Bockelmann, and F. Heslot. 1997. Mechanical separation of the complementary strands of DNA. *Proc. Natl. Acad. Sci. USA*. 94:11935–11940.
- Yan, H. 2003. DNA-templated self-assembly of protein arrays and highly conductive nanowires. *Science*. 301:1882–1884.
- Cohen, J. D., J. P. Sadowski, and P. B. Dervan. 2007. Addressing single molecules on DNA nanostructures. *Angew. Chem. Int. Ed.* 46:7956–7959.
- Winfree, E., F. Liu, L. A. Wenzler, and N. C. Seeman. 1998. Design and self-assembly of two-dimensional DNA crystals. *Nature*. 394:539–544.
- Shawn, M. D., H. Dietz, T. Liedl, B. Högberg, F. Graf, et al. 2009. Self-assembly of DNA into nanoscale three-dimensional shapes. *Nature*. 459:414–418.
- Liu, Q., L. Wang, A. Frutos, A. Condon, R. Corn, et al. 2000. DNA computing on surfaces. *Nature*. 403:175–179.
- Albrecht, C., K. Blank, M. Lalic-Multhaler, S. Hirler, T. Mai, et al. 2003. DNA: a programmable force sensor. *Science*. 301:367–370.
- Blank, K., A. Lankenau, T. Mai, S. Schiffmann, I. Gilbert, et al. 2004. Double-chip protein arrays: force-based multiplex sandwich immunoassays with increased specificity. *Anal. Bioanal. Chem.* 379:974–981.
- Blank, K., T. Mai, I. Gilbert, S. Schiffmann, J. Rankl, et al. 2003. A force-based protein biochip. *Proc. Natl. Acad. Sci. USA*. 100:11356–11360.
- Dose, C., D. Ho, H. E. Gaub, P. B. Dervan, and C. H. Albrecht. 2007. Recognition of “mirror-image” DNA by small molecules. *Angew. Chem.* 46:8384–8387.
- Ho, D., C. Dose, C. H. Albrecht, P. Severin, K. Falter, et al. 2009. Quantitative detection of small molecule/DNA complexes employing a force-based and label-free DNA microarray. *Biophys. J.* 96:4661–4671.
- Ho, D., K. Falter, P. Severin, and H. E. Gaub. 2009. DNA as a force sensor in an aptamer-based biochip for adenosine. *Anal. Chem.* 81:3159–3164.
- Kufer, S. K., E. M. Puchner, H. Gump, T. Liedl, and H. E. Gaub. 2008. Single-molecule cut-and-paste surface assembly. *Science*. 319:594–596.
- Puchner, E., S. Kufer, M. Strackham, S. Stahl, and H. E. Gaub. 2008. Nanoparticle self-assembly on a DNA-scaffold written by single-molecule cut-and-paste. *Nano Lett.* 8:3692–3695.
- Kufer, S., M. Strackham, S. Stahl, H. Gump, E. M. Puchner, et al. 2009. Optically monitoring the mechanical assembly of single molecules. *Nat. Nanotechnol.* 4:45–49.
- Rief, M., H. Clausen-Schaumann, and H. E. Gaub. 1999. Sequence dependent mechanics of single DNA molecules. *Nat. Struct. Biol.* 6:346–349.
- Cao, Y., T. Yoo, and H. Li. 2008. Single molecule force spectroscopy reveals engineered metal chelation is a general approach to enhance mechanical stability of proteins. *Proc. Natl. Acad. Sci. USA*. 105:11152–11157.
- Smith, S., L. Finzi, and C. Bustamante. 1992. Direct mechanical measurements of the elasticity of single DNA molecules by using magnetic beads. *Science*. 258:1122–1126.
- Cluzel, P., A. Lebrun, C. Heller, R. Lavery, J. Viovy, et al. 1996. DNA: an extensible molecule. *Science*. 271:792–794.
- Smith, S. B., Y. J. Cui, and C. Bustamante. 1996. Overstretching B-DNA: the elastic response of individual double-stranded and single-stranded DNA molecules. *Science*. 271:795–799.
- Wang, M., H. Yin, R. Landick, J. Gelles, and S. M. Block. 2005. Stretching DNA with optical tweezers. *Biophys. J.* 72:1335–1346.
- Cocco, S., J. Yan, J. Léger, D. Chatenay, and J. Marko. 2004. Overstretching and force-driven strand separation of double-helix DNA. *Phys. Rev. E Stat. Nonlin. Soft Matter Phys.* 70:011910.
- Storm, C., and P. C. Nelson. 2003. Theory of high-force DNA stretching and overstretching. *Phys. Rev. E Stat. Nonlin. Soft Matter Phys.* 67:051906.

26. Lebrun, A., and R. Lavery. 1996. Modelling extreme stretching of DNA. *Nucleic Acids Res.* 24:2260–2267.
27. Konrad, M., and J. Bolonick. 1996. Molecular dynamics simulation of DNA stretching is consistent with the tension observed for extension and strand separation and predicts a novel ladder structure. *J. Am. Chem. Soc.* 118:10989–10994.
28. Rouzina, I., and V. A. Bloomfield. 2001. Force-induced melting of the DNA double helix 1. Thermodynamic analysis. *Biophys. J.* 80: 882–893.
29. Piana, S. 2005. Structure and energy of a DNA dodecamer under tensile load. *Nucleic Acids Res.* 33:7029–7038.
30. Clausen-Schaumann, H., M. Rief, C. Tolksdorf, and H. E. Gaub. 2000. Mechanical stability of single DNA molecules. *Biophys. J.* 78: 1997–2007.
31. Strunz, T., K. Oroszlan, R. Schäfer, and H. Güntherodt. 1999. Dynamic force spectroscopy of single DNA molecules. *Proc. Natl. Acad. Sci. USA.* 96:11277–11282.
32. Morfill, J., F. Kuhner, K. Blank, R. Lugmaier, J. Sedlmair, et al. 2007. B-S transition in short oligonucleotides. *Biophys. J.* 93:2400–2409.
33. Friedsam, C., A. K. Wehle, F. Kuhner, and H. E. Gaub. 2003. Dynamic single-molecule force spectroscopy: bond rupture analysis with variable spacer length. *J. Phys. Condens. Matter.* 15:S1709–S1723.
34. Evans, E., and K. Ritchie. 1997. Dynamic strength of molecular adhesion bonds. *Biophys. J.* 72:1541–1555.
35. Merkel, R., P. Nassoy, A. Leung, K. Ritchie, and E. Evans. 1999. Energy landscapes of receptor-ligand bonds explored with dynamic force spectroscopy. *Nature.* 397:50–53.
36. Oesterhelte, F., M. Rief, and H. E. Gaub. 1999. Single molecule force spectroscopy by AFM indicates helical structure of poly(ethylene-glycol) in water. *N.J. Phys.* 1:1–11.
37. Zimm, B. H., and J. K. Bragg. 1959. Theory of the phase transition between helix and random coil in polypeptide chains. *J. Chem. Phys.* 31:526–535.
38. Bockelmann, U., B. Essevez-Roulet, and F. Heslot. 1997. Molecular stick-slip motion revealed by opening DNA with piconewton forces. *Phys. Rev. Lett.* 79:4489–4492.
39. Bockelmann, U., B. Essevez-Roulet, and F. Heslot. 1998. DNA strand separation studied by single molecule force measurements. *Phys. Rev. E Stat. Phys. Plasmas Fluids Relat. Interdiscip. Topics.* 58:2386–2394.
40. Cocco, S., R. Monasson, and J. F. Marko. 2001. Force and kinetic barriers to unzipping of the DNA double helix. *Proc. Natl. Acad. Sci. USA.* 98:8608–8613.
41. Bornschloegl, T., and M. Rief. 2006. Single molecule unzipping of coiled coils: sequence resolved stability profiles. *Phys. Rev. Lett.* 96:118102.
42. Bornschloegl, T., and M. Rief. 2008. Single-molecule dynamics of mechanical coiled-coil unzipping. *Langmuir.* 24:1338–1342.
43. Gotoh, O., and Y. Tagashira. 1981. Stabilities of nearest-neighbor doublets in double-helical DNA determined by fitting calculated melting profiles to observed profiles. *Biopolymers.* 20:1033–1042.
44. SantaLucia, J. 1998. A unified view of polymer, dumbbell, and oligonucleotide DNA nearest-neighbor thermodynamics. *Proc. Natl. Acad. Sci. USA.* 95:1460–1465.
45. Kafri, Y., D. Mukamel, and L. Peliti. 2000. Why is the DNA denaturation transition first order? *Phys. Rev. Lett.* 85:4988.
46. Hanke, A., M. G. Ochoa, and R. Metzler. 2008. Denaturation transition of stretched DNA. *Phys. Rev. Lett.* 100:018106.
47. Kafri, Y., D. Mukamel, and L. Peliti. 2002. Melting and unzipping of DNA. *Eur. Phys. J. B.* 27:135–146.
48. Einert, T. R., P. Naeger, H. Orland, and R. R. Netz. 2008. Impact of loop statistics on the thermodynamics of RNA folding. *Phys. Rev. Lett.* 101:048103.
49. Altan-Bonnet, G., A. Libchaber, and O. Krichevsky. 2003. Bubble dynamics in double-stranded DNA. *Phys. Rev. Lett.* 90:138101.
50. Lifson, S. 1964. Partition functions of linear-chain molecules. *J. Chem. Phys.* 40:3705–3710.
51. Rubinstein, M., and R. H. Colby. 2003. *Polymer Physics.* Oxford University Press, Oxford, United Kingdom.
52. Kuhner, F., M. Erdmann, L. Sonnenberg, A. Serr, J. Morfill, et al. 2006. Friction of single polymers at surfaces. *Langmuir.* 22:11180–11186.
53. Polanyi, M., and E. Wigner. 1928. Regarding the interference of resonant oscillations as the cause of energy fluctuations and chemical reactions. *Z. Phys. Chem. Abt. A.* 139:439.
54. Hänggi, P., P. Talkner, and M. Borkovec. 1990. Reaction-rate theory: fifty years after Kramers. *Rev. Mod. Phys.* 62:251–342.
55. Bockelmann, U., P. Thomen, and F. Heslot. 2008. Dynamics of the DNA duplex formation studied by single molecule force measurements. *Biophys. J.* 87:3388–3396.
56. Andreatta, D., S. Sen, J. Lustres, S. Kovalenko, N. Ernstring, et al. 2006. Ultrafast dynamics in DNA: “fraying” at the end of the helix. *J. Am. Chem. Soc.* 128:6885–6892.
57. Guéron, M., and J. L. Leroy. 1995. Studies of base pair kinetics by NMR measurement of proton exchange. *Methods Enzymol.* 261: 383–413.
58. Butt, H. J., and M. Jaschke. 1995. Calculation of thermal noise in atomic-force microscopy. *Nanotechnology.* 6:1–7.
59. Kühner, F., M. Erdmann, and H. E. Gaub. 2006. Scaling exponent and Kuhn length of pinned polymers by single molecule force spectroscopy. *Phys. Rev. Lett.* 97:218301.
60. Albrecht, C., G. Neuert, R. Lugmaier, and H. E. Gaub. 2008. Molecular force balance measurements reveal that double-stranded DNA unbinds under force in rate-dependent pathways. *Biophys. J.* 94:4766–4774.
61. Birshtein, T. M., and O. B. Ptitsyn. 1966. *Conformations of Macromolecules.* John Wiley, New York.
62. Rupprecht, A., J. Piskur, J. Schultz, L. Nordenskiöld, Z. Song, et al. 1994. Mechanochemical study of conformational transitions and melting of Li-, Na-, K-, and CsDNA fibres in water-ethanol solutions. *Biopolymers.* 34:897–920.
63. Buhot, A., and A. Halperin. 2000. Extension of rod-coil multiblock copolymers and the effect of the helix-coil transition. *Phys. Rev. Lett.* 84:2160–2163.
64. Hyeon, C., and D. Thirumalai. 2007. Measuring the energy landscape roughness and the transition state location of biomolecules using single molecule mechanical unfolding experiments. *J. Phys. Condens. Matter.* 19:113101.
65. Dudko, O. K., A. E. Filippov, J. Klafter, and M. Urbakh. 2003. Beyond the conventional description of dynamic force spectroscopy of adhesion bonds. *Proc. Natl. Acad. Sci. USA.* 100:11378–11381.

**Supporting Material**

**Force-driven separation of short double stranded DNA**

Dominik Ho, Julia L. Zimmermann, Florian A. Dehmelt, Uta Steinbach, Matthias Erdmann, Philip Severin, Katja Falter, and Hermann E. Gaub

## MATERIALS AND METHODS

Theoretical calculations were performed using Mathematica version 5.1 (Wolfram Research, Champaign, IL). The experimental data presented in this study was obtained according to Morfill and colleagues [1]. In the following paragraphs we briefly discuss the experimental setup and data analysis.

**DNA constructs.** DNA oligomers **1**: SH-5'-TTT TTT TTT TTT TTT TTT TTC GTT GGT GCG GAT ATC TCG GTA GTG GGA TAC GAC GAT ACC GAA GAC AGC TCA TGT TAT ATT ATG-3', **2**: SH-5'-TTT TTT TTT TTA TCC CAC TAC CGA GAT ATC CGC ACC AAC G-3' and **3**: SH-5'-TTT TTT TTT TCC GAG ATA TCC GCA CCA ACG-3' were purchased HPLC grade from IBA GmbH (Goettingen, Germany).

**Preparation of slides and cantilevers.** The used oligonucleotides modified with a thiol group at their 5'-termini were immobilized on amino-functionalized surfaces using a hetero-bifunctional poly(ethylene glycol) (PEG) spacer [2]. Oligonucleotide **1** was immobilized on the cantilever and oligonucleotide **2**, respectively **3**, was coupled to the surface. Before use, the cantilevers (Bio-lever, Olympus) were cleaned as described earlier [3]. After this cleaning procedure, amino-modified cantilevers were prepared using 3-aminopropyltrimethoxysilane (ABCR GmbH, Karlsruhe, Germany). For the surface-coupling of oligonucleotide **2**, respectively **3**, commercially available amino-functionalized slides (Slide A, Nexterion, Mainz, Germany) were used. From now on, both surfaces (cantilever and slide) were treated in parallel as described previously [4]. They were incubated in borate buffer pH 8.5 for 1 h in order to deprotonate the amino groups to ensure coupling to the N-hydroxysuccinimide (NHS) groups of the heterobifunctional NHS-PEG-maleimide (molecular weight, 5000 g/mol; Nektar, Huntsville, AL). After dissolving the PEG at a concentration of 50 mM in borate buffer at pH 8.5, this solution was incubated on the surfaces for 1 h. In parallel, the thiol groups of oligonucleotides **1**, **2** and **3** were recovered from disulfide bonds. Oligonucleotides were reduced using tris (2-carboxyethyl) phosphine hydrochloride beads (Perbio Science, Bonn, Germany). After washing the surfaces with ultrapure water, a solution of the oligonucleotides **1** and **2**, respectively **3**, (1.75 mM) was incubated on the cantilever tip and the surfaces for 1 h. During this incubation time, the free functional maleimide group of the PEG was allowed to react with the 5'-thiol end of the respective oligonucleotide, yielding a thioester bond. Finally, the cantilever and the surfaces were rinsed with PBS to remove noncovalently bound oligonucleotides and stored in PBS until use.

**Force spectroscopy.** The force measurements were performed in PBS containing 150 mM NaCl at room temperature using an MFP-3D AFM (Asylum Research, Santa Barbara, CA). Cantilever spring constants were measured as described previously [5] [6]. During one experiment, the approach and retract velocity were held constant. To obtain measurements over a broad range of different loading rates, several experiments were performed each at a different retract velocity ranging from 50 nm/s to 10 mm/s.

**Data Analysis.** The obtained data were converted into force-extension curves. From these force-extension curves, the rupture force (the force at which the dsDNA separates into two single strands) and the corresponding loading rate were determined using the software Igor Pro 5.0 (Wavemetrics, Lake Oswego, OR) and a custom-written set of procedures. The rupture force is defined as described previously [7]. To determine the loading rate, the freely jointed chain model was used, according to previous studies [9].

## POLYMER MODELS

Herein, we employ polymer extension models for B-DNA, S-DNA and single stranded DNA according to the three-state equilibrium model of Cocco and colleagues [8]. The poly(ethylene-glycol) is modeled according to Oosterhelt and colleagues [9].

**Double-stranded B-DNA.** B-DNA elasticity is very well described by chain bending fluctuations leading to an entropic elasticity, while elastic stretching of the double helix generates the roughly linear stretching between 20 and 50 pN with a spring constant per base pair of  $f_B/C_B = 1200/0.34$  pN/nm. According to previous work [10], the extension per base-pair is

$$x_B(f) = C_B \left( 1 - \sqrt{\frac{k_B T}{4 A_B f} + \frac{f}{f_B}} \right),$$

where the persistence length is  $A_B = 50$  nm, the force constant  $f_B = 1230$  pN and the contour length  $C_B = 0.34$  nm. The free energy correspondingly becomes

$$w_B(f) = - \int_{f'=0}^f x_B(f') df'$$

**Double-stranded S-DNA.** For S-DNA elasticity a linear response to elongation was suggested [8] with an extension per base pair of

$$x_S(f) = x_1 + \frac{f - f_1}{S}.$$

and a free energy function of

$$w_S(f) = w_B(f_0) - \frac{1}{2} \left( (x_0 + x_1)(f_1 - f_0) + 2x_1(f - f_1) + (f - f_1)^2 / S \right)$$

where the parameters are  $x_0 = 0.32$  nm,  $x_1 = 0.58$  nm,  $f_0 = 62$  pN,  $f_1 = 68$  pN and  $S = 4700$  pN/nm. The values for  $f_0$  and  $f_1$  are salt dependent parameters and given for a salt concentration of 500 mM. They shift down by 5 pN for each decade reduction in NaCl concentration. Thus the above set of parameters is chosen such that experimental data on the B-S transition, the salt dependence [11] and the stretching data for forces between 68 and 150 pN [12] are reproduced well.

**Single-stranded DNA.** The ssDNA polymer model is phenomenological [8] and includes the logarithmic dependence of extension on force seen at  $>50$  mM NaCl concentration [13] as well as the reduction in contour length generated at low force by self-adhesion (“folding”) of the chain. The extension per base pair is

$$x_{ss}(f) = C_{ss} \left( \frac{a_1 \ln(f/f_1)}{1 + a_3 \text{Exp}(-f/f_3)} \right),$$

where  $C_{ss} = 0.34$  nm,  $a_1 = 0.21$ ,  $a_2 = 0.34$ ,  $f_1 = 0.0037$  pN,  $f_2 = 2.9$  pN and  $f_3 = 8000$  pN. The parameter  $a_3 = 2.1 \ln(M/0.0025)/\ln(0.15/0.0025) - 0.1$  depends on NaCl concentration  $M$  (mol). The free energy correspondingly becomes

$$w_{ss}(f) = - \int_{f'=0}^f x_{ss}(f') df'.$$

**Poly(ethylene glycol).** For the PEG extension per monomer we used a two state model develop by Oosterhelt and colleagues [1].

$$x_{PEG}(f) = \left( \frac{C_{planar}}{\text{Exp}(\Delta G(f)/k_B T) + 1} + \frac{C_{helical}}{\text{Exp}(-\Delta G(f)/k_B T) + 1} \right) \cdot \left( \coth\left( \frac{f \cdot A_{PEG}}{k_B T} \right) - \frac{k_B T}{f \cdot A_{PEG}} \right) + \frac{f}{K_{PEG}},$$

where  $C_{planar} = 3.58$  A,  $C_{helical} = 2.8$  A,  $A_{PEG}$  of 7 A,  $K_{PEG} = 150$  N/m and

$$\Delta G(f) = \Delta G_0 - f(C_{planar} - C_{helical}),$$

where  $\Delta G_0 = 3.3 k_B T$ . This model takes into account that the PEG monomers appear in two conformations.

## PARTITION SUM CORRECTIONS

**Boundary Condition.** The partition sum of Equation 8 does not account for the boundary conditions at the end of the DNA duplex yet. As boundary conditions, we therefore introduce two additional base-pairs at  $i = 0$  and  $i = N + 1$ , which are single stranded. The partition sum  $Z'$  including the two boundary base pairs becomes

$$Z' = \sum_{\substack{\text{all matrix} \\ \text{elements}}} \begin{bmatrix} 0 & 0 & 0 \\ 0 & 0 & 0 \\ \exp(-w_{ss}(f) - C_{ds-ss}) & \exp(-w_{ss}(f) - C_{ds-ss}) & \exp(-w_{ssDNA}(f)) \end{bmatrix} \times Z \times \begin{bmatrix} 0 & 0 & 0 \\ 0 & 0 & 0 \\ 0 & 0 & \exp(-w_{ssDNA}(f)) \end{bmatrix}.$$

**Strand-separated states.** All states with less than two remaining base-pairs are already strand separated. We subtract the Boltzmann probabilities of these states from the partition sum such that the partition sum that we use for all further calculations becomes

$$Z'' = Z' - (Z_0 + Z_1),$$

$$\text{where } Z_0 = \sum_{\substack{\text{all matrix} \\ \text{elements}}} \begin{bmatrix} 0 & 0 & 0 \\ 0 & 0 & 0 \\ \exp(-w_{ss}(f) - C_{ds-ss}) & \exp(-w_{ss}(f) - C_{ds-ss}) & \exp(-w_{ss}(f)) \end{bmatrix}^{N+1} \times \begin{bmatrix} 0 & 0 & 0 \\ 0 & 0 & 0 \\ 0 & 0 & \exp(-w_{ss}(f)) \end{bmatrix}$$

$$\text{and } Z_1 = \sum_{i=1}^N \sum_{\substack{\text{all matrix} \\ \text{elements}}} \begin{bmatrix} 0 & 0 & 0 \\ 0 & 0 & 0 \\ \exp(w_{ss}(f) - C_{ds-ss}) & \exp(w_{ss}(f) - C_{ds-ss}) & \exp(w_{ss}(f)) \end{bmatrix}^i \times \begin{bmatrix} 0 & 0 & 0 \\ 0 & 0 & 0 \\ \exp(w_{ss}(f) - C_{ds-ss}) & \exp(w_{ss}(f) - C_{ds-ss}) & \exp(w_{ss}(f)) \end{bmatrix} \times \begin{bmatrix} 0 & 0 & 0 \\ 0 & 0 & 0 \\ \exp(w_{ss}(f) - C_{ds-ss}) & \exp(w_{ss}(f) - C_{ds-ss}) & \exp(w_{ss}(f)) \end{bmatrix}^{N-i} \times \begin{bmatrix} 0 & 0 & 0 \\ 0 & 0 & 0 \\ 0 & 0 & \exp(w_{ss}(f)) \end{bmatrix}$$



## TRANSITION STATE THEORY

**Equilibrium Flux.** The equilibrium flux is simply the sum of the Boltzmann probabilities of all states  $s_{tst}$  times the base pair opening rate:

$$\begin{aligned}
 k(f) &= \langle \delta[n - n_{tst}] \dot{n}_+ \rangle_{equilibrium} \\
 &= \frac{1}{Z(f)} \sum_{s_{tst}} \dot{n}_+ \exp(-\Delta G_{total}(s_{tst}, f)) \\
 &= \frac{1}{Z''} \dot{n}_+ \sum_{k=1}^{N-1} \sum_{\substack{\text{all matrix} \\ \text{elements}}} \left[ \begin{array}{ccc} 0 & 0 & 0 \\ 0 & 0 & 0 \\ \exp(-g_{ss}(f) - C_{ds-ss}) & \exp(-g_{ss}(f) - C_{ds-ss}) & \exp(-g_{ss}(f)) \end{array} \right]^k \times \\
 &\quad \left[ \begin{array}{ccc} \exp(-g_B(f) + J_k) & \exp(-g_B(f) + J_k - C_{B-S}) & \exp(-g_B(f) - C_{ds-ss}) \\ \exp(-g_S(f) + J_k - C_{B-S}) & \exp(-g_S(f) + J_k) & \exp(-g_S(f) - C_{ds-ss}) \\ 0 & 0 & 0 \end{array} \right] \times \\
 &\quad \left[ \begin{array}{ccc} \exp(-g_B(f) + J_{k+1}) & \exp(-g_B(f) + J_{k+1} - C_{B-S}) & \exp(-g_B(f) - C_{ds-ss}) \\ \exp(-g_S(f) + J_{k+1} - C_{B-S}) & \exp(-g_S(f) + J_{k+1}) & \exp(-g_S(f) - C_{ds-ss}) \\ 0 & 0 & 0 \end{array} \right] \times \\
 &\quad \left[ \begin{array}{ccc} 0 & 0 & 0 \\ 0 & 0 & 0 \\ \exp(-g_{ss}(f) - C_{ds-ss}) & \exp(-g_{ss}(f) - C_{ds-ss}) & \exp(-g_{ss}(f)) \end{array} \right]^{N-k-1} \times \begin{bmatrix} 0 & 0 & 0 \\ 0 & 0 & 0 \\ 0 & 0 & \exp(-g_{ss}(f)) \end{bmatrix}
 \end{aligned}$$

**Thermodynamic Equilibrium Prevails.** To appropriately describe the separation of dsDNA employing the canonical transition state theory, thermodynamic equilibrium must prevail within the binding potential. Two scenarios would contradict such an assumption: Either, the changes of state occurred on timescales equal to or slower than the rate of escape or if, in order to reach the transition states, an intermediate free energy barrier needs to be crossed. In the following, we discuss these scenarios and conclude that, for the experimentally observed force range between 0 and 100 pN, the canonical transition state theory is applicable.

The changes in state from dsDNA to ssDNA occur at base-pair opening and closing rates. Within the present work, we assumed that these rates are in the order of  $10^8 \text{ s}^{-1}$ . From our numerical calculations, we deduce that the base-pair opening rate is about two orders of magnitude faster than the rate at which short dsDNA dissociates for forces below 100 pN. We therefore conclude that the escape process does not critically disturb the thermodynamic equilibrium.

Due to the base-pair heterogeneity the transition state might only be reached by crossing intermediate free energy barriers [8]. In this case, this intermediate barrier crossing would become rate limiting and the

populations of states would not be Boltzmann distributed. In order to investigate this effect, we calculated the free energy as a function of the open base-pairs explicitly for the two dsDNAs used here (Figure S1). Hereby, we neglected the simultaneous formation of more than one DNA bubble. Figure S1b illustrates that no significant energy barriers appear for forces up to 100 pN.

Since the changes in state occur much faster than the separation of the strands and, apart from the transition state, no significant energy barriers arises along the reaction coordinate, we conclude that the canonical transition state theory is appropriate for modeling the rate of strand separation for tens of base-pair long dsDNA. However, for forces significantly higher than 100 pN, the requirements for the canonical transition state theory fail: The rate of escape becomes comparable to the timescale of internal fluctuations, i.e. the base-pair opening and closing rates. Further, rate-dominating barriers apart from the transition state arise. Both effects result in a significant perturbation of the equilibrium distribution and consequently in the breakdown of the canonical transition state theory.

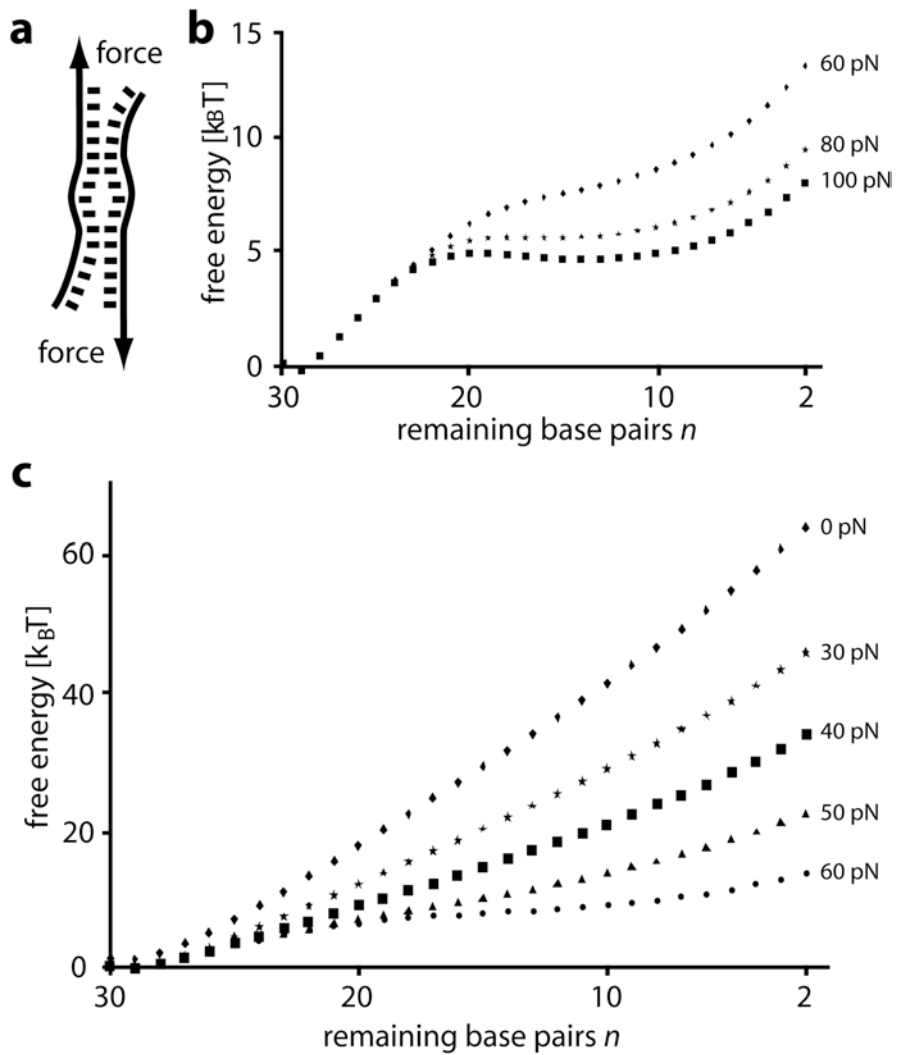


**Figure S1.** (a) The calculated energy landscape collapsed onto one coordinate  $n$ , the number of remaining base pairs, is calculated from equilibrium theory. Thereby, we allow the double strand to open up from its ends as well as to form a bubble of ssDNA. In order to speed up the numerical calculations, we do not account for the simultaneous opening of more than one bubble. (b) Free energy landscape of the 1·2 DNA duplex at 60, 80 and 100 pN calculated from the partition sum. (c) Free energy landscape of the 1·2 DNA duplex at forces smaller than 60 pN. The transition state is located at  $n_{ts} = 2$  and no significant barriers apart from the transition state are observed for forces up to 100 pN.

## REFERENCES

- [1] Morfill, J., F. Kuhner, K. Blank, R. Lugmaier, J. Sedlmair and H. E. Gaub. 2007. B-S Transition in Short Oligonucleotides. *Biophys. J.* 93:2400-2409.
- [2] Kuehner, F., J. Morfill, R. A. Neher, K. Blank, and H. E. Gaub. 2007. Force-induced DNA slippage. *Biophys. J.* 92:2491–2497.
- [3] Neuert, G., C. Albrecht, E. Pamir, and H. E. Gaub. 2006. Dynamic force spectroscopy of the digoxigenin-antibody complex. *FEBS Lett.* 580:505–509.35.
- [4] Blank, K., J. Morfill, and H. E. Gaub. 2006. Site-specific immobilization of genetically engineered variants of *Candida Antarctica* lipase B. *ChemBioChem.* 7:1349–1351.11180–11186.
- [5] Butt, H. J., and M. Jaschke. 1995. Calculation of thermal noise in atomic-force microscopy. *Nanotechnology.* 6:1–7.
- [6] Hugel, T., and M. Seitz. 2001. The study of molecular interactions by AFM force spectroscopy. *Macromol. Rapid Commun.* 22:989–1016.
- [7] Evans, E., and K. Ritchie. 1999. Strength of a weak bond connecting flexible polymer chains. *Biophys. J.* 76:2439–2447.
- [8] Cocco, S., J. Yan, J. Léger, D. Chatenay, J. Marko. 2004. Overstretching and force-driven strand separation of double-helix DNA. *Phys. Rev. E.* 70:011910.
- [9] Oesterhelt, F., M. Rief, and, H. E. Gaub. 1999. Single molecule force spectroscopy by AFM indicates helical structure of poly(ethylene- glycol) in water. *N. J. Phys.* 1:1–11.
- [10] Marko, J., and E. Siggia. 1995. Stretching DNA. *Macromolecules.* 28:8759-8770.
- [11] Wenner, J. R., M. C. Williams, I. Rouzina, and V. A. Bloomfield. 2002. *Biophys. J.* 82:3160.
- [12] Leger, J.-F., G. Romano, A. Sarkar, J. Robert, L. Bourdieu, D. Chatenay, and J. F. Marko. 1999. *Phys. Rev. Lett.* 83:1066.
- [13] Y. Zhang, H. J. Zhou, and Z. C. Ou-Yang. 2001. *Biophys. J.* 81:1133.

DOI: 10.1002/smll.

**DNA-protein binding force chip\*\***

*Philip M. D. Severin, and Hermann E. Gaub\**

[\*] Prof. H. E. Gaub, P. M. D. Severin  
Lehrstuhl für Angewandte Physik and Center for Nanoscience (CeNS), Ludwig-Maximilians-Universität  
Amalienstrasse 54, 80799 Munich (Germany)  
Munich Center For Integrated Protein Science (CIPSM), Ludwig-Maximilians-Universität,  
Butenandtstrasse 5-13, 81377 Munich (Germany)  
E-mail: [gaub@physik.uni-muenchen.de](mailto:gaub@physik.uni-muenchen.de)

**Acknowledgments:**

The authors are grateful to P.B. Dervan for providing the pyrrole-imidazole hairpin polyamide and to J. Buchner for providing human p53. The authors thank J. Buchner, M. Retzlaff and D. Ho for helpful discussions. P.S. was supported by the Elite Network of Bavaria (IDK- NBT) with a doctoral fellowship. Financial support was provided by the Deutsche Forschungsgemeinschaft, the Nanosystems Initiative Munich and the German Science Foundation (SFB 863).

Supporting Information is available on the WWW under <http://www.small-journal.com> or from the author.

**Keywords:** Assays, Biophysics, DNA-protein interactions, Microarrays, Molecular mechanics

Force measurements provide new fundamental and complementary information on biomolecular interactions, particularly in the high and low affinity regimes, which may hardly be obtained otherwise. We introduce a label free parallel format assay to quantify the binding forces in protein-DNA complexes on a chip in crowded environments. It employs arrays of molecular force balances with fluorescent read-out and fulfills all essential criteria for high throughput screening. The assay is fast, easy to operate and requires only a quantitative fluorescence microscope as instrumentation.

Despite years of intensive research, the need for a deeper understanding of protein-DNA interactions remains eminent. A multitude of different techniques were introduced over the past years to characterize intrinsic affinities and dissociation constants in low throughput formats.<sup>[1]</sup> However, the growing complexity of the systems e.g. in epigenetics or systems biology, spurs the urgent need for precise and reliable high-throughput methods, which can provide large data sets not only on the qualitative level but moreover give quantitative information on the underlying biophysics of protein-DNA interactions.

Conventional techniques measure protein-DNA interactions by comparing them with the energy of thermal excitations, e.g. by “counting” the number of proteins bound to DNA at different concentrations, or determine rates by measuring the kinetics of the return to equilibrium after a disturbance. Weak interactions will thus result in fast off rates and may be missed in washing steps whereas strong interactions will result in off rates beyond the time span of the experiments. These protein-DNA interactions are the result of forces between the binding partners, which promise higher accuracy when measured directly. Single molecule force techniques, like optical or magnetic tweezers or AFM, have successfully been used to quantify binding forces with superb precision, but none of these methods offers high

throughput.<sup>[2-4]</sup> The lack of suitable methods to achieve a high level of parallelization in force measurements was up to now the dominant bottleneck.

Recently we introduced a comparative force assay, which employs molecular force probes (MFP) consisting of a reference complex as force sensor and labels for the fluorescent readout. We successfully used this assay to measure DNA-ligand binding in crowded and complex molecular environments. The format requires no labeling of the DNA binding ligand itself, and is applicable over a broad range of affinities (pM to mM).<sup>[5-9]</sup> Here, we present a binding force chip, which for simplicity we refer to as BiFo-Chip. It is a consequent miniaturization and parallelization, which uses an array of different MFPs to characterize the binding forces between DNA and proteins in a very sensitive manner. Parallel arrays of MFPs with different reference complexes are used acting as analog to digital converters for the binding forces under investigation. The size of the MFP spots was reduced to a diameter of approximately 20  $\mu\text{m}$ , providing the feature density needed for high-throughput applications.

As depicted in **Figure 1**, the MFPs used in this study are anchored covalently via one DNA strand to the (lower) chip surface at a density of around  $10^4$  MFPs per  $\mu\text{m}^2$ . Each MFP is comprised of three DNA strands. These three DNA strands form two DNA duplexes coupled in series, a 20 bp target duplex (upper duplex, red), as well as a reference duplex with 15 bp to 50 bp (lower duplex, black and blue). The middle DNA strand carries Cy5 as a fluorescent marker while the other strand of the target duplex has a Cy3 fluorescence marker at one end and biotin at the other end for coupling via streptavidin to the upper surface, which consists of an elastomer stamp with a square pattern of drainage channels. Upon separation of the two surfaces, a force builds up gradually in each individual MFP until either the target duplex or the reference duplex ruptures. Subsequently, the ratio of ruptured target to reference duplexes is read out on the lower surface with a quantitative fluorescence microscope and analyzed to calculate the normalized fluorescence (NF). The NF is defined as the ratio of broken target

bonds to the total number of MFPs that were under load. Accordingly, the NF is a quantitative measure which describes the relative mechanical stability between target and reference DNA duplexes of a MFP. The color-coded fluorescence maps of the two experiments (see Figure 1) show clearly that in the symmetric case NF is close to 0.5 with small local variations, whereas the asymmetric MFP shows a NF of close to 1.0. It should be noted here that the physical force measurement - the comparison of the sample force with a reference force - occurs simultaneously in all  $10^{11}$  MFPs on the  $\text{cm}^2$  chip within fractions of a second in the moment when the stamp is removed, while the readout via fluorescence may occur serially at a much later time e.g. via slow scanning.

In **Figure 2**, the implementation of the BiFo-Chip at different length scales is demonstrated in a series of representative experiments. The BiFo-Chip utilizes eight different reference duplexes ranging in 5 bp steps from 15 bp through 50 bp and the target duplex has a length of 20 bp. While in Figure 2 (a) a BiFo-Chip experiment was performed as proof of principle with 1 mm (diameter) spots per type of reference duplex, in Figure 2 (b) a NF-image section of a BiFo-microarray with identical units is shown, and Figure 2 (c) presents a high resolution NF-image of a single BiFo-microarray unit. A comparison of the NF-values for the BiFo-Chip at different length scales is illustrated in Figure 2 (d). In summary, fluctuations in the NF values are virtually independent of the feature size, which means that we can achieve even further miniaturization with no degradation in readout accuracy. The dashed curve is the analytical solution based on the Bell-Evans model (Supporting Information).<sup>[10, 11]</sup>

The central idea of the BiFo-Chip as a sensor for DNA-ligand interactions is based on a zero-compensation measurement, a concept which is widely used for extremely sensitive measurements and is best understood by analogy to a simple balance, where the gravitational force of an object is compared to that of a reference and where more and more counterweights are added until finally the difference converges to zero. In the case of BiFo-Chip, we design



the target duplex such that it will bind to the analyte, whereas the reference duplex does not. We now compare the binding force of the analyte-complexed target duplex with the binding force of the reference duplexes. On different spots of the array, we offer MFPs with different reference duplex lengths. We offer, so to say, an array of balances with different counterweights and identify that spot where  $NF = 0.5$ , which means that the difference is zero. A demonstration of the wide range of application of BiFo-Chip as a force sensor for three different types of DNA binders (pyrrole-imidazole hairpin polyamide, restriction endonuclease and transcription factor) is given in **Figure 3**. The target duplexes contain the corresponding target sequences, while the reference duplexes are lacking any binding site (alternatively L-DNA may be chosen for the reference duplexes). The BiFo-chip was incubated with the corresponding analyte at a concentration at least two orders above the dissociation constant. A description of the DNA oligomers, which were used to assemble the  $3 \times 8$  different MFPs, can be found in the Methods section online.

Figure 3 (a) shows the interaction of a pyrrole-imidazole hairpin polyamide (P1), which is programmed to bind to the six-base-pair DNA sequence 5'-TGGTCA-3'.<sup>[6, 7]</sup> Figure 3 (b) demonstrates the interaction of a type II restriction endonuclease (EcoRI). EcoRI binds as a dimer to the palindromic DNA target site 5'-GAATTC-3' without enzymatic activity in the absence of  $Mg^{2+}$  ion cofactor. Finally, Figure 3(c) shows the interaction of the tumor suppressor protein p53 DNA-binding domain with the DNA consensus sequence CON2x5.<sup>[12]</sup> The p53 protein belongs to the family of transcription factors. The DNA-binding domain of p53 binds cooperatively as a dimer to CON2x5. In Figure 3, dark blue circles represent the measurement without ligand and light blue squares the equivalent experiment with ligand. In all three cases the NF drops to a lower value in the presence of the ligand. The red dashed line at  $NF = 0.5$  marks the difference in mechanical stability caused by the ligand-DNA interaction. The dashed gray curve originates also from the 2-state model but should not be

over-interpreted, since a 2-state model omits the details of the energy landscape that must be overcome in the rupture process and therefore represents the rupture process of the ligand-DNA complex only in a zero order approximation.

If needed, the absolute values of the forces in Figure 3 in units of pN may be obtained by a comparison with AFM-based single molecule force spectroscopy data. At a loading rate of  $10^5$  pN s<sup>-1</sup> the 10 bp duplex ruptures at 45 pN and the 30 bp at 54 pN.<sup>[13]</sup> More importantly for the discussion here, and also more intuitive, is the relative comparison. Figure 3 (a) illustrates that the peptide stabilizes the DNA duplex in the same way as an extension of the duplex by 9.5 bp would do, and the interaction of EcoRI stabilizes it even more, equivalent to an extension of the duplex by 27.7 bp. To match a p53-DNA complex, one would have to extend the reference duplex by more than 30 bp. It should be noted here, that this method not only provides interaction forces but has also the potential to determine the dissociation constant in one measurement when the binding stoichiometry is known and the titration curve is determined for one target sequence.<sup>[14]</sup> In addition, BiFo-Chip measurements with different pulling velocities may also provide lifetimes and characteristic interaction distances of the prominent activation barriers of protein-DNA interactions on a high-throughput level, which is not possible with binding affinity assays and until now was only accessible with force-based techniques.<sup>[14]</sup> Furthermore, the BiFo-Chip is by principle not affected by unspecific binding of the protein to the chip surface, since the BiFo-Chip detects the interaction between DNA and ligand and not merely the presence of ligand. Therefore, the BiFo-Chip does not exhibit stringency washing or background problems as do binding affinity assays.<sup>[9]</sup>

In summary, we have demonstrated the first high-throughput format for biomolecular force measurements. We characterized with this assay the interaction forces of three different types of unlabeled analytes. This force-based method enables the measurement of new type of interaction parameters that thus far have been inaccessible for high-throughput techniques.

## Experimental Section

The fabrication of the BiFo-chip and the PDMS stamp can be found in the Supporting Information.

*Ligands and Incubation:* Prior to the measurement, the DNA-chips were incubated with the corresponding buffer solution. Synthesis, composition and function of the pyrrole-imidazole hairpin polyamide P1 have been described previously.<sup>[6, 15]</sup> Polyamide measurements were performed in 1× PBS containing 10 nM P1. Commercial grade EcoRI (32 kDa per monomer,  $2 \times 10^6$  U mg<sup>-1</sup> specific activity, 100 000 U ml<sup>-1</sup> stock concentration) was purchased from NEB and used in the experiment directly without further purification at a final concentration of 7 nM. EcoRI buffer solution is composed of 10 mM HEPES, 50 mM DTT, 100 mg ml<sup>-1</sup> BSA, 170 mM NaCl and 1 mM EDTA (pH of 7.6). Wild-type p53DBD consists of residues 94-312 of human p53. Expression and purification of human p53DBD has been described elsewhere.<sup>[12]</sup> The p53DBD buffer is composed of 50 mM potassium phosphate, pH 6.8, 50 mM KCl and 5 mM DTT. The p53DBD measurements were performed at a concentration of 3 μM. All control measurements were carried out with the same buffer solutions but without ligand. Each DNA-chip was incubated for at least 1 h prior to measurement. All experiments were performed at room temperature.

*Contact process, readout and analysis:* A detailed description of the measurement process can be found in a previous paper.<sup>[9]</sup> Briefly, a custom-built contact device mounted on a fluorescence microscope controls contact and separation between PDMS stamp and DNA-chip via a closed-loop piezoelectric actuator. At first, DNA-chip and the soft PDMS stamp are apart. Cy5 is excited with a LED (627 nm peak wavelength) and the fluorescence signal ( $F_A^A$ ) of the DNA-chip is measured. Then Cy3 is excited with a second LED (530 nm peak wavelength) and the fluorescence signal ( $F_D^A$ ) of Cy3 is measured. The PDMS stamp is lowered with the piezoelectric actuator until both surfaces are brought into contact, allowing

to connect strand 3 of the MFPs to the streptavidin on the PDMS surface (complex formation of biotin • streptavidin). After 10 min the PDMS stamp is moved upwards to separate the surfaces with a retract velocity of  $5 \mu\text{m s}^{-1}$ . Afterwards,  $F_A^A$  and  $F_D^A$  is read out a second time. For each region of interest the four fluorescence images ( $F_A^A$  and  $F_D^A$  before contact and after separation) are analyzed to determine the normalized fluorescence intensity with custom-build analysis software written in LabVIEW.

- [1] R. Nutiu, R. C. Friedman, S. Luo, I. Khrebtukova, D. Silva, R. Li, L. Zhang, G. P. Schroth, C. B. Burge, *Nat. Biotechnol.* **2011**, *29*, 659-664.
- [2] F. Kuehner, L. T. Costa, P. M. Bisch, S. Thalhammer, W. M. Heckl, H. E. Gaub, *Biophys. J.* **2004**, *87*, 2683-2690.
- [3] S. B. Smith, Y. J. Cui, C. Bustamante, *Science* **1996**, *271*, 795-799.
- [4] T. R. Strick, J. F. Allemand, D. Bensimon, V. Croquette, *Biophys. J.* **1998**, *74*, 2016-2028.
- [5] C. H. Albrecht, K. Blank, M. Lalic-Mülthaler, S. Hirler, T. Mai, I. Gilbert, S. Schiffmann, T. Bayer, H. Clausen-Schaumann, H. E. Gaub, *Science* **2003**, *301*, 367-370.
- [6] C. Dose, D. Ho, H. E. Gaub, P. B. Dervan, C. H. Albrecht, *Angew. Chem. Int. Ed.* **2007**, *46*, 8384-8387.
- [7] D. Ho, C. Dose, C. H. Albrecht, P. M. D. Severin, K. Falter, P. B. Dervan, H. E. Gaub, *Biophys. J.* **2009**, *96*, 4661-4671.
- [8] D. Ho, K. Falter, P. M. D. Severin, H. E. Gaub, *Anal. Chem.* **2009**, *81*, 3159-3164.
- [9] P. M. D. Severin, D. Ho, H. E. Gaub, *Lab Chip* **2011**, *11*, 856-862.
- [10] G. I. Bell, *Science* **1978**, *200*, 618-627.
- [11] E. Evans, K. Ritchie, *Biophys. J.* **1999**, *76*, 2439-2447.

- [12] A. Dehner, C. Klein, S. Hansen, L. Müller, J. Buchner, M. Schwaiger, H. Kessler, *Angew. Chem. Int. Ed.* **2005**, *44*, 5247-5251.
- [13] T. Strunz, K. Oroszlan, R. Schäfer, H. J. Güntherodt, *Proc. Natl. Acad. Sci. USA* **1999**, *96*, 11277-11282.
- [14] S. J. Koch, M. D. Wang, *Physical Review Letters* **2003**, *91*, 028103.
- [15] D. M. Herman, E. E. Baird, P. B. Dervan, *J. Am. Chem. Soc.* **1998**, *120*, 1382-1391.

Received: ((will be filled in by the editorial staff))  
Revised: ((will be filled in by the editorial staff))  
Published online on ((will be filled in by the editorial staff))

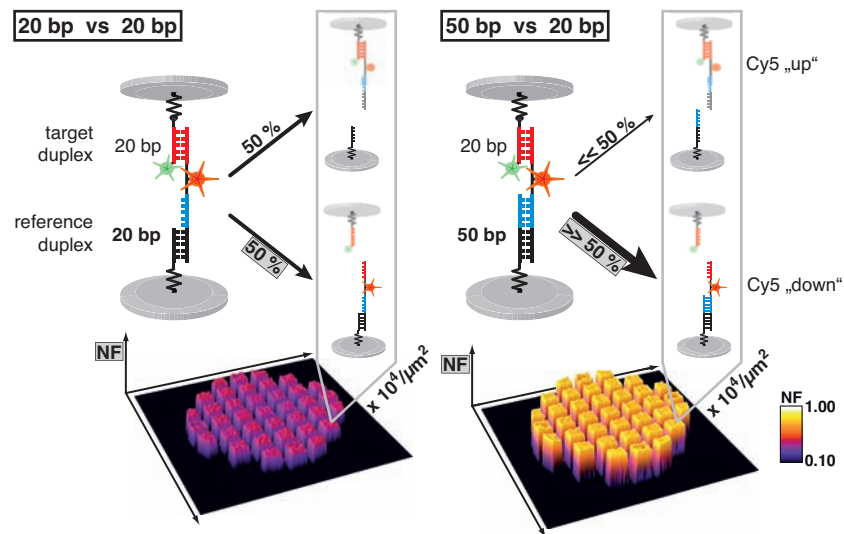


**Figure 1.** Schematics of a BiFo-Chip. The MFPs are composed of two dsDNA duplexes, a target duplex and a reference duplex, which are coupled in series and connected between two surfaces. After separation of the surfaces: 20 bp reference duplex versus 20 bp target duplex results in a normalized fluorescence (NF) of 0.5 (left), while 50 bp reference duplex versus 20 bp target duplex results in a  $NF \gg 0.5$ . In the NF image the contacted and probed areas are clearly visible (microstructure of 100 μm x 100 μm squares).

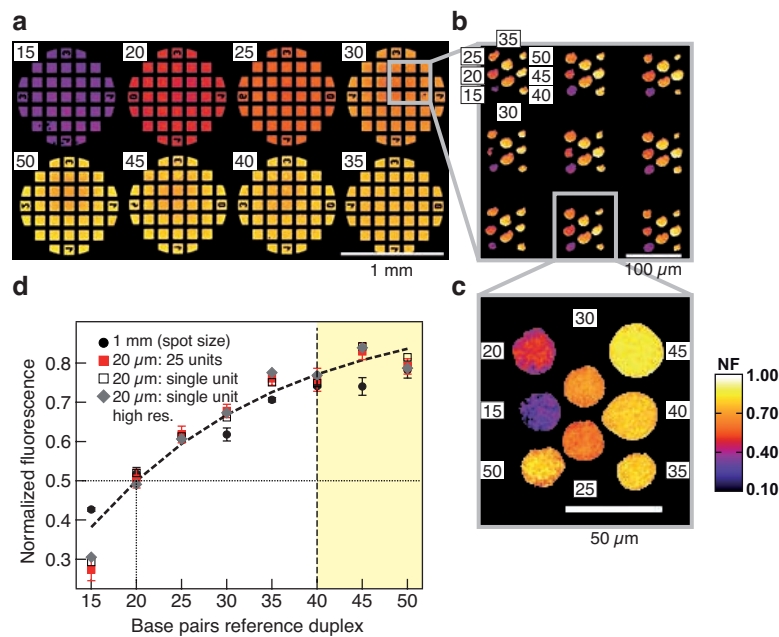


**Figure 2.** Implementation of the BiFo-Chip. Numbers in white boxes specify the reference duplex length in base pairs. **(a)** NF images of a representative BiFo-Chip experiment with a spot-size of 1 mm per type of MFP. **(b)** BiFo-microarray. **(c)** NF high-resolution image of a single BiFo-unit. **(d)** Graph of the mean NF against the reference duplex length. With growing reference duplex length the NF increases from approx. 0.35 at 15 bp to approx. 0.80 at 50 bp. Above a length of 40 bp (light yellow), the rupture forces of the DNA-oligomers reach significantly into B-S transition of DNA at 65 pN, which results in a plateau in NF. Black filled circle: NF-mean and s.e.m. of 32 spots of 1 mm diameter (as in (a)); filled red square: NF-mean and s.e.m. of 25 units BiFo-microarray; black empty square: single, typical BiFo-microarray unit; grey filled diamond: high-res. NF-image (as in (c)).

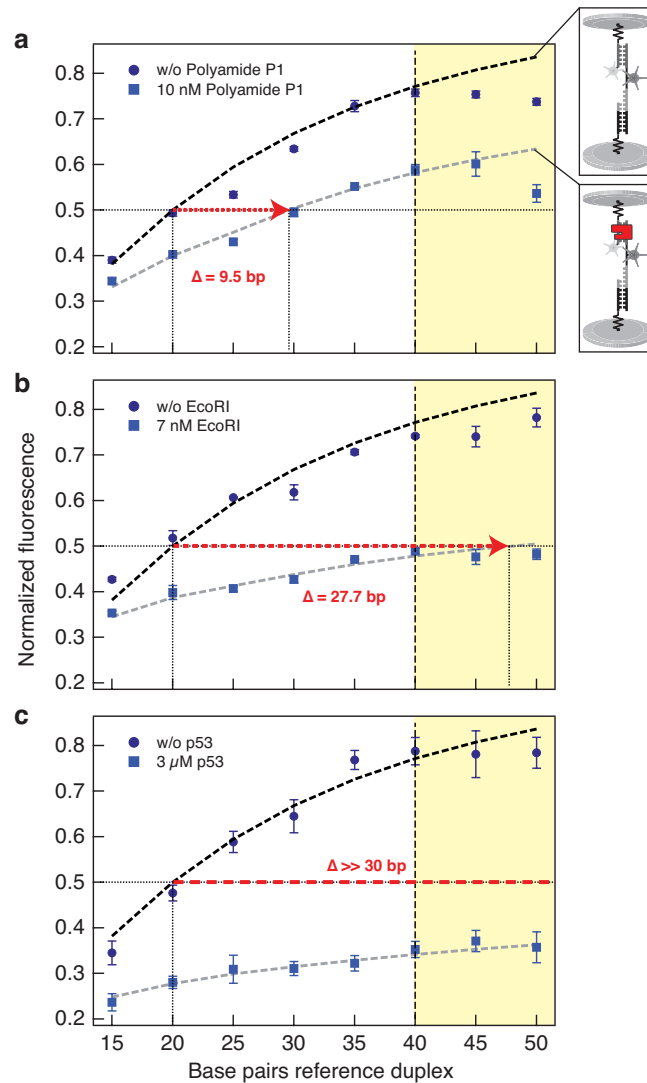


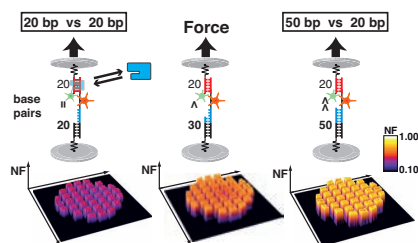
**Figure 3.** Characterization of DNA-binders via the BiFo-Chip. **(a)** Polyamide P1 **(b)** Endonuclease EcoRI **(c)** Transcription factor p53 DNA-binding domain. In all three cases the target duplex carries a specific recognition sequence for the corresponding ligand, while the reference duplex does not. The complex of ligand and target DNA duplex exhibits a higher unbinding force as the target duplex itself. Thus, the NF is shifted to a lower value. The dashed curves represent the analytical solution based on the Bell-Evans two-state model.



**The table of contents entry**

DNA-protein binding force chip

Philip M. D. Severin, and Hermann E. Gaub\*



The binding force chip (BiFo-chip) allows the quantification of DNA-protein interactions. It employs arrays of molecular force probes. Each molecular force probe functions comparable to a balance, which is influenced by the binding of a protein to one of the two DNA duplexes. The BiFo-chip is easy to operate, requires only a quantitative fluorescence microscope and fulfills all essential criteria for high throughput screening.

## Supporting Information

### DNA-protein binding force chip

*Philip M. D. Severin, and Hermann E. Gaub\**

#### ***1. Fabrication of the BiFo-chip (Bottom surface)***

The DNA-chip has been assembled as described previously except for some minor modifications described here.<sup>[1]</sup> DNA oligomers were purchased HPLC grade from IBA GmbH (Goettingen, Germany). Each MFP is composed of three DNA oligomers **1**, **2** and **3**. These 3 DNA strands form 2 hybridized dsDNA duplexes, **1 • 2** and **2 • 3**, which are coupled in series via DNA oligomer **2**. Thereby, DNA oligomer **1** is covalently linked to the glass slide. DNA oligomer **3** is modified with biotin in order to form a link to the top surface (PDMS stamp) after contact. DNA oligomer **1** has an amine-modification at the end of the spacer, which allows covalent linkage to aldehyde-functionalized glass slides (Schott GmbH, Jena, Germany). For the 1 mm spot size DNA-chip, we spotted 1 µl drops of 5× SSC (saline sodium citrate; Sigma-Aldrich GmbH, Munich, Germany) containing 25 µM oligomer **1** on the aldehyde slide in a 4 × 4 pattern and incubated the slide in a saturated NaCl ddH<sub>2</sub>O atmosphere overnight.

For the production of BiFo-microarrays, we deposited the same DNA oligomer **1** solution on the glass slide with a microplotter (GIX, Sonoplot, Middleton, USA). A standard glass capillary (World Precision Instruments, Inc.) with an inner diameter of 5 µm was used, which resulted in spots of the diameter of around 20 µm on the glass slide (dispenser voltage 2 V and 0.1 s dispensing time). The spots were deposited in a hexagonal grid with a 30 µm spot-to-spot distance at a controlled humidity of 65%.

Afterwards, we washed the slide with ddH<sub>2</sub>O containing 0.2% sodium dodecyl sulfate (SDS; VWR Scientific GmbH, Darmstadt, Germany) and thoroughly rinsed it with ddH<sub>2</sub>O. Then, we reduced the resulting Schiff bases with 1% aqueous NaBH<sub>4</sub> (VWR Scientific GmbH, Darmstadt, Germany) for 90 min. Subsequently, the slide was washed with 1× SSC and thoroughly rinsed with ddH<sub>2</sub>O. In order to reduce nonspecific binding, the slide was blocked in 1× SSC containing 4% bovine serum albumin (BSA; Sigma-Aldrich GmbH, Munich, Germany) for 20 min. The 100 nM Cy5-modified oligomer **2** and 200 nM biotin-modified oligomer **3** were hybridized to the latter for 30 min, completing the **1 • 2 • 3** complex on the glass slide. After incubation with DNA oligomer **2** and **3**, the slides were washed with a self-made fluidic system driven by a multi-channel peristaltic pump (Ismatec GmbH, Wertheim-Mondfeld, Germany) to remove any unspecific bound DNA oligomers. The slide was rinsed subsequently with 2× SSC, 0.2× SSC containing 0.1% Tween 20 (VWR Scientific GmbH, Darmstadt, Germany) and 1× PBS each with 50 ml in 5 min. For the BiFo-microarray it is also possible, to deposit the mixture of oligomer **2** and **3** directly with the microplotter. In this

case the glass slide remains fixed in the microplotter in order to keep the position calibration between capillary and slide, while the washing steps are performed.

## 2. Fabrication of the PDMS stamp (Top surface)

The stamp consists of polydimethylsiloxane (PDMS) and was fabricated and functionalized on the surface as described previously.<sup>[2, 3]</sup> Briefly summarized, the PDMS stamps were cut into a  $4 \times 4$  or a single pillar arrangement. Each pillar has a diameter and height of 1 mm, and is furnished with a microstructure on the flat surface: quadratic pads with a side length of 100  $\mu\text{m}$  are separated by 41  $\mu\text{m}$  wide and 5  $\mu\text{m}$  deep trenches, which allow the liquid drainage during the contact and separation process. For surface functionalization, the PDMS was activated overnight in 12.5% hydrochloric acid and subsequently derivatized with (3-glycidyloxypropyl)-trimethoxysilane (ABCRC, Karlsruhe, Germany) to generate epoxide groups.  $\text{NH}_2\text{-PEG-Biotin}$  ( $3400 \text{ g mol}^{-1}$ ; Rapp Polymere, Tuebingen, Germany) was melted at 80 °C, and  $\sim 1 \text{ ml}$  was spotted on each pillar followed by overnight incubation in argon atmosphere at 80 °C. The excess polymers were thoroughly removed with 80 °C hot  $\text{ddH}_2\text{O}$ . Shortly before the experiment, the PDMS was incubated for 120 min with a  $1 \times$  PBS containing 0.4% BSA and  $1 \text{ mg ml}^{-1}$  streptavidin (Thermo Fisher Scientific, Bonn, Germany). Lastly, the PDMS was rinsed with  $1 \times$  PBS containing 0.1% Tween 20 and then gently dried under  $\text{N}_2$  gas flow.

## 3. Oligomer sequences

Oligonucleotides employed had the following sequences and modifications:

**1<sub>15</sub>**, 5'-NH<sub>2</sub>-(T)<sub>20</sub>-CTG ATA AGT CGT CAA-3'

**1<sub>20</sub>**, 5'-NH<sub>2</sub>-(T)<sub>20</sub>-CTG ATA AGT CGT CAA CGT AT-3'

**1<sub>25</sub>**, 5'-NH<sub>2</sub>-(T)<sub>20</sub>-CTG ATA AGT CGT CAA CGT ATG CAA T-3'

**1<sub>30</sub>**, 5'-NH<sub>2</sub>-(T)<sub>20</sub>-CTG ATA AGT CGT CAA CGT ATG CAA TAT GCT-3'

**1<sub>35</sub>**, 5'-NH<sub>2</sub>-(T)<sub>20</sub>-CTG ATA AGT CGT CAA CGT ATG CAA TAT GCT CGC TT-3'

**1<sub>40</sub>**, 5'-NH<sub>2</sub>-(T)<sub>20</sub>-CTG ATA AGT CGT CAA CGT ATG CAA TAT GCT CGC TTA CTA A-3'

**1<sub>45</sub>**, 5'-NH<sub>2</sub>-(T)<sub>20</sub>-CTG ATA AGT CGT CAA CGT ATG CAA TAT GCT CGC TTA CTA ACT GGT-3'

**1<sub>50</sub>**, 5'-NH<sub>2</sub>-(T)<sub>20</sub>-CTG ATA AGT CGT CAA CGT ATG CAA TAT GCT CGC TTA CTA ACT GGT ATA GC-3'

**2<sub>P1</sub>**, 3'-GAC TAT TCA GCA GTT GCA TAC GTT ATA CGA GCG AAT GAT TGA CCA TAT CG-(T)<sub>6</sub>-5'-(Cy5)-5'-(T)<sub>6</sub>-AGA TAT GGT CAA TCA TTC GC-3'

**3<sub>P1</sub>**, 5'-biotin-(T)<sub>10</sub>-GCG AAT GAT TGA CCA TAT CT(Cy3)-3'

**2<sub>EcoRI</sub>**, 3'-GAC TAT TCA GCA GTT GCA TAC GTT ATA CGA GCG AAT GAT TGA CCA TAT CG-(T)<sub>6</sub>-5'-(Cy5)-5'-(T)<sub>6</sub>-AGA TAT GCG AAT TCA TTC GC-3'

**3<sub>EcoRI</sub>**, 5'-biotin-(T)<sub>10</sub>-GCG AAT GAA TTC GCA TAT CT(Cy3)-3'

**2<sub>p53DBD</sub>**, 3'-GAC TAT TCA GCA GTT GCA TAC GTT ATA CGA GCG AAT GAT TGA CCA TAT CG-(T)<sub>6</sub>-5'-(Cy5)-5'-(T)<sub>6</sub>-GAA CAT GTC CCA ACA TGT TG-3'

**3<sub>p53DBD</sub>**, 5'-biotin-(T)<sub>10</sub>-CAA CAT GTT GGG ACA TGT TCT(Cy3)-3'

## 4. Analytical model of the BiFo-Chip measurements

In the following section we present the deduction of an analytical model for the BiFo-Chip. The central aspect of this model is based on the Bell-Evans model. The Bell-Evans model<sup>[4, 5]</sup> has been proven to accurately describe experimental results in the field of single molecule force spectroscopy in many different cases, such as the rupture of the biotin-streptavidin

interaction.<sup>[6]</sup> Even though the Bell-Evans model is a two-state model, it has been shown that it describes to a first approximation very well more complex interaction patterns such as the unbinding of a hybridized dsDNA into two single DNA strands in a shear-geometry, a result which has been demonstrated experimentally multiple times.<sup>[7-9]</sup> Typically, the Bell-Evans model is used to analyze experimental data and extract the natural dissociation rate  $k_{off}$  and the potential width  $\Delta x$  for a certain molecular interaction.

Here, we approach the Bell-Evans model by inserting experimentally determined parameters  $\Delta x$  and  $k_{off}$  for the force-based dissociation of hybridized dsDNA oligomers in order to obtain the bond rupture probability density function  $p(f, \dot{f})$  for a given loading rate ( $\dot{f}$ ):

$$p(f, \dot{f}) = \frac{k_{off}}{\dot{f}} \cdot \exp\left(\frac{f \cdot \Delta x}{k_B T}\right) \cdot \exp\left(-\frac{k_{off}}{\dot{f}} \cdot \int_0^f du \cdot \exp\left(\frac{u \cdot \Delta x}{k_B T}\right)\right)$$

where  $k_B$  is the Boltzmann constant,  $T$  is the temperature and  $\dot{f} = df/dt$  is the loading rate.

In order to calculate  $p(f, \dot{f})$  for different long dsDNA oligomers, the corresponding  $\Delta x$  and  $k_{off}$  values must be known. In a previous study the correlation of  $\Delta x$  and  $k_{off}$  with the length of the dsDNA ( $n$  = number of base pairs) was experimentally characterized.<sup>[9]</sup> Thereby, they found the following relation for  $\Delta x$  and  $k_{off}$ :

$$k_{off}(n) = 10^{\alpha - \beta n} \cdot s^{-1} \quad \text{and} \quad \Delta x(n) = (t + n \cdot m) \cdot \text{\AA}$$

with  $\alpha = (3 \pm 1)$ ,  $\beta = (0.5 \pm 0.1)$ ,  $t = (7 \pm 3)$  and  $m = (0.7 \pm 0.3)$ .

Based on the Bell-Evans model and the relation between  $\Delta x$  and  $k_{off}$  with the number of base pairs, an analytical relation for NF can be deduced as follows. The molecular force probe consists of two dsDNA duplexes that are coupled in series. The probability with which one of the duplexes ruptures is measured by NF, and can be calculated from the overlap of the bond rupture probability density functions of the two DNA duplexes using the Bell-Evans model. Hereby, the NF is defined as the ratio of broken target bonds to the total amount of probed MFPs.

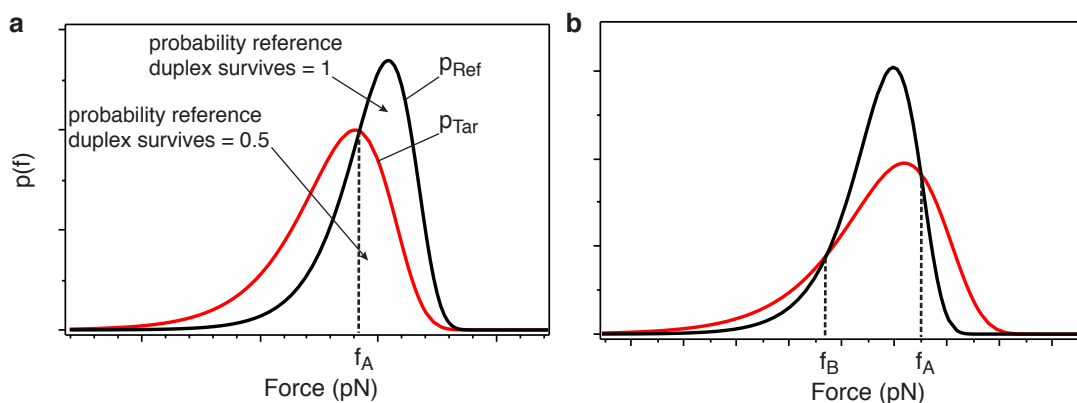


**Figure S1.** Calculated probability density functions. (a) Overlapping probability density functions with one intersection. (b) Arbitrary case with two intersections.

Figure S1 (a) shows an example for two overlapping probability density functions (e.g., 20 bp and 30 bp DNA duplexes). When the two probability density functions overlap, three areas can be distinguished (Figure S1 (a)); one area represents the probability that the reference duplex survives. In the overlap area, the probability that the reference duplex (respectively the

target duplex) survives is 0.5. After some simplification steps, this can be expressed in the following mathematical equation:

$$NF(\dot{f}, n_R, n_T) = \frac{1}{2} \left[ 1 + \int_{f^A}^{\infty} df (p_{REF}(f, \dot{f}, n_R) - p_{TAR}(f, \dot{f}, n_T)) \right]$$

This equation describes the MFP without ligand (black dashed curve in Figure 2 and Figure 3), since in this case the two probability density functions have only one intersection ( $n_T = n_R$ ) = number of base pairs of the target (reference) duplex). A generalization for arbitrary parameters  $\Delta x$  and  $k_{off}$ , which can result in probability density functions with two intersections (see Figure S1 (b)), is fulfilled by the following equation:

$$NF(\dot{f}, n_R, n_T) = \frac{1}{2} \left[ 1 + \int_{f^A}^{\infty} df (p_{REF}(f, \dot{f}, n_R) - p_{TAR}(f, \dot{f}, n_T)) + \int_{f^B}^{\infty} df (p_{REF}(f, \dot{f}, n_R) - p_{TAR}(f, \dot{f}, n_T)) \right]$$

In the case of only one intersection (i.e.  $f_B = 0$ ), this equation simplifies to the previous one. Finally, the applied loading rate must be determined before the NF can be calculated. This was already described in detail by Albrecht et al.<sup>[10]</sup> Briefly, since the PDMS-stamp is elastic, the stamp deforms in the separation process, which results in a vertical separation velocity acting on the MFPs that is different from the applied one. In order to assess the applied loading rate, the stamp-chip separation process is recorded on the inverted microscope. Stamp-chip contact areas are separated at the edge of a propagating cleft at which the MFPs are loaded and ruptured. Interference patterns emerge after separation behind the moving cleft, which allow measurement of the angle of the propagating cleft between stamp and chip. This angle translates the measured lateral separation velocity into a vertical separation velocity, which acts directly on the MFPs. By knowing the separation velocity acting on the MFPs, and the length of the PEG- and poly-t-spacer that define the spring constant of the system, the most probable loading rate can be estimated as described earlier.<sup>[10]</sup> Here, we applied in all measurements a separation velocity of  $5 \mu\text{m s}^{-1}$  on the PDMS-stamp, which resulted on average in a most probable loading rate of  $1.43 \times 10^6 \text{ pN s}^{-1}$ .

We applied the NF-model to the measured BiFo-chip data. Fitting the values for  $\alpha$ ,  $\beta$ ,  $t$  and  $m$  resulted in the optimized curve progression shown in Figures 2 and 3 ( $\alpha = 2.8$ ,  $\beta = 0.48$ ,  $t = 6.4$  and  $m = 0.76$ ). The values  $\alpha$ ,  $\beta$ ,  $t$  and  $m$  are within the error bars of the values determined by Strunz et al.<sup>[9]</sup> The fitted values for  $\alpha$  and  $\beta$  are slightly lower than those obtained by Strunz et al., which reflects a lower dependence of  $k_{off}$  on the number of base pairs.  $\Delta x$  showed a slightly higher base pair-dependence. This may be due to the fact that the DNA duplexes used for BiFo-Chip have a GC-content of 40% to 42%, while the DNA oligomers used by Strunz et al. had a GC-content of around 60% to 65%. Furthermore, in the article by Strunz et al., only 3 different oligomers were investigated, while the BiFo-Chip uses 8 different long reference duplexes, which should allow a more precise measurement.

[1] P. M. D. Severin, D. Ho, H. E. Gaub, *Lab Chip* **2011**, *11*, 856-862.

[2] D. Ho, C. Dose, C. H. Albrecht, P. M. D. Severin, K. Falter, P. B. Dervan, H. E. Gaub, *Biophys. J.* **2009**, *96*, 4661-4671.

[3] C. H. Albrecht, H. Clausen-Schaumann, H. E. Gaub, *Journal of Physics: Condensed Matter* **2006**, *18*, 581-599.

[4] G. I. Bell, *Science* **1978**, *200*, 618-627.

[5] E. Evans, K. Ritchie, *Biophys. J.* **1999**, *76*, 2439-2447.

- [6] R. Merkel, P. Nassoy, A. Leung, K. Ritchie, E. Evans, *Nature* **1999**, *397*, 50-53.
- [7] J. Morfill, F. Kuehner, K. Blank, R. A. Lugmaier, J. Sedlmair, H. E. Gaub, *Biophys. J.* **2007**, *93*, 2400-2409.
- [8] P. M. D. Severin, X. Zou, H. E. Gaub, K. Schulten, *Nucleic Acids Research* **2011**, *39*, 8740-8751.
- [9] T. Strunz, K. Oroszlan, R. Schäfer, H. J. Güntherodt, *Proc. Natl. Acad. Sci. USA* **1999**, *96*, 11277-11282.
- [10] C. H. Albrecht, G. Neuert, R. A. Lugmaier, H. E. Gaub, *Biophys. J.* **2008**, *94*, 4766-4774.

# Cytosine methylation alters DNA mechanical properties

Philip M. D. Severin<sup>1,2</sup>, Xueqing Zou<sup>3,4</sup>, Hermann E. Gaub<sup>1,2,\*</sup> and Klaus Schulten<sup>3,5,\*</sup>

<sup>1</sup>Lehrstuhl für Angewandte Physik and Center for Nanoscience (CeNS), Ludwig-Maximilians-Universität, Amalienstrasse 54, 80799 Munich, <sup>2</sup>Munich Center For Integrated Protein Science (CIPSM), Ludwig-Maximilians-Universität, Butenandtstrasse 5-13, 81377 Munich, Germany, <sup>3</sup>Beckman Institute, University of Illinois, Urbana, Illinois, USA, <sup>4</sup>School of Physics, Peking University, Beijing, China and <sup>5</sup>Department of Physics, University of Illinois, Urbana, Illinois, USA

Received March 27, 2011; Revised June 14, 2011; Accepted June 28, 2011

## ABSTRACT

**DNA methylation plays an essential role in transcriptional control of organismal development in epigenetics, from turning off a specific gene to inactivation of entire chromosomes. While the biological function of DNA methylation is becoming increasingly clear, the mechanism of methylation-induced gene regulation is still poorly understood. Through single-molecule force experiments and simulation we investigated the effects of methylation on strand separation of DNA, a crucial step in gene expression. Molecular force assay and single-molecule force spectroscopy revealed a strong methylation dependence of strand separation. Methylation is observed to either inhibit or facilitate strand separation, depending on methylation level and sequence context. Molecular dynamics simulations provided a detailed view of methylation effects on strand separation, suggesting the underlying physical mechanism. According to our study, methylation in epigenetics may regulate gene expression not only through mechanisms already known but also through changing mechanical properties of DNA.**

## INTRODUCTION

DNA methylation is a fundamental epigenetic mechanism of the gene-regulatory machinery in vertebrates (1–3). It occurs at the 5 position of cytosine in CpG dinucleotides, replacing a hydrogen atom by a methyl group without interfering with CG base pairing. Although methylation does not change the DNA sequence itself, strong evidence exists for a correlation between DNA

methylation and alteration of gene expression (4–6). For example, in healthy cells, CG-rich regions, so-called CpG islands, of DNA are usually not methylated, but hypermethylation of CpG islands in the promoter regions of genes is often observed in cancer cells (7–9). DNA methylation also underlies genomic imprinting, where the expression of a gene depends on whether it was inherited from mother or father (10). Moreover, the pattern of DNA methylation can be stably inherited during DNA replication via maintenance DNA methyltransferases (11).

DNA methylation usually conducts transcriptional control in two ways. First, methylation prevents the binding of transcription factors to promoters, which is a simple and direct mechanism. Second, effects of DNA methylation are mediated by so-called methyl-CpG-binding domain (MBD) proteins, which recognize methylation sites on DNA (12,13). Such proteins bind to methylated DNA (mDNA) and regulate genes by further blocking the binding of RNA polymerase to the promoter (7). Although several DNA binding proteins were identified to be sensitive to methylation (14–18), the mechanism of methylation recognition is still poorly understood. Furthermore, DNA methylation can alter the structure and stability of chromatin relevant for transcriptional control of genes (19–21). For instance, nucleosomes assembled with non-methylated DNA (nDNA) appear less stable than those assembled with mDNA (22,23).

Melting curve measurements showed a minor change to higher or lower values of the melting temperature depending on the adjacent bases (24,25). In NMR experiments methylation of the CpG step was observed to reduce the dynamics of the DNA phosphate-sugar backbone (26). Molecular dynamics (MD) simulations suggest that steric hindrance and hydrophobicity of the methyl groups are causing reduced flexibility of DNA (27,28).

\*To whom correspondence should be addressed. Tel: 217-244-1604; Fax: 217-244-6078; Email: kschulte@ks.uiuc.edu  
Correspondence may also be addressed to Hermann E. Gaub. Tel: +49 89 2180 3172; Fax: +49 89 2180 2050; Email: gaub@physik.uni-muenchen.de

The authors wish it to be known that, in their opinion, the first two authors should be regarded as joint First Authors.

Apparently, the dynamics of DNA has an influence on protein-DNA binding specificities (29) and it is possible that methylation-induced alteration of local DNA dynamics contributes to the methylation recognition. Furthermore, prior studies suggest that methylation has an effect on the bending flexibility of DNA (30,31). Because formation of chromatin involves wrapping of DNA around the histone octamer, which requires DNA flexibility, the structure of chromatin could also be influenced by DNA methylation.

All experiments mentioned assessed thermodynamic equilibrium properties of DNA. However, the biological function of DNA involves non-equilibrium mechanical processes, such as DNA replication and transcription (32). For example, T7 DNA polymerase functions as a molecular motor and can work against a maximum DNA template tension of  $\sim 34$  pN (33). DNA and RNA helicases, another type of motor protein, are involved in nearly all aspects of DNA and RNA metabolism to separate two hybridized nucleic acid strands. As recently shown, the helicases' processivity is strongly affected by forces of only a few pN (34,35). The question arises if DNA methylation has an influence on the mechanical stability of double-stranded DNA (dsDNA) under load, in particular, on the forces needed for strand separation, which would affect translocation of helicases on DNA. In an earlier study it was shown through electromechanical experiments and simulation that cytosine methylation renders dsDNA, stretched in the electric field of a synthetic nanopore, more ordered than native dsDNA does (36).

In the present study, we conducted complementary types of force measurements using a molecular force assay (MFA) (37) and single-molecule force spectroscopy (38,39) to characterize the mechanical properties of DNA, and how they change upon methylation. Steered MD simulations (40) were carried out to characterize the influence of methylation on force-driven strand separation at atomic resolution. A strong influence of methylation on the mechanical stability of strand separation of dsDNA as well as a significant change in mechanical properties of DNA due to methylation was found in experiments. In MD simulations both mDNA and nDNA were observed to undergo a B-DNA  $\rightarrow$  zipper-like DNA transition during force-induced strand separation, zipper-like mDNA containing less faults, called bubbles (41), than zipper-like nDNA does; the concentration of faults was seen to control the propensity for strand separation such that methylation influences strongly the rupture force of DNA duplexes pulled at their two 5'-ends.

## METHODS

### MFA DNA-chip

The DNA-chip for the MFA measurements, shown in Figure 1, has been assembled as described by Severin *et al.* (37) except for some modifications. DNA oligomers labeled **1** and **2** form the bottom duplex, oligomers **2** and **3** the top duplex.

At the bottom surface, DNA oligomer **1** is amine-modified for covalent linkage to aldehyde-functionalized

glass slides. In the experiments with three methylation levels the bottom duplex **1•2** contained zero, one or three 5-methylcytosine (mC) per strand. In order to avoid artifacts in the force measurements, which could be caused by structural changes of the DNA duplex or unwanted hybridizations of the strands, we chose a well-characterized DNA sequence with minimal self-complementarity and, hence, minimal hairpin-formation (42). The top surface of the chip was a polydimethylsiloxane (PDMS) stamp, fabricated and functionalized as described previously (43,44). DNA oligomer **3** was biotinylated and linked to the stamp. The sequences of the DNA oligomers and details of the preparation of the MFA DNA-chip are provided in [Supplementary Data](#).

### MFA contact process, readout and analysis

A complete description of the overall MFA measurement can be found in a previous paper (37). A custom-built contact device is mounted on a fluorescence microscope to control contact and separation between PDMS stamp and DNA-chip via a closed-loop piezoelectric actuator. All experiments are carried out in  $1\times$  PBS (phosphate buffered saline) at room temperature. Initially, the DNA-chip and the soft PDMS stamp are separated. Cy5 is excited and the fluorescence signal ( $F_A^A$ ) of the DNA-chip is measured. Subsequently Cy3 is excited and the fluorescence signal ( $F_D^A$ ) of Cy5 is measured. Both surfaces are brought into contact, allowing to connect strand **3** of the MFPs to the streptavidin on the PDMS surface via biotin • streptavidin complexation (Figure 1a). After 10 min the surfaces are separated with a retract velocity of  $5\ \mu\text{m/s}$  and  $F_A^A$  and  $F_D^A$  read out a second time. Typically around  $10^4$  duplicates of molecular force probes (MFPs) are probed in parallel per  $\mu\text{m}^2$ .

For each pad of a stamp the four fluorescence images ( $F_A^A$  and  $F_D^A$  before contact and after separation) are analyzed to determine the normalized fluorescence intensity (NF) following (37). The NF is defined as the ratio between broken reference bonds and total amount of MFPs that have been under load and reflects the relative mechanical stability between the target duplex **1•2** and the reference duplex **2•3** of a MFP. Higher values for the NF denote an increased mechanical stability of the target duplex over the reference duplex.

### Atomic force microscopy measurement and analysis

All atomic force microscopy (AFM) experiments were performed at room temperature in PBS buffer. Sample preparation is described in [Supplementary Data](#). Spring constants  $k$  of the cantilever were determined in solution employing the expression (45,46)  $k = k_B T / \langle d_C^2 \rangle$  where  $k_B$  is the Boltzmann constant,  $T$  the absolute temperature and  $\langle d_C^2 \rangle$  the mean square displacement of the free cantilever end in solution. In this way typical values for spring constants of 10 to 15 pN/nm for the MLCT-C and around 70 pN/nm for the BL-AC40 were determined. The experiments were carried out with constant retract velocity and the contact time on the surface was adjusted to obtain single DNA binding events. In order to achieve satisfactory statistics, several hundred force-curves were recorded



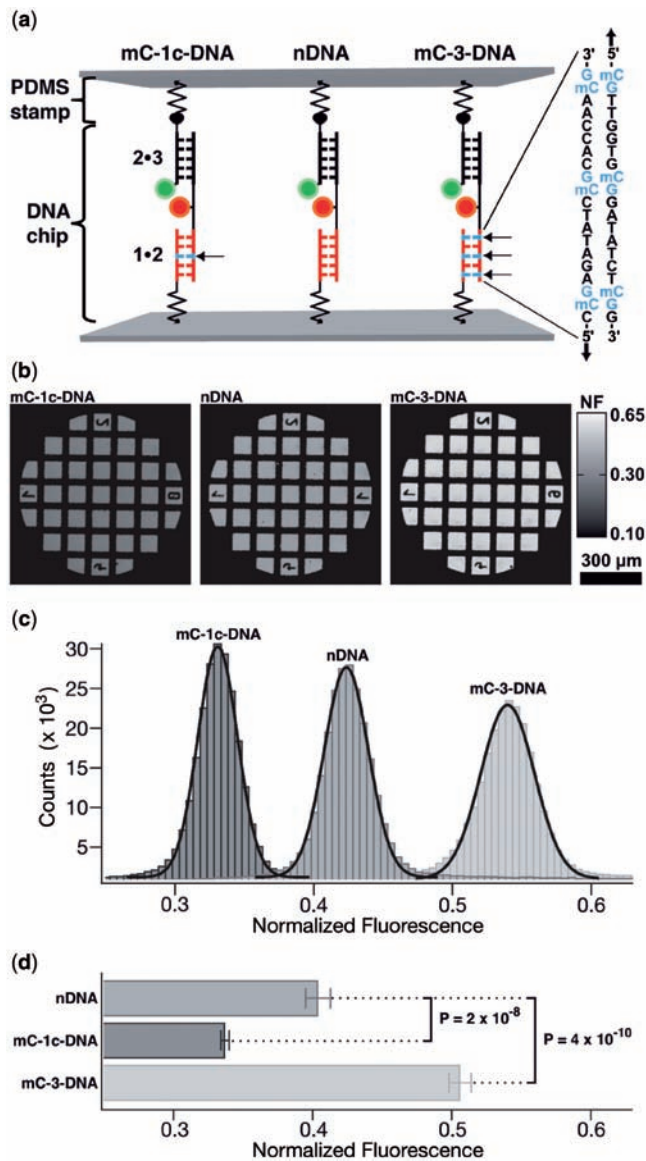


**Figure 1.** (a) Schematic representation of MFA. The MFPs are anchored via DNA strand 1 to the lower surface. Each MFP is comprised of DNA strands 1, 2 and 3. These three DNA strands from two DNA duplexes are coupled in series, the target duplex 1•2 involving nDNA, DNA with one center-methylated CpG step (mC-1c-DNA) and DNA with three methylated CpG steps (mC-3-DNA) per strand as well as a reference duplex 2•3. DNA strand 2 carries a Cy5 as fluorescent marker and strand 3 a Cy3 fluorescence marker at the one end and a biotin at the other end for coupling to streptavidin on the upper surface. (b) NF images of one representative MFA experiment. The NF images constitute a quantitative result of the comparison of the unbinding forces between reference and target duplex. In the NF image the contacted and probed area of the PDMS stamp is clearly visible. Each pad of the PDMS stamp has a diameter of 1 mm and a microstructure of  $100\ \mu\text{m} \times 100\ \mu\text{m}$ . Due to the highly parallel measurement format around  $10^4$  MFPs are probed per  $\mu\text{m}^2$ . (c) Histograms of the three NF images in (b). The Gaussian fit of the histograms results in the following mean values and standard deviations:  $\text{NF}(\text{nDNA}) = (0.424 \pm 0.016)$ ,  $\text{NF}(\text{mC-1c-DNA}) = (0.331 \pm 0.014)$  and  $\text{NF}(\text{mC-3-DNA}) = (0.539 \pm 0.019)$ . (d) Analysis of six individual experiments. Each experiment consists on average of  $4 \times 13$  analyzed pads. mC-1c-DNA shows a lower and mC-3-DNA a higher mean rupture force compared to nDNA.

for every distinct retract velocity. To obtain information about the potential width  $\Delta x$  and the natural dissociation rate  $k_{\text{off}}$  of the DNA duplexes, several experiments were carried out, each at a different retract velocity ranging from 150 nm/s to 20  $\mu\text{m/s}$ .

The analysis of the force–extension curves was performed as described previously (47), based on the Bell-Evans-model (48,49) and using custom-made analysis software (Igor Pro 5.03, Wave Metrics). The rupture forces and corresponding loading rates of one experiment at one distinct retract velocity were plotted in two histograms, force histogram (Figure 2c) and loading rate (plotted logarithmically) histogram (Figure 2d), both fitted to a Gaussian distribution to determine the maxima of the particular histograms. These maxima were determined for each retract velocity experiment and then plotted (see Figure 2f) in a force versus loading rate (plotted logarithmically) graph; through a linear fit of the graph the natural dissociation rate at zero force and the potential width  $\Delta x$  of the DNA duplex were determined.

### MD simulations

Non-methylated DNA (nDNA), center-methylated DNA (cDNA) and fully-methylated DNA (fdDNA), as employed in the experiments, were studied in steered molecular dynamics (SMD) simulations. In each simulation, a DNA was placed in a water box of size  $300\ \text{\AA} \times 60\ \text{\AA} \times 60\ \text{\AA}$  and neutralized with 100 mM KCl, amounting to 87  $\text{K}^+$  and 47  $\text{Cl}^-$  ions. The resulting system is shown in Figure 3a. Each simulated system contained about 110 000 atoms. Simulations were performed using NAMD 2.6 (50). The DNA models employed and simulation details are provided in [Supplementary Data](#).

SMD simulations, in which external forces are applied to a group of atoms, enable researchers to conduct single-molecule experiments *in silico* and see biomolecular mechanics in action. For a review of SMD simulations see (40,51,52). In our SMD simulations, one 5'-end of DNA was fixed, and the other 5'-end was pulled, as shown in Figure 3b. Three pulling conditions were applied: (i) constant velocity pulling at 10  $\text{\AA/ns}$ ; (ii) constant velocity pulling at 1  $\text{\AA/ns}$ ; and (iii) constant force pulling at 200 pN. In constant velocity SMD simulations, the 5'-end of DNA is attached to one end of a virtual spring; the other end of the spring is moved at a constant velocity  $v$  along the stretching  $x$ -direction and the force  $f$  applied on the 5'-end of DNA is determined through the extension of the virtual spring:  $f = -k[x(t) - x(t_0) - v(t - t_0)]$ . In constant force SMD simulations, a force along the stretching direction is continuously applied on the 5'-end of DNA. Five independent SMD simulations with 10  $\text{\AA/ns}$ -pulling velocity were conducted for nDNA, cDNA and fdDNA; one SMD simulation with 1  $\text{\AA/ns}$ -pulling velocity covered 118 ns for each DNA; the constant force simulation covered 90 ns for nDNA and fdDNA.

Due to limited computational resources, we could not employ slower pulling velocities. Because of the high pulling velocity in our SMD simulations, the rupture force of DNA seen ( $\sim 1000$  pN) is much higher than the

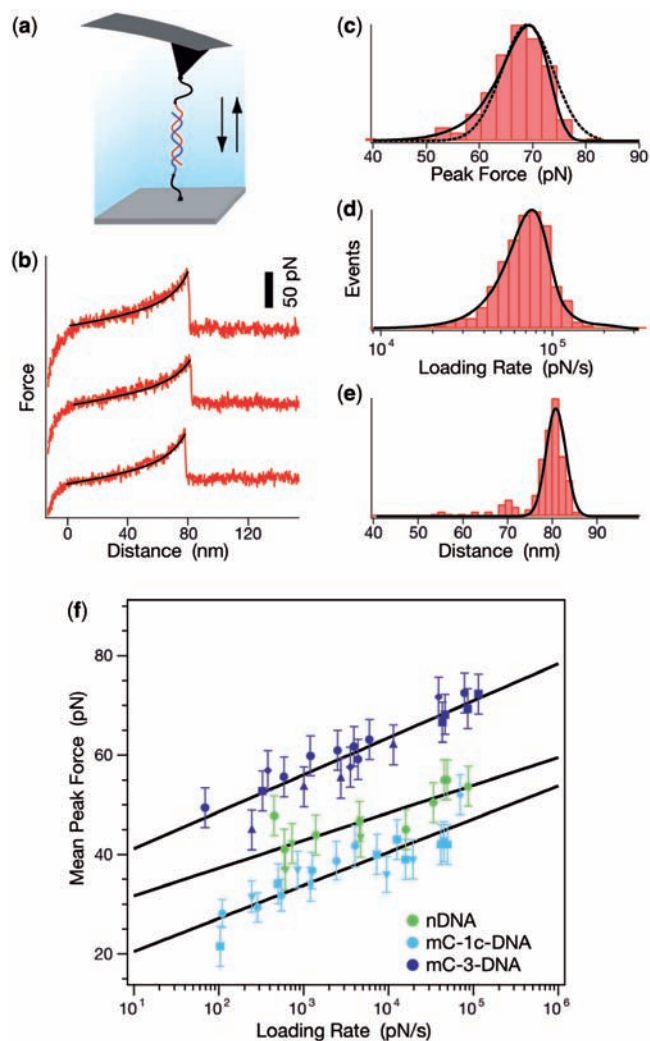


**Figure 2.** (a) Single-molecule-force-spectroscopy setup. Complementary single strands of methylated and non-methylated 20 bp DNA duplexes possessing a thiol-group at their 5'-ends were covalently immobilized on amino-functionalized glass slides and cantilevers using hetero-bifunctional PEG spacers. (b) Typical force-extension curves of the mC-3-DNA duplex. The force-extension curves show three sequential rupture events of a hybridized 20 bp DNA duplex, recorded at a pulling velocity of  $15 \mu\text{m/s}$ . The force-extension curves of the PEG-DNA complex follow the two-state freely jointed chain-fit (black). (c) Typical histogram of the unbinding force of the mC-3-DNA duplex, i.e. the peak force in (b), at a pulling velocity of  $15 \mu\text{m/s}$ . The histogram contains approximately 300 rupture events and the mC-3-DNA duplex dissociates at a mean force of 68 pN. The histogram is fitted with the probability density function  $p(F)$  (solid curve) and a Gaussian (dotted curve). (d) Histogram of loadings-rates corresponding to (c); the loading rate is the slope of the curves in (b) just before the peak (rupture) force, multiplied by the pulling velocity. The histogram is fitted with the probability density function  $p(F)$  (black). (e) Histogram of the rupture distance distribution corresponding to (c) and (d); the distance is the value corresponding to the peak force in (b). (f) Graph showing the most probable rupture force plotted against the corresponding most probable loading rate for nDNA, mC-1c-DNA and mC-3-DNA. The data points were gained from Gaussian fits of the rupture force histogram [see (c)] and of the histogram of the loading rates [see (d)]. Experimental results conducted with the same cantilever for nDNA, mC-1c-DNA or mC-3-DNA are depicted with one type of marker. The data points are fitted to a straight line according to the loading-rate-based analysis method yielding the values of  $\Delta x$  and  $k_{\text{off}}$  as given in the text.

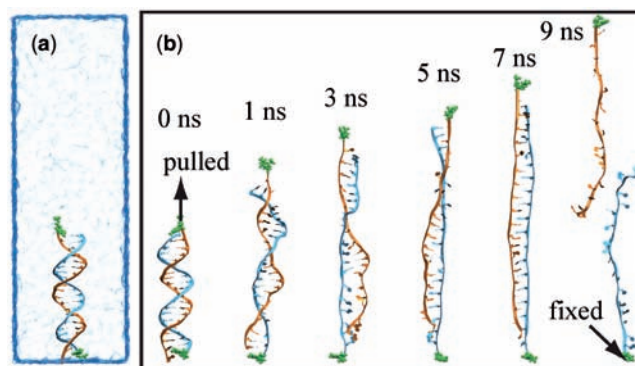


**Figure 3.** Strand separation of DNA under tension from simulation. (a) Simulated system of dsDNA in a bath of solvent and ions, as described in 'Methods' section. (b) Snapshots of DNA during a steered molecular dynamics simulation (simulation F1, see Supplementary Table S1). The atoms, at the 5'-end of the DNA strands, subject to constraint force (at bottom) and stretching force (at top), are highlighted in green. A movie (Supplementary Movie S1) showing the strand separation of DNA is provided in Supplementary Data.

experimental value ( $\sim 100$  pN). Hence, we conducted the constant force pulling SMD simulation with a force value of 200 pN for nDNA and fDNA. Supplementary Table S1 lists all the simulations carried out. The relationship of simulated and measured rupture forces has been discussed extensively by Sotomayor and Schulten (40).

The interaction free energy of DNA, e.g. base pairing and base stacking interaction, stabilizes double stranded DNA against spontaneous dissociation of two strands. Subjected to external pulling force, B-form DNA undergoes a series of conformational changes, as shown in Figure 3b. Monitoring the applied force and the length of stretched DNA in the simulations, we obtained the force-extension curve of DNA. The length of DNA is defined as the distance between the  $C_{\alpha}$  atoms of the fixed 5'-end cytosine and the pulled 5'-end cytosine. To further characterize the thermodynamics of the force-induced dsDNA dissociation process, we monitored the time evolution of the number of base pairs and the stacking energy of DNA. A base pair is considered broken when the distance between hydrogen bond acceptor atom and donor atom exceeds  $3 \text{ \AA}$ . Since the electrostatic contribution to DNA base stacking interaction is small (53), the stacking energy of each nucleotide was obtained by just calculating the van der Waals energy between its neighbors and itself. Most of the analysis of MD results and respective figures were prepared using the software VMD (54).

## RESULTS

We first show that 5-cytosine methylation of dsDNA has a significant effect on strand separation as observed in MFA and AFM stretching experiments. To explain these findings, we examine the methylation-dependent stress-strain behavior of DNA in SMD simulations that provide a detailed view of the role of methylation on strand separation.

### Determination of the mechanical stability of mDNA by MFA measurements

The MFA introduced in Figure 1 is a sensitive method to experimentally characterize DNA strand separation (37). The sensitivity of single molecule force spectroscopy by AFM, optical tweezers or magnetic tweezers is typically limited by thermal fluctuations of the force sensor. Shrinking of the sensor results in an elevated sensitivity (55) and in the MFA experiments we utilize a molecular bond as an extremely small force sensor, in our case the bonding between the strands of a DNA duplex. In fact, our MFA measurement directly compares the stability of a DNA strand duplex against the stability of a reference duplex under the same experimental (solvent, force actuator, etc.) conditions. The MFA functions here like a scale that balances a target weight against a reference weight. In comparison to common single molecule force spectroscopy, the strand separation of DNA duplexes is examined in MFA for different sequences within a single experiment due to the highly parallel format of the assay.

The experimental setup of the MFA at a molecular level consists of molecular force probes (MFPs). The MFPs are composed of two DNA duplexes, a target duplex **1 • 2** and a reference duplex **2 • 3**, which are coupled in series and connected between two surfaces (see Figure 1a and 'Methods' section). Here, the target DNA duplex is 20 bp long and contains zero (nDNA), one (mC-1c-DNA) or three (mC-3-DNA) 5-methylcytosines (mC) per strand, while the reference duplex is the same for all three different MFPs. About  $10^4$  MFPs per  $\mu\text{m}^2$  are anchored in parallel between a glass slide (lower surface) and a PDMS stamp (upper surface). The different MFPs are immobilized as well separated spots on the glass substrate.

During separation of the two surfaces, a force builds up gradually in the MFPs until one of their two DNA duplexes ruptures, either the target duplex or the reference duplex. After separation, the ratio of ruptured target to reference duplexes is read out via the fluorescence signal of the MFPs on the lower surface and analyzed to obtain the normalized fluorescence (NF). The NF is defined as the ratio of broken reference bonds to the total amount of MFPs that have been under load. Thus, the NF is a measure for the relative mechanical stability between target and reference DNA duplexes of a MFP: a higher NF denotes a mechanical stability of the target duplex elevated over that of the reference duplex.

A representative result of a typical experiment is shown in Figure 1b, c. The Gaussian fits of the histograms of three NF-images result in the following means and standard deviations:  $\text{NF}(\text{nDNA}) = (0.424 \pm 0.016)$ ,  $\text{NF}(\text{mC-1c-DNA}) = (0.331 \pm 0.014)$  and  $\text{NF}(\text{mC-3-DNA}) = (0.539 \pm 0.019)$ . The difference in NF reflects a significant difference in mean rupture force between nDNA, mC-1c-DNA and mC-3-DNA.

We attribute the deviation of NF for nDNA from the expected value of 0.5 to two possible effects. First, Cy3 directly attached to the end of a DNA duplex predominantly stacks on it like an additional base pair (56) and has a stabilizing effect on the DNA duplex (57). This might lead to a more stabilized reference duplex and, thus, to a

lower NF. Since all measured MFPs comprise the same reference duplex, the relative difference between the three MFPs is not influenced. Second, the MFPs are attached to different surfaces; DNA duplexes are sensitive to solution conditions such as pH value and ionic strength (58), which may differ depending on the proximity of the DNA duplex to the PDMS (top) or the glass surface (bottom). To minimize surface effects, the DNA duplexes are separated by spacers from the substrates.

After collecting results from all pads of all experiments, we determined the following NF mean values and standard errors:  $\text{NF}(\text{nDNA}) = (0.399 \pm 0.009)$ ,  $\text{NF}(\text{mC-1c-DNA}) = (0.336 \pm 0.003)$  and  $\text{NF}(\text{mC-3-DNA}) = (0.503 \pm 0.008)$ . The *P*-value between nDNA and mC-1c-DNA is  $2 \times 10^{-8}$  and for nDNA and mC-3-DNA is  $4 \times 10^{-10}$ . Hence, in the MFA experiments mC-1c-DNA exhibits a lower mechanical stability than nDNA, and mC-3-DNA a higher stability. Our results indicate that 5-cytosine methylation of DNA can both enhance and decrease the propensity for strand separation, the change being significant in either case.

In order to investigate how each mC-pair itself affects the mechanical stability of the DNA duplex, two more DNA constructs, mC-1u-DNA and mC-1d-DNA, were examined, each with one methylation close to one of the ends of the DNA duplex (see [Supplementary Data](#)). mC-1u-DNA and mC-1d-DNA revealed a stabilizing effect in comparison to nDNA.

### Determination of potential width and dissociation constant

To further investigate the differences in strand separation of methylated and non-methylated DNA, single molecule force spectroscopy rupturing the DNA double-strand was performed by AFM, as described in 'Methods' section.

In all experiments one single-stranded DNA (ssDNA) was bound with a poly-ethyleneglycol (PEG) spacer to the cantilever tip of the AFM and a second ssDNA was immobilized with a PEG spacer on a glass substrate (see [Supplementary Data](#)). While the tip of the AFM approached the surface, the ssDNA on the tip and the ssDNA on the glass substrate could form a 20 bp duplex. The tip was then retracted from the surface and the DNA duplex was loaded with an increasing force until it finally ruptured (Figure 2a). The same sequence of the DNA duplex was used as in the MFA experiments with zero (nDNA), one (mC-1c-DNA) or three (mC-3-DNA) 5-methylcytosines (mC) per strand.

The force applied to the DNA duplex was recorded as a function of the distance between cantilever tip and surface. The elastic properties of PEG lead to a characteristic force extension curve, which can be fitted with a two-state freely jointed chain (FJC) model (Figure 2b) (59). As the complementary oligonucleotides were coupled via a PEG spacer, specific interactions can be selected based on the characteristic shape of the force-extension curve resulting from the expected length of the PEG spacer. No difference between the force-extension curve profile of nDNA, mC-1c-DNA and mC-3-DNA can be discerned.

Figure 2c and d show typical histograms of the unbinding forces and corresponding loading rates of mC-3-DNA

at a pulling velocity of 15  $\mu\text{m/s}$ . The histograms contain around 300 single molecule rupture events, like those shown in Figure 2b, and are fitted to the probability density function  $p(F)$  (solid curve, see ‘Methods’ section) and a Gaussian (dotted curve, see ‘Methods’ section). The most probable rupture force in Figure 2c is 68 pN. As shown in Figure 2e, the rupture events are centered in a sharp peak at a distance of around 80 nm, which matches the length of the DNA–PEG complex and is a further proof of specificity.

In Figure 2f the most probable rupture force is plotted as a function of the corresponding most probable loading rate for nDNA, mC-1c-DNA and mC-3-DNA. Measurements at faster loading rates result in higher rupture forces as described by the Bell-Evans model (48,49). By varying the pulling velocity of the cantilever from 150 nm/s to 20  $\mu\text{m/s}$ , loading rates in the range of  $10^2$  pN/s to around  $10^5$  pN/s could be achieved. Each data point was obtained from the Gaussian fit of the force histogram such as the one in Figure 2c and the histogram of loading rates in Figure 2d. Due to the loading-rate-based analysis method, one can extract the potential width,  $\Delta x$ , and the natural dissociation rate at zero force,  $k_{\text{off}}$ , from the measurements at different pulling velocities. The following values were obtained:  $\Delta x(\text{nDNA}) = (1.66 \pm 0.35)$  nm,  $k_{\text{off}}(\text{nDNA}) = (8.4 \times 10^{-6} \pm 3.52 \times 10^{-5}) \text{ s}^{-1}$ ,  $\Delta x(\text{mC-1c-DNA}) = (1.44 \pm 0.18)$  nm,  $k_{\text{off}}(\text{mC-1c-DNA}) = (1.7 \times 10^{-4} \pm 2.6 \times 10^{-4}) \text{ s}^{-1}$ ,  $\Delta x(\text{mC-3-DNA}) = (1.24 \pm 0.12)$  nm and  $k_{\text{off}}(\text{mC-3-DNA}) = (9.4 \times 10^{-6} \pm 1.72 \times 10^{-5}) \text{ s}^{-1}$ .

Complementing the MFA experiments, the AFM experiments reveal an elevated mechanical stability for mC-3-DNA and a decreased stability for mC-1c-DNA in comparison to nDNA. Furthermore, compared to nDNA,  $\Delta x$  is significantly narrower for mC-3-DNA and mC-1c-DNA. There is a slight difference in  $k_{\text{off}}$  between the three duplexes, but the error of measurement does not permit the conclusion of a significant difference.

We employed the Bell-Evans model to explain our single molecule force measurements. The Bell-Evans model assumes a single transition barrier between B-DNA and ssDNA, namely at  $\Delta x$ , which according to the model is force-independent. The suitability of the model has been demonstrated in several experimental studies involving force-driven strand separation of short nucleic acids (48,49,60). mC-3-DNA and mC-1c-DNA exhibit a narrower  $\Delta x$  in comparison to nDNA, which can be interpreted as the mDNA duplex under load to remain more compact before rupture as compared to nDNA. The narrower  $\Delta x$  reflects also fewer fluctuations in the mDNA corresponding to a stiffer complex.

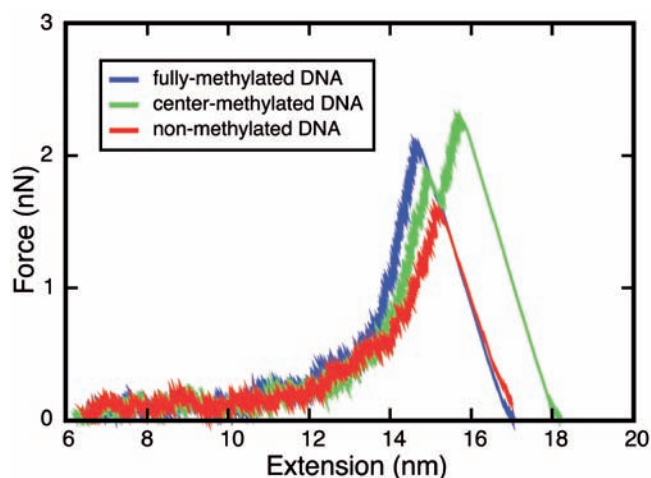
### MD simulations of DNA strand separation

When DNA is stretched in simulation, it untwists and elongates as shown in Figure 3. The dependence of the deformation on the stretching force reflects the mechanical properties of DNA. In our simulations, nDNA, cDNA and fDNA were subjected to a stretching force directed along the helical axis. Sequences of nDNA, cDNA and

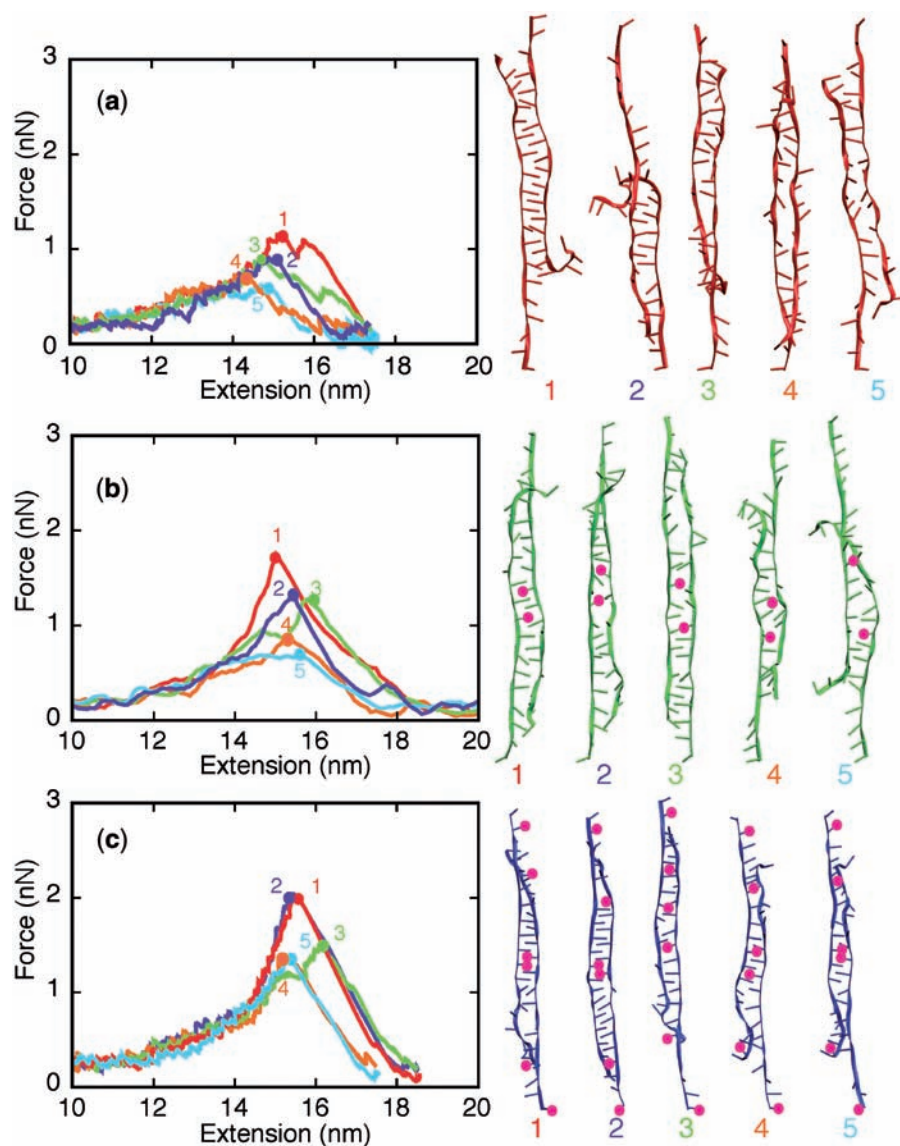
fDNA are provided in [Supplementary Data](#). The trajectories of simulations carried out are available as [Supplementary Movies S1–S4](#). Extension–force curves were monitored in slow-pulling (1  $\text{\AA}/\text{ns}$ ) and fast-pulling (10  $\text{\AA}/\text{ns}$ ) SMD simulations.

Figure 4 shows force–extension curves for nDNA, cDNA and fDNA stretched with a pulling velocity of 1  $\text{\AA}/\text{ns}$ . The force–extension profile exhibits in each case a clear peak followed by a rapid force decrease. The peak force arises for the extension at which the strands of the respective DNA duplex just begin to separate; the force decrease reflects the completion of strand separation. fDNA is seen to require a stronger force for strand separation than nDNA does. The force–extension curve of cDNA exhibits a minor and a major force peak. Examination of the respective simulation trajectory revealed that some flipped-out bases of the two already separated strands of cDNA stacked on each other after initial, partial separation (minor peak), as shown in critical DNA snapshots in [Supplementary Figure S5](#). As a result, a stronger force (major peak) was needed to completely separate the DNA strands. Before DNA reaches an extension of 13.8 nm, the force–extension curves of fDNA, cDNA and nDNA are indistinguishable. However, upon further extension the force needed to extend mDNA is larger than the force needed to extend nDNA, indicating that methylation affects the late-stage of force-induced DNA strand separation.

To gain better sampling of force-induced DNA strand separation, we carried out five independent SMD simulations for nDNA, cDNA and fDNA at a pulling velocity of 10  $\text{\AA}/\text{ns}$ . Force–extension curves of the 15 simulations are shown in Figure 5. The results reveal again that the mechanical response of DNA is methylation-dependent, e.g.



**Figure 4.** Force–extension curves for nDNA (red, simulation A1), cDNA (green, simulation B1) and fDNA (blue, simulation C1) when stretched by SMD with a pulling velocity of 1  $\text{\AA}/\text{ns}$ . [Supplementary Figure S4](#) shows corresponding snapshots of nDNA, cDNA and fDNA; [Supplementary Movies S2–S4](#) of the MD trajectories showing strand separation of nDNA ([Supplementary Movie S2](#)), cDNA ([Supplementary Movie S3](#)) and fDNA ([Supplementary Movie S4](#)) are also provided.



**Figure 5.** Force–extension curves for three different DNAs when stretched at a pulling velocity of 10 Å/ns (left) and snapshots of DNA taken at the moment of maximum stretching force (right). (a) nDNA with snapshots shown in red (simulations D1–D5). (b) cDNA with snapshots shown in green (simulations E1–E5). (c) fDNA with snapshots shown in blue (simulations F1–F5). In (b) and (c), magenta circles indicate the positions of methylated cytosines. For each DNA, color circles 1–5 in the force–extension curves correspond to the snapshots labeled in the same color.

DNA with more methylation sites requires a stronger force for strand separation.

During stretching, DNA undergoes a series of conformational transitions before its two strands become separated; an example is shown in Figure 3b and [Supplementary Movie S1](#). Figure 6a shows four typical conformations of DNA that arise during force-induced strand separation in 10 Å/ns pulling simulations. The frequency of observing values of DNA length and stacking energy during 15–10 Å/ns SMD simulations are also shown in Figure 6a. Qualitatively different transition pathways between duplex state and strand separated state are observed for fDNA, cDNA and nDNA.

During the early-stage, the pathways are very similar: stretching B-form DNA induces an unwinding of the

DNA helix; with the helically twisted strands straightening out into a rather planar, i.e. ladder, form, the Watson–Crick base pairing begins to break and bases of the two separate strands start to stack on top of each other, assuming the so-called zipper-like DNA form. The zipper-like DNA is demonstrated clearly in the 7 ns snapshot in Figure 3b. While the B-DNA → zipper-like DNA transition is common to fDNA, cDNA and nDNA, one can also discern differences.

First, the higher the level of DNA methylation, the less bubbles DNA develops during the B-form DNA → zipper-like DNA transition, as indicated in Figure 6a. Because of thermal fluctuation, some bases keep floating out of the zipper-like packing, and leave holes in the zipper, referred to here as ‘bubbles’. The amount of

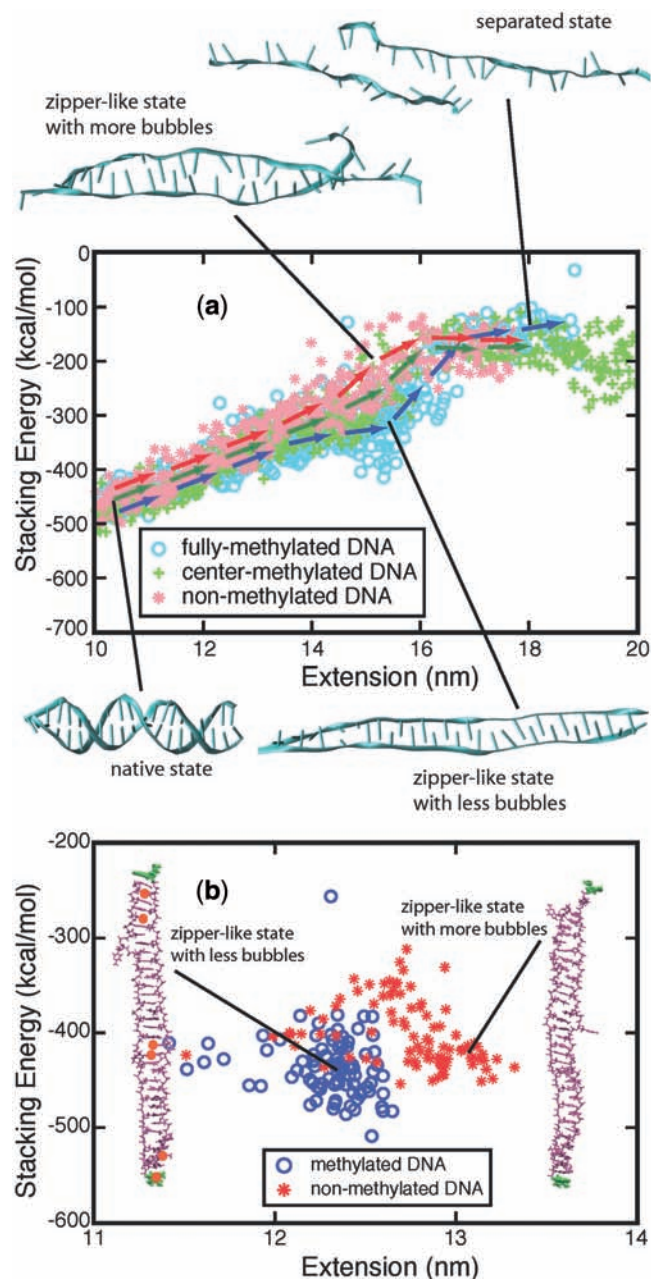


**Figure 6.** Strand separation pathway of stretched DNA. Here the pathway is characterized through 5'-end to 5'-end distance (extension), stacking energy of DNA bases, and intermediate DNA geometries. (a) Stacking energy versus extension curves of 15 trajectories of DNA pulled at 10 Å/ns velocity. Structures shown are representative snapshots taken from the simulations. Pink star: simulations D1–D5; green plus: simulations E1–E5; blue circle: simulations F1–F5. The arrows indicate three different pathways for nDNA (red arrows), cDNA (green arrows) and fDNA (blue arrows). (b) Stacking energy versus extension data from two 90-ns-long constant force ( $F = 200$  pN) simulations pulling DNA (red, simulation G1; blue, simulation H1). mDNA adopts a shorter, ordered zipper-like conformation with fewer bubbles (left), while nDNA adopts a longer, zipper-like conformation with more bubbles (right). Orange circles indicate the positions of methylated cytosines.

developed bubbles influences the stability of DNA against strand separation. As can be seen in Figure 5, the density of bubbles, on average, is lower for DNA with more methylation sites, which is consistent with the result that

fDNA requires a stronger rupture force than nDNA in our simulations.

Second, methylated ends of DNA are tighter than nonmethylated ends of DNA during stretching. The ends of most nDNAs and cDNAs are clearly separated when DNA is extended to around 15 nm, as shown in the snapshots in Figure 5. Since strand separation starts from the DNA ends under stretching, a firm end delays the separation process. As a result, rupturing DNA with methylated ends requires a stronger force than rupturing DNA without methylated ends. Supplementary Figures S6 and S7 show that the base pairing at the ends of DNA breaks more readily than that at the middle part. Methylated cytosines located at the DNA ends enable mDNA to sustain stronger force than nDNA before strands separate.

In simulations, we stretched DNA at much higher loading rates than we did in our experiments. Hence, the simulated DNA experienced a stronger pulling force and more bonds were broken in the same period of time as compared to observed DNA. To investigate the strand separation of nDNA and fDNA under conditions closer to the experimental loading force, we carried out SMD simulations at 200 pN constant force on two DNAs for 90 ns. Figure 6b shows that under 200 pN stretching, nDNA and fDNA extend along the backbone axis as the DNA increases over 90 ns its extension values. Monitoring stacking energy and length of DNA, one can distinguish two different conformational spaces occupied by nDNA and fDNA. Consistent with the strand separation pathways obtained from fast-pulling (10 Å/ns) SMD simulations, fDNA remains more compact than nDNA does. From the conformations shown in the inset of Figure 6b, one can see that zipper-like fDNA develops less bubbles than zipper-like nDNA does.

Even though we stretched dsDNA faster in MD simulations than in the experiments, the vast majority of dsDNA's degrees of freedom remain in quasi-equilibrium, fluctuating around their equilibrium values. The quasi-equilibrium behavior results from the fast relaxation of atomic velocities ( $\tau_{\text{relax}} \approx 100$  fs) and of local conformational features, e.g. bond angles or weak and medium hydrogen bonding with  $\tau_{\text{relax}} \approx 1 - 100$  ps. The relaxation times are short compared with the simulation times adopted here, of 10–100 ns and, hence, the stretched DNA remains in quasi-equilibrium during the simulations. However, there exist also relevant slow degrees of freedom in the stretched dsDNA system, namely the faults referred to above as bubbles. The faults are instrumental for strand separation and exhibit relaxation times on the order of nanoseconds as can be seen in the Supplementary Movies S1–S4. The 'slow' degrees of freedom lead to the heterogeneity of the simulation results as seen in Figure 5 and 6. The relaxation behavior of fast degrees of freedom has been discussed in (61). A key slow degree of freedom, essential for strand separation of protein  $\beta$ -sheets, has been reported in (62) and monitored over many orders of magnitude of stretching velocities in experiment and simulation as discussed in (63).

## DISCUSSION

It has been well recognized that DNA methylation conducts its biological function either, at a local level, by affecting promoter regions to recruit repressor complexes and, thereby, to induce transcriptional silencing, or at a genome-wide level, by changing structure and stability of chromatin to influence gene activity (19,20,22,23). In the last case, although MBD proteins are always involved in formation of higher inactive chromatin structure, methylation might also exert its biological effects by itself, e.g. without interfering with transcription factor and MBD protein binding, through a mechanical influence on DNA. In a previous study, it was demonstrated that methylation affects DNA's electromechanical properties (36). In the present work, we investigated the effect of 5-cytosine methylation on mechanical properties of DNA under load through force-induced strand separation measurement and simulation. The methylation-dependent strand separation behavior has been identified in MFA and AFM experiments; the underlying physical mechanism has been investigated by MD simulation.

MFA measures the relative stability of a target DNA duplex versus a reference DNA duplex during strand separation. In comparison with nDNA, the probability of strand separation for mC-3-DNA is approximately  $(NF(mC-3-DNA) - NF(nDNA)) / NF(nDNA) = 26\%$  lower and for mC-1c-DNA  $\sim 19\%$  higher. Since mC-3-DNA, mC-1c-DNA and nDNA were measured in parallel, spatially separated in the same well, their measurement conditions were identical. Hence, the measured differences in the strand separation probability between mC-3-DNA, mC-1c-DNA and nDNA are highly reliable. Complementing the MFA experiments, single molecule force measurements reveal distributions and absolute values of rupture forces as well as the corresponding loading rates. As shown in Figure 2f, compared to nDNA, mC-3-DNA has a higher mean rupture force (31% at 3 nN/s) and mC-1c-DNA a lower mean rupture force (19% at 3 nN/s), which is in agreement with a higher (lower) likelihood of DNA strand separation for mC-1c-DNA (mC-3-DNA) relative to nDNA in the MFA measurements.

SMD simulations, by examining force–extension curves, confirmed the dependence of strand separation on cytosine methylation, the method being limited, though, to small sampling. Three significantly different separation pathways were identified for nDNA, cDNA and fDNA by monitoring length and stacking energy of DNA during strand separation. The differences are attributed to the enhanced stacking interaction between methylated cytosine and its adjacent bases. Indeed, the stacking energy increases due to the additional methyl group on cytosine, reduces internal bubble formation and tightens the ends of DNA. As a result, to rupture mDNA requires stronger force than to rupture nDNA.

In all SMD simulations, we applied pulling velocities of 1 Å/ns and 10 Å/ns, which are several orders of magnitude higher than experimental pulling velocities ( $1.0 \times 10^{-6}$  Å/ns  $\sim 1.0 \times 10^{-4}$  Å/ns). Using a higher velocity increases the speed of strand separation, allowing simulations to finish

within the timescale ( $\sim 100$  ns) that our computational resources permit. The pulling velocity influences the rupture force of DNA as described for three protein systems (40). The reference demonstrates along with (63) that despite differences in pulling speed SMD simulation identified the correct physical rupture mechanisms. In our MD simulations, we could observe at atomic detail how methylation affects DNA strand separation in each independent simulation. While the simulations also show a clear difference between non-methylated and mDNA rupture forces, the main value of the results derives from the detailed picture of the strand separation process provided. In this picture, DNA duplexes are stretched into a zipper-like conformation; the eventual strand separation occurs due to random faults, here called bubbles, arising in this conformation; once enough bubbles weaken strand–strand interaction, based mainly on stacking energy contributions, separation occurs. Under the slow pulling conditions of the experiments, reaching a critical concentration of bubbles is rare, i.e. happens only over a millisecond; under the fast pulling condition of the simulations, strain favors bubble formation such that the critical concentration sufficient for strand separation is reached in 100 ns. The zipper-like DNA duplex conformation had been seen in several earlier simulation studies of nDNA (64,65), and some NMR studies have observed that zipper-like DNA can exist stably (66,67); the critical role of bubbles in strand separation has been described by Rapti *et al.* (41).

Experiments and simulations demonstrated methylation-dependent behavior of DNA during strand separation. However, comparing experimental and simulation results directly, one can notice that for cDNA, experiments showed that methylation reduces the force demand for strand separation, while simulations showed the opposite. The discrepancy between experiment and simulation should be attributed to the small sampling in MD simulations. For a low methylation level, such as cDNA with only one methylcytosine per strand, the effect of methylation is minor and easily drowned in noise. For fDNA, simulations more readily catch the effect of methylation. In fact, for fDNA, MD simulation results are indeed consistent with experimental results: methylation increases the requirement on force to separate strands. Due to limited computational power, MD simulations presently cannot sample as much as experiments can; nevertheless, MD simulation can provide key mechanistic insights complementing single-molecule experiments (40).

The goal of our study was to elucidate the methylation effect on physical properties of DNA. Comparison of strand separation of DNA with different methylation patterns illustrates that the effect of cytosine methylation is not only dependent on the methylation level, e.g. fDNA requires the strongest force for strand separation, but also on the sequence context of methylated sites, e.g. despite the same number of methylated cytosine, the relationship  $stability_{mC-1u-DNA} > stability_{nDNA} > stability_{mC-1c-DNA}$  holds (see [Supplementary Figure S1](#)). Previous studies had demonstrated significant sequence-dependence for biological functions of DNA, for example, one induced

through abnormal conformations as in the case of  $(CA)_n$  DNA tracts (68,69).

Complementing our results on DNA mechanical stability, melting curve experiments allow the determination of thermal stability. Methylation-sensitive high-resolution melting curve experiments allow an investigation of the methylation level affecting DNA duplex thermal stability in bulk (25). Lefebvre *et al.* (24) reported that methylation increases the melting temperature ( $T_m$ ) in the case of the DNA sequence ATCGAT by 3 K, while  $T_m$  decreases by 1 K for the sequence TTCGTT. This sequence-dependent effect of cytosine methylation on thermal DNA stability agrees with the sequence-dependent effect in our study of the mechanical stability. DNA methylation taking the same effect in two different transitions, namely force-induced strand separation in our study and temperature-induced melting in prior studies, suggests that methylation effects can be manipulated by the quantity and the context of methylation sites.

In contrast to the subtle changes of methylation effects as seen typically in thermal stability measurements, the differences in mechanical stability arising from methylation are pronounced, which prompts the question if this effect has a biological function. In this respect we note that the processivity of helicases is strongly affected by forces of a few piconewton (34,35). Recently, Johnson *et al.* (70) showed in single-molecule force measurements that DNA strand separation is the major barrier in T7 helicase translocation. Moreover, the strand separation rate of helicase T7 is DNA sequence-dependent and strongly influenced by a force stretching the DNA. Here, we measured a mean rupture force increase of 14 pN (at 3 nN/s) for mC-3-DNA over nDNA.

Of course, the force applied in our experiments differs from the force arising *in vivo* in the case of helicases, as we measured strand separation in shear geometry. We note, however, that mechanical manipulation of DNA in transcription initiation occurs in the confined setting of highly structured polynucleosomes. Accordingly, the shear geometry motion, which has been experimentally probed and computationally visualized in our study and which takes place more or less within the volume of non-stretched DNA, is relevant in the rather compact, structured polynucleosome setting found in the cell nucleus.

We have explored also DNA strand separation through unzipping, applying forces which may seem more representative of the action of DNA helicases. Such separation poses more spatial requirements than does strand separation through shearing as [Supplementary Movie S5](#) representing a simulation shows. We have carried out MFA measurements and MD simulations in unzipping geometry for the same sequences and under the same conditions as for the shear geometry. The MFA experimental setup and results are shown in [Supplementary Figure S2](#); [Supplementary Figure S3](#) shows results of a simulation of DNA being unzipped. As one can see from [Supplementary Figure S2](#), NF mean values and standard errors are  $(0.501 \pm 0.002)$  for nDNA,  $(0.511 \pm 0.003)$  for mC-1c-DNA and  $(0.583 \pm 0.004)$  for mC-3-DNA, i.e. methylation effects overall are significantly less than those arising

in the case of strand separation in shear geometry. The same is true in the case of the simulation results and we conclude that DNA unzipping shows likely a weaker methylation dependence than does strand separation through shearing.

In summary, we have demonstrated that cytosine methylation has a significant effect on DNA strand separation. We also suggested a microscopic picture of how strand separation arises in our experiments and how methylation plays a role on DNA strand separation in principle. There are three main mechanisms of the transcriptional regulation of gene expression: chromatin structure controlled access to genes, transcription factor control and epigenetic influence. DNA methylation, by adding a single methyl group on cytosine, is proven to be essential in epigenetics. Our study reveals that methylation could regulate gene expression through changing DNA mechanical properties. This new finding may advance our understanding of methylation-based epigenetics.

## SUPPLEMENTARY DATA

[Supplementary Data](#) are available at NAR Online.

## ACKNOWLEDGEMENTS

The authors thank B. Gaub, J. Vogelsang and M. Erdmann for helpful discussions. K.S. and X.Z. are grateful to G. Timp for introducing them to epigenetics. P.S. is grateful to the Elite Network of Bavaria (IDK-NBT) for a doctoral fellowship. K.S. is grateful for a Humboldt Foundation award. The authors gladly acknowledge supercomputer time provided by the Texas Advanced Computing Center and the National Center for Supercomputing Applications via TeraGrid Resource Allocation Committee grant MCA93S028.

## FUNDING

Deutsche Forschungsgemeinschaft; Nanosystems Initiative Munich; German Science Foundation (SFB 863); National Institutes of Health (P41-RR005969, R01 GM073655); National Science Foundation (PHY0822613). Funding open access charge: National Institutes of Health (P41-RR005969, R01 GM073655).

*Conflict of interest statement.* None declared.

## REFERENCES

- Bird, A.P. (1992) The essentials of DNA methylation. *Cell*, **70**, 5–8.
- Jones, P.A. and Takai, D. (2001) The role of DNA methylation in mammalian epigenetics. *Science*, **293**, 1068–1070.
- Bonasio, R., Tu, S. and Reinberg, D. (2010) Molecular signals of epigenetic states. *Science*, **330**, 612–616.
- Razin, A. and Riggs, A.D. (1980) DNA methylation and gene function. *Science*, **210**, 604–610.
- Rottach, A., Leonhardt, H. and Spada, F. (2009) DNA methylation-mediated epigenetic control. *J. Cell. Biochem.*, **108**, 43–51.



6. Maunakea, A.K., Nagarajan, R.P., Bilenky, M., Ballinger, T.J., D'Souza, C., Fouse, S.D., Johnson, B.E., Hong, C., Nielsen, C., Zhao, Y. *et al.* (2010) Conserved role of intragenic DNA methylation in regulating alternative promoters. *Nature*, **466**, 253–257.
7. Baylin, S.B. and Herman, J.G. (2000) DNA hypermethylation in tumorigenesis: epigenetics joins genetics. *Trends Gen.*, **16**, 168–174.
8. Tsou, J.A., Hagen, J.A., Carpenter, C.L. and Laird-Offringa, I.A. (2002) DNA methylation analysis: a powerful new tool for lung cancer diagnosis. *Nat. Oncogene*, **21**, 5450–5461.
9. Jones, P.A. (2002) DNA methylation and cancer. *Oncogene*, **21**, 5358–5360.
10. Li, E., Beard, C. and Jaenisch, R. (1993) Role for DNA methylation in genomic imprinting. *Nature*, **366**, 362–365.
11. Stein, R., Gruenbaum, Y., Pollack, Y., Razin, A. and Cedar, H. (1982) Clonal inheritance of the pattern of DNA methylation in mouse cells. *Proc. Natl Acad. Sci. USA*, **79**, 61–65.
12. Ballestar, E. and Wolffe, A.P. (2001) Methyl-CpG-binding proteins. *Eur. J. Biochem.*, **268**, 1–6.
13. Straussman, R., Nejman, D., Roberts, D., Steinfeld, I., Blum, B., Benvenisty, N., Simon, I., Yakhini, Z. and Cedar, H. (2009) Developmental programming of CpG island methylation profiles in the human genome. *Nat. Struct. Biol.*, **16**, 564–571.
14. Wakefield, R.I., Smith, B.O., Nan, X., Free, A., Soteriou, A., Uhrin, D., Bird, A.P. and Barlow, P.N. (1999) The solution structure of the domain from MeCP2 that binds to methylated DNA. *J. Mol. Biol.*, **291**, 1055–1065.
15. Ohki, I., Shimotake, N., Fujita, N., Jee, J.-G., Ikegami, T., Nakao, M. and Shirakawa, M. (2001) Solution structure of the methyl-CpG binding domain of human MBD1 in complex with methylated DNA. *Cell*, **105**, 487–497.
16. Hashimoto, H., Horton, J.R., Zhang, X., Bostick, M., Jacobsen, S.E. and Cheng, X. (2008) The SRA domain of UHRF1 flips 5-methylcytosine out of the DNA helix. *Nature*, **455**, 826–829.
17. Avvakumov, G.V., Walker, J.R., Xue, S., Li, Y., Duan, S., Bronner, C., Arrowsmith, C.H. and Dhe-Paganon, S. (2008) Structural basis for recognition of hemi-methylated DNA by the SRA domain of human UHRF1. *Nature*, **455**, 822–825.
18. Ho, K.L., McNae, L.W., Schmiedeberg, L., Klose, R.J., Bird, A.P. and Walkinshaw, M.D. (2008) MeCP2 binding to DNA depends upon hydration at methyl-CpG. *Mol. Cell*, **29**, 525–531.
19. Hashimshony, T., Zhang, J., Keshet, I., Bustin, M. and Cedar, H. (2003) The role of DNA methylation in setting up chromatin structure during development. *Nat. Genet.*, **34**, 187–192.
20. Lorincz, M.C., Dickerson, D.R., Schmitt, M. and Groudine, M. (2004) Intragenic DNA methylation alters chromatin structure and elongation efficiency in mammalian cells. *Nat. Struct. Biol.*, **11**, 1068–1075.
21. Choy, J.S., Wei, S., Lee, J.Y., Tan, S., Chu, S. and Lee, T.-H. (2010) DNA methylation increases nucleosome compaction and rigidity. *J. Am. Chem. Soc.*, **132**, 1782–1783.
22. Kass, S.U., Pruss, D. and Wolffe, A.P. (1997) How does DNA methylation repress transcription? *Trends Gen.*, **13**, 444–449.
23. Keshet, I., Lieman-Hurwitz, J. and Cedar, H. (1986) DNA methylation affects the formation of active chromatin. *Cell*, **44**, 535–543.
24. Lefebvre, A., Mauffret, O., Antri, S.E., Monnot, M., Lescot, E. and Femandjian, S. (1995) Sequence dependent effects of CpG cytosine methylation. A joint 1H-NMR and 31P-NMR study. *Eur. J. Biochem.*, **229**, 445–454.
25. Wojdacz, T.K., Dobrovic, A. and Hansen, L.L. (2008) Methylation-sensitive high-resolution melting. *Nat. Protocol.*, **3**, 1903–1908.
26. Geahigan, K.B., Meints, G.A., Hatcher, M.E., Orban, J. and Drobny, G.P. (2000) The dynamic impact of CpG Methylation in DNA. *Biochemistry*, **39**, 4939–4946.
27. Mayer-Jung, C., Moras, D. and Timsit, Y. (1998) Hydration and recognition of methylated CpG steps in DNA. *EMBO J.*, **17**, 2709–2718.
28. Derreumaux, S., Chaoui, M., Tevanian, G. and Femandjian, S. (2001) Impact of CpG methylation on structure, dynamics and solvation of cAMP DNA responsive element. *Nucleic Acids Res.*, **29**, 2314–2326.
29. Hogan, M.E. and Austin, R.H. (1987) Importance of DNA stiffness in protein-DNA binding specificity. *Nature*, **329**, 263–266.
30. Meints, G.A. and Drobny, G.P. (2001) Dynamic impact of methylation at the M. HhaI target site: a solid-state deuterium NMR study. *Biochemistry*, **40**, 12436–12443.
31. Nathan, D. and Crothers, D.M. (2002) Bending and flexibility of methylated and unmethylated EcoRI DNA. *J. Mol. Biol.*, **316**, 7–17.
32. Bustamante, C., Chemla, Y.R., Forde, N.R. and Izhaky, D. (2004) Mechanical processes in biochemistry. *Annu. Rev. Biochem.*, **73**, 705–748.
33. Wuite, G.J., Smith, S.B., Young, M., Keller, D. and Bustamante, C. (2000) Single-molecule studies of the effect of template tension on T7 DNA polymerase activity. *Nature*, **404**, 103–106.
34. Cheng, W., Dumont, S., Tinoco, I. and Bustamante, C. (2007) NS3 helicase actively separates RNA strands and senses sequence barriers ahead of the opening fork. *Proc. Natl Acad. Sci. USA*, **104**, 13954–13959.
35. Dumont, S., Cheng, W., Serebrov, V., Beran, R.K., Tinoco, I. Jr, Pyle, A.M. and Bustamante, C. (2006) RNA translocation and unwinding mechanism of HCV NS3 helicase and its coordination by ATP. *Nature*, **439**, 105–108.
36. Mirsaidov, U.M., Timp, W., Zou, X., Dimitrov, V., Schulten, K., Feinberg, A.P. and Timp, G. (2009) Nanoelectromechanics of methylated DNA in a synthetic nanopore. *Biophys. J.*, **96**, L32–L34.
37. Severin, P., Ho, D. and Gaub, H.E. (2011) A high-throughput molecular force assay for protein-DNA interactions. *Lab Chip*, **11**, 856–862.
38. Clausen-Schaumann, H., Seitz, M., Krautbauer, R. and Gaub, H.E. (2000) Force spectroscopy with single bio-molecules. *Curr. Opin. Cell Biol.*, **4**, 524–530.
39. King, G.M., Carter, A.R., Churnside, A.B., Eberle, L.S. and Perkins, T.T. (2009) Ultrastable atomic force microscopy: atomic-scale stability and registration in ambient conditions. *Nano Lett.*, **9**, 1451–1456.
40. Sotomayor, M. and Schulten, K. (2007) Single-molecule experiments in vitro and in silico. *Science*, **316**, 1144–1148.
41. Rapti, Z., Smerzi, A., Rasmussen, K.Ø. and Bishop, A.R. (2006) Healing length and bubble formation in DNA. *Phys. Rev. E*, **73**, 051902.
42. Strunz, T., Oroszlan, K., Schäfer, R. and Güntherodt, H.-J. (1993) Dynamic force spectroscopy of single DNA molecules. *Proc. Natl Acad. Sci. USA*, **96**, 11277–11282.
43. Albrecht, C.H., Clausen-Schaumann, H. and Gaub, H.E. (2006) Differential analysis of biomolecular rupture forces. *J. Phys.: Condens. Matter*, **18**, 81–599.
44. Ho, D., Dose, C., Albrecht, C.H., Severin, P., Falter, K., Dervan, P.B. and Gaub, H.E. (2009) Quantitative detection of small molecule/DNA complexes employing a force-based and label-free DNA-microarray. *Biophys. J.*, **96**, 4661–4671.
45. Butt, H.J. and Jaschke, M. (1995) Calculation of thermal noise in atomic-force microscopy. *Nanotechnology*, **6**, 1–7.
46. Florin, E.L., Rief, M., Lehmann, H., Ludwig, M., Dornmair, C., Moy, V.T. and Gaub, H.E. (1995) Sensing specific molecular interactions with the atomic force microscope. *Biosen. Bioelectron.*, **10**, 895–901.
47. Morfill, J., Kühner, F., Blank, K., Lugmaier, R.A., Sedlmair, J. and Gaub, H.E. (2007) B-S transition in short oligonucleotides. *Biophys. J.*, **93**, 2400–2409.
48. Bell, G. (1978) Models for the specific adhesion of cells to cells. *Science*, **200**, 618–627.
49. Evans, E. and Ritchie, K. (1999) Strength of a weak bond connecting flexible polymer chains. *Biophys. J.*, **76**, 2439–2447.
50. Phillips, J.C., Braun, R., Wang, W., Gumbart, J., Tajkhorshid, E., Christophe Chipot, E.V., Skeel, R.D., Kale, L. and Schulten, K. (2005) Scalable molecular dynamics with NAMM. *J. Comp. Chem.*, **26**, 1781–1802.
51. Gao, M., Sotomayor, M., Villa, E., Lee, E. and Schulten, K. (2006) Molecular mechanisms of cellular mechanics. *Phys. Chem. Chem. Phys.*, **8**, 3692–3706.
52. Israilewitz, B., Gao, M. and Schulten, K. (2001) Steered molecular dynamics and mechanical functions of proteins. *Curr. Opin. Struct. Biol.*, **11**, 224–230.

53. Friedman, R.A. and Honig, B. (1992) The electrostatic contribution to DNA base-stacking interactions. *Biopolymers*, **32**, 145–159.
54. Humphrey, W., Dalke, A. and Schulten, K. (1996) VMD – visual molecular dynamics. *J. Mol. Graph.*, **14**, 33–38.
55. Viani, M.B., Schäffer, T.E., Chand, A., Rief, M., Gaub, H.E. and Hansma, P.K. (1999) Small cantilevers for force spectroscopy of single molecules. *J. Appl. Physiol.*, **86**, 2258–2262.
56. Iqbal, A., Arslan, S., Okumus, B., Wilson, T.J., Giraud, G., Norman, D.G., Ha, T. and Lilley, D.M.J. (2008) Orientation dependence in fluorescent energy transfer between Cy3 and Cy5 terminally attached to double-stranded nucleic acids. *Proc. Natl Acad. Sci. USA*, **105**, 11176–11181.
57. Harvey, B.J., Perez, C. and Levitus, M. (2009) DNA sequence-dependent enhancement of Cy3 fluorescence. *Photochem. Photobiol. Sci.*, **8**, 1105–1110.
58. Rouzina, I. and Bloomfield, V.A. (2001) Force-induced melting of the DNA double helix 2. Effect of solution conditions. *Biophys. J.*, **80**, 894–900.
59. Oesterhelt, F., Rief, M. and Gaub, H.E. (1999) Single molecule force spectroscopy by AFM indicates helical structure of poly(ethylene-glycol) in water. *New J. Phys.*, **1**, 1998–1999.
60. Ho, D., Zimmermann, J.L., Dehmelt, F.A., Steinbach, U., Erdmann, M., Severin, P., Falter, K. and Gaub, H.E. (2009) Force-driven separation of short double-stranded DNA. *Biophys. J.*, **97**, 3158–3167.
61. Hsin, J. and Schulten, K. (2011) Improved resolution of tertiary structure elasticity in muscle protein. *Biophys. J.*, **100**, L22–L24.
62. Lu, H. and Schulten, K. (2000) The key event in force-induced unfolding of titin's immunoglobulin domains. *Biophys. J.*, **79**, 51–65.
63. Lee, E.H., Hsin, J., Sotomayor, M., Comellas, G. and Schulten, K. (2009) Discovery through the computational microscope. *Structure*, **17**, 1295–1306.
64. Lohikoski, R., Timonen, J. and Laaksonen, A. (2005) Molecular dynamics simulation of single DNA stretching reveals a novel structure. *Chem. Phys. Lett.*, **407**, 23–29.
65. Santosh, M. and Maiti, P.K. (2009) Force induced DNA melting. *J. Phys. Condens. Matter*, **21**, 101–139.
66. Shepard, W., Cruse, W.B., Fourme, R., de la Fortelle, E. and Prangè, T. (1998) A zipper-like duplex in DNA: the crystal structure of d(GCGAAAGCT) at 2.1 Å resolution. *Structure*, **6**, 849–861.
67. Chou, S.-H. and Chin, K.-H. (2001) Zipper-like Watson-Crick base-pairs. *J. Mol. Biol.*, **312**, 753–768.
68. Timsit, Y., Vilbois, E. and Moras, D. (1991) Base-pairing shift in the major groove of (CA)<sub>n</sub> tracts by B-DNA crystal structures. *Nature*, **354**, 167–170.
69. Timsit, Y. and Moras, D. (1995) Self-fitting and self-modifying properties of the B-DNA molecule. *J. Mol. Biol.*, **251**, 629–647.
70. Johnson, D.S., Bai, L., Smith, B.Y., Patel, S.S. and Wang, M.D. (2007) Single-molecule studies reveal dynamics of DNA unwinding by the ring-shaped T7 helicase. *Cell*, **129**, 1299–1309.

# Supplementary Material

## Cytosine Methylation Alters DNA Mechanical Properties

Philip M.D. Severin, Xueqing Zou, Hermann E. Gaub and Klaus Schulten

## Supporting Methods

### MFA DNA-chip (bottom surface)

The DNA-chip (see Fig. 1) has been assembled as described previously (1) except for some modifications. DNA oligomers **1**, **2**, and **3** were purchased HPLC grade from IBA GmbH (Göttingen, Germany) and Metabion GmbH (Martinsried, Germany). Oligonucleotides employed had the following sequences and modifications (methylations, **mC** represents 5-methylcytosine):

**1<sub>nDNA</sub>**, NH<sub>2</sub>-(HEGL)<sub>5</sub>-5'-(T)<sub>10</sub>-CCG AGA TAT CCG CAC CAA CG-3';

**2<sub>nDNA</sub>**, 3'-GGC TCT ATA GGC GTG GTT GC-(T)<sub>6</sub>-5'-5'-T(Cy5)-(T)<sub>6</sub>-GGC TCT ATA GGC GTG GTT GC-3';

**1<sub>mC-1c-DNA</sub>**, NH<sub>2</sub>-(HEGL)<sub>5</sub>-5'-(T)<sub>10</sub>-CCG AGA TAT **CmCG** CAC CAA CG-3';

**2<sub>mC-1c-DNA</sub>**, 3'-GGC TCT ATA **GGmC** GTG GTT GC-(T)<sub>6</sub>-5'-5'-T(Cy5)-(T)<sub>6</sub>-GGC TCT ATA GGC GTG GTT GC-3';

**1<sub>mC-3-DNA</sub>**, NH<sub>2</sub>-(HEGL)<sub>5</sub>-5'-(T)<sub>10</sub>-**CmCG** AGA TAT **CmCG** CAC CAA **mCG**-3';

**2<sub>mC-3-DNA</sub>**, 3'-**GGmC** TCT ATA **GGmC** GTG GTT **GmC**-(T)<sub>6</sub>-5'-5'-T(Cy5)-(T)<sub>6</sub>-GGC TCT ATA GGC GTG GTT GC-3';

**3<sub>Ref</sub>**, biotin-5'-(T)<sub>10</sub>-GCA ACC ACG CCT ATA GAG CC(Cy3)-3'.

Oligomers **1** contained five hexaethyleneglycol (HEGL) linkers connected via phosphate groups. The lower duplex **1 • 2** contains zero, one or three 5-methylcytosine (**mC**) per strand. DNA oligomer **1** is amine-modified, which allows covalent linkage to aldehyde-functionalized glass slides (Schott GmbH, Jena, Germany).

We spotted 1  $\mu$ L drops of 5 $\times$  SSC (saline sodium citrate; Sigma-Aldrich GmbH, Munich, Germany) containing 25  $\mu$ M oligomer **1** on the aldehyde slide in a 4 $\times$ 4 pattern and incubated the slide in a saturated NaCl ddH<sub>2</sub>O atmosphere overnight. After washing the slide with ddH<sub>2</sub>O containing 0.2% sodium dodecyl sulfate (SDS; VWR Scientific GmbH, Darmstadt, Germany) and thoroughly rinsing the slide with ddH<sub>2</sub>O we reduced the resulting Schiff bases with 1% aqueous NaBH<sub>4</sub> (VWR Scientific GmbH, Darmstadt, Germany) for 90 min. Subsequently, the slide was washed with 1 $\times$  SSC and thoroughly rinsed with ddH<sub>2</sub>O.

In order to reduce nonspecific binding, the slides were blocked in 1 $\times$  SSC containing 4% bovine serum albumin (BSA; Sigma-Aldrich GmbH, Munich, Germany) for 20 min. Custom-made 16-well silicone isolators (Grace-Biolabs, OR) were placed on top of the immobilized DNA oligomer **1**. The 100 nM Cy5-modified oligomer **2** and 200 nM biotin-modified oligomer **3** were hybridized to the latter for 30 min, completing the **1 • 2 • 3** complex on the glass slide (see Fig. 1a). After removing the silicone isolators the slides were washed with a self-built fluidic system driven by a multi-channel peristaltic pump (Ismatec GmbH, Wertheim-

Mondfeld, Germany) to remove any unspecific bound DNA oligomers. The 4×4 pattern was rinsed subsequently with 2× SSC, 0.2× SSC containing 0.1% Tween 20 (VWR Scientific GmbH, Darmstadt, Germany) and 1× PBS (phosphate buffered saline) each with 50 ml in 5 min.

### MFA PDMS stamp (top surface)

The stamp (see Fig. 1) was made of polydimethylsiloxane (PDMS) and was fabricated and functionalized as described previously (2, 3). Briefly summarized, the PDMS stamps were cut into a 4×4 pillar arrangement. Each pillar is 1 mm in diameter and 1 mm in height, and carries a microstructure on the flat surface; 100 mm×100 mm pads are separated by 41 mm wide and 5 mm deep trenches allowing for liquid drainage during the contact and separation process. Free polymers were extracted in toluene for at least one day (4). The PDMS was activated overnight in 12.5% hydrochloric acid and subsequently derivatized with (3-glycidioxypropyl)-trimethoxysilane (ABCR, Karlsruhe, Germany) to generate epoxide groups. NH<sub>2</sub>-PEG-Biotin (3400 g/mol; Rapp Polymere, Tübingen, Germany) was melted at 80°C, and ~1 mL was spotted on each pillar followed by overnight incubation in argon atmosphere at 80°C. The excess polymers were thoroughly removed with ddH<sub>2</sub>O. Shortly before the experiment, the PDMS was incubated for 60 min with 1 mg/mL streptavidin (Thermo Fisher Scientific, Bonn, Germany) that had been dissolved before in 1× PBS and 0.4% BSA. The PDMS was then washed with 1× PBS containing 0.1% Tween 20. Lastly, the PDMS was washed in 1× PBS and gently dried with N<sub>2</sub> gas.

### AFM sample and cantilever functionalization

For our AFM measurements we employed a commercial instrument (Molecular Force Probe 3D from Asylum Research) with cantilevers from Veeco (MLCT) and Olympus (BL-AC40).

A detailed description of the sample preparation can be found in reference (5). The following oligonucleotides (same sequence of the DNA duplex as in the MFA experiment) modified with a thiol group at their 5'-termini (IBA GmbH, Göttingen, Germany) were immobilized on amino-functionalized surfaces using a hetero-bifunctional poly-ethylene glycol (PEG) spacer (6):

**S<sub>nDNA</sub>**, 5'-SH-(T)<sub>20</sub>-CGT TGG TGC GGA TAT CTC GG-3';

**C<sub>nDNA</sub>**, 5'-SH-(T)<sub>10</sub>-CCG AGA TAT CCG CAC CAA CG-3';

**S<sub>mC-1c-DNA</sub>**, 5'-SH-(T)<sub>20</sub>-CGT TGG TGmC GGA TAT CTC GG-3';

**C<sub>mC-1c-DNA</sub>**, 5'-SH-(T)<sub>10</sub>-CCG AGA TAT CmCG CAC CAA CG-3';

**S<sub>mC-3-DNA</sub>**, 5'-SH-(T)<sub>20</sub>-mCGT TGG TGmC GGA TAT CTmC GG-3';

**C<sub>mC-3-DNA</sub>**, 5'-SH-(T)<sub>10</sub>-CmCG AGA TAT CmCG CAC CAA mCG-3'.

One type of oligonucleotide (**C<sub>x</sub>**) was immobilized on the cantilever and the oligonucleotide with the complementary sequence was coupled to the surface (**S<sub>x</sub>**), as shown in Fig. 2a. Amino-modified surfaces on the cantilevers were prepared using 3-aminopropyltrimethoxysilane (ABCR GmbH, Karlsruhe, Germany) (7). Commercially available amino-

functionalized slides (Slide A, Nexterion, Mainz, Germany) were used. In the following, both surfaces (cantilever and slide) were treated in parallel as described previously (8). They were incubated at pH 8.5 in borate buffer for 1 h for deprotonation of the amino groups in order to couple the surface to the N-hydroxysuccinimide (NHS) groups of the heterobifunctional NHS-PEG-maleimide (molecular weight, 5000 g/mol; Rapp Polymere, Tübingen, Germany). Subsequently, slide and cantilever were incubated for 1 h in PEG (50 mM) that had been dissolved before in borate buffer at pH 8.5. The oligonucleotides were reduced using tris (2-carboxyethyl) phosphine hydrochloride beads (Perbio Science, Bonn, Germany) to generate free thiols. After washing the surfaces with ddH<sub>2</sub>O, a solution of the oligonucleotides (30  $\mu$ M) was incubated on the surfaces for 1 h (or over night). Before measurement, the surfaces were rinsed with 1 $\times$  PBS to remove non-covalently bound oligonucleotides and stored in 1 $\times$  PBS until use.

### Simulated systems

DNA of the same sequence as employed in the experiments was studied in molecular dynamics simulations. We investigated three different DNA methylation patterns, namely, non-methylated (nDNA), center-methylated (cDNA) and fully-methylated (fDNA):

nDNA, 5'-CCGAGATATCCGCACCAACG-3',  
5'-CGTTGGTGCGGATATCTCGG-3';  
cDNA, 5'-CCGAGATATC<sub>m</sub>CGCACCAACG-3',  
5'-CGTTGGTG<sub>m</sub>CGGATATCTCGG-3';  
fDNA, 5'-C<sub>m</sub>CGAGATATC<sub>m</sub>CGCACCA<sub>m</sub>CG-3',  
5'-<sub>m</sub>CGTTGGTG<sub>m</sub>CGGATATCT<sub>m</sub>CGG-3'.

A double-stranded helix of native DNA was built with the program X3DNA (9). Methylated DNA was generated by altering cytosines to methylated cytosines employing the program psfgen (10). The topology of DNA along with the missing hydrogen atoms were generated also using psfgen (10) with the resulting topology files corresponding to CHARMM27 (11). DNA was placed in a water box of size 300 Å $\times$ 60 Å $\times$ 60 Å. 0.1 mol/L KCl was added, amounting to 87 K<sup>+</sup> and 47 Cl<sup>-</sup> ions, the difference in ion numbers serving neutralization of DNA. The resulting system is shown in Fig. 3a. Each simulated system contained about 110,000 atoms of DNA, water and ions.

### Molecular dynamics simulations

Simulations were performed using NAMD 2.6 (10) with the CHARMM27 force field for DNA (11) and the TIP3P water model (12). Periodic boundary conditions were assumed and the particle mesh Ewald (PME) summation method was employed for evaluating Coulomb forces. The van der Waals (vdW) energy was calculated using a smooth cutoff of 12 Å. The integration time step was 1 fs. The temperature was kept at 310 K by applying Langevin forces (13) with a damping coefficient of 0.1 ps<sup>-1</sup> only to the oxygen atoms of water molecules.

The system was energy minimized for 2000 steps, then heated to 295 K in 4 ps. To determine the volume leading to a suitable overall density and corresponding to the laboratory pressure, 500 ps-equilibration was conducted under NPT ensemble conditions. This equilibration was performed using Nosé-Hoover Langevin piston pressure control (13). After the system acquired in the NPT ensemble description a constant volume, 2 ns-equilibration was conducted under NVT ensemble conditions.

## Supporting Results

### Determination of the mechanical stability of mC-1u-DNA and mC-1d-DNA by MFA measurements

We investigated how each mCG-pair, close to the ends of the 20 bp DNA duplex, affects its mechanical stability. For this purpose, two new DNA constructs, mC-1d-DNA and mC-1u-DNA, were examined. Because of cost issues, a simpler construct without a 5'-5'-DNA direction correction was used, i.e., the reference duplex was pulled at the 3'-end, while the target duplex is still pulled at the 5'-end. The following sequences were used (mC represents 5-methylcytosine):

**1<sub>nDNA</sub>**, NH<sub>2</sub>-(HEGL)<sub>5</sub>-5'-(T)<sub>10</sub>-CCG AGA TAT CCG CAC CAA CG-3';

**2<sub>nDNA</sub>**, 3'-GGC TCT ATA GGC GTG GTT GC-(T)<sub>6</sub>-T(Cy5)-(T)<sub>6</sub>-GGC TCT ATA GGC GTG GTT GC-5';

**1<sub>mC-1u-DNA</sub>**, NH<sub>2</sub>-(HEGL)<sub>5</sub>-5'-(T)<sub>10</sub>-CCG AGA TAT CCG CAC CAA **mCG**-3';

**2<sub>mC-1u-DNA</sub>**, 3'-GGC TCT ATA GGC GTG GTT **GmC**-(T)<sub>6</sub>-T(Cy5)-(T)<sub>6</sub>-GGC TCT ATA GGC GTG GTT GC-5';

**1<sub>mC-1d-DNA</sub>**, NH<sub>2</sub>-(HEGL)<sub>5</sub>-5'-(T)<sub>10</sub>-**CmCG** AGA TAT CCG CAC CAA CG-3';

**2<sub>mC-1d-DNA</sub>**, 3'-GG**mC** TCT ATA GGC GTG GTT GC-(T)<sub>6</sub>-T(Cy5)-(T)<sub>6</sub>-GGC TCT ATA GGC GTG GTT GC-5';

**3<sub>Ref</sub>**, 5'-(Cy3)-GCA ACC ACG CCT ATA GAG CC-(T)<sub>10</sub>-biotin-3'.

Since we pulled DNA at the 3'-ends of the reference duplex and the pulling direction (3' or 5') on the DNA has an effect on the mechanical stability (14, 15), a direct comparison of the NF values of mC-1c-DNA and mC-3-DNA is not possible. However, not only mC-1u-DNA and mC-1d-DNA, but also nDNA was measured with this reference duplex. This allows one to compare mC-1u-DNA and mC-1d-DNA to nDNA. The same sample preparation and experimental procedure was used, as described in the Methods Section. As shown in Fig. S1, the experimental results reveal that mC-1u-DNA and mC-1d-DNA are more stable than nDNA, mC-1d-DNA slightly more so than mC-1u-DNA as it exhibits a slightly higher NF value. Summarizing all experiments, mean value and standard error are in each case  $NF_{nDNA} = (0.557 \pm 0.009)$ ,  $NF_{mC-1u-DNA} = (0.636 \pm 0.003)$  and  $NF_{mC-1d-DNA} = (0.675 \pm 0.008)$ . The P-value for mC-1u-DNA (versus nDNA) is  $3 \times 10^{-3}$  and  $6 \times 10^{-5}$  for mC-1d-DNA. mC-1u-DNA and mC-1d-DNA are more stable than nDNA in contrast to mC-1c-DNA, which shows lower mechanical stability than nDNA. This suggests that effects of methylation on

the mechanical stability of dsDNA are sequence-dependent.

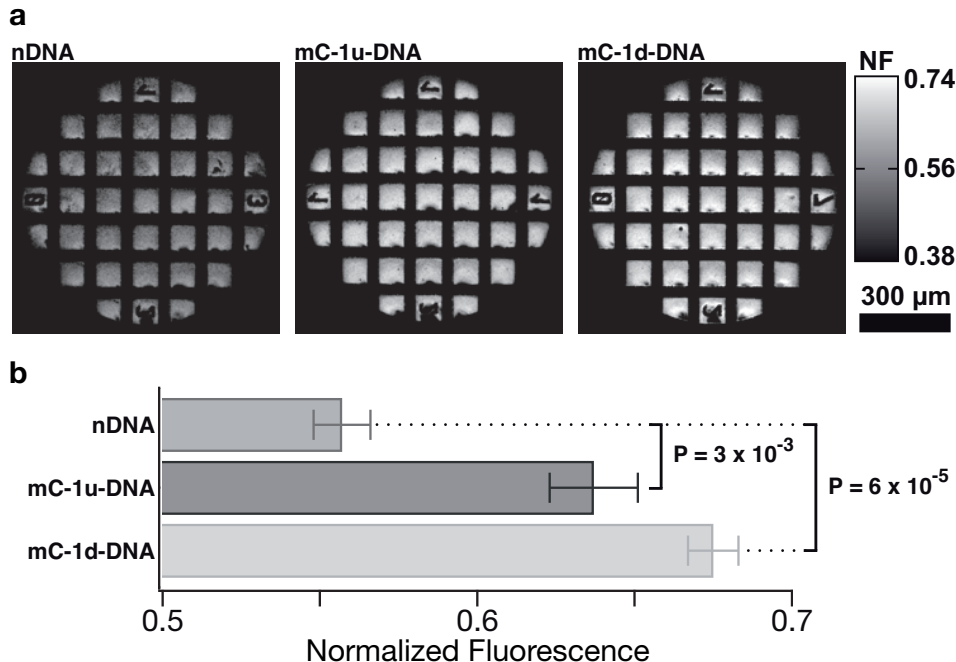


Figure S1: (a) Normalized fluorescence (NF) images of one representative experiment for nDNA, mC-1u-DNA and mC-1d-DNA. Unlike the NF signals shown in Fig. 1b, NF here is less homogeneous which is likely due to different pulling directions between reference and target duplex as the target duplex is pulled at the top at the 3'-end and at the bottom at the 5'-end. In case of Fig. 1b the duplex system was pulled at top and bottom at the 5'-ends. In comparison to nDNA ( $NF_{\text{PEAK}} = 0.549$ ), mC-1u-DNA ( $NF_{\text{PEAK}} = 0.611$ ) and mC-1d-DNA ( $NF_{\text{PEAK}} = 0.657$ ) exhibit a higher NF, i.e., the single methylation site on each end has a stabilizing effect on the DNA duplex. (b) Analysis of 24 pads from three different experiments. mC-1u-DNA and mC-1d-DNA show a higher mean rupture force compared to non-methylated DNA (nDNA).

### Determination of the mechanical stability of methylated DNA by molecular force assay measurements in unzipping geometry

Mechanical separation of the two DNA strands of a duplex in unzipping geometry provides information on the separation process that resembles helicase-induced *in vivo* strand separation. Unzipping experiments complete the picture on how methylation influences the DNA mechanics beyond what shear measurements alone reveal. We investigated the same sequence, as in shear geometry measurements, also in unzipping configuration with zero, one center and three 5-methylcytosines per strand (see Fig. S2). The DNA sequences used are listed below (mC represents 5-methylcytosine):

**1<sub>nDNAzip</sub>**, 5'-CCG AGA TAT CCG CAC CAA CG-(T)<sub>20</sub>-(HEGL)<sub>5</sub>-NH<sub>2</sub>-3';  
**2<sub>nDNAzip</sub>**, 5'-GGC TCT ATA GGC GTG GTT GC-(T)<sub>6</sub>-T(Cy5)-(T)<sub>6</sub>-CGT TGG TGC  
 GGA TAT CTC GG-3';  
**1<sub>mC-1c-DNAzip</sub>**, 5'-CCG AGA TAT **CmCG** CAC CAA CG-(T)<sub>20</sub>-(HEGL)<sub>5</sub>-NH<sub>2</sub>-3';  
**2<sub>mC-1c-DNAzip</sub>**, 5'-GGC TCT ATA GGC GTG GTT GC-(T)<sub>6</sub>-T(Cy5)-(T)<sub>6</sub>-CGT TGG  
 TG**mC** GGA TAT CTC GG-3';  
**1<sub>mC-3-DNAzip</sub>**, 5'-**CmCG** AGA TAT **CmCG** CAC CAA **mCG**-(T)<sub>20</sub>-(HEGL)<sub>5</sub>-NH<sub>2</sub>-3';  
**2<sub>mC-3-DNAzip</sub>**, 5'-GGC TCT ATA GGC GTG GTT GC-(T)<sub>6</sub>-T(Cy5)-(T)<sub>6</sub>-**mCGT** TGG  
 TG**mC** GGA TAT CT**mC** GG-3';  
**3<sub>Refzip</sub>**, biotin-5'-(T)<sub>20</sub>-(Cy3)-GCA ACC ACG CCT ATA GAG CC-3'.

As shown in Fig. S2b, nDNA separated in unzipping geometry exhibits a NF mean value and standard error of  $(0.501 \pm 0.002)$ , while mC-1c-DNA exhibits the values  $(0.511 \pm 0.003)$  and mC-3-DNA exhibits the values  $(0.583 \pm 0.004)$ . mC-1c-DNA as well as mC-3-DNA have an elevated mechanical stability compared to nDNA. The significance is characterized by a P-value of 0.017 for mC-1c-DNA versus nDNA and  $1 \times 10^{-18}$  for mC-3-DNA versus nDNA. In comparison to the shear configuration, where mC-1c-DNA has a destabilizing effect, mC-1c-DNA is more stable than nDNA in unzipping. The results suggest that for unzipping a DNA duplex, neighboring base pairs have a negligible effect on the methylated CpG step, since base pair by base pair is opened one after another, in contrast to the case of shear geometry, where all base pairs are under load at the same moment.



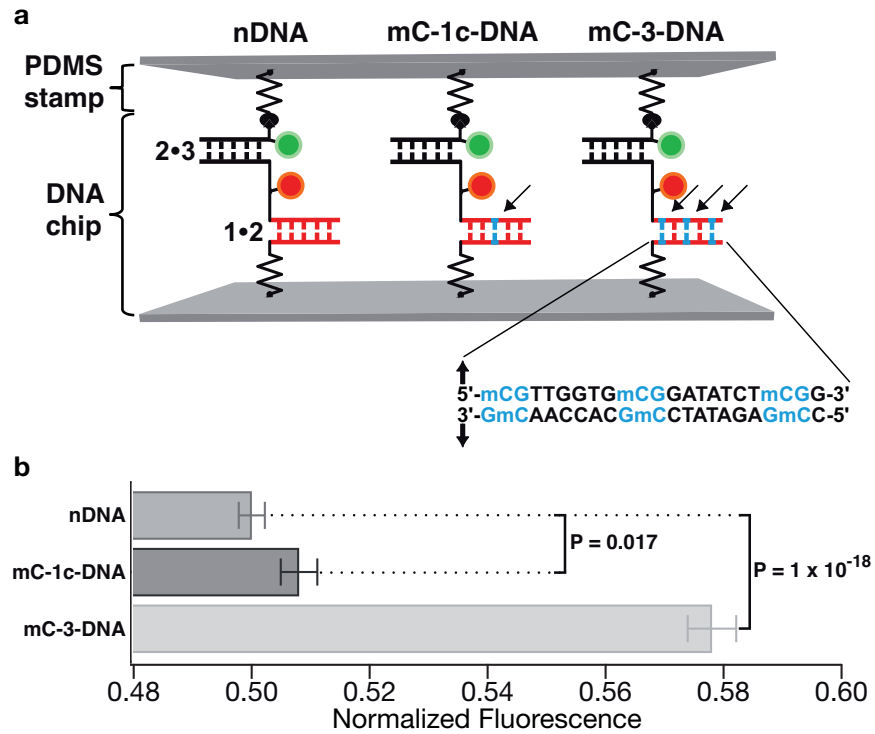


Figure S2: (a) Schematic representation of the molecular force assay in unzipping geometry. The principle of the MFA and molecular setup is the same as in Fig. 1, except that target and reference duplex are oriented such that they open like a zipper under load. The pulling velocity was 100 nm/s. (b) Analysis of 40 pads from four different experiments. mC-1c-DNA and mC-3-DNA show a higher mean rupture force than does nDNA.

## SMD simulation on DNA strand separation in unzipping geometry

To visualize how methylation affects the kinetic barriers of unzipping dsDNA, we conducted SMD simulations of DNA strand separation in unzipping geometry. DNAs with the same methylation patterns (zero, one or three methylcytosines per strand) as used in shear geometry were employed. In simulations, one 3'-end of DNA was fixed, and the adjacent 5'-end was pulled. Two independent SMD simulations with 1 Å/ns-pulling velocity were performed for each DNA. A trajectory is shown in movie S5. For all simulations, we monitored the time evolution of the applied force and the number of base pairs. The results (Fig. S3) show that the mean value of applied force for rupturing mC-3-DNA is slightly larger than those of nDNA and mC-1c-DNA. Essevaz-Roulet *et al.* reported single-molecule experiments that measured the force threshold for unzipping  $\lambda$  DNA to be around 10 ~ 15 pN (16). In our SMD simulations, the pulling velocity is much faster than that used in the experiments and, as expected, the force seen in our simulations is higher than in the experiment, namely is in the range 50 pN - 70 pN. The velocity dependence of the pulling force and its often negligible effect on the rupture mechanism have been described in the case of stretching proteins in (17, 18). Previous experiments have shown that the force threshold for unzipping dsDNA is sequence dependent (19). Since methylation enhances the stacking interaction between cytosine and its neighbors, it is likely that unzipping an mCG pair requires stronger force than unzipping a CG pair and, therefore, DNA with a higher methylation level is mechanically more stable than DNA with lower methylation level when stretched in the unzipping geometry.

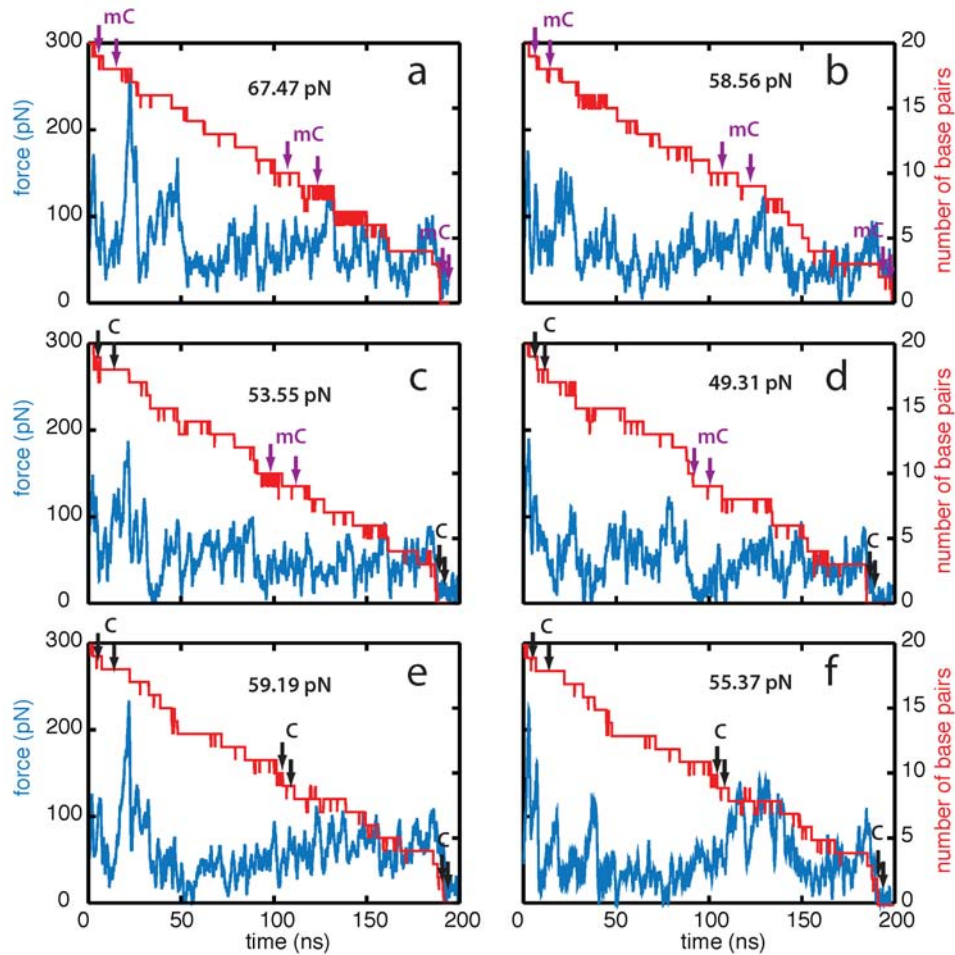


Figure S3: Time evolution of applied force (blue line) and number of base pairs (red line) as monitored in SMD simulations of unzipping mC-3-DNA (a, b), mC-1-DNA (c, d) and nDNA (e, f). Purple arrows indicate the breakage of methylated CG pairs; black arrows indicate the breakage of non-methylated CG pairs. The number given in each plot shows the mean value of force obtained from each simulation.

## Supporting Movies

- **Movie S1** shows a trajectory (simulation F1, see Table 1) of strand separation of DNA stretched in shear geometry. The six methylated cytosines in DNA are indicated in yellow; the atoms subject to constraint (at bottom) and stretching force (at top) are shown in green. See Fig. 3b.
- **Movies S2 - S4** show trajectories of nDNA (**S2**, simulation A1), cDNA (**S3**, simulation B1) and fDNA (**S4**, simulation C1) stretched in shear geometry by steered molecular dynamics with a velocity of 1 Å/ns. The methylated cytosines in DNA are indicated in yellow; the atoms subject to constraint (at bottom) and stretching force (at top) are shown in green. See Fig. 4.
- **Movie S5** shows a simulation trajectory of strand separation of DNA stretched in unzipping geometry. The six methylated cytosines in DNA are indicated in yellow; the atoms subject to constraint and stretching force are shown in green.

## Supporting Table

Name	DNA	SMD Type	Parameter	Time (ns)
A1	non-methylated (nDNA)	CVP*	1 Å/ns	118
B1	center-methylated (cDNA)	CVP	1 Å/ns	120
C1	fully-methylated (fDNA)	CVP	1 Å/ns	118
D1-D5	nDNA	CVP	10 Å/ns	8
E1-E5	cDNA	CVP	10 Å/ns	9
F1	fDNA	CVP	10 Å/ns	9
F2	fDNA	CVP	10 Å/ns	8
F3-F4	fDNA	CVP	10 Å/ns	9
F5	fDNA	CVP	10 Å/ns	8
G1	nDNA	CFP†	200 pN	90
H1	fDNA	CFP	200 pN	90

\* CVP: constant velocity pulling

† CFP: constant force pulling

Table S1: List of simulations

## Further supporting Figures S4 - S7

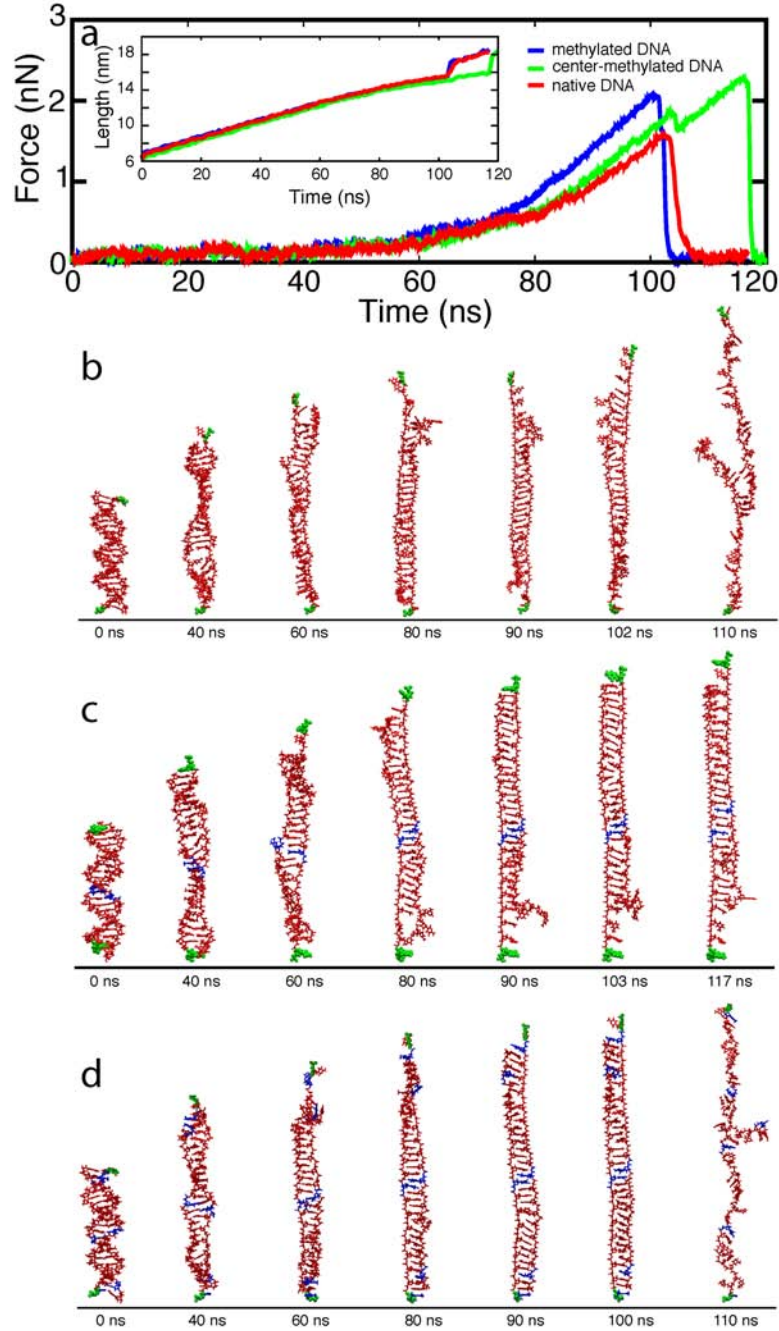


Figure S4: (a) Force and extension arising in  $1 \text{ \AA}/\text{ns}$  pulling simulations. Force and extension are shown for nDNA (red), cDNA (green), and fDNA (blue) from simulations A1, B1, and C1. (b-d) Snapshots of stretched DNA. Shown are snapshots for nDNA (b), cDNA (c) and fDNA (d). The snapshots correspond to DNA conformations at 0 ns, 40 ns, 60 ns, 80 ns, 90 ns, 102 ns (force peak of nDNA) / 103 ns (minor force peak of cDNA), 117 ns (major force peak of cDNA) / 100 ns (force peak of fDNA) and 110 ns (separated strands of nDNA and fDNA). The methylated cytosines in DNA are indicated in blue; the atoms subject to  $t_{11}$  constraint (at bottom) and stretching force (at top) are shown in green.

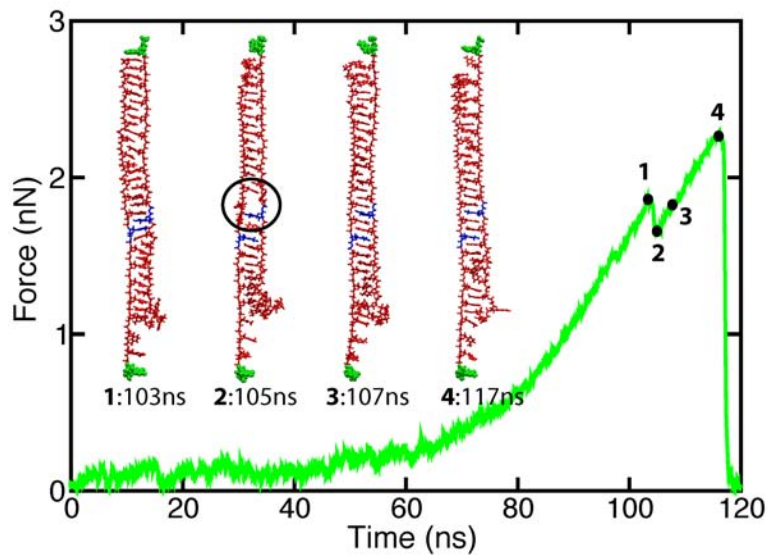


Figure S5: Snapshots of cDNA at two force peaks. The black spots on the force curve correspond to DNA conformations at 103 ns (minor force peak), 105 ns, 107 ns and 117 ns (major force peak). The black circle highlights the bubble area in DNA which results in a decrease of force at 105 ns. The methylated cytosines in DNA are indicated in blue; the atoms subject to constraint (at bottom) and stretching force (at top) are shown in green.

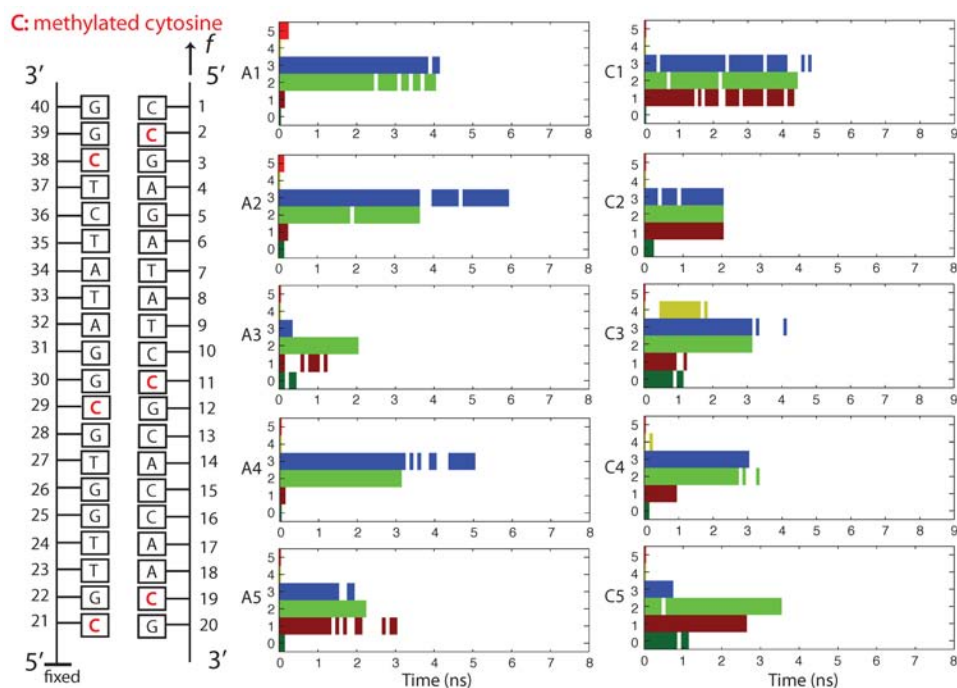


Figure S6: Progress of breaking six CG base pairs in ten  $10 \text{ \AA}/\text{ns}$  pulling simulations. Shown are the analyses of nDNA (middle) and fDNA (right). Colors differentiate six different CG base pairs: (0) C21-G20; (1) G22-C19; (2) C29-G12; (3) G30-C11; (4) C38-G3; (5) G39-C2. Colors indicate that a base pairing remains intact. Schematic representation of stretched DNA is shown at left. Methylated cytosines are marked in red.

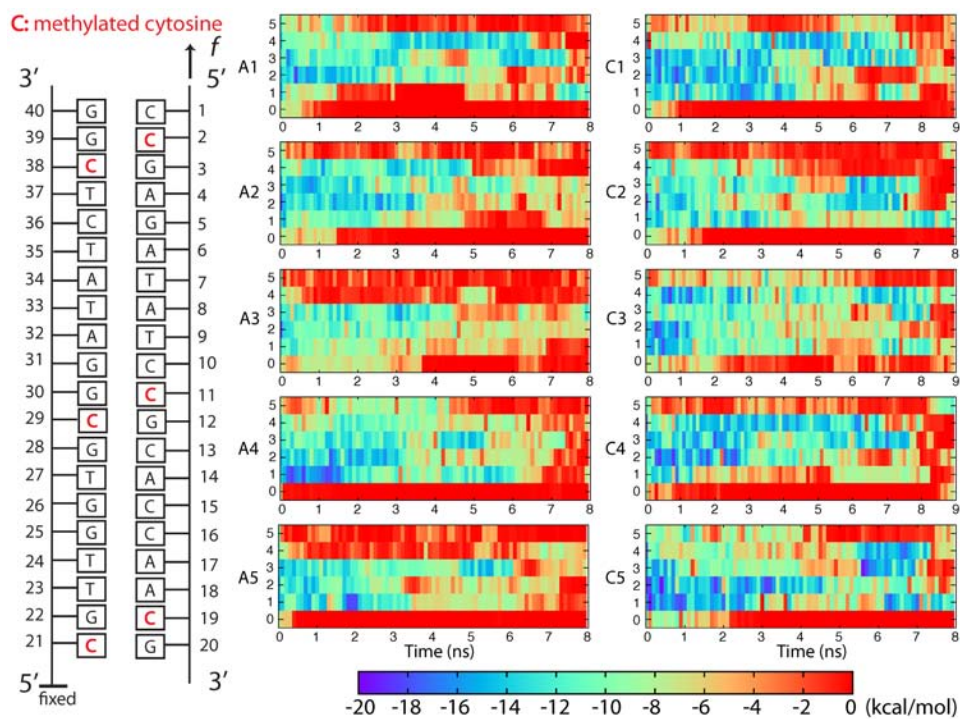


Figure S7: Time evolution of stacking energy of DNA in ten  $10 \text{ \AA}/\text{ns}$  pulling simulations. Shown are the analyses of nDNA (middle) and fDNA (right). Colors indicate the value of the stacking energy of six cytosines (see color bar at bottom). The six cytosines are: (0) C21; (1) C19; (2) C29; (3) C11; (4) C38; (5) C2. Schematic representation of stretched DNA is shown at left. Methylated cytosines are marked in red.



## References

1. Severin, P., Ho, D., and Gaub, H. E. (2011) A high-throughput molecular force assay for protein-DNA interactions. *Lab Chip*, **11**, 856–862.
2. Albrecht, C. H., Clausen-Schaumann, H., and Gaub, H. E. (2006) Differential analysis of biomolecular rupture forces. *J. Phys.: Condens. Matter*, **18**, 81–599.
3. Ho, D., Dose, C., Albrecht, C. H., Severin, P., Falter, K., Dervan, P. B., and Gaub, H. E. (2009) Quantitative detection of small molecule/DNA complexes employing a force-based and label-free DNA-microarray. *Biophys. J.*, **96**, 4661–4671.
4. Perutz, S., Kramer, E. J., Baney, J., and Hui, C.-Y. (1997) Adhesion between hydrolyzed surfaces of poly(dimethylsiloxane) networks. *Macromolecules*, **30**, 7964–7969.
5. Morfill, J., Kühner, F., Blank, K., Lugmaier, R. A., Sedlmair, J., and Gaub, H. E. (2007) B-S transition in short oligonucleotides. *Biophys. J.*, **93**, 2400–2409.
6. Kühner, F., Morfill, J., Neher, R. A., Blank, K., and Gaub, H. E. (2007) Force-induced DNA slippage. *Biophys. J.*, **92**, 2491–2497.
7. Neuert, G., Albrecht, C., Pamir, E., and Gaub, H. E. (2006) Dynamic force spectroscopy of the digoxigenin-antibody complex. *FEBS Lett.*, **580**, 505–509.
8. Blank, K., Morfill, J., and Gaub, H. E. (2006) Site-specific immobilization of genetically engineered variants of *Candida antarctica* lipase B. *Chembiochem*, **7**, 1349–1351.
9. Lu, X.-J. and Olson, W. K. (2003) 3DNA: a software package for the analysis, rebuilding and visualization of three-dimensional nucleic acid structures. *Nucl. Acids Res.*, **31**, 5108–5121.
10. Phillips, J. C., Braun, R., Wang, W., Gumbart, J., Tajkhorshid, E., Villa, E., Chipot, C., Skeel, R. D., Kale, L., and Schulten, K. (2005) Scalable Molecular Dynamics with NAMD. *J. Comp. Chem.*, **26**, 1781–1802.
11. MacKerell, Jr., A., Bashford, D., Bellott, M., Dunbrack, Jr., R. L., Evanseck, J., Field, M. J., Fischer, S., Gao, J., Guo, H., Ha, S., Joseph, D., Kuchnir, L., Kuczera, K., Lau, F. T. K., Mattos, C., Michnick, S., Ngo, T., Nguyen, D. T., Prodhom, B., Reiher, I. W. E., Roux, B., Schlenkrich, M., Smith, J., Stote, R., Straub, J., Watanabe, M., Wiorkiewicz-Kuczera, J., Yin, D., and Karplus, M. (1998) All-atom empirical potential for molecular modeling and dynamics studies of proteins. *J. Phys. Chem. B*, **102**, 3586–3616.
12. Jorgensen, W. L., Chandrasekhar, J., Madura, J. D., Impey, R. W., and Klein, M. L. (1983) Comparison of Simple Potential Functions for Simulating Liquid Water. *J. Chem. Phys.*, **79**, 926–935.

13. Martyna, G. J., Tobias, D. J., and Klein, M. L. (1994) Constant Pressure Molecular Dynamics Algorithms. *J. Chem. Phys.*, **101**(5), 4177–4189.
14. Lebrun, A. and Lavery, R. (1996) Modelling extreme stretching of DNA. *Nucl. Acids Res.*, **24**, 2260–2267.
15. Albrecht, C. H., Neuert, G., Lugmaier, R. A., and Gaub, H. E. (2008) Molecular force balance measurements reveal that double-stranded DNA unbinds Under Force in Rate-Dependent Pathways. *Biophys. J.*, **94**, 4766–4774.
16. Essevaz-Roulet, B., Bockelmann, U., and Heslot, F. (1997) Mechanical separation of the complementary strands of DNA. *Proc. Natl. Acad. Sci. USA*, **94**, 11935–11940.
17. Sotomayor, M. and Schulten, K. (2007) Single-Molecule Experiments in Vitro and in Silico. *Science*, **316**, 1144–1148.
18. Lee, E. H., Hsin, J., Sotomayor, M., Comellas, G., and Schulten, K. (2009) Discovery through the computational microscope. *Structure*, **17**, 1295–1306.
19. Rief, M., Clausen-Schaumann, H., and Gaub, H. E. (1999) Sequence-dependent mechanics of single DNA molecules. *Nat. Struct. Biol.*, **6**, 346–349.

## Peptide–Antibody Complex as Handle for Single-Molecule Cut &amp; Paste

Mathias Strackharn,<sup>[a]</sup> Stefan W. Stahl,<sup>[b]</sup> Philip M. D. Severin,<sup>[a]</sup> Thomas Nicolaus,<sup>[a]</sup> and Hermann E. Gaub<sup>\*[a]</sup>

Feynman is frequently quoted for having foreseen that individual atoms may be arranged one-by-one to form functional assemblies.<sup>[1]</sup> The seminal work by Don Eigler and colleagues<sup>[2,3]</sup> convincingly proved the validity of these concepts: functional assemblies of atoms forming quantum corrals showed emergent novel properties. In the life sciences, Hans Kuhn realized rather early that for many multistep biological reactions, not only the sequence but also the arrangement of the individual enzymes plays a crucial role. He envisaged that in order to investigate their interaction, novel approaches would be needed: he wished to have "...molecular pliers to pick and place individual enzymes to create functional assemblies with designed properties."<sup>[4]</sup> The application of bottom-up strategies to assemble biomolecular complexes, however, turned out to be rather challenging. A quite vivid dispute was fought in a series of papers between Smalley and Drexler on where these difficulties arise from and whether fundamental limitations prevent a molecule for molecule assembly of biomolecules in electrolyte ambient and at physiologic temperatures.<sup>[5]</sup> With the development of single-molecule cut-and-paste (SMC&P) we overcame these difficulties and provided a platform technology for the assembly of biomolecules at surfaces.<sup>[6]</sup> It combines the Å-positioning precision of atomic force microscopy (AFM)<sup>[7,8]</sup> with the selectivity of DNA hybridization to pick individual molecules from a depot chip and to arrange them on a target site by pasting the molecules one-by-one.<sup>[9]</sup> The advanced methods of single-molecule fluorescence detection<sup>[10–14]</sup> allowed us to localize the pasted molecules with nanometer accuracy and to show that the deposition accuracy is presently only limited by the length of the spacers used to couple the DNA handles and anchors to tip and construction site, respectively.<sup>[15]</sup>

In the various SMC&P implementations realized to date, the system of hierarchical binding forces was built from DNA duplexes of suitable geometry and sequence. Since one of the major goals, which spurs the development of the SMC&P technology, is the ability to arrange proteins, for example, in enzymatic networks of predefined composition and proximity, mo-

lecular anchors and handles should ultimately be of such a kind that they can be co-expressed with the proteins, for example, as tags on a protein chip. As a first step in this direction, we chose in this Communication a peptide–antibody complex to replace the DNA-based handle complex in the conventional SMC&P design. This single-chain antibody, which is part of a larger family, was selected by the Plückthun group to recognize a 12 aa long segment of a polypeptide chain with picomolar affinity.<sup>[16]</sup> In previous studies we had investigated by single-molecule force spectroscopy and molecular dynamics (MD) simulations several different peptides and antibodies and investigated the influence of the attachment site on the unbinding mechanisms.<sup>[17,18]</sup> We could confirm that the antibody (when covalently attached at the C-terminal end) stays intact when the peptide is pulled out of the binding pocket. Herein, we used this antibody immobilized at the AFM cantilever tip to pick up a fluorescently labeled transfer DNA–peptide chimera via its peptide tag and paste it on the target site of the chip.

Using a microspotter, we deposited microdroplets of a DNA solution onto a pretreated glass surface resulting in approximately 50 µm-sized spots with a distance of 70 µm (see Supporting Information, Figure 1). The ssDNA was allowed to covalently bind to the surface via PEG spacers. One drop contained ssDNA with a reactive 5' end. The resulting spot later on forms the depot. The other drop contained DNA with a reactive 3' end and the resulting spot forms the target. The depot area was then loaded with a complementary ssDNA strand, which was extended at the 3' end by a 13-amino-acid-long handle peptide and labeled at the 5' end with an atto647N fluorophore. For simplicity, this construct is called transfer strand. Single-chain antibodies were covalently attached via PEG spacers to the AFM cantilever tip (see Figure 1a for a cartoon of the SMC&P process).

To pick up an individual DNA strand, the AFM tip was lowered at the depot area, allowing the antibody at the tip to bind to the peptide at the end of the DNA strand to be transferred. Upon retract, typically the force gradually increased and finally dropped as shown in Figure 1b, where the force is plotted as a function of the distance. We chose the functionalization density of the tip and the surface such that typically only in every second attempt we found this characteristic force curve, indicating that exactly one DNA strand was picked up. In the majority of the other 50% of the attempts we found no measurable force upon retract, indicating that no molecule was picked up. In these cases, we repeated the pick-up cycle. Only in very rare cases (<2%) did we find higher values for the unbinding force, indicating that more than one molecule was picked up.

[a] M. Strackharn, P. M. D. Severin, T. Nicolaus, Prof. Dr. H. E. Gaub  
Center for Nanoscience and Department of Physics  
University of Munich, Amalienstrasse 54  
80799 München (Germany)  
Fax: (+49) 89-2180-2050  
E-mail: gaub@lmu.de

[b] S. W. Stahl  
Center for Integrated Protein Science (CIPSM)  
Center for Nanoscience and Department of Physics  
University of Munich, Amalienstrasse 54  
80799 München (Germany)

Supporting information for this article is available on the WWW under <http://dx.doi.org/10.1002/cphc.201100765>.

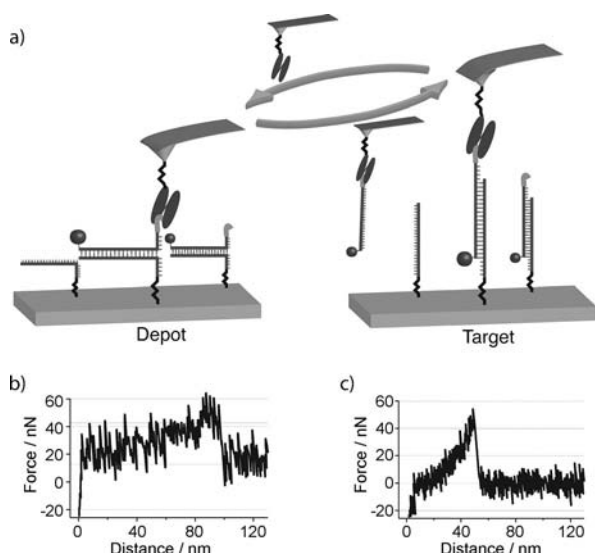


**Figure 1.** a) Schematic representation of a typical SMC&P cycle. A single-chain antibody fragment is covalently bound to the cantilever tip. When lowered to the depot area surface, the antibody binds to a peptide at the end of a DNA strand, which is attached to the surface via 40 bp in zipper mode. When the tip is pulled back, the basepairs open up one by one. The transfer construct remains attached to the cantilever and may be transferred to the target area. Here, the cantilever is lowered again such that the DNA part of the construct binds to the DNA target anchor. When the cantilever is retracted, this time the DNA bases are loaded in shear geometry and the antibody-peptide bond yields. The transfer construct remains in the target area and the cantilever can be used for the next transfer cycle again. b,c) Force-distance graphs of typical rupture events in the depot (b) and target (c) areas.

The AFM tip was now moved to a chosen position in the target area and gradually lowered, allowing the transfer strand to hybridize to the target DNA. Upon retract again, the force-versus-distance curve was recorded. A typical example is given in Figure 1c. As can be seen, the force peaks at a much higher value, typically at 40 pN. Since this value is much lower than the force required to break the DNA shear bond, we conclude with a high certainty that the transfer DNA was deposited in the target area. Details of the probabilities for the rupture of bonds in series are given elsewhere.<sup>[19]</sup>

To corroborate that the force required to unzip the anchor duplex is lower than the binding force of the peptide-antibody complex and that the latter is lower than the force required to unbind the DNA duplex in shear geometry we investigated the bond strength of the three complexes in a separate series of experiments. Since unbinding forces depend in a first-order approximation given by the Bell-Evans model on the logarithm of the force loading rate,<sup>[20]</sup> we varied the latter by one and a half orders of magnitude. The result is depicted in Figure 2. For the lowest curve, the unbinding force of the depot-transfer duplex was measured under conditions where both were covalently attached to tip and sample surface via PEG spacers. Note that the depot strand was attached at its 5' end and the transfer strand was attached at the 3' end, mimicking the geometry during pickup. For the red curve, the peptide was attached to the sample surface, allowing the antibody,

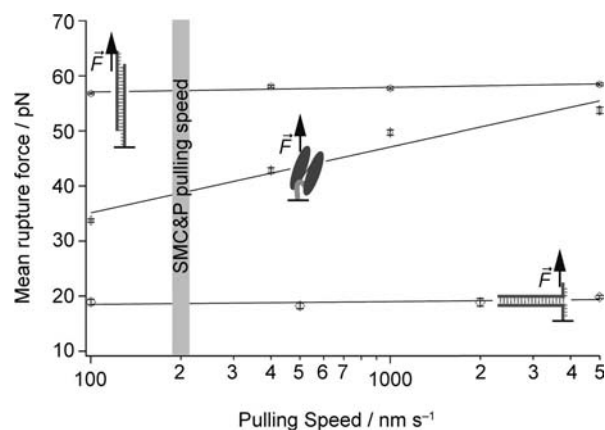


**Figure 2.** Dependency of the mean rupture force on the pulling speed. The mean rupture force for opening the 40 bp DNA in shear geometry is nearly 60 pN. The mean rupture force of the peptide-antibody complex is significantly lower than that of the DNA in shear geometry and shows a logarithmic dependence on the loading rate. The 40 bp DNA in unzip geometry opens at a mean rupture force of around 20 pN. Error bars depict fitting errors from fitting the force distributions. Highlighted is the pulling speed chosen for the deposition process.

which was covalently attached to the tip, to bind the peptide in exactly the same geometry as during pick up. As can be seen, both lines differ drastically in their slopes, but more important for the issues discussed here, the force required to unzip the two DNA strands is significantly lower than that required to break the peptide-antibody bond for the entire range of pulling speeds. Since the curve of the antibody-peptide complex lies significantly below the curve recorded for the DNA duplex in shear geometry (note that the target strand was now attached with the 3' end to the surface), it is predominantly the peptide-antibody complex that ruptures in the deposition process. From this graph we chose the optimum pulling speed window around 200 nm sec<sup>-1</sup> for the SMC&P experiments described below.

In parallel to the SMC&P experiments, we followed the deposition process of the individual molecules microscopically in total internal fluorescence excitation. Details of the device are given elsewhere,<sup>[21]</sup> but it is important to note that the custom-built combined AFM-TIRF microscope was optimized for vibrational stability, which is essential to avoid the coupling of mechanical noise into the AFM via the immersion fluid required for high NA optical microscopy. Figure 3a shows a micrograph taken at the beginning of the deposition process in the target region. In Figure 3b the left image shows the scattered light from the tip and the emission of the fluorophore. The second image depicts the same spot after the tip has left the evanescent zone, leaving only the deposited fluorophore visible (a movie of this process is provided in the Supporting Information). With standard techniques, the position of this fluorophore was then determined with an accuracy of 1.4 nm.

After the deposition of the transfer strand in the target area, the tip is again in its original state and therefore ready to pick up another transfer strand from the storage area. Since the antibody-peptide bond is reversible, this pick-up and deposit

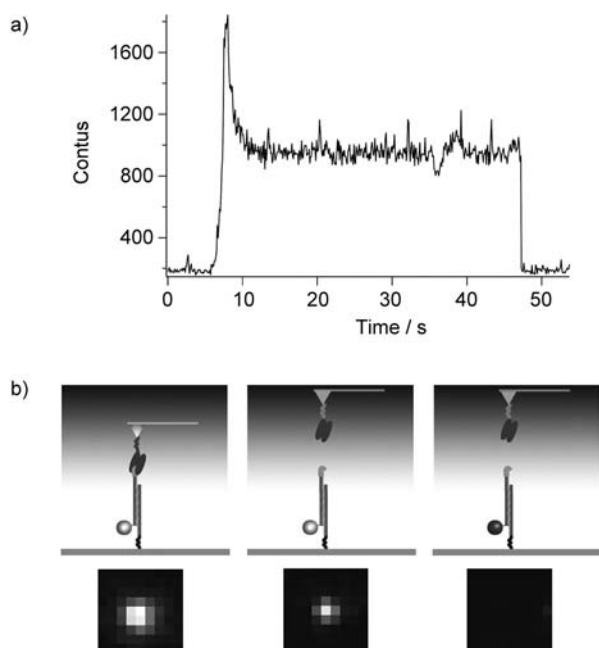


**Figure 3.** Deposition of a single DNA-peptide construct. The loaded cantilever is lowered towards the target area, where the DNA-peptide construct is deposited, when the lever is withdrawn. a) Fluorescence timetrace and b) cartoon of the process. When the cantilever enters the evanescent field of the TIR illumination, fluorescence from the dye-labeled construct and scattered light from the cantilever tip contribute to the signal, whereas after retraction of the cantilever, only fluorescence of the dye molecule is measured. No signal is measured after photobleaching of the dye.

or—in other words—molecular cut-and-paste process may be carried out for many cycles, allowing one molecule after the other to be transferred, unless damage to the antibody occurs during the forced unbinding of the antibody-peptide complex. To demonstrate that the antibody-peptide complex is robust and very well suited as handle complex at the AFM tip, we as-

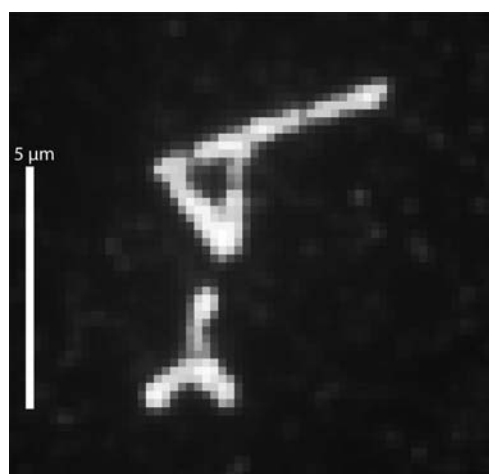


**Figure 4.** The robustness of the SMC&P process is demonstrated by the molecule-by-molecule assembly of a microscopic pattern showing a cantilever and an antibody. The pattern is assembled from approximately 600 molecules.

sembled the molecular pattern depicted in Figure 4 from approximately 600 transfer strands in a molecule-by-molecule copy-and-paste process. This convincingly demonstrates that the hierarchical force system, which is a prerequisite for SMC&P, may well be realized based on peptides or protein modules for anchor and/or handle groups. One may as well envisage covalent or organometallic coupling schemes<sup>[22,23]</sup> or even external modulation of the interaction forces by externally controlled Coulomb interactions<sup>[24]</sup> to expand the toolbox for single-molecule assembly.

## Experimental Section

All measurements described in the manuscript were carried out with a custom-designed combined AFM/TIRF microscope described in detail elsewhere.<sup>[21]</sup> We provide a detailed description of AFM measurements, TIRF microscopy, single-chain antibody fragment preparation, peptide synthesis, surface preparation, microstructuring with a microplotter, and oligomer sequences in the Supporting Information.

## Acknowledgements

This work was supported by the Volkswagen foundation, the Nano Initiative Munich and the German Science Foundation (SFB 863).

**Keywords:** biophysics • nanostructures • scanning probe microscopy • single-molecule studies • TIRF microscopy

- [1] R. P. Feynman, *Eng Sci* **1960**, *23*, 22–36.
- [2] M. F. Crommie, C. P. Lutz, D. M. Eigler, *Science* **1993**, *262*, 218–20.
- [3] T. A. Jung, R. R. Schlittler, J. K. Gimzewski, H. Tang, C. Joachim, *Science* **1996**, *271*, 181–184.
- [4] H. Kuhn, *Verhandlungen der Schweizerischen Naturforschenden Gesellschaft* **1965**, 245–266.
- [5] R. Baum, *Chem. Eng. News* **2003**, *81*, 37–42.
- [6] S. K. Kufer, E. M. Puchner, H. Gump, T. Liedl, H. E. Gaub, *Science* **2008**, *319*, 594–6.
- [7] G. Binnig, C. F. Quate, C. Gerber, *Phys. Rev. Lett.* **1986**, *56*, 930–933.
- [8] B. Drake, C. B. Prater, A. L. Weisenhorn, S. A. C. Gould, T. R. Albrecht, C. F. Quate, D. S. Cannell, H. G. Hansma, P. K. Hansma, *Science* **1989**, *243*, 1586–1589.
- [9] E. M. Puchner, S. K. Kufer, M. Strackharn, S. W. Stahl, H. E. Gaub, *Nano Lett.* **2008**, *8*, 3692–5.
- [10] W. E. Moerner, L. Kador, *Phys. Rev. Lett.* **1989**, *62*, 2535–2538.
- [11] T. Schmidt, G. J. Schutz, W. Baumgartner, H. J. Gruber, H. Schindler, *Proc. Natl. Acad. Sci. USA* **1996**, *93*, 2926–9.
- [12] R. D. Vale, T. Funatsu, D. W. Pierce, L. Romberg, Y. Harada, T. Yanagida, *Nature* **1996**, *380*, 451–3.
- [13] A. Zurner, J. Kirstein, M. Doblinger, C. Bräuchle, T. Bein, *Nature* **2007**, *450*, 705–8.
- [14] G. Seisenberger, M. U. Ried, T. Endress, H. Buning, M. Hallek, C. Bräuchle, *Science* **2001**, *294*, 1929–32.
- [15] S. K. Kufer, M. Strackharn, S. W. Stahl, H. Gump, E. M. Puchner, H. E. Gaub, *Nat Nanotechnol* **2009**, *4*, 45–9.
- [16] C. Zahnd, S. Spinelli, B. Luginbuhl, P. Amstutz, C. Cambillau, A. Pluckthun, *J Biol Chem.* **2004**, *279*, 18870–7.
- [17] J. Morfill, J. Neumann, K. Blank, U. Steinbach, E. M. Puchner, K. E. Gottschalk, H. E. Gaub, *J. Mol. Biol.* **2008**, *381*, 1253–66.
- [18] J. Morfill, K. Blank, C. Zahnd, B. Luginbuhl, F. Kuhner, K. E. Gottschalk, A. Pluckthun, H. E. Gaub, *Biophys. J.* **2007**, *93*, 3583–90.
- [19] G. Neuert, C. H. Albrecht, H. E. Gaub, *Biophys. J.* **2007**, *93*, 1215–23.

- [20] F. Kühner, H. E. Gaub, *Polymer* **2006**, *47*, 2555–2563.
- [21] H. Gump, S. W. Stahl, M. Strackharn, E. M. Puchner, H. E. Gaub, *Rev. Sci. Instrum.* **2009**, *80*, 063704.
- [22] B. M. Gaub, C. Kaul, J. L. Zimmermann, T. Carell, H. E. Gaub, *Nanotechnology* **2009**, *20*, 434002.
- [23] P. Knochel, S. Z. Zimdars, S. X. M. du Jourdin, F. Crestey, T. Carell, *Org. Lett.* **2011**, *13*, 792–795.
- [24] M. Erdmann, R. David, A. R. Fornof, H. E. Gaub, *Nat. Chem.* **2010**, *2*, 745–9.

---

Received: September 29, 2011

Published online on December 19, 2011

---

# CHEMPHYSICHEM

## Supporting Information

© Copyright Wiley-VCH Verlag GmbH & Co. KGaA, 69451 Weinheim, 2012

### **Peptide–Antibody Complex as Handle for Single-Molecule Cut & Paste**

Mathias Strackharn,<sup>[a]</sup> Stefan W. Stahl,<sup>[b]</sup> Philip M. D. Severin,<sup>[a]</sup> Thomas Nicolaus,<sup>[a]</sup> and Hermann E. Gaub<sup>\*[a]</sup>

cphc\_201100765\_sm\_miscellaneous\_information.pdf

cphc\_201100765\_sm\_2.avi

# Supplementary Information

## Peptide:Antibody Complex as Handle for Single-Molecule Cut & Paste

Mathias Strackharn<sup>1,\*</sup>, Stefan W. Stahl<sup>1,2</sup>, Philip M. D. Severin<sup>1</sup> Thomas Nicolaus<sup>1</sup>,  
and Hermann E. Gaub<sup>1</sup>

<sup>1</sup> Center for Nanoscience and Department of Physics, University of Munich, Amalienstraße 54,  
80799 Munich, Germany

<sup>2</sup> Center for Integrated Protein Science (CIPSM), Munich, Germany

\* [mathias.strackharn@physik.uni-muenchen.de](mailto:mathias.strackharn@physik.uni-muenchen.de)

All measurements described in the manuscript were carried out with a custom designed combined AFM/TIRF microscope described in detail in <sup>[21]</sup>. Here we provide the description of those parts and procedures, which are relevant to the experiments described in the main text:

### AFM measurements

The spring constants of the DNA modified cantilevers were calibrated in solution using the equipartition theorem <sup>[25]</sup>, <sup>[26]</sup>. For the single-molecule force spectroscopy BL-AC40TS-C2 levers (Olympus, Tokyo, Japan) and for SMC&P experiments MLCT-AUHW levers (Bruker, Camarillo, USA) were used. The protocol for the functional assembly as well as the data recording was programmed using Igor Pro (Wave Metrics, Lake Oswego, USA) and an Asylum Research MFP3D controller (Asylum Research, Santa Barbara, USA), which provides ACD and DAC channels as well as a DSP board for setting up feedback loops. Cantilever positioning for pick-up and delivery was controlled in closed-loop operation. The typical cycle time for one functional assembly process lies between 2 and 3 seconds depending on the sample orientation and the



traveling distance between depot and target area. The positioning feedback accuracy is  $\pm 3$  nm however long term deviations may arise due to thermal drift. Extension velocities are set to  $2 \mu\text{m/s}$  in the depot area and  $200 \text{ nm/s}$  in the target area. Force spectroscopy data was converted into force-extension curves and the most probable rupture force was obtained using the program IGOR Pro 6.22 (Wave Metrics, Lake Oswego, USA) and a set of custom-made procedures. Rupture forces for each retraction speed were plotted in histograms and fitted with Gaussians to determine the most probable rupture forces.

### **TIRF microscopy**

The fluorescence microscopy measurements were carried out with objective-type TIRF excitation on a microscope that was especially designed for a stable combination of AFM with TIRFM<sup>[21]</sup>. We excited with a fiber-coupled 637 nm diode laser (iBeam smart, TOPTICA, München, Germany) through a 100x/1.49 oil immersion objective lens (Nikon CFI Apochromat TIRF, Japan). As excitation filter, beam splitter, and emission filter a BrightLine HC 615/45, a Raman RazorEdge 633 RS, and a Chroma ET 685/70 (AHF, Tübingen, Germany) were used respectively. Images were taken with a back-illuminated EMCCD camera (DU-860D, Andor, Belfast, Ireland). Fluorescence image sequences were taken at 10 Hz frame rate, gain 150, 1 MHz readout rate in frame transfer mode. The camera was operated at  $-75 \text{ }^\circ\text{C}$ .

### **Preparation of the C11L34 single chain antibody fragment**

The C11L34 single chain antibody fragment was prepared as described in<sup>[18]</sup>. The scFv construct harbored a C-terminal His tag followed by a Cys to allow for site-specific immobilization and was obtained by periplasmic expression in *E. coli* SB536. C11L34 was purified by  $\text{Ni}^{2+}$  and immobilized antigen affinity chromatography according to standard protocols. The concentration was adjusted to  $2.5 \text{ mg/ml}$  in storage buffer containing  $50 \text{ mM}$  sodium phosphate,  $\text{pH } 7.2$ ,  $50 \text{ mM}$  NaCl and  $10 \text{ mM}$  EDTA.

### **Preparation of GCN4 peptides**

GCN4 peptides with the sequence CYHLENEVARLKK were synthesized manually in syringe reaction chambers. 0.05 g Wang resin (Iris, Marktredwitz, Germany) were incubated with 10 eq (of the maximal loading capacity of the resin) Fmoc-L-Lys(Boc)-OH (Iris, Marktredwitz, Germany) for 4 h. The incubation was repeated for another 4 h. For the measurement of the resin loading 500  $\mu$ l of DMF (Sigma, Taufkirchen, Germany) with 20 % Piperidine (Fluka, St. Gallen, Switzerland) were added to 3 mg of the resin. The solution was shaken for 1 h, the 3 ml DMF were added. By measuring the extinction at 300 nm of a 1:10 dilution with DMF with 20% Piperidine the resin loading was determined. Remaining hydroxyl groups on the Wang resin were blocked by esterification with acetic anhydride. All other Fmoc-protected amino acids (Iris, Marktredwitz, Germany) were added by applying the following procedure: 10 eq amino acid and 100 eq HOBT (Fluka, St. Gallen, Switzerland) were dissolved in DMF, 10 eq DIC (Fluka, St. Gallen, Switzerland) was added and the solution was shaken for 1 h. Then 10 eq DIPEA (Fluka, St. Gallen, Switzerland) were added and solution was shaken for 1h again. The process was once repeated. Then then the resin was washed with 10 ml DMF, 10 ml DCM, 10 ml Ether and 6 ml DMF, again. Fmoc protection groups were removed by incubating the resin in DMF with 20 % Piperidine for 20 min twice. The resin was then flushed with 10 ml DMF, 10 ml DCM (Carl Roth, Karlsruhe, Germany), 10 ml Ether (Sigma, Taufkirchen, Germany) and 6 ml DMF. The peptide was finally separated from the resin by 3 h shaking in 50  $\mu$ l p-Thiocresol (Fluka, St. Gallen, Switzerland), 50  $\mu$ l Thioanisol (Fluka, St. Gallen, Switzerland) and 300  $\mu$ l TFA (Sigma, Taufkirchen, Germany). The solution was transferred into a centrifuge tube, where the peptide was precipitated with 10 ml Ether at -80 °C. The solution was centrifuged at 4 °C and 4600 g and the pellet was washed in Ether six times. Finally the pellet was resolved in a 3:1 ddH<sub>2</sub>O/tertButanol (Sigma, Taufkirchen, Germany) solution and lyophilized.

### **Preparation of cantilevers**

Cantilevers (MLCT, Bruker, Camarillo, USA) were always oxidized in a UV-ozone Cleaner (UVOH 150 LAB, FHR Anlagenbau GmbH, Ottendorf-Okrilla, Germany). For single molecule force spectroscopy experiments and single molecule deposition they were silanized with 3-aminopropyltrimethoxysilane (ABCR, Karlsruhe, Germany), baked at 80 °C, pre-incubated with sodium borate buffer (pH 8.5), PEGylated with NHS-PEG-Maleimide (MW 5000, Rapp Polymere, Tübingen, Germany), and washed with ddH<sub>2</sub>O. According to the experiment type either C11L34 antibodies at a concentration of 2.5 mg/ml or reduced thiolated transfer DNA at a concentration of 10 μM was bound to the pegylated cantilevers at 8 °C for 2 h. Cantilevers were then washed with PBS buffer. In case of the SMC&P experiment, where molecules were assembled to the pattern of a cantilever with antibody at the tip, the cantilever was silanized with (3-Glycidoxypropyl)trimethoxysilane (ABCR, Karlsruhe, Germany), baked at 80 °C for 30 min and incubated overnight at 8 °C with 1mg/ml aminodextrane (D1861, Invitrogen, Carlsbad, USA) in sodium borate buffer (pH 8.5). NHS-PEG-Mal was then applied to the cantilever, which was then washed in ddH<sub>2</sub>O. Subsequently C11L34 antibodies at a concentration of 2.5 mg/ml were bound to the pegylated cantilevers at 8 °C for 2 h. The cantilever was finally washed with PBS.

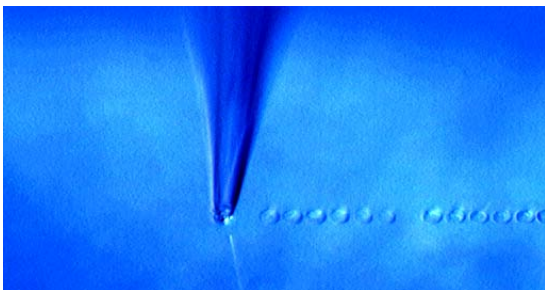
### **Preparation of cover glass surfaces**

Cover glass slips were sonicated in 50% (v/v) 2-propanol and ddH<sub>2</sub>O for 15 min and thoroughly rinsed with ddH<sub>2</sub>O. They were then oxidized in 50% (v/v) sulfuric acid and hydrogen peroxide (30%) for 45 min and were then again well rinsed with ddH<sub>2</sub>O. The oxidized cover glass slips were silanized with a mixture of 2% 3-aminopropyltrimethoxysilane, 90% EtOH, 8% ddH<sub>2</sub>O for 1 h. Cover glasses were thoroughly rinsed with pure EtOH first and ddH<sub>2</sub>O afterwards, and were baked at 80 °C for 30 min. After 30 min soaking in 50 mM sodium borate buffer, pH 8.5 the cover glasses were treated with 50 mM NHS-PEG-maleimide (MW 5000) in the sodium borate buffer for 1 h and then rinsed with ddH<sub>2</sub>O.

In case of the SMC&P experiments depot and target oligomers were reduced, purified and dissolved again. The reduced thiolated depot and target oligomers were deposited with a microplotter (GIX, Sonoplot, Middleton, USA), nonbound DNA was washed away with ddH<sub>2</sub>O. Transfer oligomers were deposited on top of the depot area. Nonbound transfer strands were washed away with 4xPBS buffer. (Details on the microstructuring process are given in the following section.) The sample was then covered with 50 mM sodium borate buffer, pH 8.5, 500 mM NaCl, 10 mM TCEP for 30 min for deprotonation of amines and quenching of unreacted maleimides. The sample was then rinsed with 50 mM sodium borate buffer, pH 8.5, 500 mM NaCl and incubated for 1h with 10 mM NHS-PEG-Mal dissolved in 50 mM sodium borate buffer, pH 8.5, 500 mM NaCl. It was washed with PBS, then reduced GCN4 peptides at a concentration of 100  $\mu$ M in 50 mM sodium phosphate buffer, pH 7.2, 250 mM NaCl, 10 mM EDTA were added for 1 h. The sample was rinsed again with PBS.

For single molecule force spectroscopy reduced thiolated depot or target oligomers or the reduced GCN4 peptide was bound to the pegylated cover glass slips and the sample was thoroughly rinsed with water.

### **Structuring surfaces with a Microplotter**



Due to the limited travel range of the AFM, the depot and target area have to be created in a distance of several micrometers. For this reason these areas are produced by microstructuring the cover glass with a microplotter (GIX, Sonoplot, Middleton, USA). A standard glass capillary (World Precision Instruments, Inc.) with an inner diameter of 30  $\mu$ m was used, which results in spots of the diameter of 45  $\mu$ m to 50  $\mu$ m on the cover glass

(dispenser voltage 3V and 0.1 s dispensing time). The prepared DNA Oligomer solutions (see previous section) were plotted on the pegylated cover glass in two 800  $\mu\text{m}$  long lines for depot and target, which were separated by a 20  $\mu\text{m}$  to 30  $\mu\text{m}$  broad gap.

After plotting the depot line, the cover glass was rinsed with 5 ml (4x PBS) directly in the sample holder without moving it. In a second step, the transfer strand was plotted onto the depot line. Operating experience showed that in the case of hybridizing DNA via Microplotter a contact time (capillary on the cover slide) of around 20 s per spot optimized the density of hybridized transfer strands. Afterwards the sample was rinsed as before. In a last step, the target strand was plotted in same manner as the depot.

### **Oligomer sequences**

thiolated depot oligomer

5' SH - TTT TTT CAT GCA AGT AGC TAT TCG AAC TAT AGC TTA AGG ACG TCA A

thiolated target oligomer

5' CAT GCA AGT AGC TAT TCG AAC TAT AGC TTA AGG ACG TCA ATT TTT - SH

transfer oligomer with amine and Atto647N

5' (Atto647N) - TTG ACG TCC TTA AGC TAT AGT TCG AAT AGC TAC TTG CAT GTT TTT TTT - NH<sub>2</sub>

thiolated transfer oligomer

5' TTG ACG TCC TTA AGC TAT AGT TCG AAT AGC TAC TTG CAT GTT TTT TTT - SH

1. H. Gump, S. W. Stahl, M. Strackharn, E. M. Puchner, H. E. Gaub, Ultrastable combined atomic force and total internal reflection fluorescence microscope [corrected]. *The Review of scientific instruments* **80**, 063704 (Jun, 2009).
2. E. Florin, Sensing specific molecular interactions with the atomic force microscope. *Biosensors and Bioelectronics* **10**, 895 (1995).
3. H. J. Butt, M. Jaschke, Calculation of thermal noise in atomic-force microscopy. *Nanotechnology* **6**, 1 (1995).

4. J. Morfill *et al.*, Affinity-matured recombinant antibody fragments analyzed by single-molecule force spectroscopy. *Biophys J* **93**, 3583 (Nov 15, 2007).
5. A. Krebber *et al.*, Reliable cloning of functional antibody variable domains from hybridomas and spleen cell repertoires employing a reengineered phage display system. *J Immunol Methods* **201**, 35 (Feb 14, 1997).
6. H. Bothmann, A. Pluckthun, Selection for a periplasmic factor improving phage display and functional periplasmic expression. *Nat Biotechnol* **16**, 376 (Apr, 1998).
7. J. Hanes, L. Jermutus, S. Weber-Bornhauser, H. R. Bosshard, A. Pluckthun, Ribosome display efficiently selects and evolves high-affinity antibodies in vitro from immune libraries. *Proc Natl Acad Sci U S A* **95**, 14130 (Nov 24, 1998).

## 7.2 Manuskripte für Publikationen

M1:

Severin, P.M.D., X. Zou, K. Schulten, and H.E. Gaub, *Cytosine methylation alters DNA mechanical properties*. **EMBO J**, submitted

M2:

Severin, P.M.D., H.E. Gaub and H. Li, *Probing the force-induced globule-coil Transition of individual polymer chains via single molecule force spectroscopy*.

# Effects of cytosine hydroxymethylation on DNA strand separation

Philip M.D. Severin <sup>\*1,2</sup>, Xueqing Zou <sup>\*3</sup>, Klaus Schulten <sup>†,3,4</sup>, and Hermann E. Gaub <sup>†1,2</sup>

<sup>1</sup>Lehrstuhl für Angewandte Physik and Center for Nanoscience (CeNS),  
Ludwig-Maximilians-Universität, Amalienstrasse 54, 80799 Munich, Germany

<sup>2</sup>Munich Center For Integrated Protein Science (CIPSM), Ludwig-Maximilians-Universität,  
Butenandtstrasse 5-13, 81377 Munich, Germany

<sup>3</sup>Beckman Institute, University of Illinois, Urbana, Illinois, USA

<sup>4</sup>Department of Physics, University of Illinois, Urbana, Illinois, USA

## Abstract

Cytosine hydroxymethylation is recently found to be a new epigenetic control factor in higher organisms. New discoveries of biological roles of hydroxymethylation raise questions about how such an epigenetic modification exerts functions and how organism discriminate cytosine hydroxymethylation from methylation. Here, we investigated the effect of cytosine hydroxymethylation on mechanical properties of DNA under load through molecular force assay (MFA) measurements and steered molecular dynamics (SMD) simulations. MFA experiments identified significant effects of hydroxymethylation on stretching-induced strand separation; the possible physical mechanism has been suggested by SMD simulations. We demonstrated that hydroxymethylation can either up-regulate or down-regulate strand separation propensity, indicating that hydroxymethylation could control gene expression by facilitating or obstructing the action of transcription machinery.

---

\*These authors contributed equally to this work

†Correspondence should be addressed to H.G. (gaub@physik.uni-muenchen.de) and K.S. (kschulte@ks.uiuc.edu)



## Introduction

Genetic information, which determines the development of an organism, is encoded in DNA sequence. Recently, more and more studies showed that there are the so-called epigenetic mechanisms that can change gene expression of the cell without altering DNA sequence, such as DNA methylation and histone deacetylation (Jones and Takai, 2001; Jaenisch and Bird, 2003). DNA methylation is found to exist widely in the CpG sites, and it plays an important role in silencing genes by impeding transcription factors (Jones, 2002; Straussman et al., 2009; Rottach et al., 2009). Histone deacetylation controls gene transcription level by remodeling the structure of chromatin (Dokmanovic et al., 2007). Cytosine hydroxymethylation was recently discovered as another important epigenetic modification on DNA in mammalian cells (Tahiliani et al., 2009; Kriaucionis and Heintz, 2009). Similar to methylation, hydroxymethylation replaces, at the 5' position in cytosine, the hydrogen atom by a hydroxymethyl group. It has been identified that cytosine hydroxymethylation is also involved in gene regulation (Tahiliani et al., 2009; Munzel et al., 2010; Münzel et al., 2011). For example, hydroxymethylation level was found to be associated with pluripotency of stem cells (Tahiliani et al., 2009). Disturbed hydroxymethylation of DNA cytosine could result in disordered cell functions, causing different types of cancers, e.g., myeloid cancers (Ko et al., 2010).

Prior studies suggested that hydroxymethylated cytosine is an intermediate in a pathway of DNA demethylation in the mammalian zygote (Tahiliani et al., 2009; Ito et al., 2010), or even may be the final product of genome-wide demethylation. Although many works were done to find out biological roles of DNA hydroxymethylation, how it induces corresponding functions is still unclear. Unlike DNA methylation, no protein is found to bind hydroxymethylation sites on DNA that can intermediate gene expression. It is speculated that DNA hydroxymethylation could exclude the binding of methylcytosine-binding proteins to influence gene activities associated with DNA methylation (Valinluck et al., 2004; Jin et al., 2010).

Cytosine hydroxymethylation was observed to be a stable DNA modification in mammalian tissues and relatively abundant in the central nervous system (Penn et al., 1972; Szwagierczak et al., 2010; Munzel et al., 2010; Feng et al., 2010). Some groups have quantified the amount of hydroxymethylated cytosines in some mammalian tissues (Robertson et al., 2011; Szwagierczak et al., 2010; Munzel et al., 2010), but the specific positions of hydroxymethylated cytosines are still unknown. The technical challenge of discrimination of methylated cytosine and hydroxymethylated cytosine is due to the similarity between them. Wanunu *et al.* utilized solid-state nanopores to discriminate methylcytosine from hydroxymethylcytosine in DNA molecules, suggesting that hydroxymethylation may affect the flexibility and stability of DNA duplexes (Wanunu et al., 2011). In many biological processes, e.g., transcription, molecular machines exert mechanical forces on other molecules such as RNA polymerase, promoting DNA strand separation to access genetic information stored in

the DNA sequence. Chemical modifications on DNA, e.g., hydroxymethylation, likely either facilitate or inhibit the strand separation of DNA. Our recently experimental-computational study (Severin et al., 2011b) have demonstrated that methylation influences double-stranded DNA’s propensity for strand separation, which might contribute to epigenetic regulation in cells. Since DNA replication, transcription and translation all involves strand separation, an in-depth characterization of hydroxymethylation effects on strand separation of DNA should be critical for our rapidly evolving understanding of epigenetics.

In the present work, we investigated the effects of hydroxymethylation on mechanical properties of DNA using molecular force assay (MFA) and molecular dynamics (MD) simulation. MFA measurements were conducted to compare the stabilities of different hydroxymethylated DNA duplexes when they are stretched in zipper and shear geometries. DNA exhibits different stabilities in two pulling geometries. It was observed that DNA with more hydroxymethylcytosine (hmC) sites is more stable than DNA with less hmC sites, when it is pulled in zipper geometry; while in the case of shear geometry, the stability of DNA not only associates with the number of hmC sites, but also their positions and context (sequence-dependence). MD simulations were performed to provide a detailed description of the pathway of DNA separation in zipper and shear geometries, as well as the influence of hydroxymethylation on DNA strand separation.

## Results

### Molecular force assay measurements

The MFA is a sensitive method to experimentally characterize the unbinding forces of interacting molecules such as DNA-protein interactions or DNA strand separation. Thermal fluctuations of the force sensor limit typically the sensitivity of single molecule force techniques (e.g., AFM, optical tweezers or magnetic tweezers) and shrinking of the sensor helps to increase the sensitivity (Viani et al., 1999). Following this idea, the MFA is designed so that a single molecular bond is utilized as a force sensor, in our case the bonding between the strands of a DNA duplex (reference duplex). Actually, the MFA measurement directly compares the mechanical stability of two DNA duplexes, a target and a reference duplex, against each other like a scale that balances a target weight against a reference weight. Due to the highly parallel format of the assay, the MFA permits the examination of different sequences under the same experimental (solvent, force actuator, etc.) conditions in a single experiment, which is crucial for the informative value of the results.

At a molecular level the MFA consists of molecular force probes (MFPs), which are anchored in parallel on a glass slide with a density about  $10^4$  MFPs per  $\mu\text{m}^2$ . Again, each MFP itself is composed of a target duplex **1 • 2** and a reference duplex **2 • 3** that are coupled in series and connected between a glass slide (lower surface) and a PDMS stamp (top surface) (see ‘Methods’ section). The target DNA duplex is 20 bp long and contains

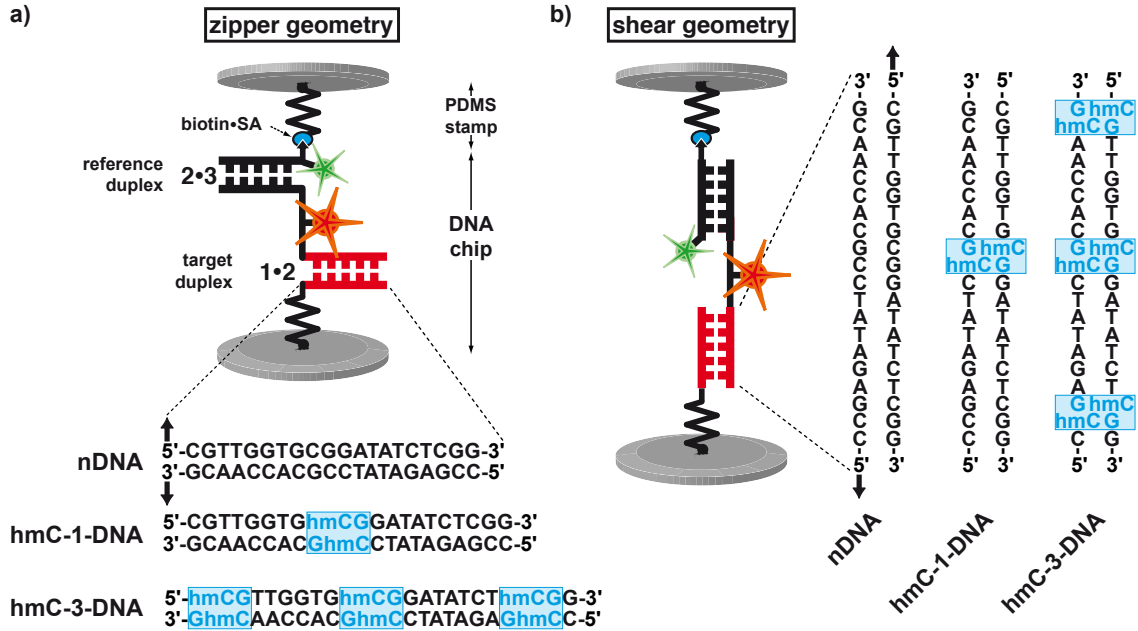


Figure 1: Schematic representation of MFP. Each MFP is comprised of DNA strands **1**, **2** and **3**, which form two DNA duplexes that are coupled in series. DNA strand **1** is anchored to the substrate (lower surface) and strand **3** is modified with a biotin for coupling to streptavidin on the PDMS-stamp (upper surface). The target duplex **1 • 2** exhibits three different variants with none (nDNA), one (hmC-1-DNA) or three 5-hydroxymethylated CpG steps (hmC-3-DNA), while the reference duplex **2 • 3** is the same for all three cases. Further DNA strand **2** carries a Cy5 and strand **3** a Cy3 fluorescent marker. Depending on the sequences of the DNA strands, the DNA duplexes are oriented such that they are loaded in shear or zipper geometry as in (a) and (b) shown.

zero (nDNA), one (hmC-1-DNA) or three (hmC-3-DNA) 5-hydroxymethylcytosines (hmC) per strand, while the reference duplex is the same for all three different MFPs. Depending on the attachment points of the modifications on each DNA strand, the MFP is build up either in a zipper (Fig. 1(a)) or in a shear geometry (Fig. 1(b)). The different MFPs are immobilized as well separated spots on the glass substrate and probed with a single PDMS stamp all at once.

In the measurement process, the PDMS stamp is moved away from the chip and detaches, a force builds up gradually in each MFP until either the target or the reference duplex ruptures. After separation of PDMS stamp and chip, the chip is read out via fluorescence: if bond **2 • 3** ruptures, the Cy5 dye is still on the lower surface (chip) and contributes to the  $F_A^A$  signal. And if bond **1 • 2** ruptures, Cy5 is on the PDMS stamp and is not contributing

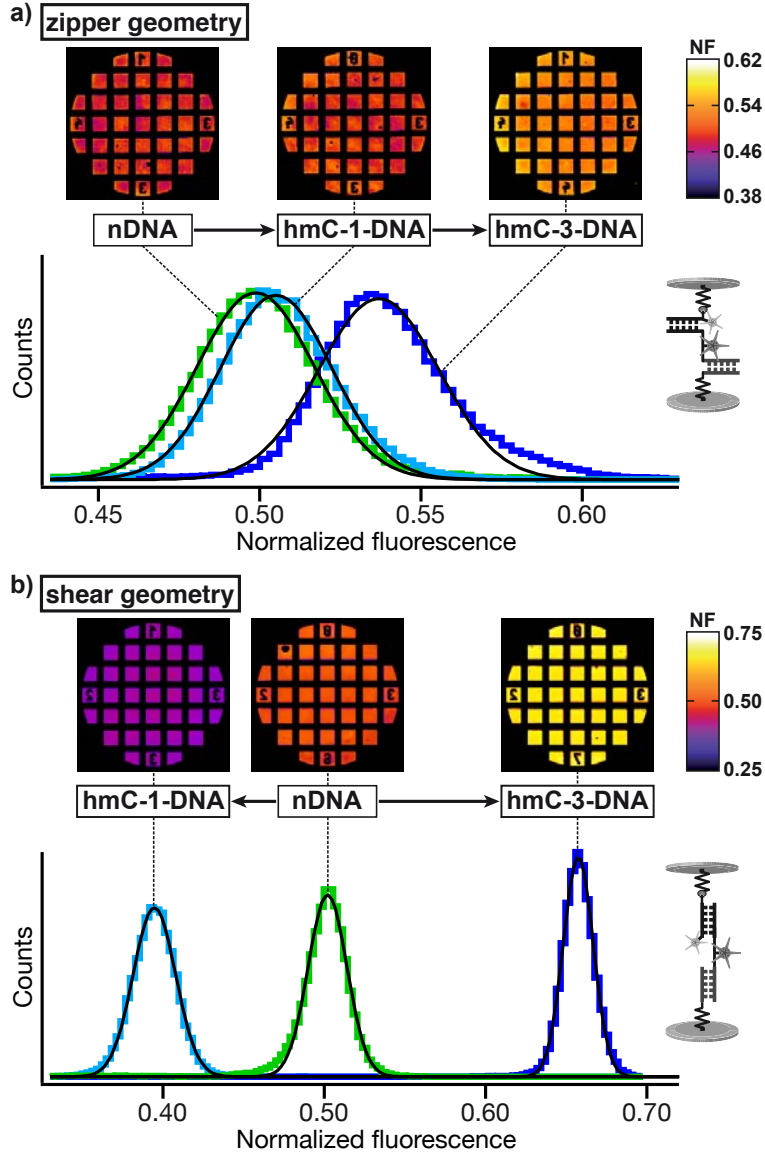


Figure 2: NF images and histograms of one representative experiment. (a) Zipper geometry: the NF images constitute the quantitative result of the relative unbinding forces between target and reference duplex. The visible squares (each  $100 \mu\text{m} \times 100 \mu\text{m}$ ) in the NF images correspond to the contacted and probed area of the PDMS stamp. Due to the highly parallel measurement format around  $10^4$  MFPs are probed per  $\mu\text{m}^2$ . Histograms of the NF images are fitted with a Gaussian. (b) Shear geometry.

to  $F_A^A$ , since the fluorescence is only read out on the lower surface. From the analysis of the fluorescence images pixel by pixel one obtains an image of normalized fluorescence (NF). The NF is defined as the ratio of broken reference bonds to the total amount of MFPs that have been under load. Accordingly, the NF is a measure for the relative mechanical stability between the target and the reference duplex. A higher NF denotes an increased mechanical stability of the target duplex over that of the reference duplex.

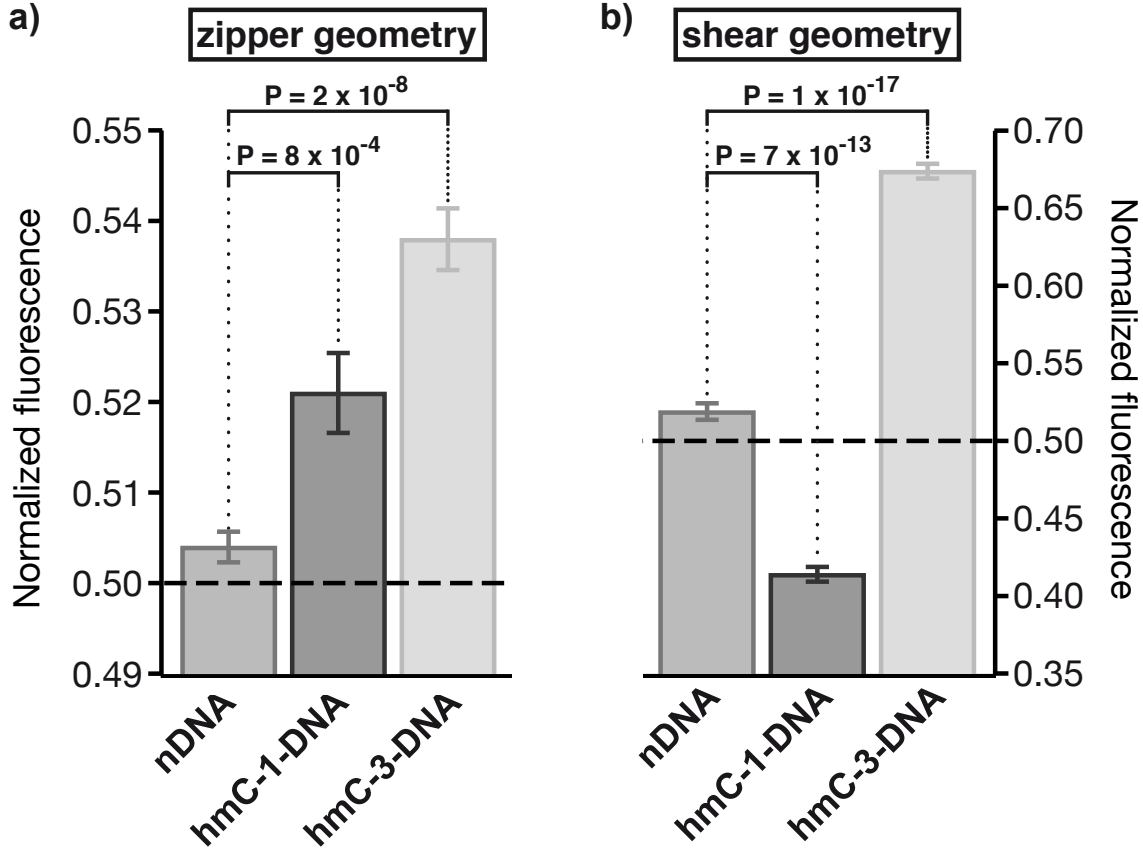


Figure 3: (a) Analysis of 42 pads from four different experiments in zipper geometry. The mean rupture force measured in NF rises with increasing number of 5-hydroxymethylated CpG steps. (b) Analysis of 39 pads from four different experiments in shear geometry. In contrast to zipper geometry, hmC-1-DNA shows a lower and hmC-3-DNA a higher mean rupture force compared to nDNA. This effect was also observed for 5-methylated CpG steps, but the hydroxymethylated DNA has an even more enhanced effect on the mechanical stability than methylated DNA: a stronger destabilization for hmC-1-DNA than mC-1-DNA and a increased stabilization for hmC-3-DNA than mC-3-DNA in shear geometry.

Representative results for a typical experiment in zipper- and shear-geometry are shown in Fig. 2. The Gaussian fits of the histograms of the NF-images result in the following mean values and standard deviations: zipper-geometry (Fig. 2(a)),  $\text{NF}(\text{nDNA}_{\text{zip}}) = (0.498 \pm 0.011)$ ,  $\text{NF}(\text{hmC-1-DNA}_{\text{zip}}) = (0.505 \pm 0.013)$  and  $\text{NF}(\text{hmC-3-DNA}_{\text{zip}}) = (0.537 \pm 0.011)$  and shear-geometry (Fig. 2(b)),  $\text{NF}(\text{nDNA}_{\text{shear}}) = (0.502 \pm 0.007)$ ,  $\text{NF}(\text{hmC-1-DNA}_{\text{shear}}) = (0.395 \pm 0.008)$  and  $\text{NF}(\text{hmC-3-DNA}_{\text{shear}}) = (0.657 \pm 0.006)$ . The difference in NF reflects a quantitative measure for difference in mean rupture force between nDNA, hmC-1-DNA and hmC-3-DNA. The width of the histograms does not necessarily reflect the width of the force distribution, since the width is influenced by the exposure time of the fluorescence images and the coupling efficiency. Typically, the coupling efficiency was around 15 to 20 % lower for zipper than for shear geometry. This might due to steric conformation differences of the MFPs in zipper and shear geometry, which might influence the accessibility of the biotin on strand 3 to the streptavidin on the PDMS stamp.

Summarizing all pads of all experiments, we determined the following mean values and standard errors: zipper-geometry (Fig. 3(a)),  $\text{NF}(\text{nDNA}_{\text{zip}}) = (0.504 \pm 0.002)$ ,  $\text{NF}(\text{hmC-1-DNA}_{\text{zip}}) = (0.521 \pm 0.004)$  and  $\text{NF}(\text{hmC-3-DNA}_{\text{zip}}) = (0.538 \pm 0.003)$  and shear-geometry (Fig. 3(b)),  $\text{NF}(\text{nDNA}_{\text{shear}}) = (0.519 \pm 0.005)$ ,  $\text{NF}(\text{hmC-1-DNA}_{\text{shear}}) = (0.414 \pm 0.005)$  and  $\text{NF}(\text{hmC-3-DNA}_{\text{shear}}) = (0.674 \pm 0.005)$ . In zipper geometry the P-value between nDNA and hmC-1-DNA is  $8 \times 10^{-4}$  and for nDNA and hmC-3-DNA  $2 \times 10^{-8}$ . Respectively, in shear geometry the P-value between nDNA and hmC-1-DNA is  $7 \times 10^{-13}$  and for nDNA and hmC-3-DNA  $1 \times 10^{-17}$ .

Therefore, the MFA experiments prove a significant influence of the hydroxymethylcytosine on the mechanical properties of DNA. The strength of the influence on the mechanical stability depends on the direction of the applied force (zipper versus shear geometry). In zipper geometry the mechanical stability increases with the number of hmC bases. In shear geometry hmC-1-DNA exhibits a lower mechanical stability than nDNA, and hmC-3-DNA a higher stability. Our results indicate that cytosine hydroxymethylation of DNA can both enhance and also decrease the propensity for strand separation. All reported cases show a significant change in mechanical stability of the DNA.

## Molecular dynamics simulations

In order to demonstrate at atomistic level how hydroxymethylation affects DNA strands separation, SMD simulations were performed to stretch DNA with different hydroxymethylation patterns, namely, zero, one or three hydroxymethylcytosines per strand in shear and zipper geometries. The DNA sequence and hydroxymethylation patterns are the same as used in experiments.

When a dsDNA is stretched in zipper geometry, DNA helix unwinds and the base pairs break one by one, forming two extended single-stranded DNA, as shown in Fig. 4(a). A movie (Movie S1) showing the dynamics of unzipping DNA is provided in Supplementary

Material. The rupture force of separating DNA in zipper geometry mainly arises from three aspects: (1) unwinding DNA helix; (2) breaking hydrogen bonds between base pairs; (3) extending single-stranded DNA. Figure 4(b) shows a typical force profile of unzipping DNA, which contains many small force peaks. During stretching, the number of DNA base pairs decreases by one at each time. One can see that almost every base pair breaking event corresponds to a small force peak (Fig. 4(b)). After averaging force value over time (data were from six independent SMD simulations), we obtained mean rupture forces for nDNA, hmC-1-DNA and hmC-3-DNA, as shown in Fig. 4(c). Consistent with MFA results that hmC-3-DNA exhibits strongest mechanical stability, in simulations hmC-3-DNA also requires strongest rupture force ( $\sim 62$  pN) in comparison with nDNA ( $\sim 53$  pN) and hmC-1-DNA ( $\sim 53$  pN). The difference between hmC-1-DNA and nDNA is not seen in simulations due to small sampling. It is notable that the error bar of mean rupture force of hmC-3-DNA is smaller than these of hmC-1-DNA and nDNA, indicating that hmC-3-DNA indeed is more stable than hmC-1-DNA and nDNA, despite of poor sampling.

Different from unzipping DNA, stretching dsDNA in shear geometry causes DNA strand separation in two steps. In the first step, DNA elongates and unwinds as shown in Fig. 4(d) snapshots at 30 ns and 60 ns. In the meantime, DNA Watson-Crick base pairs begin to break and bases of the two separate strands stack on top of each other, forming the so-called zipper-like DNA (Chou and Chin, 2001), as shown in Fig. 4(d) snapshot at 90 ns. The force increases slowly in the first step (see Fig. 4(e)). In the second step, the force acting on zipper-like DNA increases rapidly. When the pulling force reaches to a peak value, two strands of DNA eventually separate (see Fig. 4(d) snapshots of 115 ns), then the force drops immediately to around zero, as shown in Fig. 4(e). According to a typical rupture force profile of shearing DNA (Fig. 4(e)), each DNA has a peak rupture force, reflecting its stability. The stronger the peak rupture force is, the more stable the DNA is. Figure. 4(f) shows the mean of peak rupture forces of nDNA, hmC-1-DNA and hmC-3-DNA (obtained from eighteen independent SMD simulations). hmC-3-DNA requires the strongest rupture force for strand separation. The mean peak force of nDNA is stronger than that of hmC-1-DNA, which is also consistent with MFA results. However, we note that the error bar of hmC-1-DNA is very large. To understand why different DNA has different peak rupture force, we compared the conformation of DNA at the moment when its rupture force reaches peak value, as shown in Fig. S2. In general, hmC-3-DNA has most ordered zipper-like DNA forms (less bubbles inside and more compact ends) than hmC-1-DNA and nDNA do. hmC-1-DNA has two most disordered conformation, which largely reduces its mean peak rupture force. Similar to our previous study on effects of methylation on DNA strand separation (Severin et al., 2011b), hydroxymethylation also affects bubble formation during stretching DNA, which controls the propensity for strand separation.

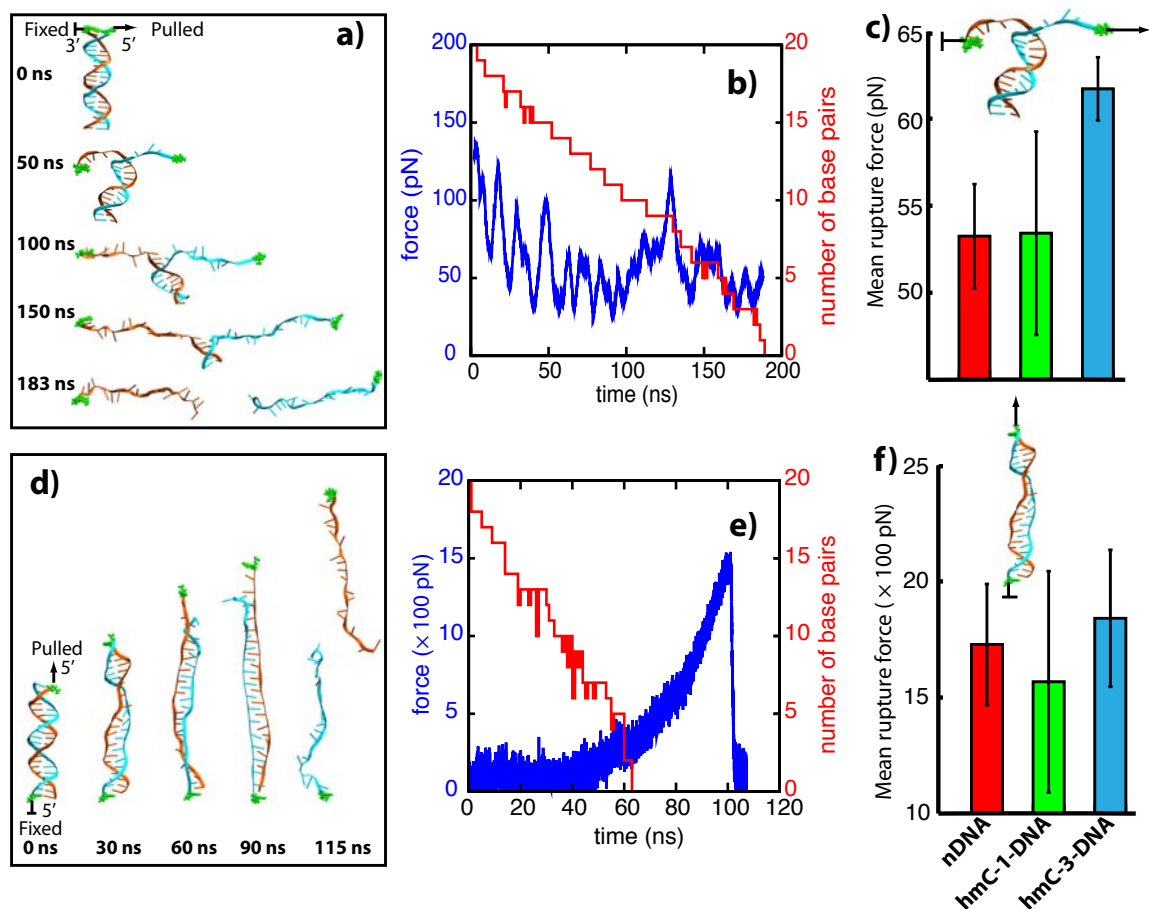


Figure 4: Analysis of MD simulations. (a) Shown are snapshots of unzipping DNA from a steered molecular dynamics simulation (simulation A1). The top 3'-end (highlighted in green) of DNA strands is subject to constraint force and the adjacent 5'-end (highlighted in green) is stretched. (b) A typical force profile (blue) of unzipping dsDNA and corresponding time evolution of number of hydrogen bonds (red). (c) Histogram of mean rupture force of separating DNA strands in zipper geometry. In comparison to hmC-1-DNA and nDNA, rupturing hmC-3-DNA requires strongest force ( $\sim 62$  pN). Due to small sampling (two independent simulations), the difference observed between hmC-1-DNA and nDNA is small. (d) Shown are snapshots of shearing DNA from a steered molecular dynamics simulation (simulation D1). The bottom 5'-end (highlighted in green) of the DNA strands is subject to constraint force and the top 5'-end (highlighted in green) is stretched. (e) A typical force profile (blue) of shearing dsDNA and corresponding time evolution of number of hydrogen bonds (red). (f) Histogram of mean rupture force of separating DNA strands in shear geometry. Consistent with experimental results, the order of rupturing force of DNA is hydrxymethylation-dependent:  $F_{\text{hmC-3-DNA}} > F_{\text{nDNA}} > F_{\text{hmC-1-DNA}}$ .



## Discussion

We demonstrated in a previous study that methylcytosine might also exert a biological function by itself through influencing the mechanical stability of the DNA double helix (Severin et al., 2011b). It was shown that the propensity of DNA strand separation is changed upon methylation of CpG, which might have a biological effect, possibly on transcription machinery or helicases (Severin et al., 2011b). Since mC can alter pronounced the mechanical properties of DNA, the question arises, if hydroxymethylation does also change DNAs mechanical properties.

In the present MFA experiments, the relative stability of a target DNA duplex is measured against a reference DNA duplex. The MFA experiments were conducted in two geometries, in shear geometry and zipper geometry. For shear geometry, the relative stability for hmC-3-DNA compared to nDNA is approximately by a difference of  $\Delta NF = 0.155$  higher and for hmC-1-DNA compared to nDNA by  $\Delta NF = 0.105$  lower. This means, the probability of strand separation is for hmC-3-DNA lower and for hmC-1-DNA higher than for nDNA. In zipper geometry, the relative stability for hmC-1-DNA is by a difference of  $\Delta NF = 0.017$  and for hmC-3-DNA by  $\Delta NF = 0.034$  higher than nDNA. Since the experiments with hmC-3-DNA, hmC-1-DNA and nDNA were conducted in parallel, with spatially separated spots in the same well, their measurement conditions were identical. Hence, the measured differences in the strand separation probability between hmC-3-DNA, hmC-1-DNA and nDNA in zipper and shear geometry are highly reliable. The effect of hydroxymethylation on the mechanical stability is more pronounced in shear than in zipper geometry (approximately by a factor of 5).

Consistent with MFA results, SMD simulations of stretching DNA in zipper and shear geometry showed that hydroxymethylation indeed affects the stability of DNA. Simulations demonstrated at atomistic level the thermodynamics of two different DNA strand separation pathways, explaining why the effect of hydroxymethylation on DNA stability is dependent on pulling fashions. Stretched in zipper geometry, DNA base pairs break one by one. Hence unzipping DNA measures the strength of single base pair. As observed in simulations, hmCG base pair is more stable than CG base pair during unzipping, therefore, more hmCG base pairs are contained in DNA, the more stable DNA is. When DNA is stretched in shear geometry, the B-form double helix unwinds, followed by breaking of Watson-Crick base pairs, and bases from two strands slip past each other forming so-called zipper-like DNA. Along with the increase of shearing force, bubbles accumulating in zipper-like DNA reach to a critical concentration such that separation occurs. Observed from MD simulations, hydroxymethylation seems to change the likelihood of DNA strand separation by affecting bubble formation during stretching. Shearing DNA measures the stability of the entire DNA duplex, therefore, not only the number of hmC, but also the context and the position of hmC influence the stability of DNA.

MD simulations provide a microscopic picture of DNA strand separation that cannot be

seen in MFA measurements. However, different from MFA experiments which conduct millions of independent measurements at one time, SMD simulations can only be performed in the condition of fast pulling velocity and small sampling, due to limitation of computational resources. The pulling velocity employed in our SMD simulation is 1 Å/ns, much faster than experimental pulling velocity which is  $10^{-6}$  Å/ns -  $10^{-4}$  Å/ns. Despite very fast pulling velocity, the total simulation time of our study still involves about 3  $\mu$ s, requiring 3 months computation on 720 CPUs. Indeed, fast pulling velocity increases the rupture force for strand separation, as more bonds were broken in a short time. Although fast pulling velocity accelerates biomolecular rupture process, the rupture pathway can still be revealed by SMD simulations (Sotomayor and Schulten, 2007; Lee et al., 2009). In the case of rupturing DNA, we observed the same strand separation pathway as reported by prior SMD studies (Lohikoski et al., 2005; Santosh and Maiti, 2009; Balaeff et al., 2011) and DNA force-extension curves show the same shape as obtained from experiments (except magnitude) (Smith et al., 1996; Bustamante et al., 2000). Hence, effects of hydroxymethylation on strand separation observed in MD simulations can be used to understand experimental data.

In a previous study, we investigated the influence of mC on the mechanical stability of DNA strand separation. Since we used in this study the same DNA sequence and same positions for methylation as for hydroxymethylation of CpG, it is possible to compare the effects of hmC with mC. First of all, the tendencies to stabilize and destabilize DNA in shear and zipper are the same: hmC-1-DNA destabilizes the DNA in shear geometry like mC-1-DNA, while hmC-3-DNA and mC-3-DNA stabilize the DNA in shear geometry. In zipper geometry, hmC-1-DNA and hmC-3-DNA as well as mC-1-DNA and mC-3-DNA stabilize the DNA. For mC-1-DNA was NF by a difference of  $\Delta NF = 0.063$  lower and for mC-3-DNA by  $\Delta NF = 0.104$  higher than the NF of nDNA (Severin et al., 2011b). Therefore, the relative difference ( $[\Delta NF(\text{hmC-1-DNA}) - \Delta NF(\text{mC-1-DNA})] / \Delta NF(\text{mC-1-DNA})$ ) in NF for hmC-1-DNA is approximately 70% higher than mC-1-DNA. For hmC-3-DNA the relative difference is with approximately 50% higher compared to mC-3-DNA. For zipper configuration it is not meaningful to calculate the relative difference in NF between hmC and mC, since  $\Delta NF$  is in the same order of magnitude as the standard error. In summary, we observed the same qualitative effects in stabilization and destabilization for hmC as for mC. But the central difference between hmC and mC is that, we could show, especially for shear geometry, that the effect for stabilization as well as for destabilization is enhanced in both directions for hmC in the range of 50% and above. Previous, we found that the effect of cytosine methylation is not only dependent on the methylation level, but also on the sequence context of methylated sites. Since we observed the same effects in stabilization and destabilization for hmC as for mC, we assume there could be comparable sequence-dependent effect for hmC as for mC.

The changes of hydroxymethylation and methylation effects as seen typically in thermal stability measurements are subtle as opposed to the pronounced differences in mechanical stability, which arise from methylation and hydroxymethylation (Wanunu et al., 2011). This prompts the question if this effect has a biological function. On one hand, processes like the

mechanical manipulation of DNA in transcription initiation or the processivity of helicases exert forces on DNA to separate DNA duplex into two single strands. On the other hand, these processes can also be influenced, e.g. regarding the rate or processivity, through the mechanical stability of the DNA double strand (Cheng et al., 2007; Dumont et al., 2006; Johnson et al., 2007).

The direction of force, which acts in vivo on the DNA double helix to separate the two DNA strands, depends on the molecular machinery. For DNA helicases a DNA unzipping geometry might be more representative (Johnson et al., 2007). The mechanical manipulation of DNA in transcription initiation happens in the confined setting of highly structured polynucleosomes. Hence, the shear geometry motion, which takes place more or less within the volume of non-stretched DNA, is relevant in the rather compact, structured polynucleosome setting found in the cell nucleus. Therefore our investigation covers with measurements and simulations in shear and zipper geometry, different force directions, which might be exploited by nature.

In summary, we identified by experiment and simulation a significant effect of hydroxymethylation on DNA mechanical properties, how the propensity of DNA strand separation is influenced by hydroxymethylation. Even though, we identified this pronounced effect, we could not uncover fully the molecular mechanism how hydroxymethylation changes DNA mechanical properties. Therefore, further investigations are needed. The effect of hydroxymethylation exceeds in strength what was previously demonstrated for the effect of methylation. Our study reveals that hydroxymethylation could regulate gene expression through altering mechanical properties of DNA. This new insight may advance our understanding of the molecular function of hydroxymethylation.

## Methods

**MFA-chip and PDMS-stamp.** The molecular setup of the MFA, shown in Fig. 1, has been assembled as described previously except for some modifications (Severin et al., 2011a,b). A molecular force probe (MFP) consists of DNA oligomers labeled **1** and **2**, which form the bottom duplex and oligomers **2** and **3**, which form the top duplex.

The MFPs are built up on the bottom surface (MFA-chip) as the following: DNA oligomer **1** is amine-modified for covalent linkage to aldehyde-functionalized glass slides. In the order of  $10^4$  duplicates of MFPs are build up in parallel per  $\mu\text{m}^2$ . The experiments are conducted with three hydroxymethylation levels so that in the bottom duplex **1** • **2**, contains zero, one or three 5-hydroxymethylcytosine (hmC) per strand. Depending on the direction of the used DNA sequences, the MFPs are realized in a zipper (Fig. 1(a)) or shear geometry (Fig. 1(b)). Artifacts in the force measurements, which could be caused by structural changes of the DNA duplex or unwanted hybridizations of the strands, are tried to keep minimal using a well-characterized DNA sequence with minimal self-complementarity and, hence, minimal

hairpin-formation (Strunz et al., 1999).

The second part of the MFA is the top surface of the chip. The top surface is a polydimethylsiloxane (PDMS) stamp, fabricated and functionalized as described previously (Albrecht et al., 2006; Ho et al., 2009). DNA oligomer **3** is biotinylated and forms a link to the stamp upon contact. The sequences of the DNA oligomers are provided in Supplementary Information. All experiments are carried out in  $1 \times$  PBS at room temperature.

**MFA contact process, readout and analysis.** A detailed description of the measurement process can be found in a previous paper (Severin et al., 2011a). In brief, a fluorescence microscope is combined a custom-built contact device. The contact device controls the distance between PDMS-stamp and MFA-chip via a closed-loop piezoelectric actuator.

At first, MFA-chip and the soft PDMS-stamp are separated and the fluorescence signal of the MFA-chip is measured twice: first, Cy5 is excited and the fluorescence signal ( $F_A^A$ ) is measured. Second, Cy3 is excited and the fluorescence signal ( $F_D^A$ ) of Cy5 is measured. Then, the stamp is lowered until both surfaces are brought into contact, allowing to connect strand **3** of the MFPs to the streptavidin on the top surface via biotin • streptavidin complexation (Fig. 1). To achieve a sufficient level of MFPs that couple to the PDMS-stamp, the contact is hold for 10 min. Then, the surfaces are separated with a retract velocity of  $5 \mu\text{m/s}$ . During the separation process, the force builds up gradually in each MFP until one of the duplexes **1 • 2** or **2 • 3** ruptures. At the last step,  $F_A^A$  and  $F_D^A$  are read out for the second time.

From the analysis of the four fluorescence images ( $F_A^A$  and  $F_D^A$  before contact and after separation) the normalized fluorescence intensity (NF) can be determined:(Severin et al, 2011a)

$$NF = \frac{(F_A^A)_{ratio} - (F_D^A)_{ratio}}{1 - (F_D^A)_{ratio}}. \quad (1)$$

$(F_{A/D}^A)_{ratio}$  is the background- and bleaching-corrected  $F_{A/D}^A$  fluorescence image (after separation) divided by the background- and bleaching-corrected  $F_{A/D}^A$  image (before contact). The NF is defined as the ratio between broken reference bonds (**2 • 3**) and total amount of MFPs that have been under load. The NF reflects the relative mechanical stability between the target duplex **1 • 2** and the reference duplex **2 • 3** of a MFP. Higher values for the NF denote an increased mechanical stability of the target duplex over the reference duplex and a NF value of 0.5 represents equal mechanical stable duplexes.

**Molecular dynamics simulations.** All oligonucleotides employed in MD simulations were of the same sequence (CGTTGGTGCGGATATCTCGG) and the same hydroxymethylation pattern, namely nDNA, hmC-1-DNA and hmC-3-DNA, as used in experiments. A double-stranded helix of nDNA was built with the program X3DNA (Xiang-Jun Lu, 2003). hmC-1-DNA and hmC-3-DNA were obtained through mutating cytosines in CpG steps to

hydroxymethylcytosines. The topology of DNA along with the missing hydrogen atoms were generated using the psfgen plugin of VMD (Humphrey et al., 1996) with a topology file corresponding to CHARMM27 force field (Foloppe and MacKerell Jr., 2000). Each DNA was placed in a water box with 0.1 mol/l KCl added. In shear stretching simulations, the size of water box is  $61 \text{ \AA} \times 61 \text{ \AA} \times 275 \text{ \AA}$ ; in unzipping simulations, the size of water box is  $240 \text{ \AA} \times 61 \text{ \AA} \times 61 \text{ \AA}$ . The total size of the simulated systems lies in 100,000-150,000 atom range.

Simulations were performed using the program NAMD 2.7 (Phillips et al., 2005) with the CHARMM27 force field for DNA (Foloppe and MacKerell Jr., 2000) and the TIP3P water model (Jorgensen et al., 1983). Periodic boundary conditions were assumed and the particle mesh Ewald (PME) summation method was employed for evaluating Coulomb forces. The van der Waals (vdW) energy was calculated using a smooth cutoff of  $12 \text{ \AA}$ . The integration time step was 1 fs. The temperature was kept at 295 K by applying Langevin forces with a damping coefficient of  $0.1 \text{ ps}^{-1}$  (Martyna et al., 1994) only to the oxygen atoms of water molecules. After energy-minimization for 4000 steps and 4 ps heating to 295 K, each simulated system was equilibrated for 500 ps with harmonic restraints applied to all DNA atoms under NPT ensemble conditions using Nosé-Andersen Langevin piston pressure control (Martyna et al., 1994; Feller et al., 1995). With restraints turned off each system was then subjected to 2 ns-equilibration under NVT ensemble conditions. Finally, production SMD simulation was carried out in the NVT ensemble. Table 1 lists all the simulations carried out in the present study.

Name	DNA	Pulling geometry	Velocity	Time (ns)
A1-A2	nDNA	Zipper	$1 \text{ \AA}/\text{ns}$	180~200
B1-B2	hmC-1-DNA	Zipper	$1 \text{ \AA}/\text{ns}$	180~200
C1-C2	hmC-3-DNA	Zipper	$1 \text{ \AA}/\text{ns}$	180~200
D1-D5	nDNA	Shear	$1 \text{ \AA}/\text{ns}$	110~120
E1-E5	hmC-1-DNA	Shear	$1 \text{ \AA}/\text{ns}$	110~120
F1-F5	hmC-3-DNA	Shear	$1 \text{ \AA}/\text{ns}$	110~120

Table 1: List of performed simulations

For each system, we separated DNA strands in two different modes, namely, zipper geometry and shear geometry. In zipper geometry, a 3' end of DNA was fixed and a 5' end was pulled by attaching a harmonic spring to the terminal O3 and pulling the other end of the spring at a constant speed of  $1 \text{ \AA}/\text{ns}$ . Two independent SMD simulations in zipper geometry were conducted for each DNA. For shear geometry, five independent SMD simulations were performed, in which a 5'-end of DNA was fixed, and the other 5'-end was pulled at  $1 \text{ \AA}/\text{ns}$ .

## Acknowledgement

P. Severin is grateful to the Elite Network of Bavaria (IDK-NBT) for a doctoral fellowship. K. Schulten is grateful for a Humboldt Foundation award. Financial support was provided by the Deutsche Forschungsgemeinschaft, the Nanosystems Initiative Munich, the National Institutes of Health grant P41-RR005969 and cell mechanics grant R01 GM073655. The authors gladly acknowledge supercomputer time provided by the Texas Advanced Computing Center and the National Center for Supercomputing Applications via TeraGrid Resource Allocation Committee grant MCA93S028.

## References

- Christian H Albrecht, Hauke Clausen-Schaumann, and Hermann E Gaub. Differential analysis of biomolecular rupture forces . *J. Phys.: Condens. Matter*, 18:81–599, 2006.
- Alexander Balaeff, Stephen L. Craig, and David N. Beratan. B-dna to zip-dna: Simulating a dna transition to a novel structure with enhanced charge-transport characteristics. *J. Phys. Chem. A*, 115(34):9377–9391, 2011.
- Carlos Bustamante, Steven B Smith, Jan Liphardt, and Doug Smith. Single-molecule studies of dna mechanics. *Curr. Opin. Struct. Biol.*, 10(3):279 – 285, 2000.
- Wei Cheng, Sophie Dumont, Ignacio Tinoco, and Carlos Bustamante. NS3 helicase actively separates RNA strands and senses sequence barriers ahead of the opening fork. *Proc. Natl. Acad. Sci. USA*, 104:13954–13959, 2007.
- Shan-Ho Chou and Ko-Hsin Chin. Zipper-like Watson-Crick base-pairs. *J. Mol. Biol.*, 312:753–768, 2001.
- Milos Dokmanovic, Cathy Clarke, and Paul A. Marks. Histone deacetylase inhibitors: Overview and perspectives. *Mol. Cancer. Res.*, 5(10):981–989, 2007.
- Sophie Dumont, Wei Cheng, Victor Serebrov, Rudolf K. Beran, Ignacio Tinoco Jr, Anna Marie Pyle, and Carlos Bustamante. RNA translocation and unwinding mechanism of HCV NS3 helicase and its coordination by ATP. *Nature*, 439:105–108, 2006.
- Scott E. Feller, Yuhong Zhang, Richard W. Pastor, and Bernard R. Brooks. Constant pressure molecular dynamics simulation: The Langevin piston method. *J. Chem. Phys.*, 103(11):4613–4621, 1995.
- Jian Feng, Yu Zhou, Susan L Campbell, Thuc Le, En Li, J David Sweatt, Alcino J Silva, and Guoping Fan. Dnmt1 and Dnmt3a maintain DNA methylation and regulate synaptic function in adult forebrain neurons. *Nat. Neurosci.*, 13:423–430, 2010.

- N. Foloppe and A. D. MacKerell Jr. All-atom empirical force field for nucleic acids: I. Parameter optimization based on small molecule and condensed phase macromolecular target data. *J. Comp. Chem.*, 21:86–104, 2000.
- Dominik Ho, Christian Dose, Christian H. Albrecht, Philip Severin, Katja Falter, Peter B. Dervan, and Hermann E. Gaub. Quantitative detection of small molecule/DNA complexes employing a force-based and label-free DNA-microarray. *Biophys. J.*, 96:4661–4671, 2009.
- William Humphrey, Andrew Dalke, and Klaus Schulten. VMD – Visual Molecular Dynamics. *Journal of Molecular Graphics*, 14:33–38, 1996.
- S. Ito, A. C. D’Alessio, O. V. Taranova, K. Hong, L. C. Sowers, and Y. Zhang. Role of Tet proteins in 5mC to 5hmC conversion, ES-cell self-renewal and inner cell mass specification. *Nature*, 466:1129–1133, 2010.
- Rudolf Jaenisch and Adrian Bird. Epigenetic regulation of gene expression: how the genome integrates intrinsic and environmental signals. *Nat. Genet.*, 33:245–254, 2003.
- S. G. Jin, S. Kadam, and G. P. Pfeifer. Examination of the specificity of DNA methylation profiling techniques towards 5-methylcytosine and 5-hydroxymethylcytosine. *Nucleic Acids Res.*, 38:e125, 2010.
- Daniel S. Johnson, Lu Bai, Benjamin Y. Smith, Smita S. Patel, and Michelle D. Wang. Single-molecule studies reveal dynamics of DNA unwinding by the ring-shaped T7 helicase. *Cell*, 129:1299–1309, 2007.
- Peter A. Jones. DNA methylation and cancer. 21:5358–5360, 2002.
- Peter A. Jones and Daiya Takai. The role of DNA methylation in mammalian epigenetics. *Science*, 293:1068–1070, 2001.
- W. L. Jorgensen, J. Chandrasekhar, J. D. Madura, R. W. Impey, and M. L. Klein. Comparison of simple potential functions for simulating liquid water. *J. Chem. Phys.*, 79:926–935, 1983.
- Myunggon Ko, Yun Huang, Anna M. Jankowska, Utz J. Pape, Mamta Tahiliani, Hozefa S. Bandukwala, Jungeun An, Edward D. Lamperti, Kian Peng Koh, Rebecca Ganetzky, X. Shirley Liu, L. Aravind, Suneet Agarwal, Jaroslaw P. Maciejewski, and Anjana Rao. Impaired hydroxylation of 5-methylcytosine in myeloid cancers with mutant TET2. *Nature*, 468:839–843, 2010.
- Skirmantas Kriaucionis and Nathaniel Heintz. The nuclear dna base 5-hydroxymethylcytosine is present in purkinje neurons and the brain. *Science*, 324(5929):929–930, 2009.

- Eric H. Lee, Jen Hsin, Marcos Sotomayor, Gemma Comellas, and Klaus Schulten. Discovery through the computational microscope. *Structure*, 17:1295–1306, 2009.
- Raimo Lohikoski, Jussi Timonen, and Aatto Laaksonen. Molecular dynamics simulation of single DNA stretching reveals a novel structure. *Chem. Phys. Lett.*, 407:23–29, 2005.
- G. J. Martyna, D. J. Tobias, and M. L. Klein. Constant pressure molecular dynamics algorithms. *J. Chem. Phys.*, 101(5):4177–4189, 1994.
- M. Munzel, D. Globisch, T. Bruckl, M. Wagner, V. Welzmler, S. Michalakis, M. Muller, M. Biel, and T. Carell. Quantification of the sixth DNA base hydroxymethylcytosine in the brain. *Angew. Chem. Int. Ed. Engl.*, 49:5375–5377, 2010.
- Martin Münzel, Daniel Globisch, and Thomas Carell. 5-hydroxymethylcytosine, the sixth base of the genome. 50:6460–6468, 2011.
- N. W. Penn, R. Suwalski, C. O’Riley, K. Bojanowski, and R. Yura. The presence of 5-hydroxymethylcytosine in animal deoxyribonucleic acid. *Biochem. J.*, 126:781–790, 1972.
- James C. Phillips, Rosemary Braun, Wei Wang, James Gumbart, Emad Tajkhorshid, Elizabeth Villa and Christophe Chipot, Robert D. Skeel, Laxmikant Kale, and Klaus Schulten. Scalable molecular dynamics with NAMD. *J. Comp. Chem.*, 26:1781–1802, 2005.
- Adam B. Robertson, John A. Dahl, Cathrine B. Vågbø, Pankaj Tripathi, Hans E. Krokan, , and Arne Klungland. A novel method for the efficient and selective identification of 5-hydroxymethylcytosine in genomic DNA. *Nucleic Acids Res.*, pages 1–10, 2011.
- Andrea Rottach, Heinrich Leonhardt, and Fabio Spada. DNA methylation-mediated epigenetic control. *J. Cell. Biochem.*, 108:43–51, 2009.
- Mogurampelly Santosh and Prabal K. Maiti. Force induced DNA melting. *J. Phys.: Condens. Matter*, 21:101–139, 2009.
- Philip Severin, D. Ho, and Hermann E. Gaub. A high-throughput molecular force assay for protein-DNA interactions. *Lab Chip*, 11:856–862, 2011a.
- Philip M.D. Severin, Xueqing Zou, Hermann E. Gaub, and Klaus Schulten. Cytosine methylation alters DNA mechanical properties. *Nucleic Acids Res.*, 39:8740–8751, 2011b.
- Steven B. Smith, Yujia Cui, and Carlos Bustamante. Overstretching B-DNA: the elastic response of individual double-stranded and single-stranded DNA molecules. *Science*, 271:795–799, 1996.
- Marcos Sotomayor and Klaus Schulten. Single-molecule experiments in vitro and in silico. *Science*, 316:1144–1148, 2007.



- Ravid Straussman, Deborah Nejman, Douglas Roberts, Israel Steinfeld, Barak Blum, Nissim Benvenisty, Itamar Simon, Zohar Yakhini, and Howard Cedar. Developmental programming of CpG island methylation profiles in the human genome. *Nat. Struct. Biol.*, 16:564–571, 2009.
- T. Strunz, K. Oroszlan, R. Schäfer, and H.J. Güntherodt. Dynamic force spectroscopy of single DNA molecules. *Proc. Natl. Acad. Sci. USA*, 96:11277–11282, 1999.
- Aleksandra Szwagierczak, Sebastian Bultmann, Christine S. Schmidt, Fabio Spada, and Heinrich Leonhardt. Sensitive enzymatic quantification of 5-hydroxymethylcytosine in genomic DNA. *Nucleic Acids Res.*, 38:e818, 2010.
- Mamta Tahiliani, Kian Peng Koh, Yinghua Shen, William A. Pastor, Hozefa Bandukwala, Yevgeny Brudno, Suneet Agarwal, Lakshminarayan M. Iyer, David R. Liu, L. Aravind, and Anjana Rao. Conversion of 5-methylcytosine to 5-hydroxymethylcytosine in mammalian DNA by MLL partner TET1. *Science*, 324:930–935, 2009.
- Victoria Valinluck, Hsin-Hao Tsai, Daniel K. Rogstad, Artur Burdzy, Adrian Bird, and Lawrence C. Sowers. Oxidative damage to methyl-CpG sequences inhibits the binding of the methyl-CpG binding domain (MBD) of methyl-CpG binding protein 2 (MeCP2). *Nucleic Acids Res.*, 32:4100–4108, 2004.
- Mario B. Viani, Tilman E. Schäffer, Ami Chand, Matthias Rief, Hermann E. Gaub, and Paul K. Hansma. Small cantilevers for force spectroscopy of single molecules. *J. Appl. Physiol.*, 86:2258–2262, 1999.
- Meni Wanunu, Devora Cohen-Karni, Robert R. Johnson, Lauren Fields, Jack Benner, Neil Peterman, Yu Zheng, Michael L. Klein, and Marija Drndic. Discrimination of methylcytosine from hydroxymethylcytosine in DNA molecules. *J. Am. Chem. Soc.*, 133:486–492, 2011.
- Wilma K. Olson Xiang-Jun Lu. 3DNA: a software package for the analysis, rebuilding and visualization of three-dimensional nucleic acid structures. *Nucleic Acids Res.*, 31:5108–5121, 2003.

# Probing The Force-induced Globule-Coil Transition of Individual Polymer Chains via Single Molecule Force Spectroscopy

Philip M.D. Severin<sup>1</sup>, Hermann E. Gaub<sup>1</sup> and Hongbin Li<sup>2</sup> \*

<sup>1</sup> Lehrstuhl für Angewandte Physik and Center for Nanoscience (CeNS), Ludwig-Maximilians-Universität Amalienstrasse 54, 80799 Munich (Germany) Munich Center For Integrated Protein Science (CIPSM), Ludwig-Maximilians-Universität, Butenandtstrasse 5-13, 81377 Munich (Germany)

<sup>2</sup> Department of Chemistry, University of British Columbia, Vancouver, BC, Canada V6T 1Z1

[\*] To whom correspondence should be addressed (hongbin@chem.ubc.ca)

## Introduction.

Hydrophobic collapse plays a central role in protein folding and is seen as major driving force in self-assembly of macromolecules.<sup>1</sup> Investigation of the hydrophobic collapse with single molecule force spectroscopy (SMFS) on a simple and well-defined system, like a homopolymer, helps to isolate the hydrophobic effect on a single molecule level and thus to characterize the effect.

Until now, the investigation of the force induced globule-coil transition in polymers, i.e. the hydrophobic collapse, with SMFS has focused on force plateaus in force extension curves of polymers in poor solvent conditions, which can be well described by model.<sup>2-5</sup> Besides this, first evidence exists that the hydrophobic collapse of a single polymer can result not only in force-plateaus in force-extension curves but also in a force peak pattern,<sup>6</sup> reminiscent of the unfolding pattern of multi-domain proteins.<sup>7-9</sup>

In this communication, we demonstrate that force peaks in the force-extension curves of the polymer dextran arise due to poor solvent conditions, and characterize these force peak pattern as a function of the solvent conditions. A conformational transition in the dextran chain serves as a fingerprint to distinguish between multiple and single molecule stretching events.

## Experimental Section.

**a. Materials and Sample Preparation.** We used dextran T2000 (Sigma), which is a 95% linear homopolymer consisting of  $\alpha$ -(1 $\rightarrow$ 6) D-glucopyranose rings. The sample was prepared by dissolving dextran in ddH<sub>2</sub>O at a concentration of 1 mg/ml. It was then applied onto a clean glass coverslip and dried slowly on a heating plate at 60 °C. By rinsing the glass coverslip extensively with water, excessive dextran was washed off so that only a thin layer of

molecules, with 50 to 100 nm thickness, tightly adsorbed to the surface remained. All experiments were carried out in phosphate-buffered saline solution (PBS) or in 1x PBS-ethanol mixtures with 10% v/v to 50% v/v fractions of ethanol.

**b. Force Measurements.** Single-molecule AFM experiments were carried out on a custom built atomic force microscope, which was constructed as described previously.<sup>10</sup> The spring constant of each individual cantilever ( $\text{Si}_3\text{N}_4$  cantilevers, MLCT from Veeco, with a typical spring constant of 40 pN/nm) was calibrated in solution using the equi-partition theorem before and after each experiment.

All single molecule force measurements were carried out in 1x PBS buffer and 1x PBS buffer-ethanol mixtures in a sealed fluid cell. Each pair of AFM cantilever and dextran sample was used in all the different solutions to minimize systematic errors. To change the solution, the sample in the fluid cell was flushed with 10 ml of the new solution over several minutes, followed by waiting for 15 to 30 min until measurement start, allowing the sample to equilibrate.

First, the AFM tip is brought into contact with the dextran layer with a defined indentation force (reaching from 1 nN to 2 nN). After a short dwell time (approx. 1 s), the cantilever moves away from the surface and multiple unspecific attached dextran polymers are pulled out of the dextran layer into solution. With further separation of the tip from the surface the shorter polymers will detach, until one, the longest, bridging molecule remains attached between the AFM tip and the substrate (see Fig. 1(a)). This single polymer is further extended up to forces in the range of 800 to 1000 pN to monitor the conformational transition. The characteristic hump in the force-extension curve, which is caused by the chair-boat transition, ensures that only a single dextran molecule is attached between both surfaces. Now, the AFM tip moves again towards the surface, but without touching the dextran layer again (approx. 30 nm distance between tip and dextran layer), and the attached molecule relaxes. This cycle of moving the AFM tip back into the conformational transition and forth above the surface (pulling cycle) is repeated with a velocity of 700 nm/s until the polymer breaks off.

## **Results and Discussion.**

As model polymer we used a linear polysaccharide, dextran. The elasticity of single dextran in good solvent has been investigated in detail before.<sup>11,12</sup> The force-extension curve of a single dextran polymer exhibits a pronounced hump in the range from 750 pN to 850 pN accompanied with a contour length increase of around 20 % (see Fig. 1(b)), which

corresponds to a force-induced chair-boat conformational transition of the glucopyranose monomers.<sup>12</sup> This conformational transition is not influenced by the solvent and represents a unique feature, which can be used as a fingerprint to identify single molecule stretching events.<sup>11</sup>

We acquired force-extension curves in the range of 150 nm to 800 nm. The contour length of the polymer segment being stretched varies due to both the polydispersity of the polymer sample and the random pick-up position on the dextran polymer by the AFM tip.

To investigate the influence of the solvent on the polymer, the solvent was changed from 1x PBS, which is a good solvent for dextran, stepwise from 10% v/v ethanol-PBS mixture up to 50% v/v ethanol-PBS mixture, which corresponds to poor solvent conditions. With advancing poor solvent conditions the dextran layer stiffness is altered from a soft to an almost perfectly stiff surface, which is seen by AFM in the force-extension curves, while the tip pushes into the dextran layer. This change in layer stiffness is due a change from a swollen coil conformation of the dextran molecules in good solvent to a collapsed state as a globule in poor solvent.

Fig. 1(b) shows a typical force-extension curve of dextran in good solvent (1x PBS). The pulling cycles of a single dextran polymer do not exhibit any force peaks or hysteresis between extension and relaxation, as in agreement with earlier publications.<sup>11,12</sup>

In contrast, if the solvent is switched to a 10% v/v ethanol-PBS mixture, peaks rarely arise in the pulling cycles. With increasing fraction of ethanol, the height and number of force peaks in the pulling cycles is growing (Fig. 1(c)). The force peaks do not have any ordered or distinct spacing or appeared in consecutive force-extension curves at the same contour length. Histograms of the force peaks of one cantilever-sample pair for different ethanol-PBS mixtures are shown in fig. 2. The maximum of the peak force distribution is growing with the ethanol concentration. Further, the histograms of these force peaks are very good describable with log-normal distribution. Therefore, without any assumption about a model, by which this histogram of force peaks might be correct described, we used a fit of a log-normal distribution to characterize the histograms. We determined from these fits the mode, i.e. the maximum of the distribution (see fig. 2, dashed line with short gaps), and the median (dashed line with long gaps).

A detailed evaluation of the maximum of the log-normal distribution fit from different experiments versus the fraction of ethanol in solution is presented in fig. 3(a). The maximum grows approximately proportional with the ethanol concentration. At 30 % v/v ethanol-PBS mixture and around 200 pN the maximum of the force peak distribution reaches saturation. In

contrast to the height of force peaks, the number of force peaks per force-extension curve continues to rise up without saturating to almost 2.5 peaks per trace in 50% v/v ethanol-PBS mixture (see Fig. 3(b)). Above 50% v/v ethanol the dextran layer is in a very compact state, and it is almost impossible neither to pick up molecules nor to accomplish the pulling cycles. Furthermore, we checked the reversibility of the experiment by flushing the fluid cell with 1x PBS after the measurement of all different ethanol-PBS mixtures and we recovered the same surface softness of the dextran layer as before and the same pulling cycles, without intermediate peaks. Also we checked, if a possible reformation of the self-associated state is hindered due to fast cycling times, we kept dwell times up to 2 s after the relaxation to assist a possible reformation, but without influence onto the curves.

Besides the force peaks, force plateaus emerged rarely in the pulling cycles in 10 to 50% v/v ethanol. We did not investigate these plateaus further, since these force plateaus have been already described in detail.<sup>2-5</sup> They are caused by increasing the poor solvent-polymer interface through sliding of the polymer chain into solution by applying a force to one end of the polymer.

One major advantage and advancement of this experimental setup in the field of single molecule force spectroscopy (SMFS) on polymers, especially in poor solvent conditions, is the application of the chair-boat confirmation as unique fingerprint for stretching a single molecule.

Up to now, typical SMFS measurements on the globule-coil transition needed a very low density of polymers on the surface that the measurement of single molecules could be assumed. This has the drawback that this single polymer can interact with both surfaces while stretching, the tip and the substrate, which might cause artifacts due to polymer-surface interaction. In our case, a thick layer (typically 50 nm to 100 nm) of dextran was used and while the pulling cycles the attached polymer was stretched and relaxed above the thick layer of dextran molecules, shielding it from the substrate and assuring that not the interaction of the polymer with the substrate is measured.

A relevant contribution of the AFM tip-dextran interaction to the force peaks can be excluded: first, we do not see peaks in good solvent, but are able to pick up dextran. Second, with increasing poor solvent conditions, it gets more difficult to pick up dextran polymers, even though the number and height of force peaks is rising, and above 50 % v/v ethanol-PBS mixture, it is almost impossible to pick up dextran.

In contrast to characterized force plateaus from previous studies,<sup>2-5</sup> the here observed force

peaks originate from a step-wise disassembly or transition of the polymer, reminiscent of the unfolding pattern of protein domains. Simulations predict that polyelectrolytes and neutral amphiphilic polymers are able to form pearl-necklace conformations under poor solvent conditions.<sup>13</sup> Elsewhere, the force peaks are described in Simulation as stick-release patterns, while the force plateaus as a sliding of chains.<sup>14,15</sup> Both pictures are compatible and depict here the dextran in poor solvent as a chain self-assembled in several domains in a pearl-necklace conformation.

Another possible model describes the force induced globule-coil transition for neutral polymers with a “ball and chain” configuration,<sup>16</sup> similar to other models.<sup>4</sup> But in contrast to other models, they predicted a large energy barrier between the “ball-and-chain” and unraveled states. And this large energy barrier results in force peaks at a constant pulling velocity, because the polymer has to overcome these barriers.

### **Conclusion.**

In summary, an experimental setup was introduced, which allows the monitoring of single molecule stretching events due to a conformational transition of dextran. We investigated with this system the hydrophobic collapse, i.e. the globule-coil transition, as a function of the solvent and showed that the chain-chain interactions of dextran result in force peaks in the force extension curves. A detailed investigation of these force peaks was presented for the first time for different solvent conditions. Thanks to the dextran layer and the unique single molecule dextran-fingerprint, highly reliable experimental data on the force-induced globule-coil transition could be gained.

## Figure Captions

**Figure 1.** (a) Schematic representation of the single molecule force spectroscopy experiment. (b) Force-extension curve of dextran in good solvent (1x PBS). Dextran exhibits a conformational chair-boat transition at around 800 pN. The pulling cycles are close to the dextran layer without toughing it again. (c) Typical force-extension curve under poor solvent conditions (20 % v/v ethanol-PBS mixture). Force peaks arise between the extensions of pulling cycles. In (a) the force-extension curve of (b) is caricatured with globular domains, which open step-by-step and thus elongating the contour length of the molecule.

**Figure 2.** Histograms of force peaks from force-extension curves for different PBS-Ethanol mixtures. To characterize the histograms, the force-distributions are fitted with a log-normal distribution. The mode, i.e. maximum of the log-normal distribution, is depicted with a dashed line with short gaps and the median with a dashed line with long gaps. Both maximum and median grow with ethanol concentration until they reach a constant value at about 30 % v/v ethanol.

**Figure 3.** (a) Maximum of the log-normal fit of the force histogram in dependence of PBS-Ethanol mixture. The Maximum of the force distribution grows with the ethanol concentration until it reaches saturation at around 200 pN and 30 % v/v ethanol-PBS mixture. (b) Number of force peaks per force-extension curve in dependence of ethanol-PBS mixture. In contrast to the mode of peak force from fig. 3 (a), the number of peaks per trace grows with ethanol concentration without reaching saturation.

## References

- (1) Chandler, D. *Nature* **2005**, *437*, 640.
- (2) Baumann, C.; Bloomfield, V.; Smith, S.; Bustamante, C.; Wang, M.; Block, S. *Biophys. J.* **2000**, *78*, 1965.
- (3) Gunari, N.; Balazs, A. C.; Walker, G. C. *J Am Chem Soc* **2007**, *129*, 10046.
- (4) Halperin, A.; Zhulina, E. B. *Macromolecules* **1991**, *24*, 5393.
- (5) Li, I. T. S.; Walker, G. C. *J Am Chem Soc* **2010**, *132*, 6530.
- (6) Gunari, N.; Walker, G. C. *Langmuir* **2008**, *24*, 5197.
- (7) Kellermayer, M.; Smith, S.; Granzier, H.; Bustamante, C. *Science* **1997**, *276*, 1112.
- (8) Marszalek, P.; Lu, H.; Li, H.; Carrion-Vazquez, M.; Oberhauser, A.; Schulten, K.; Fernandez, J. *Nature* **1999**, *402*, 100.
- (9) Rief, M.; Gautel, M.; Oesterhelt, F.; Fernandez, J.; Gaub, H. *Science* **1997**, *276*, 1109.
- (10) Fernandez, J.; Li, H. *Science* **2004**, *303*, 1674.
- (11) Marszalek, P.; Li, H.; Fernandez, J. *Nat Biotechnol* **2001**, *19*, 258.
- (12) Rief, M.; Oesterhelt, F.; Heymann, B.; Gaub, H. E. *Science* **1997**, *275*, 1295.
- (13) Vasilevskaya, V.; Khalatur, P.; Khokhlov, A. *Macromolecules* **2003**, *36*, 10103.
- (14) Wada, H.; Murayama, Y.; Sano, M. *Physical Review E* **2002**, *66*, 061912.
- (15) Wada, H.; Murayama, Y.; Sano, M. *Phys Rev E Stat Nonlin Soft Matter Phys* **2005**, *72*, 041803.
- (16) Cooke, I. R.; Williams, D. R. M. *Europhysics Letters* **2003**, *64*, 267.



**Figure 1.**

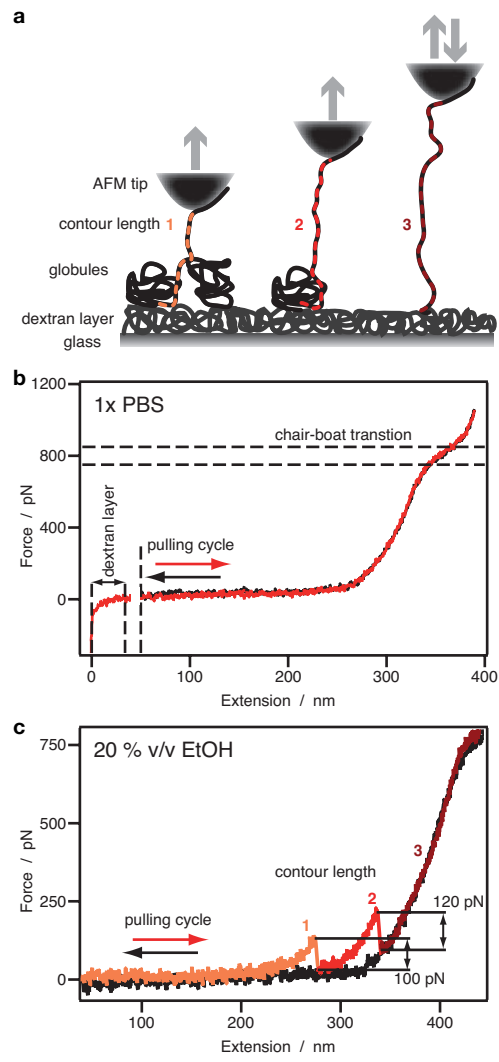


**Figure 2.**

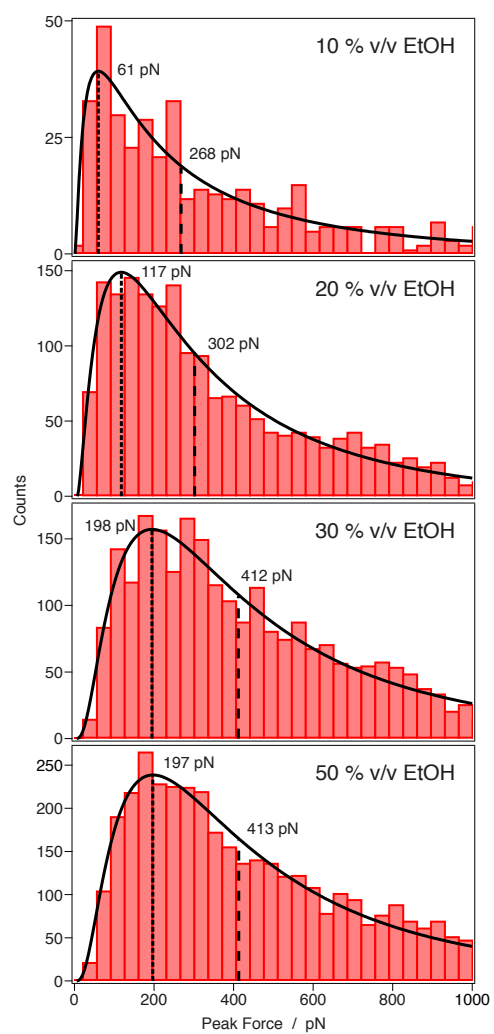
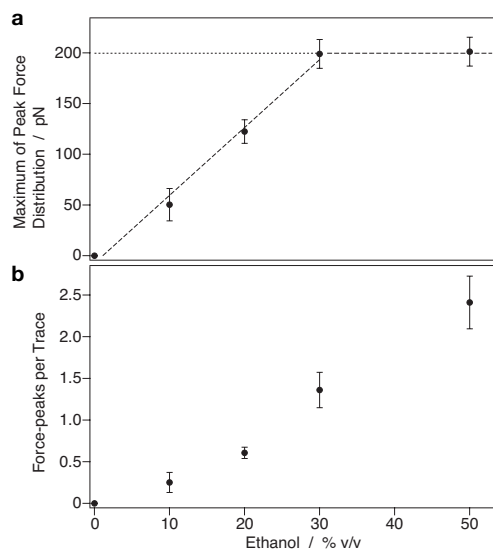


**Figure 3.**



## 8. Referenzen

1. Barabási, A.L., *The network takeover*. Nature Physics, 2011. **8**(1): p. 14-16.
2. Bulyk, M.L., *DNA microarray technologies for measuring protein-DNA interactions*. Current Opinion in Biotechnology, 2006. **17**(4): p. 422-30.
3. Fordyce, P.M., et al., *De novo identification and biophysical characterization of transcription-factor binding sites with microfluidic affinity analysis*. Nat Biotechnol, 2010. **28**(9): p. 970-976.
4. Maerkl, S.J. and S.R. Quake, *A systems approach to measuring the binding energy landscapes of transcription factors*. Science, 2007. **315**(5809): p. 233-7.
5. Segal, E., et al., *Predicting expression patterns from regulatory sequence in Drosophila segmentation*. Nature, 2008. **451**(7178): p. 535-540.
6. Evanko, D., *Next-generation protein binding*. Nat Meth, 2011.
7. Nutiu, R., et al., *Direct measurement of DNA affinity landscapes on a high-throughput sequencing instrument*. Nat Biotechnol, 2011. **29**(7): p. 659-U146.
8. Branton, D., et al., *The potential and challenges of nanopore sequencing*. Nat Biotechnol, 2008. **26**(10): p. 1146-1153.
9. Lieberman, K.R., et al., *Processive Replication of Single DNA Molecules in a Nanopore Catalyzed by phi29 DNA Polymerase*. J Am Chem Soc, 2010. **132**(50): p. 17961-17972.
10. Eid, J., et al., *Real-Time DNA Sequencing from Single Polymerase Molecules*. Science, 2009. **323**(5910): p. 133-138.
11. Pennisi, E., *GENOMICS Semiconductors Inspire New Sequencing Technologies*. Science, 2010. **327**(5970): p. 1190-1190.
12. Rothberg, J.M., et al., *An integrated semiconductor device enabling non-optical genome sequencing*. Nature, 2011. **475**(7356): p. 348-352.
13. Allis, C., et al., *Epigenetics2007*: Cold Spring Harbor Laboratory Press.
14. Babu, M.M., et al., *Structure and evolution of transcriptional regulatory networks*. Current Opinion in Structural Biology, 2004. **14**(3): p. 283-91.
15. Bartels, F., et al., *Specific binding of the regulatory protein ExpG to promoter regions of the galactoglucan biosynthesis gene cluster of Sinorhizobium meliloti - a combined molecular biology and force spectroscopy investigation*. J Struct Biol, 2003. **143**(2): p. 145-152.
16. Bizzarri, A.R. and S. Cannistraro, *The application of atomic force spectroscopy to the study of biological complexes undergoing a biorecognition process*. Chem Soc Rev, 2010. **39**(2): p. 734-749.
17. Koch, S.J., et al., *Probing protein-DNA interactions by unzipping a single DNA double helix*. Biophysical Journal, 2002. **83**(2): p. 1098-105.
18. Kühner, F., et al., *LexA-DNA bond strength by single molecule force spectroscopy*. Biophysical Journal, 2004. **87**(4): p. 2683-90.
19. Cao, Y., et al., *A functional single-molecule binding assay via force spectroscopy*. P Natl Acad Sci Usa, 2007. **104**(40): p. 15677-15681.
20. Merkel, R., et al., *Energy landscapes of receptor-ligand bonds explored with dynamic force spectroscopy*. Nature, 1999. **397**(6714): p. 50-3.
21. Moy, V.T., E. Florin, and H.E. Gaub, *Intermolecular Forces and Energies Between Ligands and Receptors*. Science, 1994. **266**(5183): p. 257-259.
22. Uhrig, K., et al., *Optical force sensor array in a microfluidic device based on holographic optical tweezers*. Lab Chip, 2009. **9**(5): p. 661-668.
23. Muenzel, M., D. Globisch, and T. Carell, *5-Hydroxymethylcytosine, the Sixth Base of the Genome*. Angew Chem Int Edit, 2011. **50**(29): p. 6460-6468.

24. Muenzel, M., et al., *Quantification of the Sixth DNA Base Hydroxymethylcytosine in the Brain*. *Angew Chem Int Edit*, 2010. **49**(31): p. 5375-5377.
25. Pfaffeneder, T., et al., *The Discovery of 5-Formylcytosine in Embryonic Stem Cell DNA*. *Angew Chem Int Edit*, 2011. **50**(31): p. 7008-7012.
26. Blackburn, G.M., M.J. Gait, and D. Loakes, *Nucleic Acids in Chemistry and Biology* 2006: RSC Publishing.
27. Kim, Y.C., et al., *Refinement of Eco RI endonuclease crystal structure: a revised protein chain tracing*. *Science*, 1990. **249**(4974): p. 1307-9.
28. Jen-Jacobson, L., *Protein-DNA recognition complexes: conservation of structure and binding energy in the transition ....* *Biopolymers*, 1997. **44**: p. 153-180.
29. Bell, G., *Models for the Specific Adhesion of Cells to Cells*. *Science*, 1978. **200**(4342): p. 618-627.
30. Dudko, O., et al., *Beyond the conventional description of dynamic force spectroscopy of adhesion bonds*. *P Natl Acad Sci Usa*, 2003. **100**(20): p. 11378-11381.
31. Evans, E. and K. Ritchie, *Dynamic strength of molecular adhesion bonds*. *Biophys J*, 1997. **72**(4): p. 1541-1555.
32. Evans, E. and K. Ritchie, *Strength of a weak bond connecting flexible polymer chains*. *Biophys J*, 1999. **76**(5): p. 2439-47.
33. Jaenisch, R. and A. Bird, *Epigenetic regulation of gene expression: how the genome integrates intrinsic and environmental signals*. *Nat Genet*, 2003. **33**: p. 245-254.
34. Ballestar, E. and A. Wolffe, *Methyl-CpG-binding proteins - Targeting specific gene repression*. *Eur J Biochem*, 2001. **268**(1): p. 1-6.
35. Straussman, R., et al., *Developmental programming of CpG island methylation profiles in the human genome*. *Nat Struct Mol Biol*, 2009. **16**(5): p. 564-571.
36. Baylin, S. and J. Herman, *DNA hypermethylation in tumorigenesis - epigenetics joins genetics*. *Trends Genet*, 2000. **16**(4): p. 168-174.
37. Derreumaux, S., et al., *Impact of CpG methylation on structure, dynamics and solvation of cAMP DNA responsive element*. *Nucleic Acids Res*, 2001. **29**(11): p. 2314-2326.
38. Geahigan, K., et al., *The dynamic impact of CpG methylation in DNA*. *Biochemistry-U.S.*, 2000. **39**(16): p. 4939-4946.
39. Mayer-Jung, C., D. Moras, and Y. Timsit, *Hydration and recognition of methylated CpG steps in DNA*. *Embo J*, 1998. **17**(9): p. 2709-2718.
40. LEFEBVRE, A., et al., *SEQUENCE-DEPENDENT EFFECTS OF CPG CYTOSINE METHYLATION - A JOINT H-1-NMR AND P-31-NMR STUDY*. *Eur J Biochem*, 1995. **229**(2): p. 445-454.
41. Wojdacz, T.K., A. Dobrovic, and L.L. Hansen, *Methylation-sensitive high-resolution melting*. *Nat Protoc*, 2008. **3**(12): p. 1903-1908.
42. Globisch, D., et al., *Tissue Distribution of 5-Hydroxymethylcytosine and Search for Active Demethylation Intermediates*. *PLoS ONE*, 2010. **5**(12): p. e15367.
43. Szwagierczak, A., et al., *Sensitive enzymatic quantification of 5-hydroxymethylcytosine in genomic DNA*. *Nucleic Acids Research*, 2010. **38**(19): p. e181.
44. Song, C.-X., et al., *Selective chemical labeling reveals the genome-wide distribution of 5-hydroxymethylcytosine*. *Nat Biotechnol*, 2010: p. 1-8.
45. Rothmund, P., *Folding DNA to create nanoscale shapes and patterns*. *Nature*, 2006. **440**(7082): p. 297-302.
46. Steinhauer, C., et al., *DNA Origami as a Nanoscopic Ruler for Super-Resolution Microscopy*. *Angew Chem Int Edit*, 2009. **48**(47): p. 8870-8873.
47. Kuzyk, A., et al., *DNA-based self-assembly of chiral plasmonic nanostructures with tailored optical response*. *Nature*, 2012. **483**(7389): p. 311-314.
48. Krishnan, Y. and F.C. Simmel, *Nucleic Acid Based Molecular Devices*. *Angew Chem Int Edit*, 2011. **50**(14): p. 3124-3156.
49. Yurke, B., et al., *A DNA-fuelled molecular machine made of DNA*. *Nature*, 2000. **406**(6796): p. 605-608.

50. Kufer, S.K., et al., *Single-molecule cut-and-paste surface assembly*. Science, 2008. **319**(5863): p. 594-596.
51. Kufer, S.K., et al., *Optically monitoring the mechanical assembly of single molecules*. Nature Nanotechnology, 2009. **4**(1): p. 45-49.
52. Essevaz-Roulet, B., U. Bockelmann, and F. Heslot, *Mechanical separation of the complementary strands of DNA*. Proc Natl Acad Sci USA, 1997. **94**(22): p. 11935-11940.
53. Krautbauer, R., M. Rief, and H.E. Gaub, *Unzipping DNA oligomers*. Nano Lett, 2003. **3**(4): p. 493-496.
54. Rief, M., H. Clausen-Schaumann, and H.E. Gaub, *Sequence-dependent mechanics of single DNA molecules*. Nat Struct Biol, 1999. **6**(4): p. 346-349.
55. Florin, E., V.T. Moy, and H.E. Gaub, *Adhesion forces between individual ligand-receptor pairs*. Science, 1994. **264**(5157): p. 415-7.
56. Puchner, E.M. and H.E. Gaub, *Force and function: probing proteins with AFM-based force spectroscopy*. Curr Opin Struct Biol, 2009. **19**(5): p. 605-614.
57. Kellermayer, M., et al., *Folding-unfolding transitions in single titin molecules characterized with laser tweezers*. Science, 1997. **276**(5315): p. 1112-1116.
58. Smith, S., Y. Cui, and C. Bustamante, *Overstretching B-DNA: The elastic response of individual double-stranded and single-stranded DNA molecules*. Science, 1996. **271**(5250): p. 795-799.
59. Strick, T., et al., *The elasticity of a single supercoiled DNA molecule*. Science, 1996. **271**(5257): p. 1835-1837.
60. Strick, T., et al., *Behavior of supercoiled DNA*. Biophysical Journal, 1998. **74**(4): p. 2016-2028.
61. Viani, M., et al., *Small cantilevers for force spectroscopy of single molecules*. Journal of Applied Physics, 1999. **86**(4): p. 2258-2262.
62. Gittes, F. and C. Schmidt, *Thermal noise limitations on micromechanical experiments*. Eur Biophys J Biophys, 1998. **27**: p. 75-81.
63. Albrecht, C.H., et al., *DNA: a programmable force sensor*. Science, 2003. **301**(5631): p. 367-70.
64. Blank, K., et al., *A force-based protein biochip*. Proc Natl Acad Sci USA, 2003. **100**(20): p. 11356-60.
65. Albrecht, C.H., H. Clausen-Schaumann, and H.E. Gaub, *Differential analysis of biomolecular rupture forces*. Journal of Physics: Condensed Matter, 2006. **18**: p. 581-599.
66. Albrecht, C.H., et al., *Molecular force balance measurements reveal that double-stranded DNA unbinds under force in rate-dependent pathways*. Biophysical Journal, 2008. **94**(12): p. 4766-74.
67. Severin, P.M.D., D. Ho, and H.E. Gaub, *A high throughput molecular force assay for protein-DNA interactions*. Lab Chip, 2011. **11**(5): p. 856-62.
68. Dose, C., et al., *Recognition of "mirror-image" DNA by small molecules*. Angew Chem Int Edit, 2007. **46**(44): p. 8384-7.
69. Ho, D., et al., *Quantitative detection of small molecule/DNA complexes employing a force-based and label-free DNA-microarray*. Biophys J, 2009. **96**(11): p. 4661-71.
70. Morfill, J., et al., *B-S transition in short oligonucleotides*. Biophysical Journal, 2007. **93**(7): p. 2400-2409.
71. Strunz, T., et al., *Dynamic force spectroscopy of single DNA molecules*. Proc Natl Acad Sci USA, 1999. **96**(20): p. 11277-82.
72. Koch, S.J. and M.D. Wang, *Dynamic force spectroscopy of protein-DNA interactions by unzipping DNA*. Phys Rev Lett, 2003. **91**(2): p. 028103.
73. Sidorova, N. and D. Rau, *The dissociation rate of the EcoRI-DNA-specific complex is linked to water activity*. Biopolymers, 2000. **53**(5): p. 363-368.
74. Bustamante, C., et al., *Mechanical processes in biochemistry*. Annu Rev Biochem, 2004. **73**: p. 705-748.

75. Dervan, P.B., et al., *Regulation of gene expression by synthetic DNA-binding ligands*. Top Curr Chem, 2005. **253**: p. 1-31.
76. Herman, D., E. Baird, and P.B. Dervan, *Stereochemical control of the DNA binding affinity, sequence specificity, and orientation preference of chiral hairpin polyamides in the minor groove*. J Am Chem Soc, 1998. **120**(7): p. 1382-1391.
77. Dehner, A., et al., *Cooperative binding of p53 to DNA: regulation by protein-protein interactions through a double salt bridge*. Angew Chem Int Edit, 2005. **44**(33): p. 5247-51.
78. Römer, L., et al., *p53--a natural cancer killer: structural insights and therapeutic concepts*. Angew Chem Int Edit, 2006. **45**(39): p. 6440-6460.
79. Kriaucionis, S. and N. Heintz, *The Nuclear DNA Base 5-Hydroxymethylcytosine Is Present in Purkinje Neurons and the Brain*. Science, 2009. **324**(5929): p. 929-930.
80. Tahiliani, M., et al., *Conversion of 5-Methylcytosine to 5-Hydroxymethylcytosine in Mammalian DNA by MLL Partner TET1*. Science, 2009. **324**(5929): p. 930-935.
81. Bloomfield, V.A., D. Crothers, and I. Tinoco, *Nucleic Acids: Structures, Properties, and Functions* 2000: University Science Books.
82. Rauch, C., et al., *C5-methylation of cytosine in B-DNA thermodynamically and kinetically stabilizes BI (Supporting Mat.)*. J Am Chem Soc, 2003: p. 1-2.
83. Cheng, W., et al., *NS3 helicase actively separates RNA strands and senses sequence barriers ahead of the opening fork*. Proc Natl Acad Sci USA, 2007. **104**(35): p. 13954-13959.
84. Dumont, S., et al., *RNA translocation and unwinding mechanism of HCVNS3 helicase and its coordination by ATP*. Nature, 2006. **439**(7072): p. 105-108.
85. Johnson, D.S., et al., *Single-molecule studies reveal dynamics of DNA unwinding by the ring-shaped T7 helicase*. Cell, 2007. **129**(7): p. 1299-1309.
86. Gerber, D., S.J. Maerkl, and S.R. Quake, *An in vitro microfluidic approach to generating protein-interaction networks*. Nat Meth, 2009. **6**(1): p. 71-4.
87. Larson, M.H., R. Landick, and S.M. Block, *Single-molecule studies of RNA polymerase: one singular sensation, every little step it takes*. Molecular Cell, 2011. **41**(3): p. 249-62.
88. Zhou, J., et al., *Applied force provides insight into transcriptional pausing and its modulation by transcription factor NusA*. Molecular Cell, 2011. **44**(4): p. 635-46.
89. Ha, T., *Need for speed: Mechanical regulation of a replicative helicase*. Cell, 2007. **129**(7): p. 1249-1250.
90. Yu, J., et al., *Coupling Translocation with Nucleic Acid Unwinding by NS3 Helicase*. J Mol Biol, 2010. **404**(3): p. 439-455.
91. Wuite, G., et al., *Single-molecule studies of the effect of template tension on T7 DNA polymerase activity*. Nature, 2000. **404**(6773): p. 103-106.

## 9. Lebenslauf

Philip Magnus Dirk SEVERIN

Geboren am 19. November 1981 in Aachen

als Sohn des Dr. rer. nat. Dirk J.E Severin und seiner Frau Carmen, geb. Schrader

1988 – 1992 Grundschule Münsing/Starnberger See

1992 – 2001 Gymnasium Starnberg, Starnberg

2001 Abitur im naturwissenschaftlich-mathematischen Zweig

2001 – 2002 Bundeswehr, Luftwaffe

ab 2002 Ludwig – Maximilians - Universität, München (LMU)

Studium der Physik mit den Schwerpunkten  
Biophysik und Physikalische Chemie

2003 Vordiplom in Physik

2006 April bis Oktober University of British Columbia, Vancouver  
Visiting Scholar and Faculty Member

2007 – 2008 Diplomarbeit am Lehrstuhl für Angewandte Physik und Biophysik  
Professor Dr. Hermann E. Gaub

2008 Diplom in Physik

2008 – 2012 Dissertation am Lehrstuhl für Angewandte Physik und Biophysik  
Professor Dr. Hermann E. Gaub

Stipendium der Bayerischen Forschungsstiftung 2006

Stipendium des Elitenetzwerk Bayern seit 2008  
(International Doctorate Program NanoBioTechnology)

Mitglied des NIM (Nanosystems Initiative Munich)  
Graduate Programs seit 2010



## 10. Danksagung

An dieser Stelle möchte ich ganz herzlich bei allen Bedanken, die mich während meiner Doktorarbeit begleitet und unterstützt haben.

Größter Dank gilt meinem Doktorvater Hermann Gaub, der mich in jeder Hinsicht gefördert hat. Er stand mir jederzeit auf herzliche Art mit Rat, Inspiration und Zuspruch zur Seite und hat mir äußerst spannende und lehrreiche Projekte ermöglicht.

Darüber hinaus möchte ich mich für das unvergleichlich gute Arbeitsklima bedanken, welches durch kulinarische Köstlichkeiten wie Spaghetti Vongole auf der Dachterrasse, Wildschwein am Spieß, russisches Weihnachtsdinner, Schwenkfleisch am Schliersee, Lachs aus der Mailbox und Gamsragout bestens gefördert wurde.

Meinem IDK-Mentor Philip Tinnefeld möchte ich für Unterstützung und Rat danken, wie auch dem IDK und seinen Mitarbeitern, vor allem Marie-Christine Blüm und Marilena Pinto für das vielseitige und interdisziplinäre Forschungs- und Bildungsprogramm.

Der ganzen Gambicrew möchte ich für die unvergleichlich angenehme, abwechslungsreiche und inspirierende Zeit Dank sagen. Besonders:

Christian Albrecht und Ferdinand Kühner, die mich für die Biophysik begeistert haben und mit denen ich meine ersten Schritte in der Forschung gegangen bin.

Dominik Ho für eine klasse Zeit am Lehrstuhl: die gemeinsame Zeit war sowohl wissenschaftlich sehr produktiv als auch außerhalb der Forschung einfach grandios.

Den „Stemplerinnen“, Katja Falter und Uta Wienken für interessante Diskussionen, große Hilfsbereitschaft und eine fantastische Zeit, auch außerhalb des Labors.

Kamila Klamecka für eine gute Zusammenarbeit und das unermüdliche Herstellen von Proteinen für das Nanobody- und MeCP2-Projekt.

Stephan Heucke, Stefan Stahl und Mathias Strackharn für sehr interessante „Zero-Mode Waveguide“- und „Single Molecule Cut- and Paste“-Experimente.

Christoph Wienken für den inneren Ausgleich, den wir zusammen in Cafés oder auch in der ein- oder anderen Bar gefunden haben.

Hermann Gump für kulinarische „Wirtshausbesuche“ und inspirierende Diskussionen, auch außerhalb der Physik.

Elias Puchner, Jan Vogelsang, Matthias Erdmann, Philip Baaske, Franz Weinert, Stefan Kufer, Ingo Stein und Stefan Scheuer für die Unterstützung bei Versuchen, hilfreiche Diskussionen, gesellige Grillzeiten und lange Poker-, Bar- und Shishaabende.

Marcus Otten und Daniela Aschenbrenner, den Nachfolgern, dass ich das Projekt des molekularen Kraftsensors in guten Händen weiß.

Astrid Zeder und Jakov Krolo für Ihr großes Engagement als Bachelorstudenten.

Ralf David, Angelika Kardinal und Thomas Nicolaus für die Unterstützung im Chemielabor.

Klaus Schulten und Xueqing Zou von der Universität in Illinois, Urbana-Champaign, möchte ich für die sehr spannende Kollaboration bezüglich der DNA-Methylierung und Hydroxymethylierung danken, für viele lehrreiche Diskussionen, und dass ihr den „Tanz der Moleküle im Nanosekunden-Tempo“ sichtbar gemacht habt.

Hongbin Li von der Universität von British Columbia, Vancouver, möchte ich für eine lehrreiche und schöne Zeit und viele inspirierende Diskussionen danken.

Heinrich Leonhardt für die gute Betreuung im Nanobody- und im MeCP2-Projekt.

Stephen Quake und Matthias Meier aus der Stanford Universität für die Einführung in die Herstellung von MITOMI-Mikrofluidik-Chips.

Jörg Kotthaus, Bert Lorenz und Philipp Altpeter für die Möglichkeit den Reinraum für die Mikrofluidik-Chipherstellung nutzen zu dürfen.

Den Korrekturlesern meiner Arbeit möchte ich für die Unterstützung im Endspurt danken: Mathias Strackharn, Jan Vogelsang und Dirk Severin.

Bei meiner Freundin Lena Tillmann möchte ich mich bedanken, die mir während meiner gesamten Doktorarbeit immer zur Seite stand.

Zuletzt möchte ich meinen Eltern Carmen und Dr. Dirk Severin danken, die mich immer auf meinem Weg unterstützt und motiviert haben.